Flows at molecular scales : probing and manipulating ultra-thin liquid films

Martin Maza Cuello

PSL UNIVERSITÉ PARIS

THÈSE DE DOCTORAT

DE L'UNIVERSITÉ PSL

Préparée à ESPCI Paris

Ecoulements aux échelles moléculaires : étude et contrôle de films liquides ultra minces

Flows at molecular scales: probing and manipulating ultra-thin liquid films

Soutenue par

Martin MAZA-CUELLO

Le 15 octobre 2021

École doctorale n°397

Physique et Chimie des Matériaux

Spécialité

Physico-chimie

Composition du jury :

M. Thomas BICKEL Professeur, Université de Bordeaux	*Président*
M. Arnaud ANTKOWIAK Professeur, Sorbonne Université	*Examinateur*
Mme. Isabelle CANTAT Professeur, Université de Rennes I	*Rapporteure*
Mme. Cécile COTTIN-BIZONNE Directeure de Recherche, Université Claude Bernard Lyon 1	*Rapporteure*
M. Christian FRETIGNY Directeur de Recherche, ESPCI Paris	*Co-directeur de thèse*
M. Matthieu ROCHÉ Chargé de recherche, Université de Paris	*Examinateur*
Mme. Laurence TALINI Directeure de Recherche, CNRS	*Directeure de thèse*

ESPCI PARIS | PSL

PSL UNIVERSITÉ PARIS

THÈSE DE DOCTORAT

DE L'UNIVERSITÉ PSL

Préparée à ESPCI Paris

Ecoulements aux échelles moléculaires : étude et contrôle de films liquides ultra minces

Flows at molecular scales: probing and manipulating ultra-thin liquid films

Soutenue par

Martin MAZA-CUELLO

Le 15 octobre 2021

École doctorale n°397

Physique et Chimie des Matériaux

Spécialité

Physico-chimie

Composition du jury :

M. Thomas BICKEL Professeur, Université de Bordeaux	*Président*
M. Arnaud ANTKOWIAK Professeur, Sorbonne Université	*Examinateur*
Mme. Isabelle CANTAT Professeur, Université de Rennes I	*Rapporteure*
Mme. Cécile COTTIN-BIZONNE Directeure de Recherche, Université Claude Bernard Lyon 1	*Rapporteure*
M. Christian FRETIGNY Directeur de Recherche, ESPCI Paris	*Co-directeur de thèse*
M. Matthieu ROCHÉ Chargé de recherche, Université de Paris	*Examinateur*
Mme. Laurence TALINI Directeure de Recherche, CNRS	*Directeure de thèse*

ESPCI PARIS | PSL

Acknowledgements

I am indebted to Laurence Talini and Christian Fretigny for their supervision during these three years. Their patient guidance, precise remarks and continuous availability have been essential for the success of this project.

I thank all the members of the jury for kindly accepting the invitation to participate in the jury of this thesis. I am grateful to Isabelle Cantat and Cécile Cottin-Bizonne for their very encouraging reports, as well as for the enriching discussions that them, together with jury members Arnaud Antkowiak, Thomas Bickel and Matthieu Roché, brought up during the defense. All their questions have served to further my understanding of my thesis' subject.

I would like to thank all the team of the SIMM lab for their conviviality, with special thanks to Antoine Chateauminois and Emily Verneuil for interesting discussions and their daily amiability throughout my time in this lab.

Part of the experimental setup used in thesis was designed and built with the help of l'atelier at the SIMM, and the experimental cells where prepared with machines at the Plateforme Technologique of the IPGG. To both teams of technicians and engineers I am grateful for their availability and help.

This project would not have been possible without the financial support of the Marie Skłodowska-Curie Actions of the European Commission through the UPtoPARIS international doctoral COFUND programme. I thank the European team of the ESPCI for providing a much-needed support with administrative procedures, and for organizing networking events and seminars to enrich the experience of the doctoral programme. Thanks to the broad scope of the programme, I could meet, learn from and share knowledge with great and passionate fellows from every corner of the world.

Many people has accompanied me at the lab during these years. I specially thank the people that welcomed me at my office when I arrived: Francisco, Cécile and Gabriel. Settling into this new environment was much simpler thanks to them. I was also very lucky to have the company of Cyprien, who was able to convince me to sing again in a choir. I dedicate a warm thank you to Anusree, Flora-Maud, Lola, Pascal and Victoria who also took care of me during these complicated times and helped me navigate the turmoil of the thesis.

I thank my friends and family, for all their long-standing support even in the distance.

I am most indebted to my parents, Diego and Paulina, for their permanent example of perseverance and integrity.

And to Raquel, for her unwavering confidence in me.

Contents

Introduction

The question of how a liquid will spread (or not) onto a solid surface has been extensively addressed in the last decades [1, 2]. At large scales, the wetting process under the action of the capillary force, possibly combined with the action of gravity, is fully described by hydrodynamical considerations. However, boundary conditions are not well determined. In particular, the description of molecular transfers at the contact line remains a matter of debate and it is not well established. As a result, the flow in a thick (i.e. thicker than a few tenths of microns) liquid film, is fully accounted for in the frame of the lubrication approximation [3], but the apparition of contact lines requires the introduction of a molecular cut-off length in order to solve the problem.

For thinner films, the description is even more complex since it becomes necessary to consider the effects of the interactions between the interfaces of the film. In most cases, these interactions are of dipolar nature and in all cases their associated energy depends on film thickness [4]. As a consequence, when the liquid flows, either spontaneously or because of some imposed external driving force, the flow is controlled by the effects of intermolecular forces; this coupling is made complex by the thickness-dependency of these interactions, which, in addition, are poorly known at nanometric thicknesses. Investigations at very small scales are therefore needed to fully understand the apparently-already-solved problem of liquids spreading or dewetting solid substrates, and the present work aims at contributing to these investigations.

In the previous decades, the development of different experimental techniques has shed light on the interfacial interactions in liquid films [5, 6]. For instance, the Surface Force Apparatus, in which two interfaces are approached at nanometric distances and both the force between the interfaces and their distance are measured [7], has been widely used to determine the thickness variations of the interactions between two interfaces. Similarly, the Thin Film Pressure Balance allows to form a film – either suspended or supported – at an imposed pressure (a review of results with this technique can be found in Ref. [6]). The variations in thickness of the films as a function of pressure provide a characterization of interfacial interactions. Other techniques with enhanced accuracy exist, which will not be detailed here; however, all these techniques, including the two cited above, explore the behaviour of liquid films of nanometric thicknesses, which is a situation different from the spontaneous spreading of a drop that involves film thicknesses ranging from nanometric to macroscopic scales.

In this thesis, we investigate the thinning dynamics of films tens of micrometres thick down to 10 nm via the thermocapillary effect, allowing us to study the effect of intermolecular interactions in a dynamical setting.

The thermocapillary effect belongs to the family of Marangoni flows, which are produced by a gradient on the surface tension of the liquid. The variation of surface tension

imposes an interfacial stress at the liquid interface, and a surface flow drags the liquid from regions of lower to larger surface tension. The gradient of the surface tension can be established by its dependence on other physical properties, such as the concentration of surfactants or the temperature. It has aroused interest in recent years because it provides ways to introduce flows in versatile geometries with numerous applications, for example the measurement of critical micelle concentration of surfactants [8], detection of ultra-small surfactant concentration [9], or propulsion of swimmers [10].

The Marangoni flow due to a thermal gradient is called the thermocapillary effect. Some explanations of the relationship of surface tension with temperature were already given a century ago by an analogy with the density of ideal gases [11]; in more recent accounts, it is still obtained from a relationship of surface tension to density (for example [12]) but it is still not perfectly understood. Experimentally, for simple liquids it is typically found to decrease linearly with increasing temperature T. The variation of surface tension γ with temperature is small, typically $|d\gamma/dT| \lesssim 1 \times 10^{-4}\,\mathrm{N\,m^{-1}\,K^{-1}}$, however flows can be easily produced with a local temperature difference of some Kelvins.

The thermocapillary effect on a liquid film was already reported more than eighty years ago [13], and it has continued to draw the attention of researchers. Several areas of research have arisen focusing on different aspects of this effect. Without begin exhaustive, we illustrate this diversity by reviewing some of the processes addressed.

For example, with the advent of the laser, studies of the coupling of hydrodynamics and heat transport proved relevant, for instance, in the context of micromachining processes with molten metals, see for example Refs.[14, 15]. In this system, a strong laser beam is shined on the surface of a body of metal, producing the melting of an upper layer which is driven mainly by the surface tension gradient. The large temperature increase of the system, on the order of $\sim 1 \times 10^3\,\mathrm{K}$, induces a strong coupling between mass and thermal transport which can induce technically undesirable capillary instabilities or drop formation. In recent years, a similar principle has been applied in the micropatterning of polymer melts for lithography techniques, see Ref. [16] for a recent review.

The thermocapillary effect has also been studied when the fluid is forced to flow against the action of gravity in an inclined plane. The opposition of these two effects can induce the apparition of shock-like structures for micrometre-thick films [17, 18], as well as different types of instabilities in millimetre-thick films [19, 20] that depend on the direction of the thermal gradient with respect to the mean flow of the liquid.

This effect cannot only be applied to films but also to the control of drops, for instance in non-wettable surfaces [21]. Understanding the behaviour of fluids at even smaller scales is needed in particular because of its implications in recent industrial applications in which fluids are highly confined like microfluidics [22–24].

In this work, we use the thermocapillary effect for controlling the local thinning of thin liquid films down to a scale of tens of nanometres, allowing us to study the intermolecular interactions of the solid/liquid/air system, still poorly known in this thickness range for non polar liquids. This process can be promoted with a small temperature difference of some Kelvins, therefore this technique has the advantage of not changing the liquid properties throughout an experiment.

This thesis is divided as follows. In the first chapter, we begin our discussion by reviewing the hydrodynamic framework leading to the thin film equation driven by the thermocapillary effect. We illustrate the resulting evolution by integrating numerically

the equation using typical experimental parameters, assuming that the liquid completely wets the surface. We focus on the apparition of an ultra-thin film at the region where the gradient of the thermal field is strongest, and describe a regime in which the local evolution at this region is solely controlled by the action of the thermocapillary effect, all pressure terms being negligible. From this point onwards, the local dynamics is a result of the interplay between the thermocapillary effect and the intermolecular forces of the system only. An approximation of the stationary state in this region brings evidence to the possibility of neglecting both capillary and gravitational pressures at long times. Finally, we explain a procedure to characterise the intermolecular forces of the system if the evolution of the thickness profile and the gradient of the thermal field imposed are known.

From the discussion of the hydrodynamical model, we obtain various time- and length-scales that must be considered in the experimental design, which is described in the second chapter. The experimental setup built to follow the dynamics of thin liquid films on glass implements two optical, non-invasive techniques destined to measure the evolution of the thickness profile of the liquid above and below the micrometre scale, respectively. Further comments about experimental considerations for performing an experiment are also given, together with a brief discussion on the numerical integration of the thin film equation.

Experimental results are discussed in the last two chapters. The third chapter is dedicated to the dynamics of silicone oils, which wet completely our glass substrate. We demonstrate experimentally the regime for which all pressure contributions are negligible against the action of thermocapillarity in a range of experimental parameters, and show that it can be further analysed to obtain the temperature gradient that is being imposed on the liquid. From the evolution of the height profile together with the gradient of the thermal field we are able to experimentally obtain the derivative of the disjoining pressure with respect to the thickness of the film.

The fourth chapter is divided in two parts. The first part deals with the evolution of two alkanes on the same system. We find that, contrary to the silicone oil, the alkane films appear to be unstable at very small thicknesses, forming a receding foot that leaves behind a region of thickness below the sensitivity of our interferometric setup. We give arguments discussing the possibility of these films being in a pseudo-partial wetting regime. The second part shows preliminary experiments on the relaxation dynamics of the films starting from the nonequilibrium steady-state, which could offer the possibility of performing spreading studies where the initial configuration is experimentally defined via the imposed temperature gradient before relaxation.

A final section gives the summary and conclusions of the thesis, indicating open questions and possibilities for future work.

Chapter 1

Hydrodynamic model

1.1 Introduction

In this thesis, we aim to explore the effect of intermolecular forces of thin liquid films supported by a solid substrate in a dynamical context, inducing the evolution of the films via thermocapillarity. The thermal field will be generated utilising the dissipated power of a printed electrical circuit on the substrate, which allows a versatile control of the geometry of the system. Furthermore, using interferometry to recover the thickness of the fluid over a large (millimetric) region allows to decouple the driving of the thermocapillary effect from the measurement of the dynamic height profile of the liquid, which can be done at the relevant length scale of the process. This will provide the control necessary to measure the effect of intermolecular forces, and moreover to recover the dependence of the disjoining pressure with the thickness in this dynamical setup. All the details of the experimental setup will be given in chapter 2.

In this chapter, we consider the theoretical background on thermocapillary-driven dynamics of thin liquid films, in particular with the aim of understanding how the effect of intermolecular forces can be recovered from the knowledge of the dynamics. In Sec. 1.2 we review the development of the thin film equation, describing the evolution of the liquid/air interface $h(t, \mathbf{x})$, driven by thermocapillary. In Sec. 1.3 we show the typical evolution by numerically integrating this equation, and analyse how the different contributions to the liquid's pressure change their relative strengths at successive time regimes. We will consider gravitational, Laplace and disjoining pressures. The disjoining pressure models the intermolecular interactions between the solid substrate and the ambient air through the liquid layer, and it is described with the form of a van der Waals term favouring the thickening of the film. In Sec. 1.4 we show that the evolution at the region of largest thermal field gradient is well described by neglecting all pressure terms against the thermocapillary effect for thicknesses on the range from 0.1 to 1 µm. We describe the transition towards a long-time regime of competition between the thinning effect of thermocapillarity opposed by the swelling effect of disjoining pressure and determine the time scale of this reduced evolution. In Sec. 1.5 we describe the characteristics of the stationary state. In particular, we show that the remaining ultra-thin film is indeed nanometric in thickness, and furthermore it may extend over a lateral range of several millimetres. We explore in Sec. 1.6 the consequences of the orders of magnitudes obtained for time and lateral extension of the dynamics to the design of the experiment. Further-

more, in Sec. 1.7 we introduce a procedure to obtain the dependence of the derivative of the disjoining pressure with respect to the thickness of the film from the dynamics of the height profile $h(t, \mathbf{x})$ that can be measured in experiments. Finally, we conclude in Sec. 1.8 by reviewing the main results and objectives set for the experiments.

1.2 Thin film equation driven by thermocapillarity

1.2.1 Characteristics of the system

We start by reviewing here the main steps of the derivation of the thin film equation in the presence of thermocapillarity, to lay the ground of the discussion of experimental measurements described in following chapters. A thin liquid film of mean thickness h_0 covers a solid surface. The liquid has uniform viscosity η and density ρ. It is incompressible and does not evaporate. The solid/liquid interface defines the $z = 0$ plane. The in-plane directions are represented by Cartesian coordinates, denoted by $\mathbf{x} = (x, y)^\top$. The local heating of the solid/liquid interface is represented by a positive temperature field $\theta(\mathbf{x})$, measured with respect to the (assumed constant) ambient temperature.

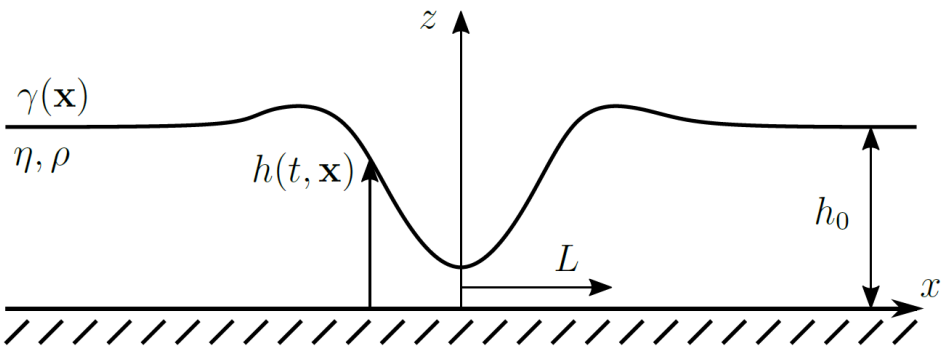

Figure 1.1: Sketch of the liquid film driven by thermocapillary, with main parameters and variables, assuming invariance on the y direction.

The presence of a non-homogeneous thermal field $\theta(\mathbf{x})$ creates a variable surface tension $\gamma(\mathbf{x})$ promoting an interfacial flow at the free interface of the liquid, $z = h(t, \mathbf{x})$, which evolves over time. This is called the thermocapillary effect. We would like to describe the evolution of the height profile $h(t, \mathbf{x})$ resulting from imposing a specific surface tension gradient.

In the thermocapillary-driven system, the complete equations should also include the coupled evolution of the temperature inside the fluid, in particular how a thermal gradient on the vertical direction is established. To know which is the prevalent thermal mechanism, we make an estimation of the thermal Péclet number measuring the ratio of advective to diffusive rates. The thermal Péclet number is defined as $\mathrm{Pe} \equiv h_0 v_0/\kappa$, where we take h_0 as the typical thickness over which the thermal gradient would be established, v_0 is a characteristic system velocity and κ the thermal diffusivity of the liquid. As we shall see in chapter 2, the experimental values of these quantities are of order $h_0 \sim 30\,\mu\mathrm{m}$,

$v_0 \sim 1\,\mu\mathrm{m\,s}^{-1}$, and the thermal diffusivity is around $\kappa \sim 1 \times 10^5\,\mu\mathrm{m}^2\,\mathrm{s}^{-1}$ for silicone oils [25]. With these values, $\mathrm{Pe} \sim 10^{-3}$ meaning that diffusion dominates the thermal transport. Furthermore, the characteristic time it takes for the fluid to establish this thermal field is of order $h_0^2/\kappa \sim 10\,\mathrm{ms}$. This scale is much smaller than any of the other time scales that will be considered later on in the dynamics. Therefore, we assume that the temperature field is instantaneously set throughout the liquid, and that its value at a given position $\mathbf{x}$ is constant along the thickness of the film.

If the imposed temperature field heating the surface is small, the surface tension of pure liquids decreases linearly [11, 12]

$$\gamma(\mathbf{x}) = \gamma_0 - \gamma_\theta \theta(\mathbf{x}) \tag{1.1}$$

where γ_0 is the value of surface tension at the reference temperature, typically of order $\gamma_0 \sim 10^{-2}\ \mathrm{N\,m}^{-1}$; and γ_θ measures the variation of surface tension with respect to temperature. This coefficient is positive for common liquids (decreasing surface tension with increasing temperature), and is of order $\gamma_\theta \sim 10^{-4}\ \mathrm{N\,m}^{-1}\,\mathrm{K}^{-1}$ for silicone oils [26]. As we will shortly see, this means that the resulting flow at the free liquid/air interface drags the liquid from hotter to colder spots.

Let us note that the order of magnitude of the surface stress imposed $\partial_x \gamma$ will not be too large. Considering experimental magnitudes to be discussed later on, a maximum thermal difference of $\theta_{max} \sim 1\,\mathrm{K}$ acting on a small region of length $\sim 100\,\mu\mathrm{m}$ amounts to a maximum local stress of $|\partial_x \gamma| \sim 1\,\mathrm{Pa}$. The velocity scale around such a thermal maximum in a film of initial thickness $h_0 \sim 30\,\mu\mathrm{m}$ is therefore at most $h_0\,|\partial_x \gamma|\,/\eta \sim 3\,\mathrm{mm\,s}^{-1}$ for a liquid with $\eta \sim 10\,\mathrm{mPa\,s}$ like the silicone oils we will use later on [25], but it will be typically much smaller as the thickness decreases.

1.2.2 PDE describing the evolution of the free interface

The hydrodynamic evolution of the liquid film under the thermocapillary effect can be described using the Navier-Stokes equations with suitable boundary conditions. In general, the thin film condition applies when the typical horizontal length-scale L of the dynamics is much larger that the relevant thickness scale, in our case the mean initial thickness h_0, as sketched in Fig. 1.1. This allows to consider the terms in the equations with respect to the small parameter $\epsilon \equiv h_0/L << 1$ [3, 27]. The Reynolds number $\mathrm{Re} = \rho v_0 L/\eta$ is small, with the typical parameters discussed above $\mathrm{Re} \sim 10^{-4}$. In this expansion, the vertical components v_z and $\partial_z v_z$ of the flow velocity and its gradient are much smaller than the corresponding magnitudes of the in-plane velocity $\mathbf{v} = (v_x, v_y)^\top$.

Under these assumptions, the Navier-Stokes equations are simplified, to lowest order in ϵ, to [27]

$$-\boldsymbol{\nabla} p + \eta \partial_z^2 \mathbf{v} = 0 \tag{1.2}$$

where $\mathbf{v} = \mathbf{v}(t, \mathbf{x}, z)$ is the in-plane velocity field, $p = p(t, \mathbf{x}, z)$ is the pressure inside the fluid, $\boldsymbol{\nabla} = (\partial_x, \partial_y)$ in Cartesian coordinates, and $\partial_u(\cdot) \equiv \partial(\cdot)/\partial u$. The time dependence of $\mathbf{v}$ and p is introduced by the fact that the height profile of the free interface, $h(t, \mathbf{x})$ evolves with time.

The problem is complemented by setting the non-slip condition at $z = 0$ and the stress

balance at $z = h(t, \mathbf{x})$. These conditions are written, respectively,

$$\mathbf{v}|_{z=0} = \mathbf{0}, \tag{1.3}$$

$$\partial_z \mathbf{v}|_{z=h(t,\mathbf{x})} = \frac{1}{\eta}\boldsymbol{\nabla}\gamma. \tag{1.4}$$

Integration of these equations gives the velocity field

$$\mathbf{v} = \frac{1}{2\eta}\left[z^2 - 2zh\right]\boldsymbol{\nabla}p + \frac{z}{\eta}\boldsymbol{\nabla}\gamma. \tag{1.5}$$

From the conservation of volume

$$\partial_t h + \boldsymbol{\nabla}\cdot\int_0^{h(t,\mathbf{x})} \mathbf{v}(t, \mathbf{x}, z)\, dz = 0, \tag{1.6}$$

an evolution equation of the height profile $h(t, \mathbf{x})$ is obtained, inserting (1.5) for $\mathbf{v}$,

$$\partial_t h + \boldsymbol{\nabla}\cdot\left\{-\frac{1}{3\eta}h^3\ \boldsymbol{\nabla}p|_{z=h(t,\mathbf{x})} + \frac{1}{2\eta}h^2\boldsymbol{\nabla}\gamma\right\} = 0. \tag{1.7}$$

The pressure

$$p = p_0 - \gamma\nabla^2(h - z) + \rho g h - \Pi(h), \tag{1.8}$$

is the result of the interplay of normal stresses. The second term is the Laplace pressure, which arises from the curvature of the interface, $\boldsymbol{\nabla}\cdot\mathbf{n}$, where $\mathbf{n} = \mathbf{n}(\mathbf{x})$ is the normal vector of the free interface pointing outwards. When gradients are small, the curvature can be approximated by $\boldsymbol{\nabla}\cdot\mathbf{n} \approx -\nabla^2 h$. This is consistent with the lubrication approximation since in-plane derivatives are of order ϵ. The third term is the gravitational pressure. Lastly, the fourth term is a disjoining pressure term, $\Pi(h)$ modelling the effects of long-ranged molecular interactions. A discussion about the origin of $\Pi(h)$ will be given in Sec. 4.2.2.1 of chapter 4.

Several forms of $\Pi(h)$ have been discussed in the literature in the context of thin liquid films [3]. In this thesis, we will use non-polar liquids supported by a glass substrate and, to make a concrete discussion, we take the common assumption that in this system $\Pi(h)$ is the result of non-retarded van der Waals interactions and takes the form

$$\Pi(h) = -\frac{A_H}{6\pi h^3}, \tag{1.9}$$

where A_H is the Hamaker constant of the solid/liquid/air system. The Hamaker constant depends on the polarizabilities of the different media under consideration, in our case the solid substrate, the liquid film and the passive gas on top. We adopt the sign convention that a negative value of the Hamaker constant indicates repulsion between the solid/liquid and liquid/air interfaces, which stabilizes the film opposing any dewetting mechanism. Usually $|A_H|$ is of order $\sim 1 \times 10^{-19}$ J [4] and in the remainder of this chapter we will focus on the case of negative A_H.

Once the pressure terms involved in the system have been defined, we derive an equation governing the evolution of the free interface $h(t, \mathbf{x})$ by inserting the pressure terms in (1.7). This gives

$$\partial_t h + \boldsymbol{\nabla}\cdot\left\{\frac{h^3}{3\eta}\boldsymbol{\nabla}\left[\gamma\nabla^2 h - \rho g h - \frac{A_H}{6\pi h^3}\right] + \frac{h^2}{2\eta}\boldsymbol{\nabla}\gamma\right\} = 0. \tag{1.10}$$

To complete the equation making the thermocapillary effect explicit, we now use the linear dependence (1.1) of γ on the thermal field θ. We will denote θ_{max} the maximum thermal difference imposed on the film. We use θ_{max} to define $\Delta\gamma \equiv \gamma_\theta \theta_{max}$, the maximum surface tension variation. With the order of magnitude given above, a thermal difference of $\theta_{max} \sim 1\,\mathrm{K}$ gives a relative variation of $\Delta\gamma/\gamma_0 \sim 10^{-2}$.

The dynamic equation (1.10) becomes, after isolating the thermocapillarity term,

$$\partial_t h + \boldsymbol{\nabla}\cdot\left\{\frac{h^3}{3\eta}\boldsymbol{\nabla}\left[(\gamma_0 - \gamma_\theta\theta)\,\nabla^2 h - \rho g h - \frac{A_H}{6\pi h^3}\right]\right\} = \boldsymbol{\nabla}\cdot\left\{\frac{\gamma_\theta}{2\eta}h^2\boldsymbol{\nabla}\theta\right\}. \tag{1.11}$$

The left hand side represents what is commonly known as the thin film equation [3], which describes the relaxation of the liquid in the absence of forces. The right hand side is the thermocapillary effect, which drives the dynamics.

This equation can be generalized in several ways. An important extension in the discussion of wetting dynamics is the inclusion of a finite slip length b. Instead of assuming that the velocity vanishes a the solid surface ($z = 0$), as we have done imposing condition (1.3), the velocity is set to vanish at a (typically nanometric) thickness b, measured in the negative z direction, allowing for either slip at the interface ($b > 0$) or a finite resting layer of liquid ($b < 0$). This extension with a resting layer of liquid is used in the study of the dynamics of a spreading drop, which helps to regularize problems of diverging stresses at the contact line since the drop essentially relaxes on top of a liquid layer that may be understood as a precursor film [3]. Since we start by considering a film that completely covers the surface and the effect of thermocapillarity is to "remove" the liquid, we do not need in principle to assume that such a slip length exists. We consider that the disjoining pressure models the main effect of the intermolecular forces.

Coming back to the thermocapillary evolution (1.11), let us briefly note here that the variation of surface tension with temperature is indeed the most relevant effect, since local variations of viscosity or density will be either negligible of will not change the character of the evolution in the range of parameters studied. This is true in particular because the temperature variations that we will consider are always below $\theta_{max} \sim 10\,\mathrm{K}$ (the same order as reported in Ref. [28] and much less than the one used in Ref. [29] for initial thicknesses over 100 µm in similar systems). In appendix A we discuss the effects of considering temperature dependent viscosity $\eta[\theta(\mathbf{x})] \equiv \eta(\mathbf{x})$ and density $\rho[\theta(\mathbf{x})] \equiv \rho(\mathbf{x})$. The main conclusion is that considering the temperature-dependence of this properties in the derivation of the thin film equation leads to the same expression (1.11) replacing the constant η for the non-homogeneous $\eta(\mathbf{x})$ and similarly for ρ. Therefore, the dynamics essentially develops in the same way, with the viscosity imposing a small local variation of the time scale of the dynamics. Furthermore, considering the specific values for the liquids used in the experiments discussed in chapters 3 and 4, the variation of density is always less than 1%. We can therefore omit these dependencies and focus on the effect of the local variation of surface tension induced by the imposed thermal field.

1.3 Overview of thermocapillary-driven dynamics

As previously noted, the effect of thermocapillarity is to drive the liquid via an interfacial flow from regions of smaller to higher surface tension, generating the local thinning of the

film around hot spots. To illustrate this dynamics, in the following sections we solve the thin film equation numerically using physical parameters similar to experimental values of silicone oil, in order to understand how this evacuation of liquid proceeds, the relative contribution of the different pressure terms, and the relevant space and time scales of this system. For simplicity, we reduce Eq. (1.11) to the 2D case, working only in the (x, z) plane. The equation now reads:

$$\partial_t h + \frac{1}{3\eta}\partial_x \left\{ h^3 \partial_x \left[(\gamma_0 - \gamma_\theta \theta)\, \partial_x^2 h - \rho g h - \frac{A_H}{6\pi h^3} \right] \right\} = \frac{\gamma_\theta}{2\eta} \partial_x \left\{ h^2 \partial_x \theta \right\} . \tag{1.12}$$

Equation (1.12) will serve as the reference equation for the discussion.

Furthermore, we use a thermal field that qualitatively behaves as an exponential decay, $\theta(x) \approx \theta_{max} \exp(-|x|/w_0)$, with a small correction at the centre to avoid a cusp. These two conditions, the dimensional reduction and the qualitative behaviour of the thermal field, are imposed based on experimental considerations that are detailed in chapter 2, the full expression of $\theta(x)$ being defined later on in chapter 3.

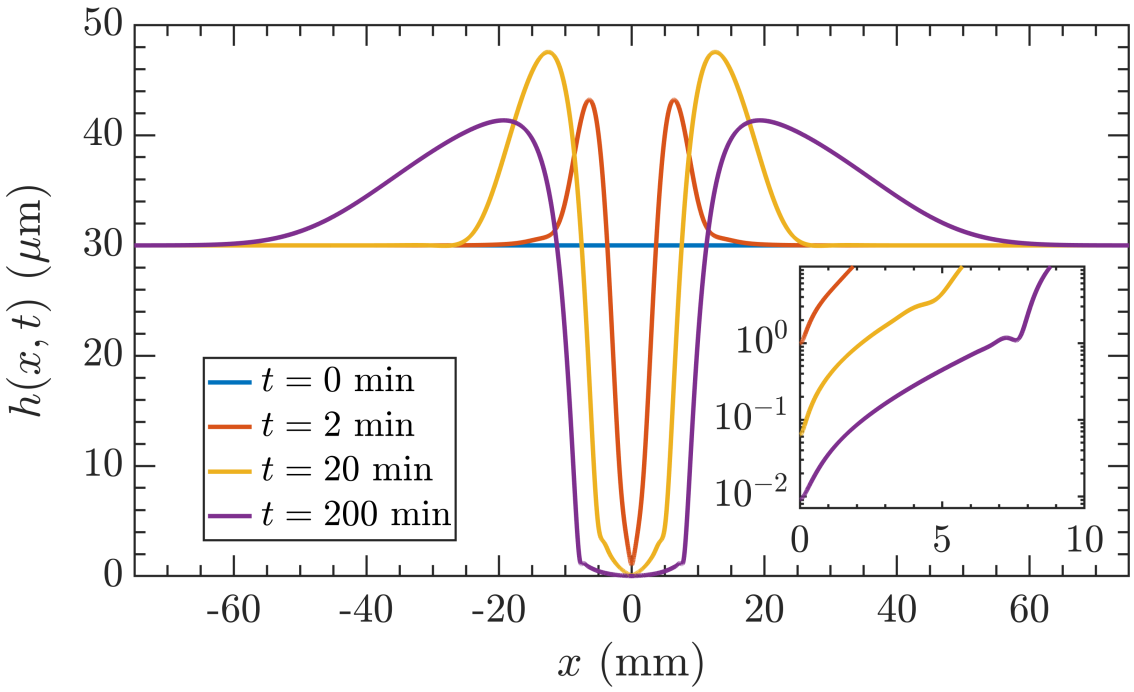

Figure 1.2: Profiles $h(t, x)$ for different times obtained from the numerical integration of Eq. (1.12) from a constant initial profile of thickness $h(0, x) = 30$ µm. Other parameters are: $\eta = 10^{-2}$ Pa s, $\rho = 10^3$ kg m^{-3}, $\gamma = 20 \times 10^{-3}$ N m^{-1}, $\Delta\gamma = 10^{-4}$ N m^{-1}, $A_H = -10^{-20}$ J, $w_0 = 3$ mm. Note that the profiles are plotted for times progressing *geometrically*, not linearly. Inset: zoom of the same profiles at the centre, with a logarithmic scale for the height.

Figure 1.2 shows thickness profiles obtained from the integration of Eq. (1.12) starting from a constant initial height profile $h(0, x) = h_0 = 30\,\mu$m and a temperature rise $\theta_{max} = 1\,$K. Other physical parameters are given in the caption of Fig. 1.2, which are close to

physical properties of the liquids used in experiments.[1] The liquid gets pushed away from where the gradient of the thermal field is greater, around the origin, generating an accumulation of fluid towards the boundary that will eventually be relaxed by gravity (see discussion about the stationary state below, Sec. 1.5). The depression left by the liquid at the centre grows in extent with time, and its width is larger than either the capillary length of the liquid $\ell_0 \equiv \sqrt{\gamma_0/\rho g} = 1.4$ mm or the thermal width $w_0 = 3$ mm. The slopes of the profiles are always below $\sim 10^{-2}$ rad (note the difference between the horizontal and vertical scales in Fig. 1.2). Therefore the small-gradient condition necessary for the validity of the thin film equation is always indeed fulfilled.

Three different dynamical regimes can be identified as times passes. Initially a small depression appears at the centre, which grows over time generating a local fluid accumulation towards the sides. Fig. 1.3 shows the film at time $t = 2$ min (corresponding to the orange curve of Fig. 1.2) coloured by the horizontal velocity v_x and showing the streamlines within the film (black curves). In this regime, the central depression is still over the micrometer scale and the liquid is pushed towards the border generating a characteristic overshoot or rim, as shown by the streamlines.

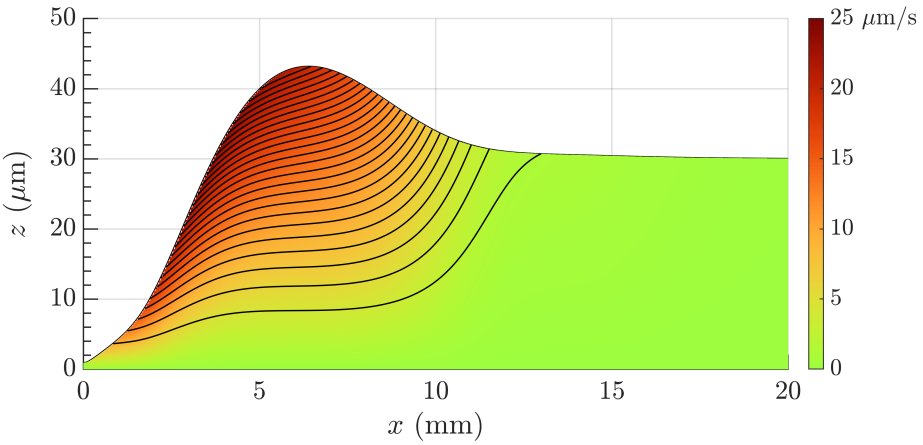

Figure 1.3: Horizontal velocity component $v_x(t, x, z)$ (colour map) and streamlines (solid black lines) corresponding to the numerical integration of Fig. 1.2 at $t = 2$ min (orange curve).

Once the overall volume of liquid at the centre is removed, as in Fig. 1.4, the depression is bounded by a wedge that recedes leaving a ultra-thin film behind. Note that at this point ($t = 20$ min) the dynamics has already slowed down considerably, and v_x is a factor of 5 times smaller than for the previous regime, Fig. 1.3. The presence of a small ripple at the wedge that can be deduced from the streamlines around $x \approx 5$ mm is characteristic of thin films driven by thermocapillary when the film is pushed against gravity [17, 18].

[1] A discussion about the numerical integration method of Eq. (1.12) and numerical issues we have encountered is provided in Sec. 2.5 of chapter 2.

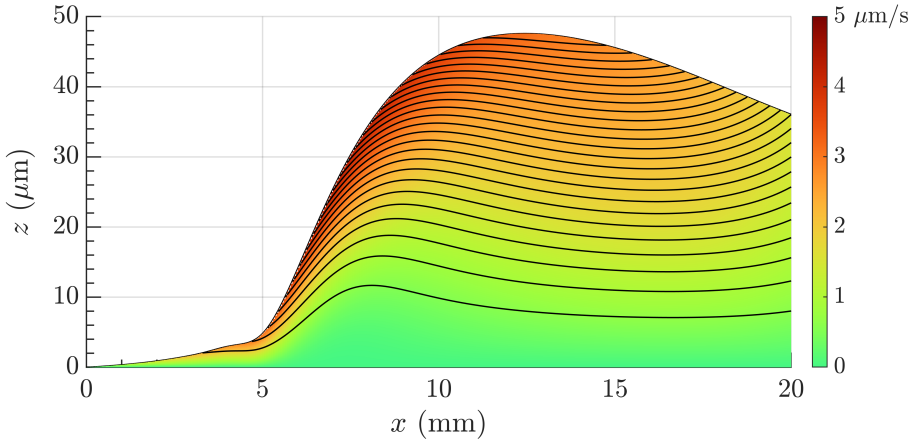

Figure 1.4: Same as Fig. 1.3 but for $t = 20\,\text{min}$ (yellow curve of Fig. 1.2). Note the difference in colour scales between the plots.

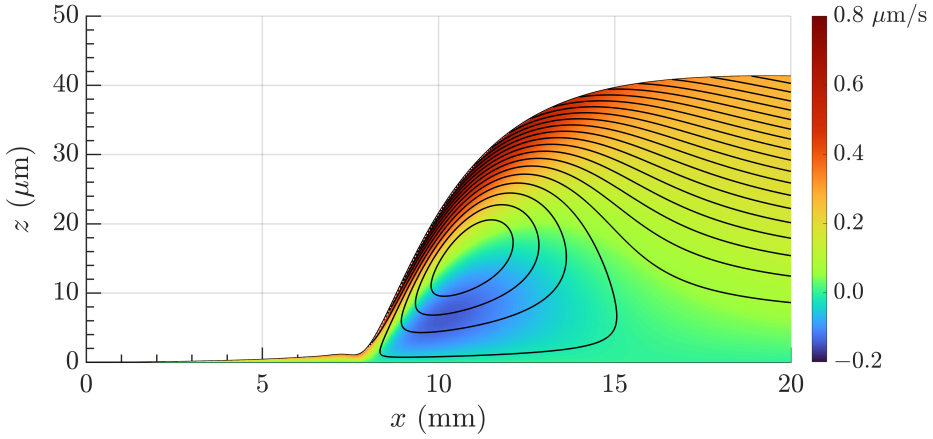

Figure 1.5: Same as Fig. 1.3 for $t = 200\,\text{min}$ (purple curve of Fig. 1.2). Note the difference in colour scales between the plots. The central region is not empty: there is a ultra-thin film with a thickness of tens of nanometres (see inset of Fig. 1.2).

At the position of the wedge a recirculating flow appears at long times, as shown in Fig. 1.5. The conditions giving rise to the recirculation can be understood by considering when the horizontal velocity v_x can become zero. From the general velocity profile given by Eq. (1.5), the horizontal component is

$$v_x(t,x,z) = \frac{z}{\eta}\left\{\left[\frac{1}{2}z - h\right]\partial_x p - \gamma_\theta \partial_x \theta\right\}, \tag{1.13}$$

so that $v_x = 0$ will occur at a height z^* satisfying

$$z^* = 2\left(h + \gamma_\theta \frac{\partial_x \theta}{\partial_x p}\right). \tag{1.14}$$

To be physically meaningful, the condition $0 < z^* < h$ must also be satisfied. Taking into account that, as mentioned earlier, the imposed thermal field decays exponentially,

its derivative is $\partial_x\theta(x) = -\theta(x)/w_0$. In addition, from Fig. 1.5, the height z^* appears to be on the micrometre scale, so that the van der Waals contribution to the pressure can be neglected. We consider only the effect of gravity as a first approximation $\partial_x p \simeq \rho g \partial_x h$ (see the discussion of the pressure terms at this time below in Sec. 1.3.3). Therefore, from Eq. (1.14), this recirculating flow can appear when the thickness of the film satisfies

$$z_r \leq h \leq 2\, z_r \tag{1.15}$$

where we have defined

$$z_r \equiv \frac{\gamma_\theta \theta(x)}{\rho g w_0 \partial_x h(t,x)}. \tag{1.16}$$

Since the slope of the height profile $\partial_x h$ is typically very small and $\theta(x)$ decays with the distance, condition (1.15) can only be satisfied in the intermediate region between the ultra-thin film at the centre and the thin film on the outer region. This means that the recirculating flow appears around the position of the wedge, as is the case in Fig. 1.5.

At this stage the dynamics is very slow, as can be seen by the scale of v_x. This will eventually lead to a stationary state with a combination of an ultra-thin film at the centre ending in a wedge that connects it to the bulk thin film, as will be discussed later on in Sec. 1.5, over a time scale of several days. Regrettably, this very large timescale has had the consequence of impeding us integrate the equation up to the establishment of stationary state for physically reasonable parameters, since the method we use does not converge for long times. Solving numerically the stationary equation by itself has been a difficult task due to its nonlinear nature. These numerical issues are discussed in Sec. 2.5 of chapter 2. However, as we shall later show, an approximated stationary state describing the ultra-thin film region at the centre can be computed analytically, as will be explained later on in Sec. 1.5.2.

As the thermocapillary effect empties the central region, the local thickness traverses scales that make different pressure contributions more or less effective in resisting its drag. To understand which pressure terms are opposing the thermocapillary effect at each regime, and especially in the long-term regime when the ultra-thin film has been established, let us plot their contributions at the corresponding times of Fig. 1.2, and discuss each one separately.

1.3.1 Pressure contributions at short times

Let us focus our attention on the profile at $t = 2$ min on Fig. 1.2, and plot the corresponding pressures given by Eq. (1.8). This is done in Fig. 1.6.

At this moment, gravity (blue line) gives the overall shape of the total pressure (black dashed line), with modulations arising from the curvature of the overshoots generated by the exiting liquid, that generates a strong Laplace contribution (red line). At the central region, the Laplace pressure is the dominant contribution due to the strong curvature of the depression. Since the thickness is still over the micrometer scale (see inset of Fig. 1.2), no measurable effect from van der Waals forces (yellow line) is expected. The pressure exhibits non-monotonic behaviour at the centre where it changes sign several times, as a result of the relation between gravity and Laplace contributions against the thermocapillary flow [17, 18]. We can expect the precise form of this interaction to vary for different fields $\theta(x)$.

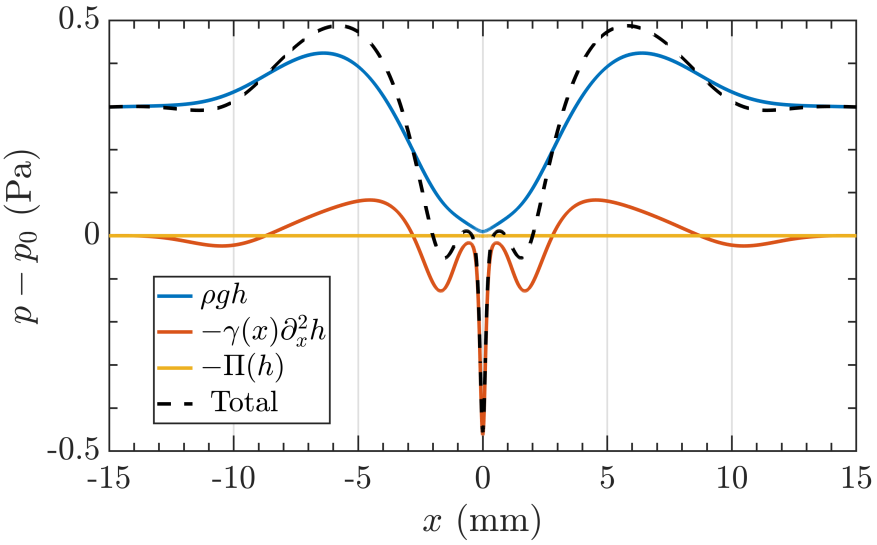

Figure 1.6: Pressures corresponding to the height profile $h(t, x)$ at $t = 2$ min in Fig. 1.2.

Since we are interested in the effect of intermolecular forces, we will not discuss further the dynamics at this short-time regime. However, it will be useful when comparing the generic dynamics of different liquids, since the system-dependent intermolecular forces play no role yet.

1.3.2 Pressure contributions at intermediate times

As more liquid is removed from the central region, the extent of the emptied area grows, limiting the effect of the Laplace pressure. Towards the borders, the exiting liquid has generated a surface modulation with a very large wavelength that will be relaxed by gravity. At the same time, the local thickness at the centre starts to be in the range of hundreds of nanometres (see inset of Fig. 1.2), and locally the contribution of van der Waals forces may be the most relevant one. An example of this situation is presented in Figure 1.7, which shows the pressure contributions corresponding to the height profile at time $t = 20$ min of Fig. 1.2.

We see that, for $|x| > 3$ mm, the pressure profiles resemble those of Fig. 1.6 in the interplay of gravity and Laplace pressures. However, the small film thickness at the centre makes gravity weaker. At the same time, the curvature of the profile has been greatly reduced since the solid surface is almost reached, giving a very small Laplace contribution. The profile right at the centre ($|x| < 1$ mm) has reached the scale in which intermolecular forces become effective ($h \sim 10$ nm, see inset of Fig. 1.2), and the disjoining pressure clearly dominates here.

The overall shape of the pressure is given by intermolecular forces at the centre and gravity at large scales, with an intermediate section modulated by Laplace at the wedge position. This distinction into regions will be maintained as time passes, as we have seen before in the discussion of Fig. 1.5. The change of regime from a disjoining-pressure-dominated to a gravity-dominated region allows us to define a crossover thickness between a thin film and what we will call an ultra-thin film. Let us consider the height h_{G} at which gravity and the disjoining pressures have the same strength. For the van der Waals-type

interaction considered for the numerical integration it is, using Eq. (1.9),

$$h_{\mathrm{G}} \equiv \left(\frac{-A_H}{6\pi\rho g}\right)^{1/4}. \tag{1.17}$$

With $\rho \sim 10^3$ kg m^{-3} and $|A_H| \sim 10^{-20}$ J, one finds $h_{\mathrm{G}} \sim 0.5$ µm, and the corresponding gravitational pressure is $\rho g h_{\mathrm{G}} \sim 0.3$ Pa. For thicknesses $h \gg h_{\mathrm{G}}$, gravity is the main pressure contribution, and disjoining pressure is negligible. Conversely, when the local thickness is $h \ll h_{\mathrm{G}}$, disjoining pressure dominates. In this later case we will say that the film is ultra-thin.

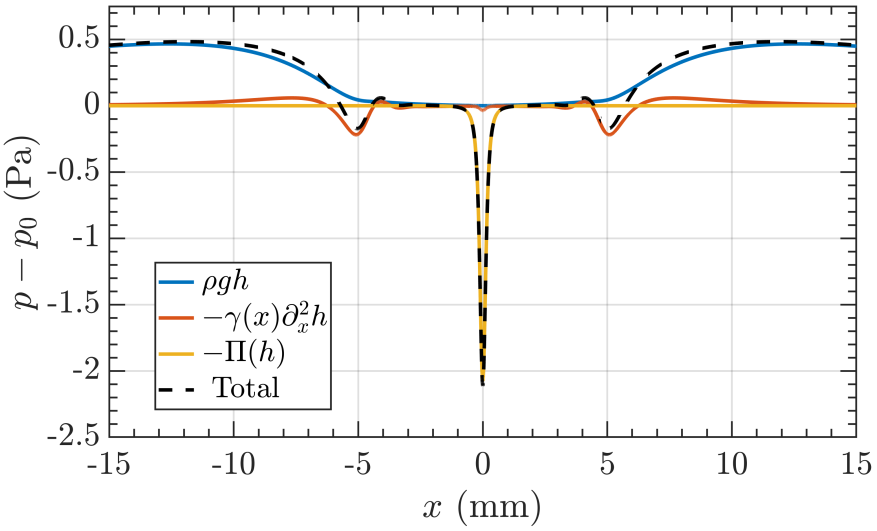

Figure 1.7: Pressures corresponding to the height profile $h(t, x)$ at $t = 20$ min in Fig. 1.2.

From the inset of Fig. 1.2, we can see that the thickness profile at this moment traverses the range from 0.1 µm to 2 µm in the central region ($x < 5$ mm) so that the contributions of gravity and disjoining pressures are comparable at this moment, which can be seen in Fig. 1.7. Let us discuss in more detail what should we expect from the dynamics at this central region, as the three pressure contributions should be compared to the thermocapillary term in the thin film equation (1.12). This equation can be rewritten as

$$\partial_t h = \frac{1}{3\eta}\partial_x \left\{ h^2 \left[\frac{3}{2}\gamma_\theta \partial_x \theta(x) + h\partial_x p \right] \right\} \tag{1.18}$$

so that the evolution is controlled by the relative strengths of $\gamma_\theta \partial_x \theta$ and the product $h\partial_x p$. It is clear from Fig. 1.7 that the gradient of the pressure is generally small, except perhaps locally around $x \approx 0$ and at the wedge, while the typical thickness at the central region is about $h \sim 1$ µm. Thus, the product $h\,\partial_x p$ is small enough so it can be neglected against the action of thermocapillary characterised by $\gamma_\theta \partial_x \theta$ term. In such a "pure" thermocapillary regime, the dynamic equation would be greatly simplified.

The relevance of such an evolution will be further explored in Sec. 1.4 to understand the dynamics of the profiles $h(t, x)$ at this intermediate-time regime. This pure-thermocapillary evolution will be of interest also for the analysis of the experiments, since

it will mark the moment from which Laplace and gravitational pressures can be (locally) neglected. Of course, the intermolecular forces represented by the disjoining pressure will become more relevant for smaller thicknesses. Indeed, for $h \ll h_{\mathrm{G}}$ we will have to take into account that, in the case of van der Waals interactions, $h\partial_x p \sim \partial_x h/h^3$, so that this term grows as thermocapillary thins down the film and cannot be further neglected. This eventual failure of the pure-thermocapillary description will be utilized to obtain information about the processes occurring at the solid/liquid interface in chapter 3, using a procedure that we detail below in Sec. 1.7.

We can see the strong effect of the disjoining pressure contribution by studying the pressure for long times. We turn to this regime in the following section.

1.3.3 Pressure contributions at long times

Once the central depression gets sufficiently near the solid/liquid interface, so that the thickness is smaller than h_{G}, a receding wedge forms. This wedge recedes, leaving an ultra-thin film behind. Indeed, from the macroscopic point of view of the initial thickness h_0, it is indistinguishable from a region "empty" of liquid. This ultra-thin film remains whenever the intermolecular interactions are repulsive as in the situation we are considering (modelled here by a negative Hamaker constant A_H), otherwise the film may become unstable and break up [27, 29].

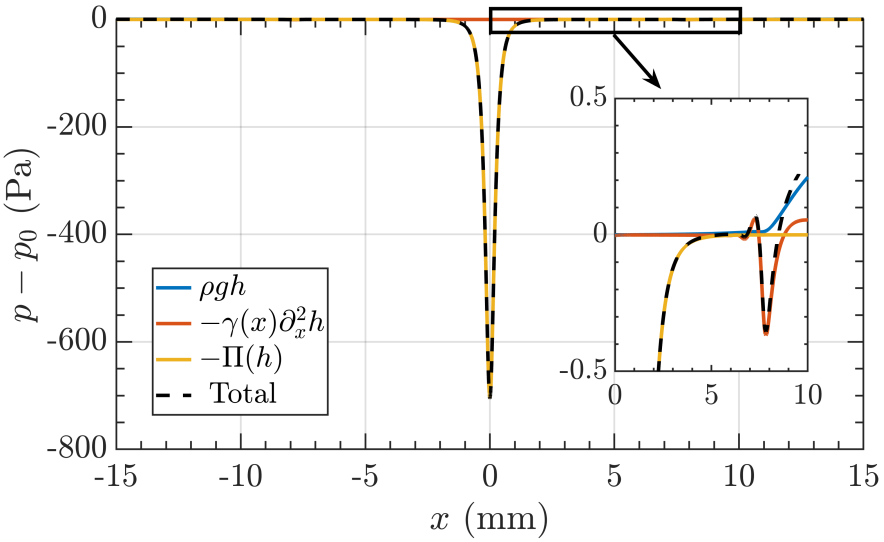

Figure 1.8: Pressures corresponding to the height profile $h(t, x)$ at $t = 200$ s in Fig. 1.2. Inset: zoom of the same profiles in the rectangle marked in the main panel.

Since the thickness is on the tens of nanometres scale (see inset of Fig. 1.2), the van der Waals pressure is the only relevant contribution at the central region, as is clearly seen in Fig. 1.8. The contribution of the Laplace pressure is confined to a modulation of the pressure at the wedge that joins this central region with the external, almost flat thin-film dominated by gravity.

However, since the (gradient of the) thermal field has an inherent decaying length, w_0, we expect that the lateral extent of this central, ultra-thin film region will be bounded,

as will be discussed in Sec. 1.5.2. Therefore, a stationary state of similar features as the long-term profiles is expected, which will be described later on in Sec. 1.5.

1.3.4 Conclusion

In this section, we have considered the evolution arising when a thin liquid film is driven by the thermocapillary effect, by providing a numerical integration of the dynamical equation (1.12). We have especially focused on the local behaviour near the maximum thermal field gradient, where an ultra-thin film ($h \ll h_{\mathrm{G}} \sim 0.5\,\mu\mathrm{m}$) is established, and analysed the relative contribution of the different pressure terms.

The dynamics is separated into three different time regimes. Initially, the thermocapillary effect drags the liquid away from the region where the thermal field is maximum generating a rim that moves away from the centre. We are considering initial thicknesses of around $h_0 = 30\,\mu\mathrm{m}$, so that disjoining pressure does not play any role here ($h \gg h_{\mathrm{G}}$). Gravity acts against the formation of the overshoots, and the Laplace pressure is biggest around the central depression. Once the central depression reaches a thickness around the micrometre scale, a wedge forms that recedes from the centre. This leaves behind a roughly homogeneous film, where all three pressure contributions (Laplace, gravity and disjoining pressure) are small. The thinning effect of thermocapillarity is thus locally unopposed. The characteristics of this pure-thermocapillary regime will be the focus of the next section. At longer times, the local thickness reaches the range where disjoining pressure is relevant ($h \ll h_{\mathrm{G}}$) and an ultra-thin film establishes. From this point onwards the dynamics becomes increasingly slower.

Note that in the ultra-thin film region both Laplace and gravitational pressures are negligible, since the film is almost flat and with a thickness on the tens of nanometres. Therefore, since the aim of this thesis is to characterise the dynamical effect of disjoining pressure, it is essential to characterise how the pure-thermocapillary regime is established and how disjoining pressure affects its dynamics.

1.4 Pure-thermocapillary regime

We have seen that, near the peak of the temperature distribution, both Laplace and gravitational pressures are negligible after a transient initial period. We can thus expect three temporal regimes around this central area. At short times, thermocapillarity must overcome the contributions of gravity and Laplace. At intermediate times, the latter loses strength due to the thinning of the profile. If the local height is still of the order $\sim 1\,\mu\mathrm{m}$, thermocapillarity alone will drive the dynamics. At long times, the ultra-thin film enters the region were disjoining pressure effects become important, leading to the formation of the stationary state.

To describe the height dynamics at intermediate times, we will assume that all pressure terms are negligible and the dynamics is solely described by thermocapillarity. This assumption is admittedly a strong one, which will be valid at restricted times and regions, such at the one noted above in Sec. 1.3.2 in the discussion of Fig. 1.7. Nevertheless, we will see in following chapters that this is a fruitful assumption and that, indeed, this regime can be seen under experimental conditions. It will be precisely the end of this

regime that will signal the contribution of the interfacial effects that are the main concern of this thesis.

1.4.1 Dynamics driven solely by thermocapillarity

The equation for a height profile $h_{\mathrm{M}}(t,x)$ driven solely by Marangoni forces is written as

$$\partial_t h_{\mathrm{M}} - \frac{\gamma_\theta}{2\eta}\partial_x\left\{h_{\mathrm{M}}^2\partial_x\theta\right\} = 0. \tag{1.19}$$

This equation can be solved by separation of variables, as shown in appendix B. The solution is

$$h_{\mathrm{M}}(t,x) = \frac{h_0}{1+c\,(t/t_0)}\,\frac{c}{2\sqrt{|\partial_X\Theta|}}\int_0^X \frac{ds}{\sqrt{|\partial_s\Theta|}}, \tag{1.20}$$

where $X \equiv x/w_0$ is the dimensionless transversal distance, $\Theta(X) \equiv \theta(x)/\theta_{max}$ is the normalized temperature field, $c \equiv |\partial_X^2\Theta(0)|$ is the (dimensionless) curvature of the thermal field at the centre, and

$$t_0 \equiv \frac{2\eta w_0^2}{\Delta\gamma h_0} \tag{1.21}$$

is the timescale of the thermocapillary evolution. With the orders of magnitude used for the numerical integration of Sec. 1.3, we get $t_0 = 60\,\mathrm{s}$.

Note that for $t \gg t_0$, one obtains

$$h_{\mathrm{M}}(t \gg t_0, x) \approx \frac{2\eta w_0^2}{\Delta\gamma t}\,\frac{1}{2\sqrt{|\partial_X\Theta|}}\int_0^X \frac{ds}{\sqrt{|\partial_s\Theta|}}. \tag{1.22}$$

The profile maintains its shape but the thickness decreases everywhere as $\propto 1/t$. The approximate evolution (1.22) does not depend on h_0, which implies that the system loses memory of its initial thickness.

Fig. 1.9 shows a comparison between the profiles of the numerical integration of Fig. 1.2 and the height profiles $h_{\mathrm{M}}(t,x)$ obtained from expression Eq. (1.20) at the corresponding times. Initially ($t = 2$ min), the dynamics is still affected by the contributions of Laplace and gravity pressures, so that the pure-thermocapillary regime has not been reached. Nevertheless, close to the centre ($x < 1\,\mathrm{mm}$) it is possible to see how the numerical profile and h_{M} have a similar shape. The pure-thermocapillary behaviour has been locally established throughout the central region after 20 min. As the wedge recedes, the region described by Eq. (1.20) enlarges concurrently, reaching a remarkable extension of several millimetres at $t = 200$ min.

We can therefore conclude that the local dynamics at the centre quickly reaches and follows the pure-thermocapillary regime for the choice of parameters used. This means that, near the centre (but for several millimetres), the contributions of Laplace and gravity pressures can be neglected from early on in the dynamics. The thickness of the profiles shown are typically on the range from 0.1 to 1 µm, when we can expect a small contribution of the disjoining pressure since $h \sim h_{\mathrm{G}}$.

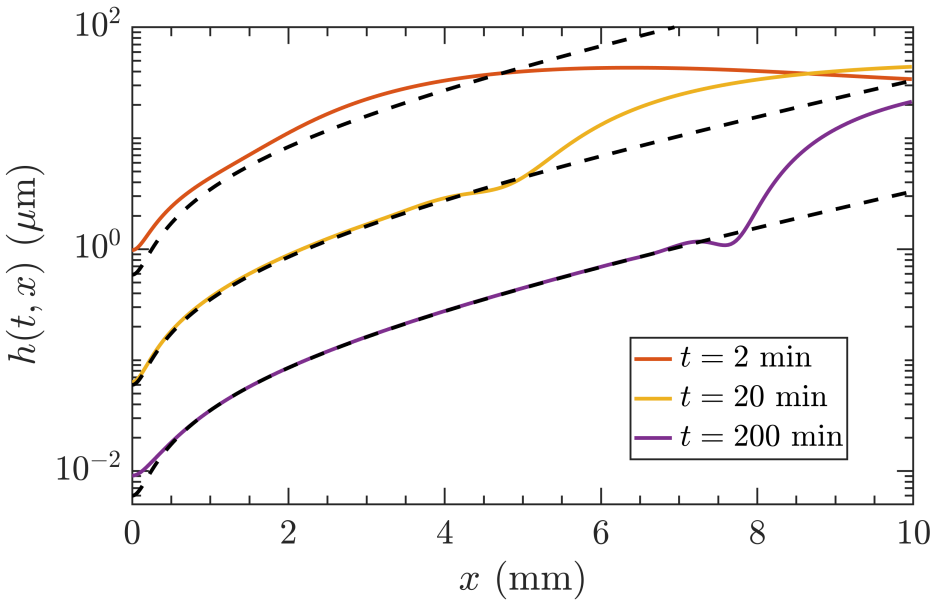

Figure 1.9: Comparison of profiles obtained from numerical integration and from the pure-thermocapillary regime. Solid curves are the height profiles $h(t, x)$ obtained from the numerical integration of the thin film equation shown earlier in Fig. 1.2. The dashed black curves are the height profiles $h_{\text{M}}(t, x)$ at corresponding times obtained from Eq. (1.20). The vertical axis is in logarithmic scale.

However, it is possible to see a deviation from this behaviour in the last profile near the centre ($x < 0.5\,\text{mm}$). Here $h \ll h_{\text{G}}$ and the disjoining pressure effects are starting to be felt by the ultra-thin film. From this moment on, the dynamics starts deviating from the pure-thermocapillary regime by the increasingly strong effect of disjoining pressure only. To take advantage of the fact that neither Laplace pressure nor gravity are relevant, we start exploring the reduced dynamics without these contribution on the next section. Later on in Sec. 1.7 we will show how this deviation can be used to extract the disjoining pressure of the system from the knowledge of the height profile $h(t, x)$ and the thermal field $\theta(x)$. This procedure can be experimentally achieved, as shown in chapter 3.

1.4.2 The effect of disjoining pressure

A profile locally evolving as predicted by Eq. (1.22) will eventually become thin enough so as to enter the region where intermolecular forces become effective, as shown previously in Sec. 1.3.3 and in Fig. 1.9. We are considering repulsive interface interactions (negative A_H), so that the ultra-thin film is stable and will remain in the stationary state. The contribution of the intermolecular interactions therefore opposes the further thinning of the film, decelerating the dynamics.

It is therefore important from the experimental point of view to obtain a time scale of the thermocapillary plus disjoining pressure evolution. We thus consider the reduced equation arising from the general evolution, Eq. (1.7), when the contribution of the Laplace and gravity pressures is neglected, and write

$$\partial_t h - \frac{A_H}{6\pi\eta}\partial_x\left\{\frac{\partial_x h}{h}\right\} = \frac{\gamma_\theta}{2\eta}\partial_x\left\{h^2\partial_x\theta\right\}, \tag{1.23}$$

where we maintain the van der Waals disjoining pressure $\Pi(h) = -A_H/6\pi h^3$.

We now consider the following dimensionless variables

$$t = t_{\text{utf}} T, \quad x = w_0 X, \quad h(t,x) = h_{\text{utf}} Z(T,X), \tag{1.24}$$

where "utf" stands for "ultra-thin film". h_{utf} and t_{utf} are, respectively, thickness- and time-scales to be defined. We get

$$2\eta \frac{h_{\text{utf}}}{t_{\text{utf}}} \partial_T Z - \frac{A_H}{3\pi w_0^2} \partial_X \left\{ \frac{\partial_X Z}{Z} \right\} = \frac{\Delta\gamma h_{\text{utf}}^2}{w_0^2} \partial_X \left\{ Z^2 \partial_X \Theta \right\}. \tag{1.25}$$

Hence, taking (recall that $A_H < 0$)

$$h_{\text{utf}} = \sqrt{\frac{-A_H}{6\pi\Delta\gamma}}, \quad t_{\text{utf}} = \eta w_0^2 \sqrt{\frac{6\pi}{-A_H \Delta\gamma}}, \tag{1.26}$$

we obtain the dimensionless equation

$$\partial_T Z = \partial_X \left\{ \frac{Z^2}{2} \Theta' - \frac{Z'}{Z} \right\}. \tag{1.27}$$

With the values given above, the thickness scale of the ultra-thin film is $h_{\text{utf}} = 2.3\,\text{nm}$, indeed at the scale of relevance of interfacial forces. The associated time scale is $t_{\text{utf}} \simeq 4.5$ days, much longer than the thermocapillary scale $t_0 = 60\,\text{s}$.

These scales, h_{utf} and t_{utf}, allow us to understand the deviation from the pure-thermocapillary regime that we saw earlier on in Fig. 1.9. In Fig. 1.10 we show the product $h(t,x) \times t$ for the profiles of Fig. 1.9, together with the corresponding prediction from the approximation (1.22). Since $t \ll t_{\text{utf}}$ and $h \gg h_{\text{utf}}$, the curves corresponding to height profiles that have reached the pure-thermocapillary regime collapse over all the central area.

However, as the inset details, the curve corresponding to $t = 200\,\text{min}$ (in purple) has a deviation from the pure-thermocapillary regime at the centre. For this profile, the thickness close to the centre is below 50 nm (recall Fig. 1.2) and the disjoining pressure effects are starting to be relevant. The region affected by this deviation will grow as time passes, since the rest of the profile satisfies the pure-thermocapillary dynamics that continuously decay as $\sim 1/t$ by Eq. (1.22). Therefore, in the system considered where the repulsive intermolecular forces oppose the effect of the thermocapillary effect, the local dynamics will become slower until some stationary state is reached.

The slow nature of this relaxation will make a complete measurement of the process until reaching the stationary state a challenging task, especially due to dust particles being adsorbed at the surface as will be explained in chapter 2. Instead, we will focus on the transition from the pure-thermocapillary driven dynamics, introduced above, to a long-time regime in which the presence of the disjoining pressure contribution begins to modify the profiles starting from the centre. How to obtain information about the disjoining pressure from this effect will be investigated in Sec. 1.7. Before developing this analysis, we need to consider the conditions under which the central ultra-thin film develops. For doing this, we analyse in the next section the characteristics of the stationary state.

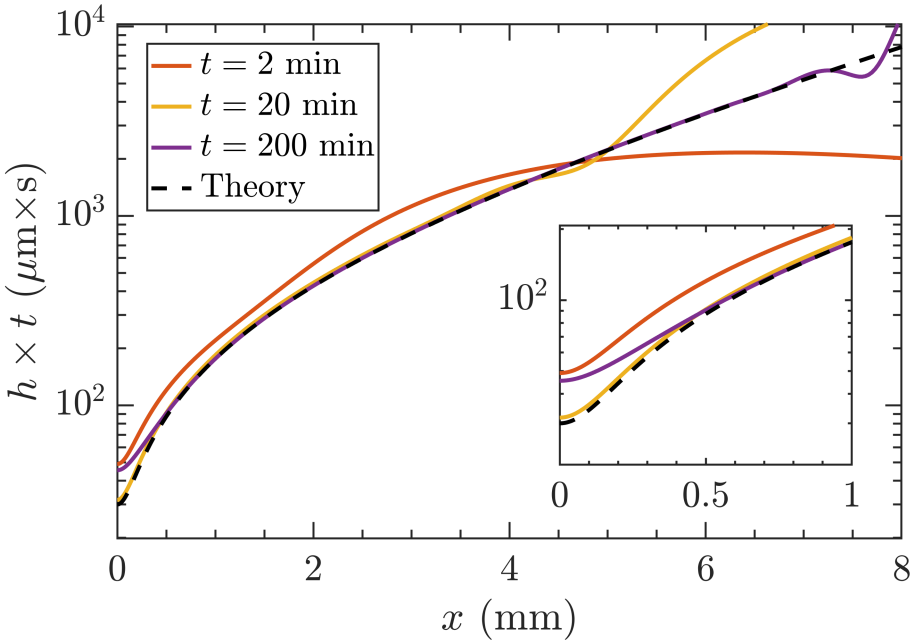

Figure 1.10: Product $h(t,x)\times t$ of the thickness profiles $h(t,x)$ shown in Fig. 1.9, together with the approximated pure-capillary regime given by Eq. (1.22) (black dashed curved referred to as "Theory"). The curves that correspond to profiles satisfying the pure-thermocapillary evolution collapse. Inset: zoom of the region closer to the centre.

1.5 The stationary state

In previous sections, we have analysed the evolution of the dynamics of a thin liquid film driven by thermocapillary. We have seen that two distinct regions appear. Near the centre, an ultra-thin film is established through the opposition of intermolecular forces to the thinning effect of thermocapillarity. This ultra-thin film is bounded by a macroscopic wedge that joins the central region with an outer one with thicknesses around the initial value h_0, in our case typically 30 µm. The wedge is where Laplace pressure is most relevant, since the outer region is almost flat and dominated by gravity.

The dynamics starts to slow down when these two regions have been established, as we saw in Sec. 1.3. Since the driving of the dynamics is produced by the gradient of the thermal field, which decays in space as an exponential with characteristic decay length w_0, the thermocapillary will not be able to effectively push the wedge indefinitely. When the effect of intermolecular forces is more relevant, we have seen in Sec. 1.4.2 that it slows down the dynamics and the flow exiting the ultra-thin film region is also small. We hence expect that the dynamics will eventually reach a stationary state.

In this section, we analyse the equation of the stationary state. This analysis will provide a characterization of the minimum thickness and lateral extent of the ultra-thin film given the maximum thermal field θ_{max} and the initial thickness h_0. This will further allow us to obtain an approximated critical minimum value for θ_{max} that must be overcome for the ultra-thin film to exist.

1.5.1 Equation of the stationary state

The stationary profile $\overline{h}(x)$ satisfies the following equation

$$\partial_x \left\{ \overline{h}^3 \partial_x \left[(\gamma_0 - \gamma_\theta \theta)\, \partial_x^2 \overline{h} - \rho g \overline{h} \right] + \frac{A_H}{2\pi} \frac{\partial_x \overline{h}}{\overline{h}} \right\} = \partial_x \left\{ \frac{3}{2} \Delta\gamma \overline{h}^2 \partial_x \Theta \right\}, \tag{1.28}$$

by disregarding the temporal derivative in Eq. (1.12).

To better understand the characteristics of $\overline{h}(x)$, we integrate this equation twice, from x to infinity,[2] by making two observations. Firstly, the thermal field we consider (and its derivatives) vanishes at infinity. Secondly, and as a consequence, we expect no change on the height profile of the film at the boundary. Therefore it maintains its initial height, $\overline{h}(\infty) = h_0$, and all derivatives vanish (flat profile).

The first integration is immediate, and all terms vanish when evaluated at infinity. For the second integration, we divide everything by $\overline{h}^2$. This assumes that $\overline{h} \neq 0$ everywhere. Although this will turn out to be generally true for wetting liquids with $A_H < 0$ (repulsive interface interactions), this may not be the case for dewetting scenarios ($A_H > 0$) where the film breaks and dry spots appear.

We have

$$\gamma_0 \overline{h}\, \partial_x^3 \overline{h} - \rho g \overline{h}\, \partial_x \overline{h} + \frac{A_H}{2\pi} \frac{\partial_x \overline{h}}{\overline{h}^3} = \frac{3}{2} \gamma_\theta \partial_x \theta \left[1 + \frac{2}{3} \overline{h}\, \partial_x^2 \overline{h} \right]. \tag{1.29}$$

Note that the last term on the right hand side is of order $\epsilon^2 = (h_0/L)^2 << 1$, therefore it can be neglected in the thin film approximation.

We integrate each term of Eq. (1.29) independently to obtain

$$\gamma_0 \left[\overline{h} \partial_x^2 \overline{h} - \frac{1}{2} \left(\partial_x \overline{h} \right)^2 \right] - \frac{1}{2} \rho g \overline{h}^2 - \frac{A_H}{4\pi \overline{h}^2} = \frac{3}{2} \gamma_\theta \theta(x) - \frac{1}{2} \rho g h_0^2 - \frac{A_H}{4\pi h_0^2}. \tag{1.30}$$

To better discuss the characteristics of this equation, we rewrite this equation it terms of the dimensionless variables $\zeta^2 = \overline{h}/h_0$ (note the square) and $X = x/w_0$, where h_0 is the initial thickness and w_0 the thermal decay length. The dimensionless thermal field is $\Theta(X) = \theta(x)/\theta_{max}$. We get

$$4\kappa_c^2 \zeta^3 \partial_X^2 \zeta - \zeta^4 + \frac{3E}{\zeta^4} = M\, \Theta(X) - 1 + 3E \tag{1.31}$$

where $\kappa_c^2 \equiv (\ell_c/w_0)^2 = \gamma_0/\rho g w_0^2$ is the dimensionless capillary length, $E \equiv (h_{\mathrm{G}}/h_0)^4$ and the dimensionless number $M \equiv 3\Delta\gamma/(\rho g h_0^2)$ represents the strength of the thermocapillary effect against gravity. Due to the symmetry of the thermal field, we can define the boundary conditions as $\partial_X \zeta(0) = 0$, $\zeta(\infty) = 1$ and focus on the positive X range.

Note that the right hand side decays as the thermal field, $\Theta(X) \simeq \exp(-X)$. Therefore, the stationary equation introduces a characteristic width

$$X_c \simeq \log\left(\frac{M}{1 - 3E} \right) \tag{1.32}$$

[2] This is different from the approach taken in Ref. [27], in which they consider a finite domain with periodic boundary conditions, leading to some technical difficulties at the borders. Since the behaviour of the thin film on the outer region lies outside the scope of this thesis, we assume that the extent of the original liquid film is much larger than any of the length scales relevant for the dynamics.

at which the right hand side vanishes. This width gives a scale over which the thermocapillary effect is effective. There is also a characteristic thickness, which can be obtained by equating the gravity and the disjoining pressure terms, which is

$$\zeta_c = (3E)^{1/8}\,, \tag{1.33}$$

which is, in dimensional variables, of the same order of the threshold thickness h_{G} between a gravity- and a disjoining-pressure dominated regime.

With the typical parameters used in previous sections, the order of the dimensionless parameters is $\kappa_c \simeq 0.25$, $E \sim 10^{-7}$ and $M \sim 34$. From these values, we obtain that $X_c \approx \log M \simeq 3.5$ and $\zeta_c \simeq 0.15$, which in dimensional variables represents a width $x_c \simeq 10.5\,\mathrm{mm}$ and a thickness $h_c \simeq 635\,\mathrm{nm}$, which indicates that the profile shown earlier in Fig. 1.5 for the long-term regime should be fairly similar to the stationary state. From the discussion of the dynamics at the long term in Sec. 1.3.3, the central region $x \ll x_c$ will be where the ultra-thin film ($\overline{h} \ll h_c$) is established.

The nonlinear equation (1.31) is complicated to compute numerically due to the large exponents in ζ and the transition between the ultra-thin film at the centre and the thin-film at the boundaries, specially because the Hamaker constant is very small giving $E \lll 1$. We have been unable to obtain its numerical solution with the typical values of M and E because numerical instabilities appeared easily. Nevertheless, to obtain some insights about the characteristics of the stationary state in the ultra-thin film region, we introduce in the next section an approximation for the stationary state of the ultra-thin film at the central region, $X \ll X_c$.

1.5.2 Approximate stationary state

We are interested in how the interplay between the thermocapillary effect and the intermolecular interactions shapes the ultra-thin film at the central region at the stationary state. We show here that we can obtain an approximation of the stationary state at the ultra-thin film region that only depends on these two contributions.

At the thickness scale of the ultra-thin film, much smaller than the threshold thickness $h_{\mathrm{G}} = (-A_H/6\pi\rho g)^{1/4} \simeq 0.5\,\mu\mathrm{m}$, we have argued that gravity should have a negligible effect. The contribution of capillary forces should also be very small for the typical parameters we are discussing, as explained earlier in Sec. 1.3.3. For $X \ll X_c$ and $\zeta \ll \zeta_c$, we thus neglect the terms coming from Laplace and gravitational pressures in Eq. (1.31), and the solution can be obtained directly,

$$\zeta(X) = \left(\frac{3E}{M\,\Theta(X) - 1 + 3E}\right)^{1/4}. \tag{1.34}$$

This expression satisfies the boundary condition $\partial_X \zeta(0) = 0$. It can only be a valid solution for $\zeta \ll \zeta_c$, a condition which can be rewritten as $M\,\Theta(X) - 1 + 3E \gg \sqrt{3E}$. Since the thermal field decays exponentially, this condition can only be valid for $X \ll X_c - \log\left(1 + \sqrt{3E}\right) \simeq X_c$. Therefore, expression (1.34) is valid in almost all the central domain $0 < X_c \ll X_c$.

As a further check, we plot in Fig. 1.11 the different terms of Eq. (1.31) in absolute value, computed with the solution (1.34). Throughout the central region the contribution

of disjoining pressure is several orders of magnitude greater than either the capillary or the gravity pressures, therefore this approximation is a valid description of the central region.

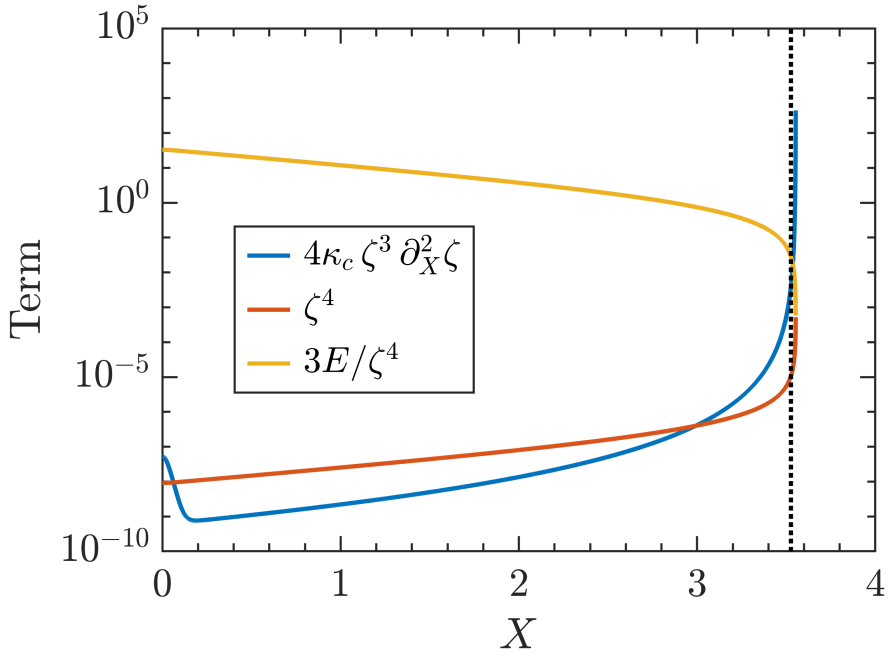

Figure 1.11: Comparison of different terms of Eq. (1.31), in absolute value, computed with the solution at the centre (1.34). The dotted line is at X_c.

In the original variables, the thickness of the film at the central region $x \ll x_c$ behaves as

$$\overline{h} = \frac{h_{\text{utf}}}{\sqrt{\Theta(x/w_0) - \Theta_c}} \tag{1.35}$$

where $h_{\text{utf}} \equiv \sqrt{-A_H/6\pi\Delta\gamma}$ was defined in (1.26) of the previous section as the thickness scale of the ultra-thin film. With our typical parameters, $h_{\text{utf}} \simeq 2.3\,\text{nm}$. Θ_c can be seen as a critical (dimensionless) temperature defined as

$$\Theta_c \equiv \frac{\rho g h_0^2}{3\Delta\gamma}\left(1 - 3\frac{h_{\text{G}}^4}{h_0^4}\right) \simeq \frac{\rho g h_0^2}{3\Delta\gamma}. \tag{1.36}$$

With the typical parameters used above, $\Theta_c \simeq 0.03$. The importance of Θ_c for deciding if the ultra-thin film will be established is commented in the next section.

1.5.3 Condition of existence of the ultra-thin film

In the preceding discussion, we have assumed that all the expressions were well-defined for the parameters considered, in particular for obtaining the approximate stationary state (1.35) at the central region. However, it is clear that the ultra-thin film region does not need be always promoted. Indeed, for a vanishing contribution of thermocapillary ($\theta_{max} \to 0$) one can expect only a small deformation of the profile around the peak of

the thermal field controlled by the action of Laplace and gravity pressures. We can use the expressions obtained in the preceding section to obtain an approximate condition of existence of the ultra-thin film region. To have such a condition is important to know the most interesting range of parameters for performing the experiments.

Consider again Eq. (1.35) describing the stationary height profile at the ultra-thin film, which behaves as $\overline{h} \propto [\Theta(x/w_0) - \Theta_c]^{-1/2}$. Since the maximum value of the dimensionless thermal field is $\Theta(0) = 1$, a minimum condition for this expression to be defined is that $\Theta_c < 1$. Therefore, in order to promote the ultra-thin film, the maximum temperature difference θ_{max} has to be greater than

$$\theta_{max} > \frac{\rho g h_0^2}{3\gamma_\theta}\left(1 - 3\frac{h_{\rm G}^4}{h_0^4}\right) \equiv \theta_c. \tag{1.37}$$

We can see that an increase of the initial film thickness requires a higher strength of the thermocapillary effect to overcome the initial response of the Laplace and gravity pressures against it and establish the ultra-thin film. For the parameters considered here, this approximated critical temperature difference is only $\theta_c \simeq 0.03\,\mathrm{K}$, which will be an easily attainable temperature difference under experimental conditions, as detailed in chapter 2. We have seen that when the ultra-thin film is established it can be several millimetres wide, $x_c \simeq 10.5\,\mathrm{mm}$. This lateral dimension is of relevance when designing the experimental cell to be able to diminish the role of boundary effects.

The values shows that the the ultra-thin film slowly becomes thicker away from the centre, from $h_{\rm utf} \sim 2\,\mathrm{nm}$ to $h_{\rm G} \sim 500\,\mathrm{nm}$, in a region that can be several millimetres wide. This continuous small growth over such a large region ($h_{\rm G} \ll x_c$) will allow us to isolate the effects of intermolecular interactions on the film and, as we will see, to measure these effects from a dynamical point of view.

1.5.4 Conclusion

In this section, we have analysed the steady-state regime of the thermocapillary-driven dynamics of the thin liquid film. In the experiments, we are interested in obtaining information about the intermolecular forces, which are relevant only for thicknesses well below the micrometre scale. Hence, we have focused on obtaining a description of the ultra-thin film region near the centre as a function of the imposed thermal field, and we have found a condition on the maximum temperature difference θ_{max} imposed for the existence of this ultra-thin film, given an initial thickness h_0.

We have seen that the ultra-thin film appears if the thermal field θ_{max} is higher that a critical value $\theta_c \simeq \rho g h_0^2/(3\gamma_\theta)$. The critical value with typical experimental parameters is $\theta_c \sim 0.03\,\mathrm{K}$, a small threshold that will be easy to overcome experimentally as will be shown in chapter 2.

Above this threshold, when $\theta_{max} > \theta_c$, the steady-state will have two delimited regions, characterised by which contribution is predominant against the thermocapillary effect. In the central region, the effect of (repulsive) intermolecular interactions against thermocapillarity will generate an ultra-thin film that can have a nanometric minimum thickness, and then extend for several millimetres with a thickness in the tens of nanometres scale. Due to the decay of the thermal field, the thermocapillary effect cannot be efficient against Laplace and gravity pressures indefinitely, and the ultra-thin film joins

to the outer region, where the thickness is of the order of the initial film, through a macroscopic wedge.

The ultra-thin film, with the typical experimental parameters chosen, can extend several millimetres, even to the scale of the centimetre, until a characteristic size depending on the decay of the thermal field. For the exponential decay of typical length w_0 we are discussing based on experimental considerations, $x_c \simeq w_0 \log(\Delta\gamma/[3\rho g h_0^2])$, where we recall that $\Delta\gamma = \gamma_\theta \theta_{max}$ is the surface tension variation. Its minimal thickness $\overline{h}(0)$ is of the order of $h_{\text{utf}} = \sqrt{-A_H/6\pi\Delta\gamma} \simeq 2.3\,\text{nm}$, indeed deep in the range in which intermolecular interactions are effective.

These limiting behaviours and scales will determine the experimental range of parameters that are interesting to explore. In the next section, we turn our attention to a more quantitative analysis of these thickness and thermal ranges, tacking also into account the time scales obtained in Sec. 1.4, when the specific physical values of the liquids used in experiments are considered.

1.6 The parameter space

We have described in previous sections the dynamics of a thin liquid film driven by thermocapillarity, establishing different scales for the duration of successive dynamical regimes and the typical thickness of the regions dominated by different pressure contributions.

This section is devoted to consider the ultra-thin film scales $h_{\text{utf}} = \sqrt{-A_H/6\pi\Delta\gamma}$ and $t_{\text{utf}} = \eta w_0^2 \sqrt{6\pi/[-A_H\Delta\gamma]}$ (see Sec. 1.4.2) in the context of the experimental design, where the two main controllable parameters are the initial thickness h_0 and the maximum thermal difference θ_{max} (through the dissipated power P of a microprinted electrical circuit via the Joule effect as we shall see in chapter 2). The remaining quantities relevant to the dynamics are fixed by the choice of the liquid. We exemplify the following discussion with physical properties corresponding to a silicone oil we will use in the experiments (Rhodorsil 47V20, see chapter 2): $\eta = 19\,\text{mPa s}$, $\rho = 950\,\text{kg m}^{-3}$ [25], $\gamma_\theta = 8.5 \times 10^{-5}\,\text{N m}^{-1}\,\text{K}^{-1}$ [26]. Assuming that the disjoining pressure depends on the thickness as $\Pi(h) = -A_H/(6\pi h^3)$ (the same dependence we have used in all our preceding discussions, Eq. 1.9), it has been recently shown in our group that the Hamaker constant of this oil on coloured glass is $A_H \approx -1 \times 10^{-19}\,\text{J}$ [28] (a brief discussion of the method used is provided in Sec. 3.4.1 of chapter 3).

In the experiments, we want to choose θ_{max} and h_0 such that the ultra-thin film will be established, and its minimum thickness goes down to the tens of nanometres scale. At the same time, θ_{max} should not be very high so that other effects relating to temperature do not appear. We have seen that the minimum thickness that would be attained in the steady state when $\Pi(h) = -A_H/(6\pi h^3)$ is

$$\overline{h}(0) = \frac{h_{\text{utf}}}{\sqrt{1-\Theta_c}} = \sqrt{\frac{-A_H}{6\pi\gamma_\theta\theta_{max}\,[1-\Theta_c]}}. \tag{1.38}$$

The critical (dimensionless) temperature Θ_c scales as $\Theta_c \propto h_0^2/\theta_{max}$. Therefore, fixing a certain $\overline{h}(0)$ gives a relationship between the values of h_0 and θ_{max} needed to obtain a specific minimum thickness. Figure (1.12) shows curves of constant $\overline{h}(0)$ in the (θ_{max}, h_0) parameter space (dotted lines marked with 15, 20 and 25 nm). For initial thicknesses of

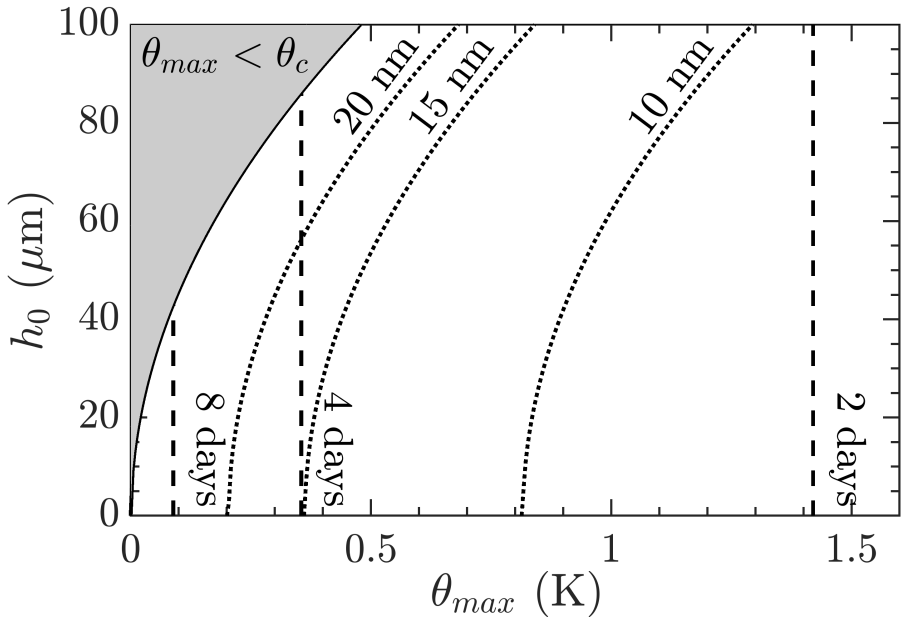

Figure 1.12: Parameter space of the main experimentally controllable variables (θ_{max}, h_0) (maximum thermal difference and initial film thickness) using physical parameters of silicone oil (Rhodorsil 47V20). The grey region is defined by $\theta_{max} < \theta_c$, in which the stationary state does not have an extended ultra-thin film. Dotted lines: curves of constant minimum stationary thickness $\overline{h}(0)$. Dashed lines: lines of constant time scale of the ultra-thin film dynamics, t_{utf}. More details are given in the main text.

tens of micrometers ($h_0 \ll h_{\text{G}}$), we can see that a small temperature difference is enough to promote ultra-thin films with thicknesses down to tens of nanometres. For example, with $h_0 = 30\,\mu\text{m}$ and $\theta_{max} = 1\,\text{K}$ the minimum stationary thickness is $\overline{h}(0) = 9.2\,\text{nm}$.

In principle, studying the ultra-thin film established in the stationary state would allow the study of intermolecular forces. However, as discussed at the end of Sec. 1.4.2, the time scale of the evolution becomes extremely slow once the local height profile at the centre has entered the thickness range at which intermolecular forces are most relevant. In Fig. 1.12 we include lines of constant $t_{\text{utf}} = \eta w_0^2 \sqrt{6\pi/[-A_H \Delta\gamma]}$ (dashed vertical lines), the time scale of the ultra-thin film defined earlier in Eq. (1.26), to also characterise the typical times associated with the long-term dynamics that eventually will give rise to a particular stationary state. As we can see, the experiments should last for several days before reaching the stationary state.

We insist on the fact that t_{utf} is not the time needed to reach the stationary state, which will be larger. Trying to attain this theoretical stationary state experimentally in this range of parameters is impractical, specially due to the deposition of dust particles over this long time scale as will be discussed in chapter 2. However, as shown before in Sec. 1.4.1, the pure-thermocapillary dynamics is nonetheless attained within a sensible time scale. Therefore, it will be in the transition from the intermediate- to the long-time regime when, following the dynamics of the height profile $h(t, x)$, we will be able to observe and measure the contribution of intermolecular forces to the dynamics. The procedure to obtain this measurement is explained in the next section.

1.7 Dynamical measurement of disjoining pressure

The results of the pure-thermocapillary regime in Sec. 1.4 indicate that the thinning dynamics of the liquid film under the action of thermocapillarity can induce a local regime where both Laplace and gravity contributions are negligible. The local dynamics once the thickness of the film is sufficiently low is characterised in general by the interplay of the disjoining pressure $\Pi(h)$ modelling the intermolecular forces of the substrate/liquid/air system and the thermocapillary effect.

These two effects are the only ones needed to describe the evolution of the local height profile $h(t,x)$ when it reaches an ultra-thin film regime. However, the remaining dynamics can be very slow, with a typical time scale on the order of days for the range of parameters considered, as shown in Fig. 1.12 above. It is therefore impractical to wait for the steady state to be established before trying to measure the disjoining pressure. Instead, we address in this section the problem of obtaining a measurement of $\Pi(h)$ from a dynamical point of view, that is, extracting information about the dependence of $\Pi(h)$ on the thickness from the knowledge of the evolution of the height profile $h(t,x)$ and the gradient of the thermal field $\theta(x)$ imposed.

1.7.1 General procedure

To obtain a measurement of the disjoining pressure $\Pi(h)$, we consider again the reduced thin film equation Eq. (1.23) disregarding Laplace and gravity pressures, but without imposing a specific form for $\Pi(h)$

$$\partial_t h - \frac{1}{3\eta}\partial_x\left\{h^3\partial_x\Pi[h]\right\} = \frac{\gamma_\theta}{2\eta}\partial_x\left\{h^2\partial_x\theta\right\}. \tag{1.39}$$

Isolating the disjoining pressure term,

$$-\partial_x\left\{h^3\,\partial_x h\,\partial_h\Pi\right\} = \frac{3}{2}\gamma_\theta\partial_x\left\{h^2\partial_x\theta\right\} - 3\eta\partial_t h, \tag{1.40}$$

and then integrating over x from the centre and rearranging,

$$-\partial_h\Pi = \frac{1}{h^3\,\partial_x h}\left[\frac{3}{2}\gamma_\theta h^2\partial_x\theta - 3\eta\int_0^x \partial_t h(t,u)\,du\right], \tag{1.41}$$

we obtain a relationship between the derivative of the disjoining pressure with respect to the thickness of the film and the difference between the thermocapillary effect driving the dynamics and the exiting flux of liquid.

Note that the right hand side of this equation is exactly zero when $h(t,x) = h_{\mathrm{M}}(t,x)$, that is, when the dynamics is purely driven by the thermocapillary effect. Since we assume that we are studying the ultra-thin film where Laplace and gravity pressures are negligible, any contribution remaining will be the signature of processes occurring at the interface level. In particular, as time goes on and the evolution slows down, the second term on the right hand side of Eq. (1.41) will become gradually smaller until the steady state is reached.

Equation (1.41) states that from the knowledge of the gradient of the thermal field $\theta(x)$ and the dynamic profiles $h(t,x)$ it should be possible to recover the derivative of the disjoining pressure with respect to the thickness, $\partial_h\Pi(h)$. Moreover, this evaluation does not require any assumptions about the origin of the disjoining pressure of the system.

1.7.2 Numerical example

We provide an example of the evaluation of Eq. (1.41) with the height profiles of the numerical integration of the thin film equation that we discussed in Sec. 1.3 above. This represents an ideal case since we both know the height profiles $h(t,x)$ and the thermal field $\theta(x)$ that drives the dynamics. Later on, in chapter 3, we will explain how it is possible to use the pure-thermocapillary regime to obtain the gradient of the thermal field $\partial_x\theta(x)$ from experimental profiles in order to evaluate Eq. (1.41). In profiles from experiments, the evaluation of numerical derivatives will require also a filtering procedure to reduce the effect of noisy data.

To mimic the situation of experiments, we have chosen to obtain numerical profiles at a time interval of 10 min and interpolate the numerical profiles in a spatial lattice with a spacing similar to the pixel resolution of the experiments (the details of the numerical integration for obtaining $h(t,x)$ are given in Sec. 2.5 of chapter 2.)

We only consider profiles once the pure-thermocapillary regime has been established ($t > 20$ min, see Fig. 1.10). We showed in Sec. 1.4 that the dynamics near the centre follows first the thermocapillary evolution, $h(t,x) \simeq h_{\rm M}(t,x)$, and then deviates from it starting from the centre where the thickness is always minimum. Hence, we do not expect to see deviations due to the contributions of Laplace and gravity pressures that have been neglected, as explained in Sec. 1.4. In particular, for this example we have chosen profiles in the range 100 min $< t <$ 200 min.

We evaluate numerically Eq. (1.41) taking the analytical thermal field gradient $\partial_x\theta$, and we numerically evaluate the derivatives $\partial_x h$ and $\partial_t h$ of the profile $h(t,x)$ at each time using 5-point stencils. The integration of the second term is done for the resulting $\partial_t h(t,x)$ at each time roughly up to $x \approx 4$ mm, which is the extent of the pure-thermocapillary regime for the first profiles considered. Indeed, coming back to the profiles shown in Sec. 1.4, the pure-thermocapillary regime in this particular case describes the profiles up to the apparition of a ripple (as briefly noted earlier, this ripple can be related to the thermocapillary pushing against the action of gravity [17, 18]). Finally, we combine this result with the first term in the square brackets of Eq. (1.41) to obtain $-\partial_h\Pi(h)$ for each numerically obtained profile $h(t,x)$. This means that we evaluate $-\partial_h\Pi(h)$ at each considered time ($t = 100, 110, 120, ..., 200$min), but the result should be independent of time if indeed the dynamics is described by the reduced equation (1.39) combining thermocapillary and disjoining pressure only. Afterwards, we limit ourselves to results in which the thicknesses is up to roughly $h \lesssim 200$ nm $< h_{\rm G}$ (which is similar to the thickness range for which this procedure could be implemented experimentally, as explained in chapter 3).

The disjoining pressure used for illustrating the dynamics was $\Pi(h) = -A_H/6\pi h^3$, so that we can compare the result of Eq. (1.41) with the analytical expression $-\partial_h\Pi(h) = -A_H/2\pi h^4$. We insist on the fact that in evaluating Eq. (1.41) this information is not used.

In Fig. 1.13 we show the evaluation of Eq. (1.41) according to the procedure we have detailed. A perfect agreement is found as expected between the obtained $-\partial_h\Pi(h)$ (blue dots, 11 curves) and the analytical expression (dashed black line) in the thickness range between 10 and 100 nm, which roughly traverse 4 decades in the derivative $-\partial_h\Pi(h)$. As expected, since the contribution of the Laplace and gravitational pressures is negligible

and the dynamics are dictated by the reduced equation (1.39), the curves obtained at different times collapse.

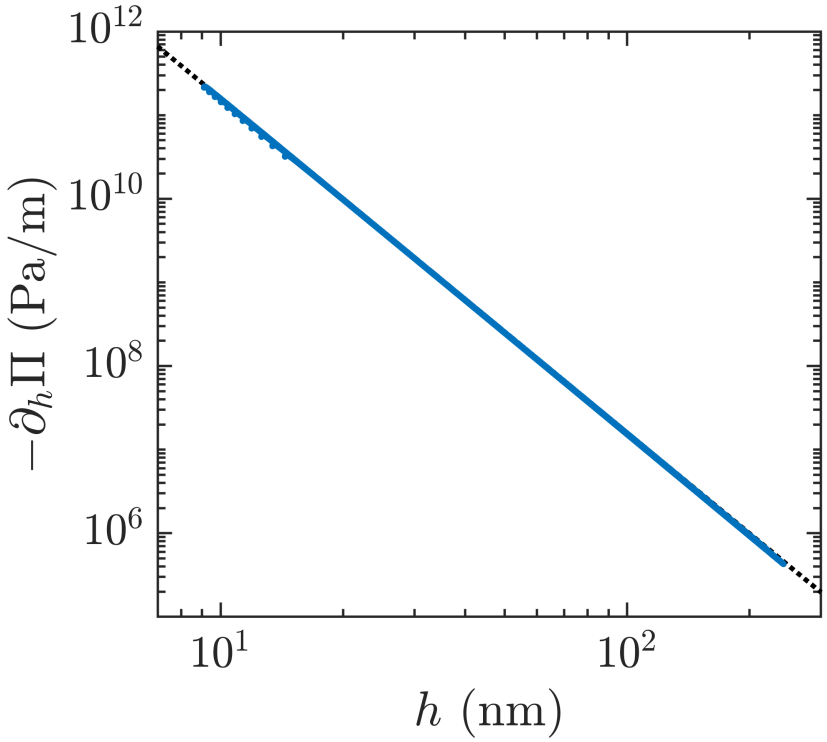

Figure 1.13: Extraction of $-\partial_h \Pi$ from profiles obtained by numerical integration (blue solid line) compared to the analytical expression (black dashed line).

1.7.3 Conclusion

We have thus shown that it is possible, by measuring the dynamics of the height profile $h(t, x)$ of the thin film and knowing the gradient of the thermal field $\partial_x \theta(x)$ driving the dynamics, to recover the disjoining pressure acting on the system and thus obtaining a characterization of intermolecular interactions. We stress the fact that we do not assume any dependence of the disjoining pressure $\Pi(h)$ for the evaluation of expression (1.41), and that the contribution of Laplace and gravity pressures can be neglected once the pure-thermocapillary regime is established.

Later on in chapter 3 we will we use this method to analyse the effect of intermolecular forces on the thermocapillary dynamics of silicone oil films on a glass substrate. The experimental limitations of evaluating this expression, in particular coming from the evaluation of the derivatives, will be also discussed. However, we will find a good collapse of curves that will allow us to characterise the dependence of the effective disjoining pressure of wetting, ultra-thin liquid films on its thickness.

1.8 Conclusion

In this chapter, we have reviewed the thermocapillary-driven evolution of thin liquid films, and we have characterized the existence and characteristics of a local ultra-thin liquid film at the region of greater temperature gradient. This ultra-thin liquid film, of nanometric thickness, can be established with a small temperature difference, $\theta_{max} \sim 1\,\mathrm{K}$, for films of typical thicknesses $h_0 \sim 30\,\mu\mathrm{m}$, and extends laterally for several millimetres.

It has been shown that the establishment of this ultra-thin film is preceded by a local regime in which all pressure contributions can be neglected and the dynamics is purely described by the thermocapillary effect, and we have provided an analytic solution for this local evolution. Within this pure-thermocapillary regime, the height profile follows a master curve given by the gradient of the thermal field. We will show in chapter 3 that this master curve can be observed experimentally, and can lead to the determination of the gradient of the thermal field from experimental measurements.

The further thinning of the layer down to the tens of nanometres scale provokes that interfacial effects, here characterised by a disjoining pressure term, become important. The dynamics at the transition between a pure thermocapillary-driven regime and another one where there exists a competition with disjoining pressure can be used to extract information about the interfacial processes. In particular, from the evolution of the height profile $h(t, x)$ we have shown how it is possible to obtain the dependence of the gradient of the disjoining pressure with respect to the thickness of the film, $\partial_h \Pi(h)$, simultaneously in a continuous range of thicknesses roughly from 10 to 100 nm, if the imposed thermal gradient $\partial_x \theta$ is known.

Once this competition is established, the time scale necessary to attain the stationary state is very long compared to the characteristic time of the thermocapillary evolution. We will therefore restrict ourselves to the monitoring of the dynamics of the height profile until the aforementioned transition of dynamic regimes occurs.

The results obtained in this chapter about thermocapillary driven dynamics can be generalised to an axisymmetric geometry. This extension has been relevant for the understanding of the formation of ultra-thin films under a laser beam, which has constituted the post-doctoral work of Cécile Clavaud [28]. Her results investigating the effect of intermolecular interactions in surface thermal fluctuations are summarized in Sec. 3.4.1 of chapter 3.

Later on in chapter 3 we will study how the procedures described in this chapter can be applied experimentally to obtain the signature of intermolecular forces by measuring the derivative of the disjoining pressure with respect to the thickness of the film. Before that, in chapter 2 we describe the experimental setup that we have used to measure the evolution of a nanometric ultra-thin liquid films over millimetre-sized regions. The experimental design will have to take into account the information about length- and time-scales obtained throughout this chapter's discussion.

Chapter 2

Experimental techniques

2.1 Introduction

In the previous chapter, we discussed the evolution of the thermocapillary dynamics on thin liquid films. Using typical experimental values for the physical properties of the liquid (viscosity η, density ρ, surface tension γ_0, variation of surface tension with temperature γ_θ, and Hamaker constant A_H), a thin film supported by a solid substrate will be dragged away from a heated region. For initial thicknesses of the order of $h_0 = 30\,\mu\text{m}$, we have shown that a relatively small local temperature difference $\theta_{max} = 1\,\text{K}$ is enough to promote the apparition, on a very large extent $x_c \simeq 10.5\,\text{mm}$ ($\gg h_0$), of an ultra-thin film of thickness below 100 nm around the peak of the thermal field. It is this area which interests us, as we would like to obtain a measurement of interface phenomena from the dynamical evolution of the film.

Typical length- and time-scales of the problem when the thermal field decays exponentially, with a decay scale w_0 on the millimetre scale, were established by noting that there exists a local regime in which the height profile is driven by thermocapillarity alone, since all pressure contributions are negligible. The local temperature increase to promote this effect can be quite small, and therefore a complex heating architecture is not needed. The associated time scale of this evolution is on the order of minutes, which makes it possible to follow the evolution of the film using common imaging techniques as will be explained below. The final extent of the ultra-thin film region is proportional to w_0, thus the area to be imaged needs to be correspondingly large. At the same time, an accuracy close to the nanometre scale in thickness measurements is needed to uncover the effects of intermolecular forces.

With these constraints in mind, we present in this chapter the experimental setup designed for exploring the thermocapillary evolution of thin liquid films. We start by introducing in Sec. 2.2 the characteristics of the experimental cell, which is based on a thin glass slide to which an electric circuit is printed on its bottom side. We characterise the thermal field imposed by performing infrared measurements on bare substrates. The experimental setup is complemented with a LED panel and a camera.

Once the characteristics of the setup have been defined, in Sec. 2.3 we explain how the height profile of the film is obtained from image analysis during the dynamics. A brief comment is done about the deposition of the film with a spin coater and the measurement of the mean initial thickness of the film with a profilometer. Afterwards, two different

imaging techniques, each one providing dynamical measurements of the thickness profile either above or below the micrometre scale, are introduced. The limitations of both techniques are discussed.

The procedure followed for preparing, monitor and analyse an experiment is summarised in Sec. 2.4. This allows us to touch upon some other technical aspects of the experiments relating to the deposition of the films, the synchronization of the lighting with the camera, and the selection of a region of interest in the images.

The chapter ends with an independent section, Sec. 2.5, dedicated to the numerical integration of the thin film equation that we used in chapter 1 to illustrate the expected dynamics. We explain the difficulties of performing the numerical integration that have been encountered as a consequence of the multi-scale nature of the problem and the long time scale that may arise, as we briefly discussed for the numerical integrations of chapter 1. Notwithstanding these limitations, the numerical solution of the thin film equation up to the onset of disjoining pressure effects has been an important source of insights about the dynamic regimes of the thermocapillary evolution, as has been seen in chapter 1.

2.2 Experimental setup

In this section, we begin by introducing the experimental cell, that consists of a glass substrate over which a thin liquid film will be deposited, and an auxiliary support to help the manipulation of the cell. We discuss in detail the characteristics, solutions and compromises made in the design of the experimental cell in view of the thermocapillary length scales obtained previously in chapter 1. Next, using an infrared camera we characterise the thermal field used in experiments for promoting the thermocapillary effect. This thermal field is generated by heat dissipation at an electric circuit printed on the bottom side of the glass surface. Finally, we introduce the simple image acquisition setup used to monitor the dynamics, in particular to measure the evolution of the height profile of the liquid.

2.2.1 Experimental cell

Let us discuss the precautions that need to be considered in the cell design.

To promote the thermocapillary effect we will want to apply a thermal field through the solid substrate (a glass slide), to avoid a direct contact between the liquid and the heating source. We are interested in surface interactions, and this contact would introduce a local variation of intermolecular forces that would complicate the analysis. However, a thin glass slide is difficult to manipulate without breaking it, so that it will be glued to an external support. This external support cannot be too big, since then it will be too heavy to be used in the spin coating of the initial liquid film.

From these desired characteristics, a compromise is done to obtain a working cell, which is depicted in Fig. 2.1. Its components are described in the next sections.

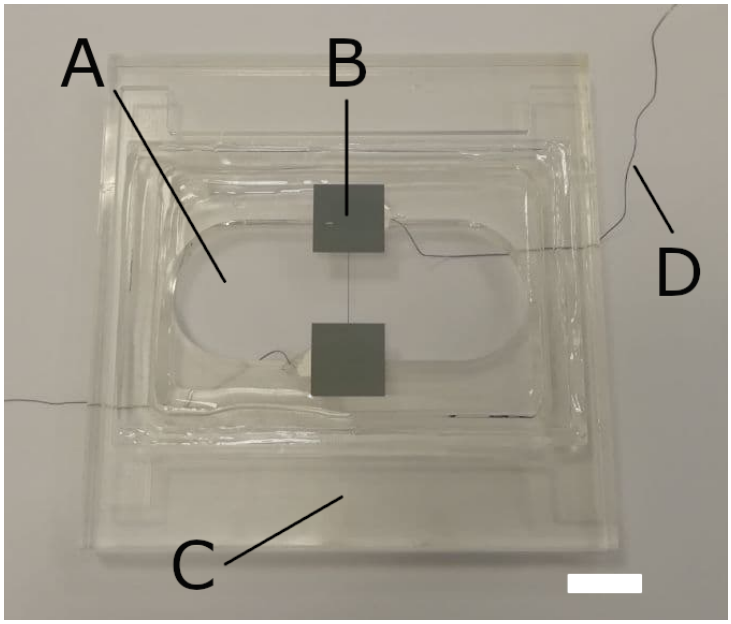

Figure 2.1: Experimental cell. A thin microscope slide (A), previously printed with a electric circuit (B), is glued to a plexiglas support (C). The circuit is printed on the bottom side of the slide, while the liquid film will be spread on the top side. The support has a central aperture from which the electrical contacts (D) can be connected to an external power supply. Scale bar: 1 cm.

2.2.1.1 Surface

The substrate is a cover glass slide (Menzel-Gläser, Thermo Scientific) of thickness 100 µm and area $40\times60\,\mathrm{mm}^2$. The thickness is small so that the thermal field can rapidly reach the stationary configuration (see the discussion of Fig. 2.4 in Sec. 2.2.2). On its bottom side, an electrical circuit is printed as explained in the next section. As previously discussed in chapter 1, the transversal length scale of the flow driven by thermocapillarity can reach the scale of a centimetre, even for liquid films with thicknesses on the tens of micrometers. It is because of this that the lateral sizes of the substrate need to be much larger than its thickness, which makes the manipulation of the slide difficult and requires of the auxiliary support as commented below.

The top side of the slide (the side opposite to the printed circuit) will be covered by a liquid film. The surface of glass is known to have a roughness characterised by nanometric deformations with a typical length scale of micrometres, which may have a role on the wetting of the liquid film. To know whether a wetting liquid will conform to the deformations of the surface, the length scale of the roughness must be compared to the healing length of the liquid film, $\xi = h^2/\sqrt{-A_H/(2\pi\gamma_0)}$ [30], where h is the thickness of the liquid film, A_H is its Hamaker constant (recall that for wetting liquids $A_H < 0$) and γ_0 is its surface tension. If the healing length ξ is smaller than the roughness scale, then the fluid will conform to the roughness of the surface. For the case of a typical silicone oil used in the experiments of chapter 3, we have $A_H = -2\times10^{-19}\,\mathrm{J}$ [28] and $\gamma_0 = 2\times10^{-2}\,\mathrm{N\,m^{-1}}$ [25]. Taking a characteristic thickness $h = 10\,\mathrm{nm}$, a thickness that we can expect in the ultra-thin film established by the thermocapillary effect as discussed in chapter 1, we find $\xi \simeq 80\,\mathrm{nm}$. The healing length is much smaller than the length scale

of the deformations, so that the ultra-thin film can conform to the surface landscape in the long-time regime. However, these deformation would be averaged out in our images, since the resolution of the camera (see Sec. 2.2.3) is about 12 µm/px.

In fact, as we will later see, the most important defect of our setup are surface inhomogeneities appearing due to the deposition process, or else particles deposited during the length of an experiment, and not the surface itself.

2.2.1.2 Printed circuit

The dissipation of heat of an electric circuit printed on the bottom side of the substrate will generate the thermal field gradient driving the dynamics of the thin liquid film. The use of microheaters on microfluidic devices has been shown to be a powerful technique to control the movement of drops and bubbles, see e.g. section 5 of Ref. [22] and section 6 of Ref. [24], and references therein.

The microfabrication of this circuit is done using a standard procedure of photolitography. First the slide is spin-coated with a positive photoresist (Microposit S1805). Using a negative mask of the desired circuit pattern, the photoresist is shined with UV light (MJB4 Suss MicroTec Mask aligner) to obtain a negative mask on the glass slide (Megaposit MF-26A developer). The circuit can be afterwards printed by the deposition of a conductive material. Depending on the machines availability, we have used either a hybrid sputter deposition system (Plasmionique) or an evaporator (Edwards Evaporator Auto500). In the majority of the experiments discussed in following chapters, the circuit was made of a double layer of chrome and gold (typically 20+20 nm). Other materials (ITO, copper) were also sometimes used depending on stock availability, without affecting experimental procedures or results. After deposition, the remaining photoresist was lifted off with sonication on an acetone bath.

The circuit we have studied consists on a heating line with a nominal width of 0.1 mm and a length of 10 mm, see Fig. 2.1. However, it sometimes have defects and its contour is not well defined. Its width can vary up to a 10%. These local defects will have an impact in the reproducibility of the thermal field, as we shall see below in Sec. 2.2.2.2.

The width of the heating line measures the same as the thickness of the glass, so that both are much smaller than the typical lateral size of the substrate and can be neglected, reducing the length scales involved in the system. This choice is also made to avoid a large widening of the thermal field on the surface, so as to obtain a well defined thermal gradient. A model of the thermal field is obtained in appendix C making use of the fact that these sizes are small compared with the extension of the surface, that compares well with infrared measurements shown below in Sec. 2.2.2.

At the end of the heating line lie two square paddles (side of 10 mm), to which electrical connections are added using a conductive glue. We will show in section Sec. 2.2.2 that all the heat is dissipated in the line, the square paddles do not contribute noticeably to the dissipation.

Before proceeding, it is important to note that the deposition of the circuit is one of the main sources of surface inhomogeneities, because the slide must be posed on the side where the liquid will afterwards be deposited. This is a serious drawback, since the surface can become contaminated or marked. Furthermore, we cannot use proper cleaning procedures (e.g. using a piranha solution) on the glass slides once the circuit is printed

because it would be damaged or destroyed (not to speak of the glued contacts). The consequences of these surface inhomogeneities will be patent when we discuss experiments with alkane films in chapter 4.

2.2.1.3 Support

To help the manipulation of the slide, it is carefully glued to a plexiglas support using an epoxy resin. The support overall dimensions are $75 \times 75 \times 5\,\mathrm{mm}^3$. This size is enough to provide a better manipulation of the slide, while being light enough to be used in a spin coater. A perforation at the centre permits both direct bottom illumination and to extract the electrical connections of the circuit from below, see Fig. 2.1 above and Fig. 2.8 below. This support also has a pattern serving as a small reservoir for the liquid that may leak from the main surface both during the deposition of the film or during very long experiments (due to the long-ranged nature of the flow), to maintain the boundary conditions fixed. We will discuss the effect of borders in Sec. 2.3.4, showing that the central region dominated by the interplay of thermocapillary and intermolecular forces is not greatly affected by the details at the boundaries.

2.2.2 Characterization of the thermal field

In order to characterize the thermal field at the surface of the substrate generated by the printed circuit, we have performed measurements with an infrared camera. We characterise the thermal field $\theta(\mathbf{x})$ for a bare slide, and discuss its shape when only the direction normal to the heating line is considered. These measurements allow us to obtain a relationship between the dissipated electrical power P at the heating line and the maximum temperature difference θ_{max} attained, as well as a rough idea of the decaying length w_0 of the thermal field.

Since the dissipated power P is the main controllable parameter of the experiment, these orders of magnitude are useful to decide the conditions of an experiment. Furthermore, knowing the expected shape of the thermal field will prove useful in the analysis of the experiments, as we shall see in following chapters.

2.2.2.1 Infrared measurements

We use an infrared camera (FLIR Série SC7300L MCT, spectral response 7.7 to 9.3 µm) to measure the thermal field on the surface that will be in contact with the liquid film. That is, this is the resulting thermal field through the glass slide as a result of the heat generated at the printed circuit.

Performing the infrared measurements is a cumbersome task. The infrared measurement requires a detailed calibration of several parameters, which are indicated in the sketch of Fig. 2.2. The parameters to be provided include the thermal emissivity ε of the material under study in the spectral range of the camera and the transmission τ of the surrounding medium (air in our case). Other parameters to be specified include the temperature of the room T_{atm} (typically 25 °C) and an effective temperature modelling other radiation sources T_{rad}. To adjust these values and perform image analysis we use the manufacturer's software providing live thermal images from the camera. The received

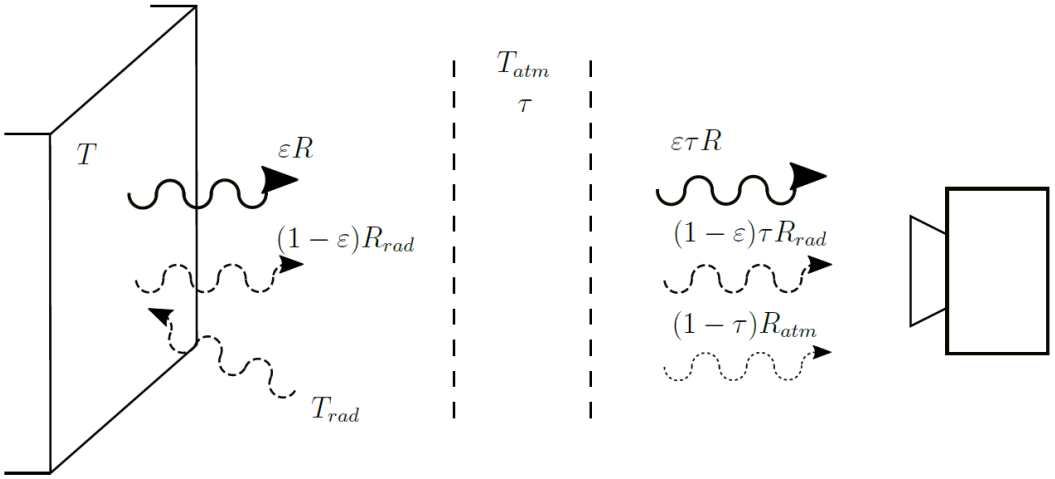

Figure 2.2: Sketch of the thermal system for performing infrared measurements with main variables, based on the photometry form provided with the infrared camera, Ref. [31].

thermal radiation by the camera is expressed as [31]

$$R_{tot} = \varepsilon\tau R(T) + (1-\epsilon)\tau R_{rad}(T_{rad}) + (1-\tau)R_{atm}(T_{atm}), \tag{2.1}$$

where R is the radiation power of the object under study (emitted by the surface in focus), R_{rad} comes from other radiant sources (e.g. room lighting) and R_{atm} from the atmosphere. All these powers are modelled as the power emitted by a black body at temperature T. The calibration curves to convert R_{tot} from the digital signal of the detector into temperature measurements are non-linear and depend upon the temperature range and image integration time [31, 32]. Moreover, the technical specification of the camera states that a continuous, automatic temperature variation compensation is performed adjusting for the housing temperature of the camera, in an unspecified way (which may be related to a radial thermal distortion found on the images, see Sec. 2.2.2.3).

To obtain the emissivity ε of the glass slide, we used a two-point measurement procedure included in the camera controller software. This procedure consists in taking a thermal image of the substrate at two different (known) constant temperatures (i.e. without dissipating heat), from where ε can be deduced. A slide was homogeneously heated with a Peltier device first to 40 °C and then to 80 °C. The obtained emissivity of the glass slide is $\varepsilon \simeq 0.8$.

The measurement of the thermal field $\theta(\mathbf{x})$ is performed in a closed, dark space, so that we usually set $T_{rad} = T_{atm}$ and $\tau = 99\%$. Sometimes we found that these values could be tuned for obtaining a better agreement between the mean temperature of the live image and the room temperature. Once the parameters are fixed, the live camera image shows a homogeneous temperature T_{atm} (see however Sec. 2.2.2.3 below).

The procedure to measure the thermal field for a given a dissipation power P is as follows. The camera is turned on and thermalized for some minutes automatically set by the camera controller. Once thermalization is achieved, we set a given power and the live infrared image begins to show the apparition of the thermal field on the surface that reaches the stationary configuration after a couple of minutes (see discussion of Fig. 2.4

below). Therefore, after some minutes an image of the thermal field is taken and the camera shut down again. This resulting image is obtained by averaging several consecutive frames to reduce high frequency variations, and a median filter was furthermore applied due to the existence of defective pixels in the camera sensor. Several images at different powers could not be taken on a single run because the heating up of the camera produced a spurious thermal contribution to the infrared images, as explained in Sec. 2.2.2.3 below.

An extra image is taken without current ($P = 0$) that serves as the reference for measuring the *excess* temperature field from previous thermal images. The reference temperature background is removed from the thermal images at each dissipated power. An example of obtained dissipated thermal field $\theta(\mathbf{x})$ is shown in Fig. 2.3. We indicate for reference the position of the heating line. We have never seen any indication of the square paddles perturbing the thermal field, all the dissipation is produced at the line.

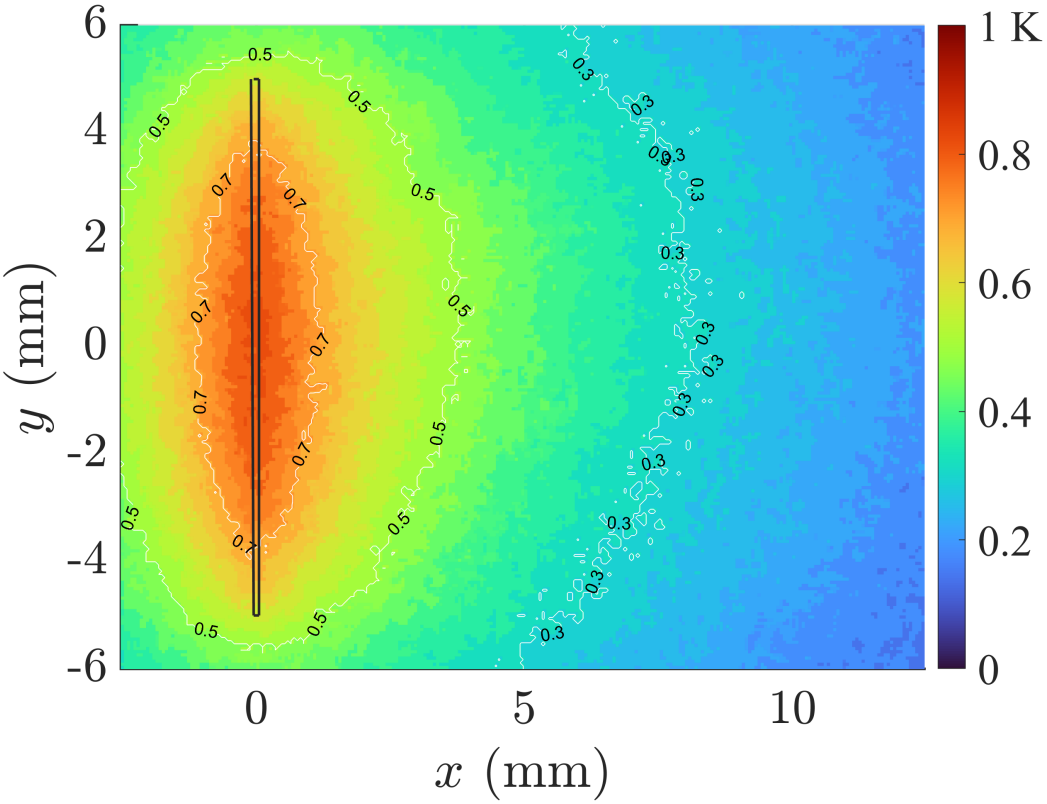

Figure 2.3: Example of thermal field $\theta(\mathbf{x})$ obtained with the infrared camera. In this case, the dissipated power is $P = 2.56(3)\,\mathrm{mW}$. The rectangle indicates the position and size of the heating line. The maximum temperature attained is $\theta_{max} \simeq 0.82\,\mathrm{K}$.

To obtain a time scale associated to the establishment of the stationary thermal field, we have performed measurements of the evolution of the maximum thermal field $\theta_{max}(t)$ from the moment the current is turned on. We took 15 thermal images for minute and the value of $\theta_{max}(t)$ at each time is obtained by averaging the thermal field on a small region around the centre of the heating line ($|x| \lesssim 0.1\,\mathrm{mm}$, $|y| \lesssim 0.25\,\mathrm{mm}$). This region needs to be small because, as we shall see, the thermal field decays exponentially in the x-axis. For typical values of dissipated power P, the the maximum thermal difference $\theta_{max}(t)$ takes a

couple of minutes to establish, as shown in Fig. 2.4. The measurements of $\theta_{max}(t)$ for the two different powers show a very similar time scale, and both have reached and 80% of its stationary value in less than half a minute. In several of the experiments discussed in chapters 3 and 4, the dissipated power will be much smaller than these values, $P \lesssim 1\,\mathrm{mW}$. Therefore, we can conclude that in experiments the establishment of the thermal field will be fast compared to the typical time scales of the dynamics discussed in chapter 1. We will thus make the approximation that the thermal field is immediately in equilibrium after the current is turned on.

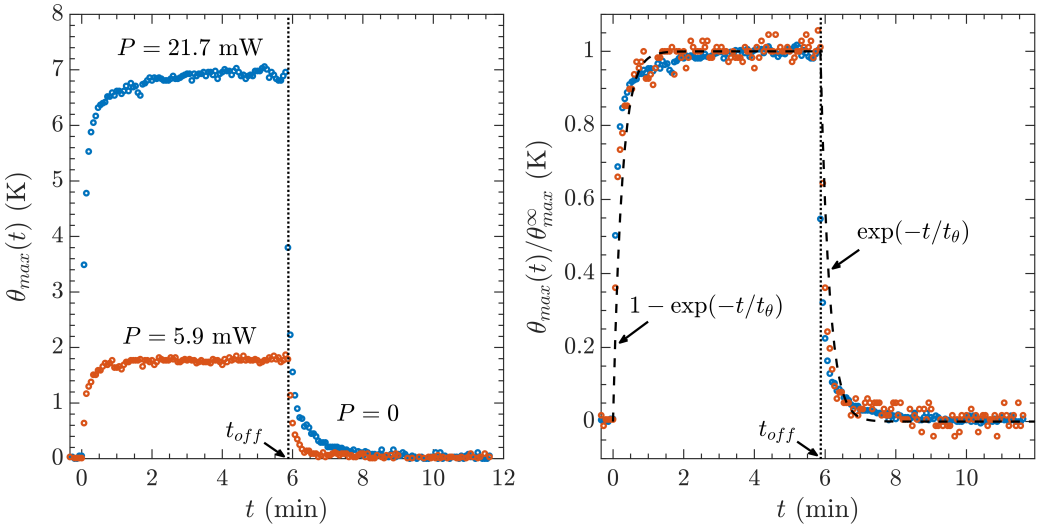

Figure 2.4: Evolution of the maximum thermal field $\theta_{max}(t)$ for two different dissipated powers P. Time starts at the moment at which the current through the circuit is established. The dotted line marked as t_{off} indicates the moment at which the current is turned off for both experiments ($P = 0$) and the slide cools down. Left panel: experimental data, point size represents the camera temperature resolution. Right: same data but rescaled respectively by the final value θ^{∞}_{max} obtained from the average of $\theta_{max}(t)$ from $t = 2.5$ min to $t = 5.5$ min. Note that the last points for the lower power (orange points) show discontinuous jumps due to the limit of the camera thermal sensitivity. Dashed lines are only phenomenological curves for the purpose of comparison, the time scale is $t_\theta = 15$ s in both cases (heating and cooling).

In appendix C we develop a minimal model to describe the thermal field generated by an infinitely thin heating line of a given length L, assuming thermal losses proportional to the temperature field. The resulting field can be expressed as

$$\theta(\mathbf{x}) = \theta_{max} \frac{\int_{y-L/2}^{y+L/2} K_0\left(\mu\sqrt{s^2+x^2}\right) ds}{\int_{-L/2}^{L/2} K_0\left(\mu|s|\right) ds}. \tag{2.2}$$

This model includes two fitting parameters, the maximum thermal difference θ_{max} and a dissipation length μ^{-1} assumed independent of temperature. In Fig. 2.5, we show the temperature field computed with Eq. (2.2) for $\theta_{max} = 0.76\,\mathrm{K}$ and $\mu^{-1} = 10\,\mathrm{mm}$, which agrees well with the experimental field of Fig. 2.3. Note the large value of μ^{-1}, which is

as large as the length of the heating line and on the same order of magnitude as the size of the glass slide.

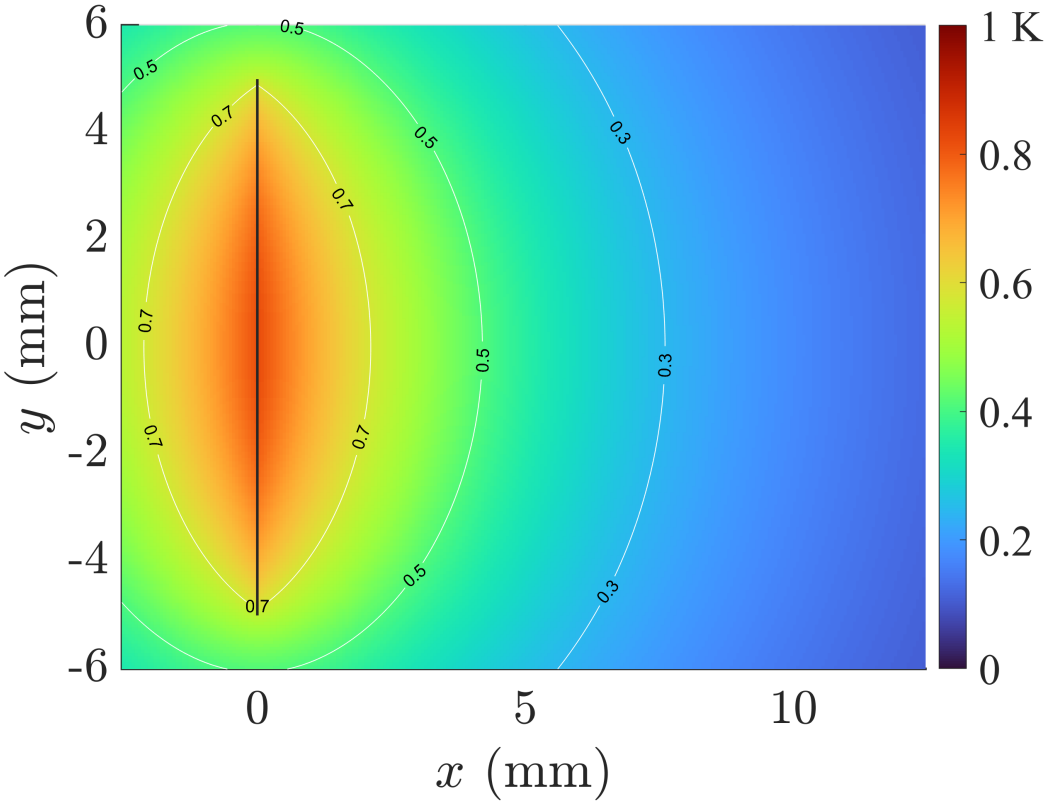

Figure 2.5: Theoretical $\theta(\mathbf{x})$ with $\theta_{max} = 0.82\,\mathrm{K}$ and $\mu^{-1} = 10\,\mathrm{mm}$. The model recovers the behaviour of the experimental thermal field shown in Fig. 2.3. The line indicates the position of the heating source.

2.2.2.2 Calibration: θ_{max} vs. P

In appendix C, we also show that the thermal field along the direction normal to the heating line (the x axis in the plots) can be approximated as an exponential decay, $\theta(x, y = 0) \simeq \theta_{max} \exp(-|x|/w_0)$, with a decay length w_0 that is generally smaller than the dissipation length μ^{-1}.

We thus focus on the thermal field averaged over the central region $y \approx 0$. In the left panel of Fig. 2.6 we show the thermal field obtained in this fashion for several dissipated powers P in a slide with a Cr+Au circuit. This range of powers is similar to the ones used in the experiments that will be discussed in chapter 3.

For a small dissipated power, P, we expect a linear dependence of the thermal field, in particular of its maximum θ_{max}. In the right panel of Fig. 2.6 we divide the curves $\theta(x)$ of the left panel by the corresponding power P used to obtain them. We see that the curves are roughly proportional to each other, with a collapse that is better as the dissipated power increases. The decay of the profiles is approximately exponential, as can be seen by fitting the average of the data of the right plot (except the blue points). We obtain $\theta(x)/P \sim c \exp(-|x|/w_0)$ with a calibration constant $c = 0.3\,\mathrm{K\,mW^{-1}}$ and a

decay length $w_0 \simeq 4.9\,\text{mm}$ (see however Fig. 2.7 below). For small powers (such as for the blue data), the sensitivity of the camera is not enough to obtain precise measurements of the thermal field. We also note that the thermal field does not have a cusp at $x \approx 0$ but that there is a small region roughly of the size of the heating line's width and the substrate thickness $\delta \simeq 0.1\,\text{mm}$ in which the thermal field is approximately constant.

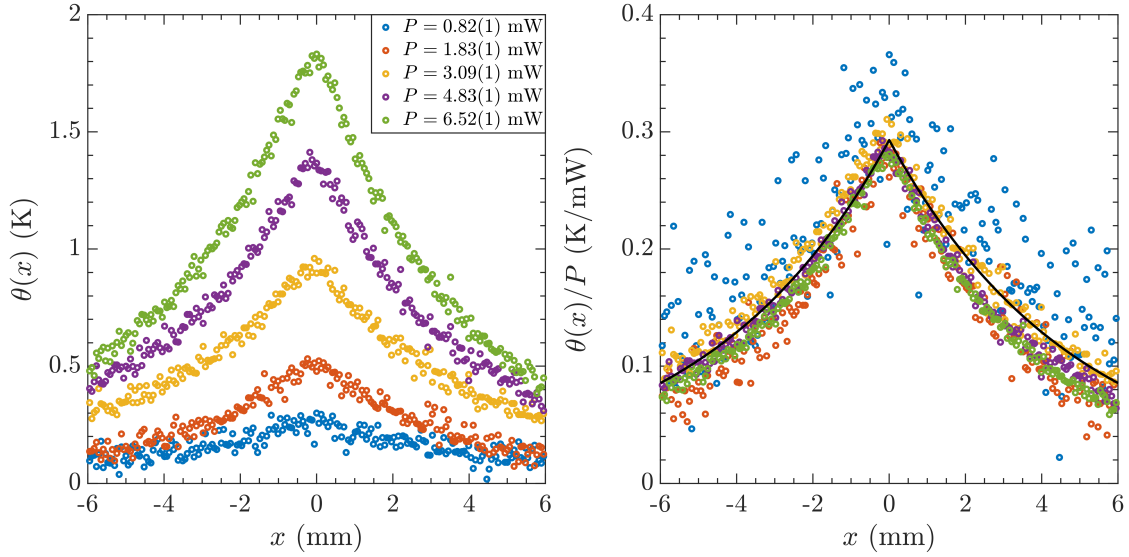

Figure 2.6: Left panel: thermal field $\theta(x)$ obtained with the infrared camera by performing an average over a 0.5 mm region around the $y = 0$ line of the 2D field, such as the one shown in Fig. 2.3. Right panel: same profiles, each one divided by their corresponding dissipated power P. The black line represents $\theta(x)/P \sim c\,\exp(-|x|/w_0)$ where $c = 0.3\,\text{K}\,\text{mW}^{-1}$ and $w_0 \simeq 4.9\,\text{mm}$.

However, we find that the relationship between θ_{max} and P depends on the slide, as shown in Fig. 2.7. The points for different slides with circuits of Cr+Au (circles, different colours) show a similar order of magnitude of θ_{max} for a given power, but the specific calibration constant c is not the same. For example, for the yellow data $\theta_{max} = \left(0.24\,\text{K}\,\text{mW}^{-1}\right) P$, while for the blue data $\theta_{max} = \left(0.67\,\text{K}\,\text{mW}^{-1}\right) P$. We also show data for a slide with an ITO circuit (purple triangles), which also gives a dependency on the same order. This means that we can only obtain a rough approximation of the maximum thermal field imposed, θ_{max}, knowing the dissipated power P. A linear fit of all the Cr+Au data gives the estimate $\theta_{max} \sim \left(0.4\,\text{K}\,\text{mW}^{-1}\right) P$, which describes also the dependency for an ITO circuit. Although we always find an exponential decay, the same variation also applies to the decay length of the thermal field w_0, which is usually between 4 and 6 mm.

These variations are most probably connected to the homogeneity and quality of the printed circuit. As explained before, the width of the heating line can have variations up to 10% from the nominal value $\delta = 0.1\,\text{mm}$. These variations change the heat transfer specially on top of the line, where we measure θ_{max}. Moreover, it changes the shape near the centre, affecting the fitting of w_0.

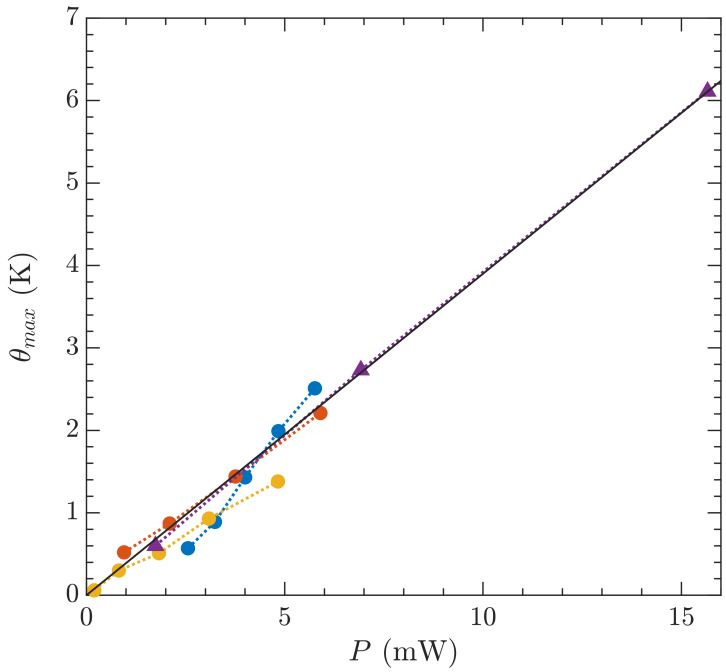

Figure 2.7: Calibration of θ_{max} as a function of the dissipated power P. Different circle points are obtained with different slides with a Cr+Au circuit, the triangle points were obtained with a slide with an ITO circuit.

We have thus obtained an approximate calibration between the maximum thermal field attained θ_{max} with respect to the dissipated power P, and the typical value for the decay thickness of the thermal field, w_0. Both the calibration and the fitted w_0 show variations between different slides, that we relate to specific changes on the printed circuit. Nevertheless, the thermal field reduced to one spatial dimension, $\theta(x)$ indeed can be fitted to an exponential decay, as predicted by the model of appendix C. We can thus expect that the thermocapillary-driven dynamics of the thin liquid films generated by this thermal field will thus be similar to the results of chapter 1.

2.2.2.3 Other limitations

As noted before, after taking a thermal image it was needed to shut down the camera to let it cool down. This was necessary because the thermal images had a radial distortion that grew steadily over time, independently of the object in focus, an effect probably linked to the heating of the camera itself.

Although we tried to minimize this effect by taking an image shortly after the camera was turned on, we cannot completely disregard it. In particular, this effect rendered the centre of the image colder and the borders hotter. Its magnitude increased over time at a rate that reached the order of a couple of degrees after around 10 min. This spurious distortion therefore affects specially a situation of small thermal field, which is already difficult because the resolution of the infrared camera used is roughly of 0.025 K. We have seen that the maximum thermal difference needed to promote the appearance of a ultra-thin film is small, even much less than 1 K. Therefore, when trying to measure the thermal field for small powers, the deviation of the recovered thermal field as explained

in the last paragraph with respect to the true thermal field may be large.

Note that this radial effect, that makes the measured thermal field hotter at the boundaries, may result in the measured μ^{-1} (and w_0) being larger than the real one, again specially for small dissipated power. Since this effect was measurement-dependent, it adds another source of variation to the fitted decay length w_0.

2.2.3 Image acquisition setup

To monitor the dynamics of the thin film driven by thermocapillarity, we measure the thickness of the film at a given time using one of two techniques: an implementation of the free-surface synthetic Schlieren method, introduced in Ref. [33]; or 3-colour interferometry (similar to the methods of Refs.[34, 35]). These techniques will be explained in detail in following sections.

In either case, the analysis is made from images of the film. Since we use both a transparent substrate and transparent liquids, the illumination is done from below the cell, and the images are always taken from the top of the film, as sketched in Fig. 2.8. The illumination is provided by a LED panel (PHLOX RGB led Backlight 50x50) able to emit light in three quasi-monochromatic wavelengths independently, as detailed below. A monochrome camera on top (SVS-Vistek exo174MU3) serves to take images from the experiments at a given period. As will be explained later on in Sec. 2.4, the LED panel and the camera are synchronized with a custom Labview program so that images with different wavelengths can be taken at specified times.

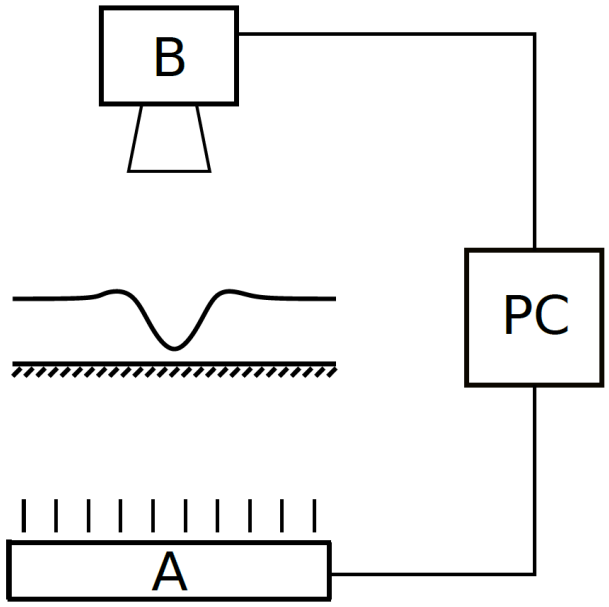

Figure 2.8: Sketch of the image acquisition system (not to scale). The RGB LED panel (A) is located under the experimental cell. The light emitted by the LED traverses the cell and it is recorded with a monochrome camera on top (B). Both LED panel and camera are connected to a computer (PC) that allows to synchronize the image acquisition with the change of colour using a custom LabView program.

The spectral emission of each wavelength is shown in Fig. 2.9, from where the wave-

lengths λ_C of peak emission for each channel ($C = R,\ G,\ B$), together with the typical half-widths λ_C of the peaks can be determined: $\lambda_R = 635\,\text{nm}$, $\Delta\lambda_R \approx 10\,\text{nm}$ for the red light; $\lambda_G = 518\,\text{nm}$, $\Delta\lambda_G \approx 20\,\text{nm}$ for the green light; and $\lambda_B = 463\,\text{nm}$, $\Delta\lambda_B \approx 15\,\text{nm}$ for the blue light.

As we shall see, this setup is already good enough to allow the measurement of thicknesses down to the tens of nanometres over a field of view covering several cm^2.

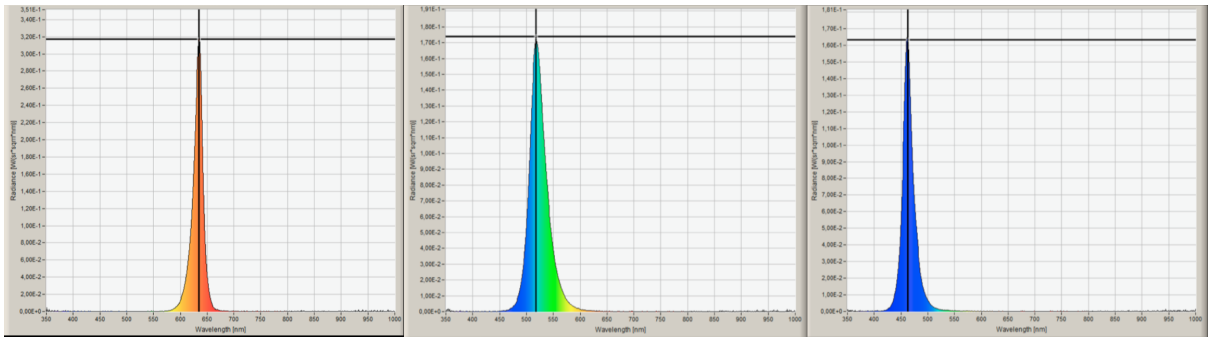

Figure 2.9: Spectral radiance of the LED channels as a function of the wavelength λ (ranging from 350 to 1000 nm), provided by the manufacturer. The cross at each panel indicates the maximum peak emission, defining the central wavelength λ_C for each colour, $C = R,\ G,\ B$. Left: red, $\lambda_R = 635\,\text{nm}$, $2\Delta\lambda_R \approx 20\,\text{nm}$ (maximum spectral radiance $0.3185\,\text{W}\,\text{sr}^{-1}\,\text{m}^{-2}\,\text{Hz}^{-1}$). Centre: green, $\lambda_G = 518\,\text{nm}$, $2\Delta\lambda_G \approx 40\,\text{nm}$ (maximum spectral radiance $0.1738\,\text{W}\,\text{sr}^{-1}\,\text{m}^{-2}\,\text{Hz}^{-1}$). Right: blue, $\lambda_B = 463\,\text{nm}$, $2\Delta\lambda_B \approx 30\,\text{nm}$ (maximum spectral radiance $0.1635\,\text{W}\,\text{sr}^{-1}\,\text{m}^{-2}\,\text{Hz}^{-1}$).

2.3 Thickness measurements

To study the dynamics of the film, we aim to measure its thickness profile at any given time. In this section, we explain the two methods that we have used to monitor the evolution of the thickness.

Each technique is used for measuring the dynamics at different scales. We first explain the free-surface synthetic Schlieren method (FS-SS). This technique gives the overall height profile above roughly one micron. It is used to explore the scale of the initial thickness h_0, that is, on the tens of micrometres scale. Later on, we discuss the 3-colour interferometric technique used to resolve the dynamics of the ultra-thin film below $\sim 1\,\mu\text{m}$.

Before explaining these main experimental techniques, we briefly comment on how we determine the initial thickness of the film, once it has been deposited with the spin coater and before starting the experiment.

2.3.1 Measurement of the initial thickness

Following the discussion about the space parameter leading to Fig. 1.12 of chapter 1, giving the conditions for establishing the ultra-thin film with a temperature field imposing a maximum difference $\theta_{max} \sim 1\,\text{K}$, we consider initial mean thicknesses of the liquid film h_0 in the range roughly from 10 to 60 µm. The film is deposited with a spin coater, as explained below in Sec. 2.4.2, and we measure it with an optical profilometer.

The film obtained by spin coating may not be completely homogeneous, especially for the thicker films. Therefore, we take several measurements of a same film at different points, typically two to four depending on the thickness variations that we encounter. The initial thickness h_0 indicated in the discussion of experiments of chapters 3 and 4 is the average over these measurements. The standard deviation is typically of some micrometres.

These measurements must be done as quickly as possible after deposition because of two main reasons. The first one is that the measurements are done in a regular atmosphere and thus it is possible that some dust particles are deposited on the film during this process. The second one is the fact that heating from the light of the profilometre is enough to promote the thermocapillary effect on the film. Although the light intensity is not high and the absorption of the liquids very small, it can induce a local depression on the liquid film of some micrometres on the scale of half an hour. Hence each measurement, which may take up to 3 minutes, must be done in a different spot of the slide each time to prevent the formation of severe local depressions.

2.3.2 Free-surface synthetic Schlieren method

In chapter 3, we will be particularly focused on analysing the dynamics of the ultra-thin film that appears when the thermocapillary effect empties a region around the heating line. In our case, ultra-thin film refers to layers of thicknesses below the micrometer scale.

Before doing this, we will do a characterisation of the dynamics above the micrometer scale when both Laplace and gravitational pressure are acting on the liquid. In this section we explain the principle and implementation of a free-surface synthetic Schlieren (FS-SS) method [33] to measure the height profile $h(t, \mathbf{x})$ of the liquid film. This technique is based in a two-step process. The first step is based in digital image correlation and allows to obtain the gradient of the height profile, $\boldsymbol{\nabla} h$, over the field of view of the camera, from the refracted image of a speckle pattern, in our case situated between the LED panel and the experimental cell. The second step consists on integrating this gradient to obtain a measurement of the relative height Δh with respect to a homogeneous film.

We explain the details of this technique as implemented in our setup and discuss its limitations in the following sections.

2.3.2.1 Principle

FS-SS is based on the relationship between the refracted image of a dot pattern situated below the film, and the deformations of the free interface of the liquid film that generates it. Fig. 2.10 sketches the system.

Initially, when the film is homogeneous, a reference image of the speckle pattern trough the film is taken. When the surface is deformed, a second image of the speckle pattern appears distorted due to the refraction of light as shown in Fig. 2.10. The distortion at each point $\mathbf{x}$ with respect to the reference image defines a displacement field $\boldsymbol{D}(\mathbf{x})$, that is related to the gradient of the surface $\boldsymbol{\nabla} h(\mathbf{x})$.

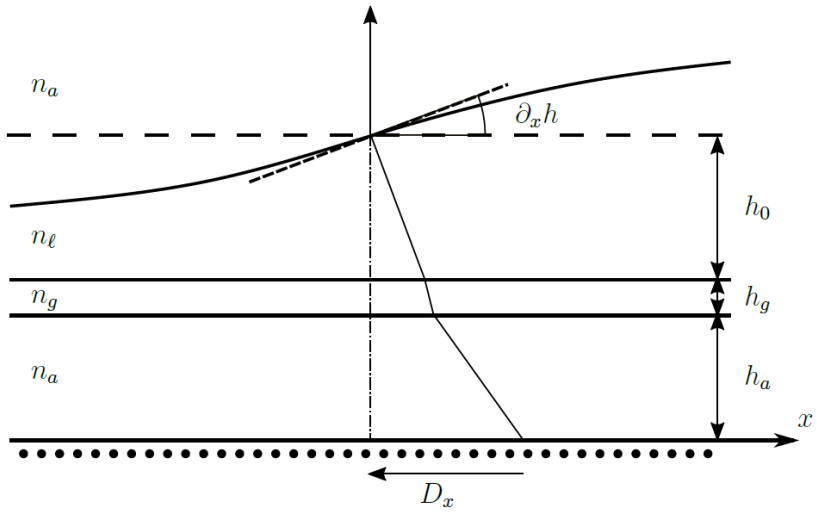

Figure 2.10: Sketch in 2D (not to scale) of the relationship between the slope of the surface, $\partial_x h$ and the refracted image of a point on a speckle pattern, which appears in the camera at a displaced position D_x with respect of its real position. The same principle applies simultaneously along the y-axis. n_a: air refractive index. n_g: glass refractive index. n_ℓ: liquid refractive index. h_a: air gap height. h_g: glass slide thickness. h_0: initial mean thickness. The speckle pattern is represented by the grid of dots a the bottom, although in experiments is not homogeneous, see Fig. 2.11.

The relationship between the displacement field and the surface gradient is linear if the following conditions are satisfied [33]. First, the small parallax approximation, which requires the pattern-to-camera distance to be much larger that the characteristic size of the field of view, so that only normal incidence can be considered. In our system, the camera is at about $H_c \simeq 30\,\text{cm}$ above the experimental cell, and the imaged field of view has a typical size of $W_{FOV} \simeq 2\,\text{cm}$. The maximum parallax angle $\beta_{max} = W_{FOV}/(\sqrt{2}H_c)$ is therefore small, $\beta_{max} \simeq 2.7°$.

Second, the small angle approximation, that requires the surface slopes to be sufficiently small so that only first order effects can be considered, and preventing against the formation of optical caustics. This criterion is intrinsically considered in our system since we aim to work in the conditions described by the thin film equation. Recalling the numerical profiles showed in Sec. 1.2 of chapter 1, the region of maximum slope of the dynamics is at the wedge between the central ultra-thin film and the outer region of the film. At this region, the slope is about $1 \times 10^{-2}\,\text{rad} \simeq 0.6°$ at its maximum, so that the approximation should be satisfied in our system. In all the measurements we have performed with this technique, we have never measured angles above $1 \times 10^{-1}\,\text{rad} \simeq 6°$ for the wedge. Since the central and outer regions are flatter, with typical slopes below $1 \times 10^{-3}\,\text{rad}$, our system does not show optical caustics in the range of parameters explored.

In the third place, the weak amplitude approximation, requiring the disturbance Δh measured to be small compared to the optical distance between the dot pattern and the free surface of the liquid. Since the optical distance h_{opt} between cell and pattern is essentially equal to the thickness of the auxiliary support, which is $h_{opt} \simeq 5\,\text{mm}$ (see below); and we work with films of typical thicknesses $h_0 \sim 30\,\mu\text{m}$, even if the deformation

of the surface Δh at the region where the ultra-thin film has formed is of the order of the initial thickness, $\Delta h \sim -h_0$, we will still have $|\Delta h| \ll h_{opt}$. This satisfies the third condition.

Under these conditions, it is possible to show that the gradient of the surface $\boldsymbol{\nabla} h$ is proportional to the displacement field $\boldsymbol{D} = (D_x, D_y)$ (see Fig. 2.10 above) of the image of the speckle pattern with respect to a reference image [33],

$$\boldsymbol{\nabla} h = -\frac{\boldsymbol{D}}{h_{opt}} \tag{2.3}$$

where

$$h_{opt} = \left(\frac{n_a}{n_l} - 1\right) h_0 + \frac{n_a}{n_g} h_g + h_a \tag{2.4}$$

represents an optical pattern-to-surface length, where the variables are defined in Fig. 2.10. We take the refractive indexes at the reference temperature, we have checked that for small temperature variations Eq. 2.3 does not change. With the parameters of our system, $h_{opt} = 5.05\,\text{mm} \simeq h_a = 5\,\text{mm}$.

2.3.2.2 Image analysis

In our experiments, the speckle pattern is provided by a tracing paper firmly attached below the auxiliary support of the cell. Before turning the current on to generate the thermal field, we take a reference image of the pattern trough the cell, including the initial, homogeneous liquid layer. Once the thermal field is established, the thermocapillary effect deforms the surface as we have seen in chapter 1. This produces the refraction in which the FS-SS measurement is based.

Digital image correlation (DIC) is a technique that recovers the displacement field by performing, in its simplest form, a convolution of small image subwindows from the reference image with all subwindows of the refracted image. The displacement of the original subwindow is obtained from where the maximum correlation peak is found. This method allows to obtain subpixel resolution.

To recover the displacement field $\boldsymbol{D}(\mathbf{x})$, we use NCorr [36], an open-source implementation of DIC available as a library for MATLAB [37]. NCorr uses circular subwindows, we set their radius to 10 px with centres at a grid with interspaces of 4 px (the minimum values the program allowed). In Fig. 2.11, we show an example of the displacement D_x (direction normal to the heating line) in a thermocapillary experiment performed with silicone oil (similar to the experiments explained later on in chapter 3), superimposed to the corresponding experimental image. The brighter areas correspond to the wedges (regions of higher slopes) appearing as a result of the thermocapillary dynamics as explained in chapter 1. The change in sign represents the opposite slopes of $h(t, \mathbf{x})$.

To check that the system was properly set up, we performed the following calibration. We interposed a glass slide of known thickness and refractive index between the speckle pattern and the camera. This glass slide was supported in a goniometer stage, so that a given angle β with respect to the horizontal plane could be fixed. The rotation axis is set so that the displacement is mainly in the x direction, $\boldsymbol{D} \simeq D_x \boldsymbol{e}_x$ as in Fig. 2.10. A reference image was taken with the glass slide in a horizontal position. A sequence of images were taken with the glass slide tilted to different angles, and we obtained

in each case an homogeneous displacement D_x with NCorr throughout the image. The averaged displacement $\langle D_x \rangle$ over all the subwindows can be compared with the theoretical expectation of this simple system, where the displacement D_x measured is proportional to the tangent of β. For small angles, since $\tan(\beta) \approx \beta$ we have $D_x \propto \beta$. The resulting measurements is compared with the theoretical expectation in Fig. 2.12. The agreement is very good and the errors small for the range of angles considered, validating the setup.

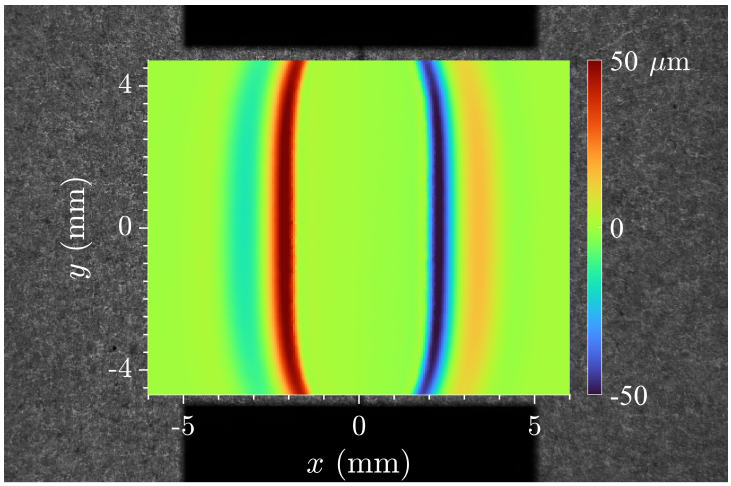

Figure 2.11: Example of horizontal displacement D_x (coloured area) obtained from NCorr in an experiment with silicone oil, overlaid on top of the corresponding experimental image. The integrated surface obtained from this displacement, together with the vertical displacement D_y (not shown), is shown in Fig. 2.13.

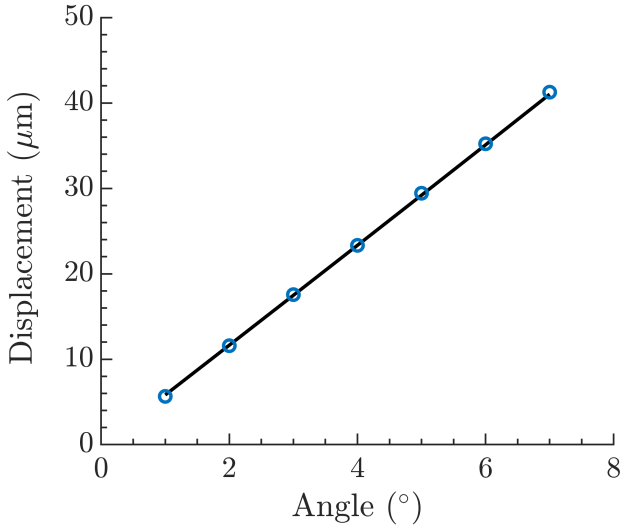

Figure 2.12: Calibration of DIC procedure. Points represent the measured mean displacement D_x of a glass slide tilted with respect to the x that has been interposed between the LED and the camera, compared with a reference image taken with the glass slide in horizontal position. Errors are smaller than the symbol size. The black solid line is the theoretical expectation. Other details are given in the main text.

We note, however, that slopes of the surface are usually smaller than 1°. From Eq. (2.3), a local slope $|\partial_x h| \sim 1 \times 10^{-3}$ rad would require to measure $|D_x| \sim 5\,\mu$m. The typical resolution of the images is around 12µm/px. Although NCorr is capable of subpixel resolution [36], we shall see that the ultra-thin film region is not recovered with enough accuracy after the integration of the profiles, and that another technique is needed to obtain information in this region.

2.3.2.3 Integration

Once the displacement field $\boldsymbol{D}(\mathbf{x})$ has been obtained, the gradient of the surface $\boldsymbol{\nabla} h$ can be computed using expression (2.3). The last step to obtain the disturbance Δh of the thickness with respect to the original film of homogeneous thickness h_0 is the integration of $\boldsymbol{\nabla} h$. This is done using a global integration scheme that recovers the surface Δh such that its gradient best approximates the provided $\boldsymbol{\nabla} h$ in a least-squares sense, with a regularizing procedure to avoid bias induced by noise [38]. This method is available as a library for MATLAB [39]. This method uses a representation of the surface with a set of orthonormal functions. Due to the symmetry of the gradient (proportional to the displacement as shown in Fig. 2.11), we chose a cosine decomposition from the options available to the library.

It is important to note that after integration the recovered surface Δh is obtained up to an overall constant. This implies that we do not have an absolute thickness, but a relative one measured with respect to a horizontal plane. In principle, if the disturbance of the surface does not reach the boundaries of the image, one can offset the surface so that the boundaries correspond to h_0. However, due to the long-ranged nature of the dynamics as shown in chapter 1, this does not always give consistent results for recovered profiles at successive times.

The recovered surface $h(\mathbf{x})$ corresponding to the experimental image of Fig. 2.11 is shown in Fig. 2.13. In this case, we offset the resulting surface with the initial thickness $h_0 \simeq 18\,\mu$m.

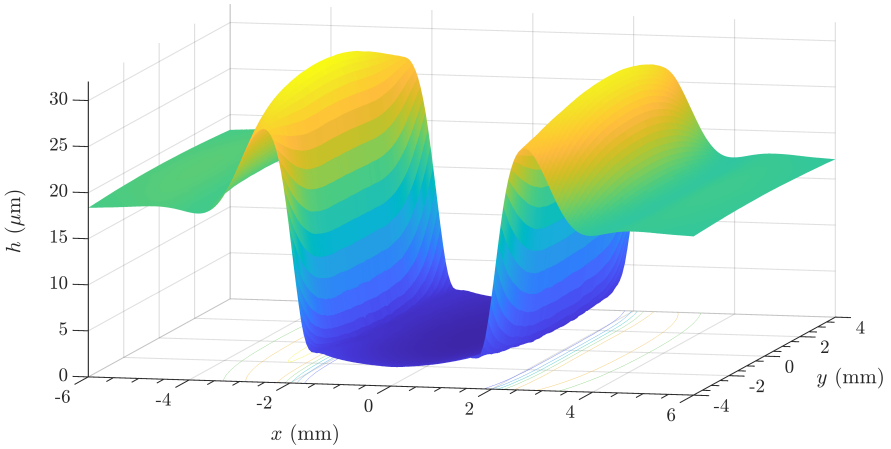

Figure 2.13: Integrated surface corresponding to the experiment whose horizontal displacement D_x was shown in Fig. 2.11. To recover the surface the displacement in the y axis, D_y must also be provided (not shown).

As noted previously in the discussion of the thermal field, we will focus only in the dynamics in the direction normal to the heating line (representing the x axis) around $y = 0$. Therefore, for discussing the dynamics, we average the surface $h(\mathbf{x})$ in a region typically of about half to one millimetre in the y direction, to obtain a profile on one spatial direction $h(x)$. For example, the profile $h(x)$ corresponding to the surface of Fig. 2.13 is shown in Fig. 2.14. We can see that the profile recovered resembles those obtained numerically in chapter 1 by integrating the thin film equation. There are some asymmetries in the profiles which, as we discuss later on in Sec. 2.3.4, can be both caused by border effects and from some spurious displacements coming from intensity variations.

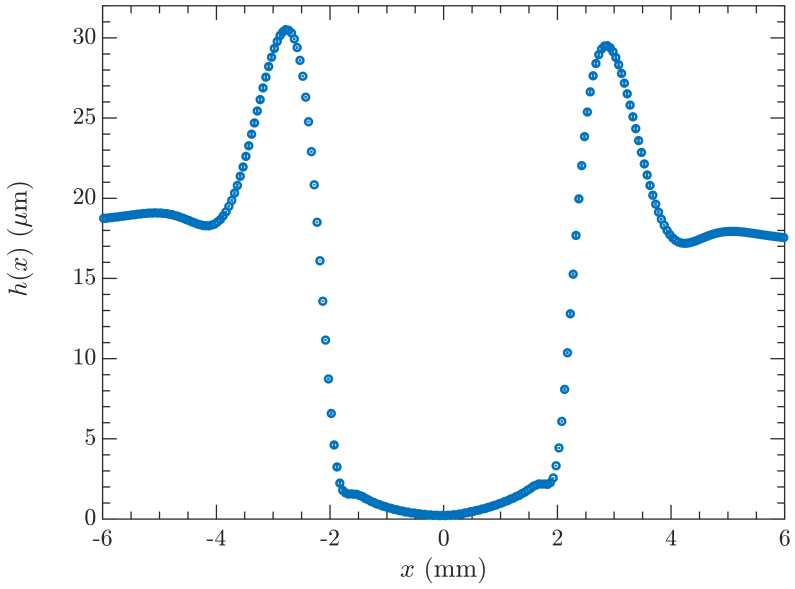

Figure 2.14: Height profile recovered by an average of the surface of Fig. 2.13 over a small strip around $y = 0$. The standard deviation is of the order of the symbols size.

This FS-SS technique thus allows to measure the thin film on the scale of the initial thickness, h_0, of several tens of micrometres. Therefore, throughout the following chapters we consider this technique as a method to recover the thermocapillary dynamics at large scales, providing an initial validation of the hydrodynamics description of chapter 1 for the different liquids used. For example, it will allow us in chapter 4 to establish the similarities between the evolution of silicone oil films and alkanes films at short times, where the generic contributions of Laplace and gravity pressures to the dynamics are dominant.

Nevertheless, we are also interested in measuring the effect of intermolecular forces on the dynamics. Since these effects appear below the scale of the micrometre, we present in the following section an interferometric technique for the measurement of the height profiles at these very small scales.

2.3.3 3-colour interferometry

In the previous section we have presented a method for measuring the micrometric thickness variations of the initial thin film. However, in the thermocapillary-driven dynamics

explained in chapter 1, the formation of an ultra-thin film is observed. This ultra-thin film, with a thickness on the tens-to-hundreds of nanometres, arises from the interplay of the thinning dynamics of the thermocapillary effect and the specific nature of intermolecular forces of the solid/liquid/air system.

To recover the dynamics of the ultra-thin film, we use an interferometric technique that allows to obtain the absolute thickness of the film from the interference pattern of three different light wavelengths. Similar methods have been used in the literature, see for instance [34, 35].

2.3.3.1 Principle

To obtain an absolute measurement of the height profile of the ultra-thin film at a given time, we will use a method based on comparing the periodicities of equal-thickness interference fringes obtained with different wavelengths. Since both substrate and liquid are transparent, we consider the interference in transmission. The interference is sketched in Fig. 2.15.

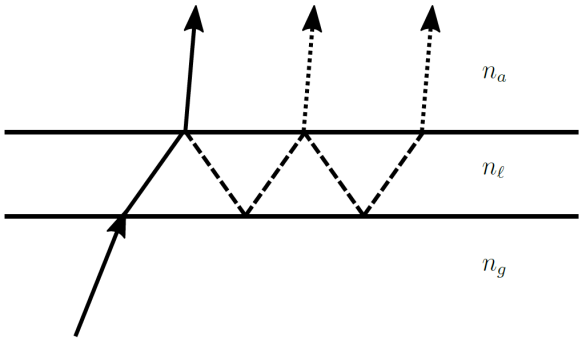

Figure 2.15: Sketch of the multiple beam interference in the three-layer glass/liquid/air system.

We study the transmission interference in a three layer system. Only the medium in between, that is the liquid, is considered to be thin enough to provoke the interference. Both the substrate (glass) and the surrounding air are thus considered to be semi-infinite media. These layers are characterized by their corresponding refractive indices n_g (glass), n_ℓ (liquid), and n_a (air). In our case $n_g > n_\ell > n_a$. The incident light enters from the glass, interferes on the thin liquid film and is transmitted to the surrounding air before being collected by the camera.

We start the description of the interference intensity from the simplest case of a point source of monochromatic emission, and then discuss how this intensity becomes modified when considering that the source is extended and its emission quasi-monochromatic.

Ideal case

In general, the transmitted intensity of a three-layer system as the one sketched in Fig. 2.15 can be obtained from the transfer matrix method that relates the electromagnetic field computed from the Fresnel reflection and transmission coefficients at the different interfaces [40]. The transmitted intensity of coherence monochromatic light of wavelength

λ from a point source, at normal incidence, can be written for our system as

$$I_t(h;\lambda) = \frac{A}{1 + B\cos(\phi(h;\lambda))} \tag{2.5}$$

where the phase $\phi(h;\lambda)$ depends on the film's thickness as

$$\phi(h;\lambda) = \frac{4\pi n_\ell h}{\lambda}, \tag{2.6}$$

and the amplitudes are

$$A = \frac{8 n_g n_\ell^2 n_a}{n_\ell^4 + n_\ell^2\left(n_g^2 + 4 n_g n_a + n_a^2\right) + n_g^2 n_a^2}, \tag{2.7}$$

$$B = \frac{(n_g^2 - n_\ell^2)(n_\ell^2 - n_a^2)}{n_\ell^4 + n_\ell^2\left(n_g^2 + 4 n_g n_a + n_a^2\right) + n_g^2 n_a^2}. \tag{2.8}$$

In our system, $n_g = 1.50$, $n_a = 1.00$, and n_ℓ depends on the liquid used. For example, for silicone oils (chapter 3) $n_\ell = 1.40$ and the amplitudes are hence $A = 0.971$, $B = 0.012$. The small value of B allows to approximate Eq. (2.5) to obtain the well-known form

$$I_t(h;\lambda) \simeq A\left[1 - B\cos(\phi(h;\lambda))\right]. \tag{2.9}$$

In our setup, the light source is a LED panel. Therefore, it is an extended incoherent source of quasi-monochromatic emission on each wavelength, which affects the visibility of the interference fringes.

Extended source

Since the source has a finite size, each ray reaching the camera may have an intensity contribution coming from different points on the source. This situation is sketched in Fig. 2.16, where we define the maximum illumination aperture angle β_{max} from the LED-to-cell distance and the half size of the LED. In our setup this angle is small, $\beta_{max} \sim 6°$. For simplicity, we approximate this effect by considering that every point on the focused plane receives light from the same incident light cone with homogeneous irradiance. This situation is analogous to the finite illumination numerical aperture that has an important contribution to the visibility of the fringes in reflection interference contrast microscopy [35, 41].

For small incident angle β the coefficients A and B remain constant. The phase ϕ depends also on the incident angle as

$$\phi(h,\beta;\lambda) = \frac{4\pi n_\ell h}{\lambda}\cos(\beta), \tag{2.10}$$

so that the complete intensity is now approximated as an integration of the contributions for the cone of semi-angle β_{max}

$$I_t(h;\lambda) \propto \int_0^{\beta_{max}} \left[1 - B\cos(\phi(h,\beta;\lambda))\right]\sin(\beta)d\beta \tag{2.11}$$

which gives

$$I_t(h;\lambda) \propto 1 + B\ \text{sinc}\left[\phi(h,0;\lambda)\sin^2(\beta_{max}/2)\right]\cos\left[\phi(h,0;\lambda)\cos^2(\beta_{max}/2)\right]. \qquad (2.12)$$

A finite β_{max} has hence two effects. The first is a modulation of the interference amplitude B in expression 2.5, introducing a dependency with the thickness h which makes the interference visibility vanish as h grows. The second one is a small change in the position of the interference extrema, since the phase $\phi(h;\lambda)$ inside the cosine is multiplied by a small factor depending on β_{max}.

In our current setup, $\cos^2(\beta_{max}/2) = 0.9973 \simeq 1$, so that this effect can be neglected.

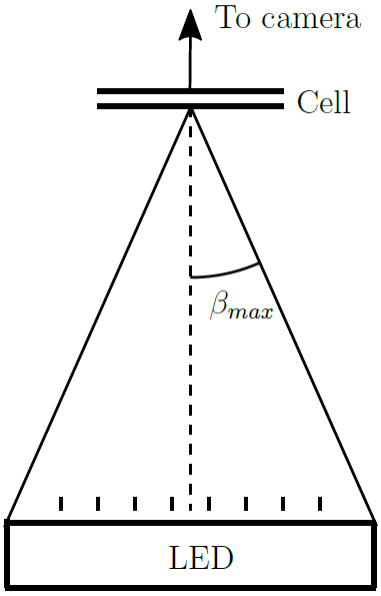

Figure 2.16: Sketch of the illumination numerical angle considered for the influence of the finite source size.

Quasi-monochromatic emission

The main effect that will decrease the visibility of the interference fringes in our setup is the finite band-width emission of the LED. As we saw in Fig. 2.9, the LED we use can emit in a fairly narrow band for each of three wavelengths independently. We denote λ_C the wavelength at peak emission and $\Delta\lambda_C$ the typical half-width of the emission peak, for $C = R, G, B$: $\lambda_R = 635\,\text{nm}$, $\Delta\lambda_R \approx 10\,\text{nm}$ (red light); $\lambda_G = 518\,\text{nm}$, $\Delta\lambda_G \approx 20\,\text{nm}$ (green light); and $\lambda_B = 463\,\text{nm}$, $\Delta\lambda_B \approx 15\,\text{nm}$ (blue light).

To obtain the transmission intensity as a function of the film thickness $I_C(h)$, we need to integrate the intensity at each wavelength $I_t(h;\lambda)$ given by Eq. (2.5) with a weight function representing the relative emission of each wavelength. We approximate this weighting function as a Gaussian distribution

$$p(\lambda;\lambda_C,\Delta\lambda_C) \propto \exp\left(-\frac{1}{2}\left[\frac{\lambda-\lambda_C}{\Delta\lambda}\right]^2\right). \qquad (2.13)$$

The transmitted intensity $I_C(h) \equiv I_t(h; \lambda_C, \Delta\lambda_C)$ as a function of the film's thickness for each wavelength λ_C is therefore computed as

$$I_C(h) \propto \int_0^\infty p(\lambda; \lambda_C, \Delta\lambda_C) I_t(h; \lambda) d\lambda. \tag{2.14}$$

Integrating this distribution we obtain the final intensity depending solely on the thickness. In Fig. 2.17 we compare the intensity obtained with Eq. 2.14 (solid curves) with the ideal model of Eq. (2.5), taking the emission parameters of the LED panel we use. We plot the thickness range from 0 to 2 µm, which is the range we are interested in resolving and which coincides with the range in which fringes of the three colours can be seen. The effect of the finite distribution of emission wavelengths is mainly the loss of coherence as the thickness grows, which translates into a reduced visibility of the fringes. The fringes disappear completely when the thickness of the film reaches the tens of micrometres scale. For high-order fringes, there is also a small variation on the periodicity of the interference, which for the ideal source is $\propto \lambda_C/(2n)$. Other experimental factors that may impact the visibility are discussed later on in Sec. 2.3.4.

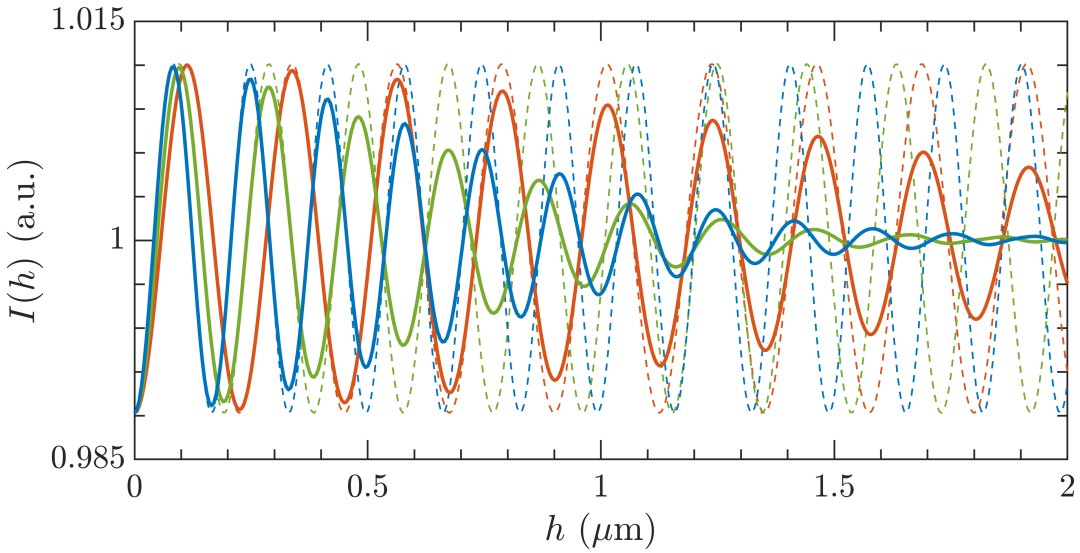

Figure 2.17: Transmission interference model Eq. (2.14) with experimental optical parameters for the three wavelengths of the LED panel used for illumination. The dashed curves corresponds to the interference with similar emission in the ideal case of a point-like, monochromatic source from Eq. (2.5).

From the images of the interference fringes due to the different wavelengths appearing in the experiments, we can use expression (2.14) to obtain the thickness h of the film, as explained below.

2.3.3.2 Experimental implementation

A LED with three quasi-monochromatic wavelengths, each of which can be independently controlled, is located under the experimental cell as explained above in Sec. 2.2.3.

Since we are using a monochrome camera, independent images must be taken to obtain the interference patterns of each wavelength. In an experiment, we take an image for each colour with a setted delay between them that is typically of 2 s. We have seen that the typical timescale of the dynamics is of several minutes, and can become of the order of days when the ultra-thin film is established, see Sec. 1.6 of chapter 1. Therefore this small delay between the images does not introduce any noticeable effect, as we show below.

Data acquisition

To obtain the interference pattern of an image with an ultra-thin film, we proceed as follows. Before turning on the current through the circuit, we take an image of the initial homogeneous film. Since the thickness is on the tens of micrometres, there is no visible interference. This image serves as the reference (homogeneous) intensity $I_0(\mathbf{x})$. We maintain the location dependence because there are small intensity inhomogeneities from the source itself. Afterwards, when we take an experimental image with an ultra-thin film provoking interferences, we divide this image by the reference frame taken at the beginning, to obtain a relative intensity.

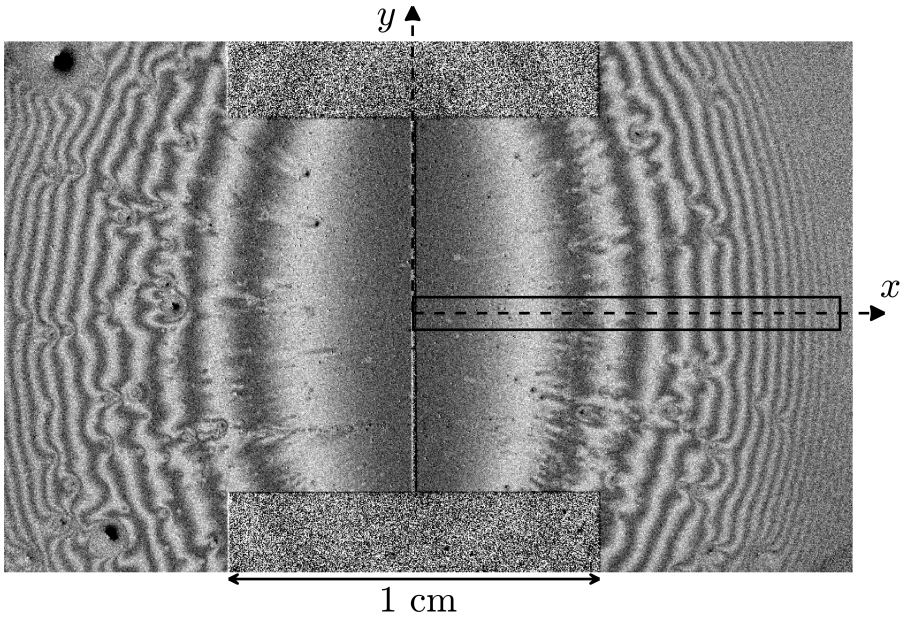

Figure 2.18: Typical interference image after several hours of an experiment, taken with the red light $\lambda_R = 635\,\text{nm}$. The black points, especially at the left of the image, are dust particles that have deposited during the length of the experiment. Dust particles have a wake in the direction of the flow that produces the modulations on the fringes. The tiny white spots are imperfections of the slide that were present before the experiment began. The rectangle indicates the region of interest used for analysing the height dynamics, with a vertical size of 1 mm. The intensity profile on this region, averaged in the vertical direction y, can be seen below in Fig. 2.19.

An example of an experimental image showing the interference pattern of the film in the long-term regime of the dynamics is shown in Fig. 2.18, obtained in the way just explained. We will discuss the effect of dust particles deposited on the slide (such as the

black points on the left of the image) later on in Sec. 2.3.4. Note that the fringes of equal thickness have a similar shape as the full thermal field imposed, see Fig. 2.3 above. In order to apply the approximation that the flow is perpendicular to the heating line (in the x direction), it is imperative to find a clean region of interest close to the centre of the heating line ($y = 0$). An experiment where no such region can be found is discarded.

We limit our measurements to obtaining the height profile $h(t, x)$ along the x direction near $y = 0$. To reduce the effect of noise coming from individual pixel variations, each interference profile is averaged over a suitable region of interest, as the one delimited by the rectangle of Fig. 2.18. The averaged intensity $I_R(x)$ along the vertical direction of this strip is shown in Fig. 2.19. We have checked that performing the measurement procedure to be now described on each intensity line (row of pixels) first, and then averaging the resulting thickness profiles, gives the same result (within experimental errors) as working directly with the averaged intensity.

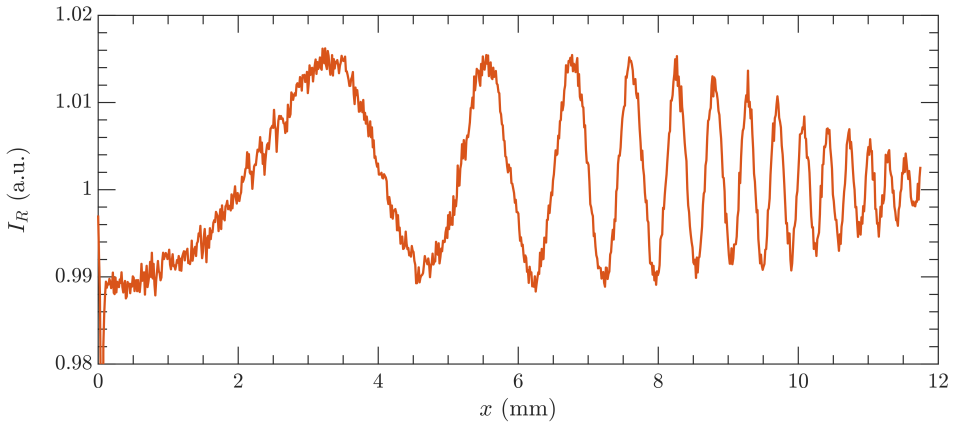

Figure 2.19: Intensity profile $I_R(x)$ at the region of interest delimited by the rectangle of Fig. 2.18, obtained by averaging in the y direction.

Performing this averaging process for all the images of an experiment, the spatio-temporal evolution of the intensity can be obtained for each colour. An example corresponding to the intensity of the experiment of Fig. 2.18 is shown in the left panel of Fig. 2.20. We have noted that images at individual times may have a small overall background intensity shift (at most a 1% variation around the mean image intensity) from high frequency intensity shifts of the LED panel. These shifts can be seen in the left panel of Fig. 2.20, which corresponds to the evolution of the region of interest marked by the rectangle of Fig. 2.18.

Hence, once the collection of intensity profiles at the region of interest has been obtained, every profile is slightly shifted so that its mean intensity value is equal to 1, which is the expected relative intensity at infinite thickness. For some experiments the fringes do not reach the boundary of the image, which stays with the homogeneous initial intensity for large x. If there is a range at large x that does not show fringes, then it is this region which is used to shift the relative intensity of this profile to 1 if needed. The corresponding corrected interference pattern of the left panel of Fig. 2.20 is given in the right panel.

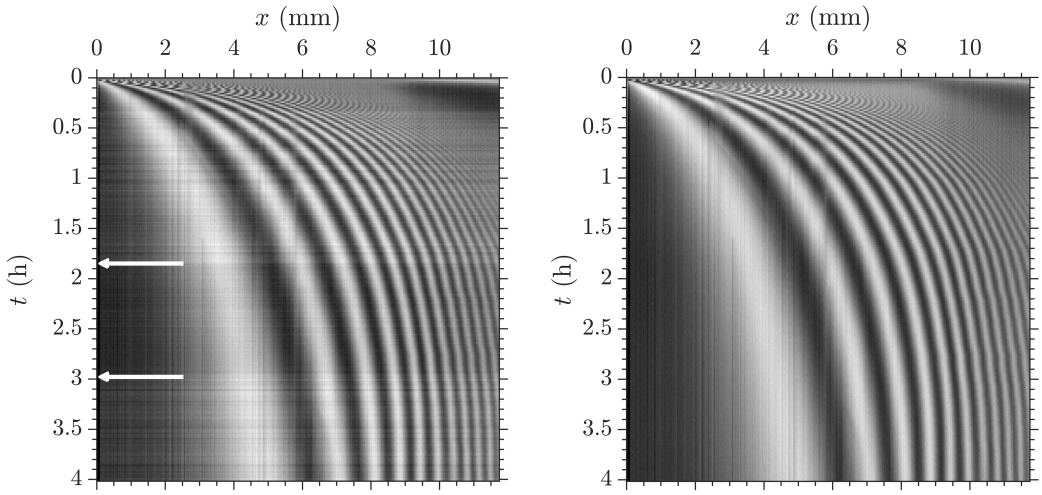

Figure 2.20: Evolution of the intensity profile $I_R(t, x)$ for the red light $\lambda_R = 630\,\text{nm}$ over several hours at the region of interest marked by a rectangle in Fig. 2.18. Left panel: evolution as directly obtained for the intensity averages of the the ROI at each image. Right panel: corrected evolution so that the average of the intensity at any given time is equal to 1 (the expected relative intensity at infinite height). See for example the change of intensity between 1.85 and 2.9 h (the time range between the arrows on the left panel) with respect to the intensity at shorter and longer times.

Thickness measurements

From any of the three intensity profiles, it is possible to obtain the thickness at the extrema (maxima and minima) of the interference, which for the ideal source are $h_{ext} \propto \lambda_C/(4n)$. In Fig. 2.21, we show an example of thickness profile obtain solely from the interference extrema of each wavelength for a typical experiment. The usefulness of having three wavelengths available is that the fringes' order can be obtained unequivocally, as shown by the fact that the independent measurements for each wavelength lie on the same curve. We can furthermore see that the small delay between images with different colours has no impact in the determination of the height profile.

The minimum thickness obtained in this fashion, coming from the first order maximum of the blue interference, is $\lambda_B/(4n_\ell) \approx 81\,\text{nm}$. However, we would like to recover the thickness below this scale, to better analyse the influence of intermolecular interactions at the surface level on the thermocapillary dynamics. Below the thickness of the first interference maxima, a method for inverting the intensity is thus needed.

In Fig. 2.22, we show the intensity curves $I_C(h)$ in pairs for h in the range from 50 to 300 nm (solid curves), together with intensity data of the same experiment we considered for Fig. 2.21 corresponding to the region $x < 1\,\text{mm}$. The thickness range considered has been chosen from the information gained from the interference extrema for this region. We can see that the data points lie close to the theoretical curve on all plots.

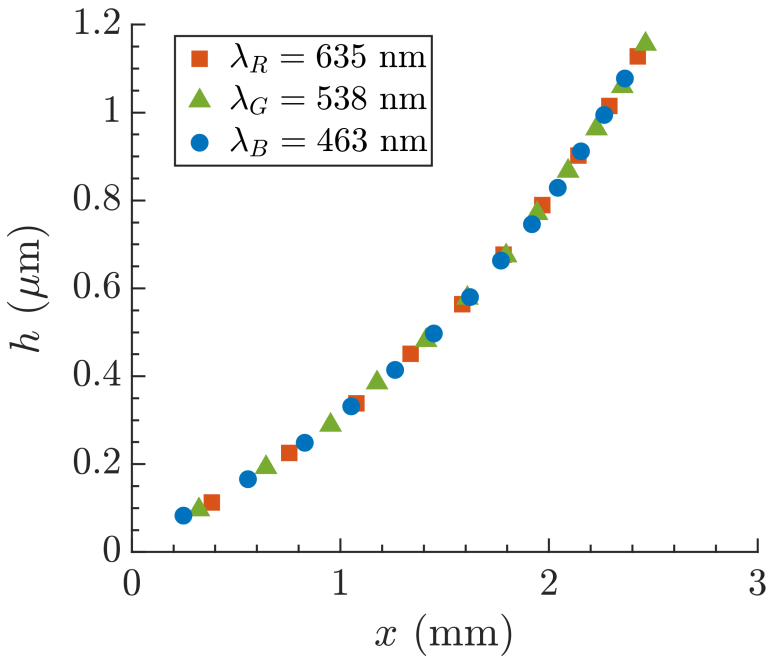

Figure 2.21: Thickness measurements obtained from the interference extrema of the three different wavelengths of the LED. The thickness corresponds to an experiment performed with silicone oil of initial thickness $h_0 = 36\,\mu\text{m}$ and dissipated power $P = 0.81\,\text{mW}$, at $t = 2.5\,\text{h}$ after establishing the thermal field. More details about the development of an experiment can be found in Sec. 2.4.

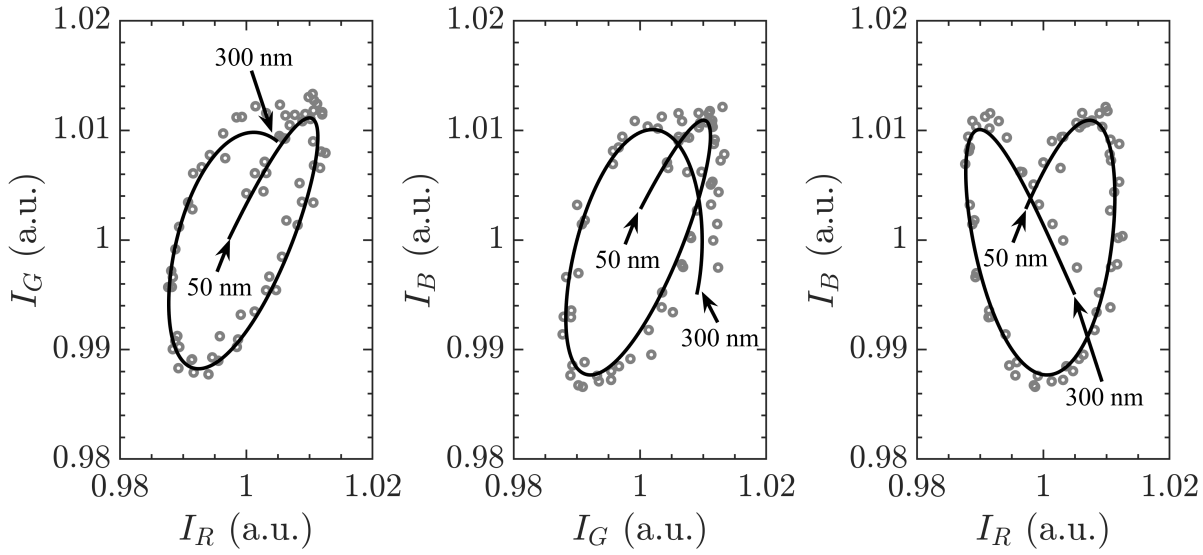

Figure 2.22: Experimental data of interference intensities. Each panel corresponds to a pair of colours, the data points correspond to the same data on all plots, obtained at different thicknesses. These plots can be seen as 2D projections of a common curve in the (I_R, I_G, I_B) space. The different phase of the intensities, $\phi(h; \lambda_C) \propto h/\lambda_C$ allows to use the thickness as a fitting parameter when an intensity profile is represented as a function of another.

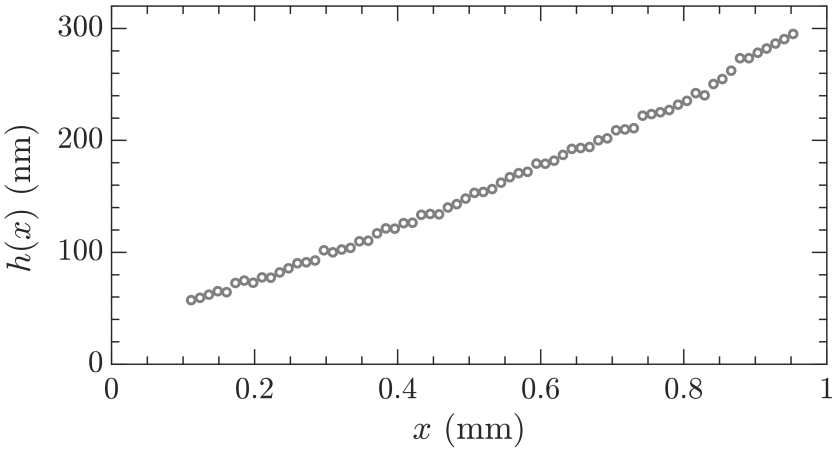

Figure 2.23: Thickness measurements obtained from the fitting of h performed by comparing experimental intensity to the theoretical curves, as shown in Fig. 2.22 (grey circles). This profile corresponds to the ultra-thin film region of the same experiment as of Fig. 2.21.

We consider the intensity at a given pixel for the three colours. Comparing it to the theoretical intensity curves, we assign to this pixel the thickness h that minimizes the Euclidean distance between the intensity at this point and the theoretical curve $\boldsymbol{I}(h) = (I_R(h), I_G(h), I_B(h))$ in the intensity space. This procedure gives, for the data in Fig. 2.22, the thickness profile shown in Fig. 2.23. As for the FS-SS method, we have used the nominal values of refractive index in the theoretical formulas of the intensity, Eq. (2.14). The refractive index changes very slightly with the wavelength and temperature. For example, for hexadecane (used in chapter 4) $|dn_\ell/dT| \sim 5 \times 10^{-4}\,\mathrm{K}^{-1}$ and $|dn_\ell/dT| \sim 5 \times 10^{-5}\,\mathrm{nm}^{-1}$ [42], while for silicone oils $|dn_\ell/dT| \sim 3 \times 10^{-4}\,\mathrm{nm}^{-1}$ [43]. In our case, these variations amount typically to a change of less than 1% in the refractive indexes. We have checked that computing the theoretical intensities with this variation, the result of Fig. 2.23 does not change. Hence, these variations can be neglected.

Errors in the thickness at any given point are thus linked to experimental high frequency intensity variations, as can be seen in Fig. 2.19 above, which we can estimate with the sensitivity of the inversion procedure for very small thicknesses. In chapter 4, we will study thickness profiles in the long-time regime as the one shown in Fig. 2.24. In this figure, we can see that the sensitivity threshold of our procedure is around 20 nm since we cannot say with certainty which is the height profile for thicknesses below this values. The order of magnitude of the precision of the measurements, linked to the dispersion of the data, can be approximated by the standard deviation of the points below this sensitivity threshold, which is about 10 nm. This threshold is one of the main technical limitations of our current setup, which may be improved with a refined optical setup accounting for, e.g., the chromatic aberration of the objective lens. Nonetheless, as we shall see in later chapters, the slow time scale of the dynamics lets us acquire multiple height profiles for each experiment, and this redundancy of data will help us obtain consistent results in a ample range of experimental parameters.

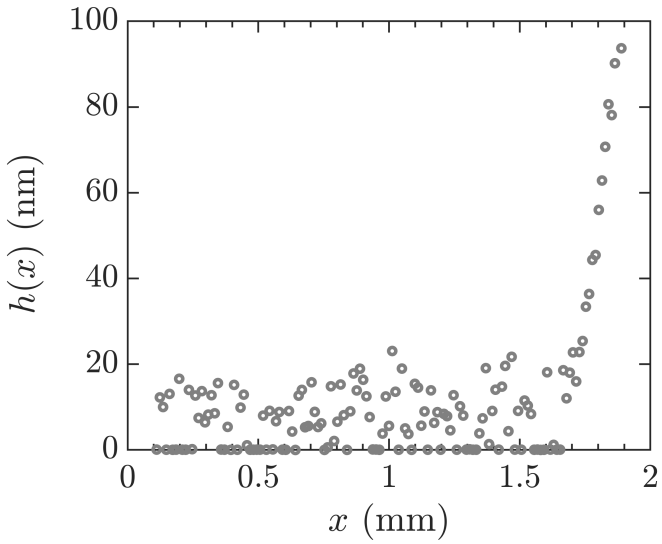

Figure 2.24: Thickness measurement obtained with the same procedure as for Fig. 2.23 showing the sensitivity threshold of the measurement at roughly 20 nm. This experiment, performed with 2,2,4,4,6,8,8-heptamehtylnonane, will be explained later on in chapter 4.

Coming back to the experiment we discussed in figures 2.21 and 2.23, we can combine the results of these two figures to obtain a complete profile like the one shown on the left panel of Fig. 2.25. Since this thickness range covers a couple of decades, we will usually plot the figures showing thickness profiles in a semi-logarithmic plot like the one on the right panel of Fig. 2.25. We are thus able to obtain the thickness in a range from the tens of nanometres to the micrometer, the error in the thickness being of around 10 nm according to the previous discussion.

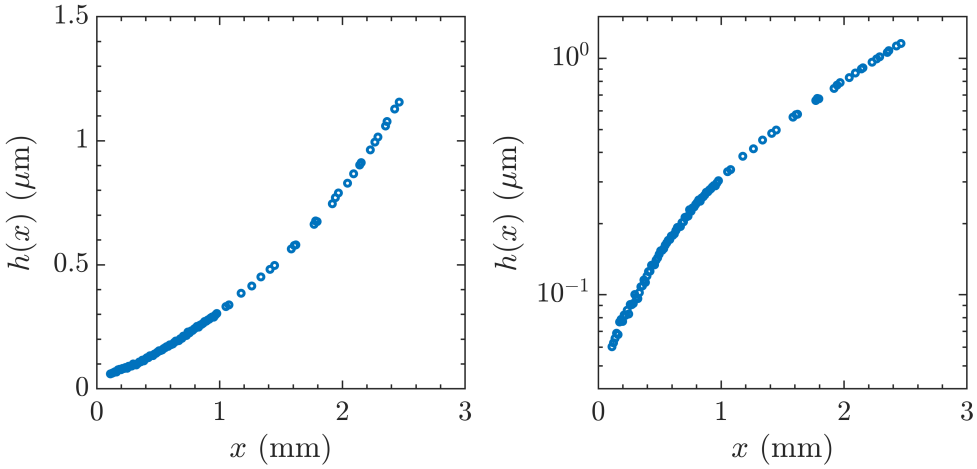

Figure 2.25: Combination of thickness measurements shown in Figs. 2.21 and 2.23. The right panel shows the same data as the left panel, but with a logarithmic y-axis to see the detail at the scale of tens of nanometres.

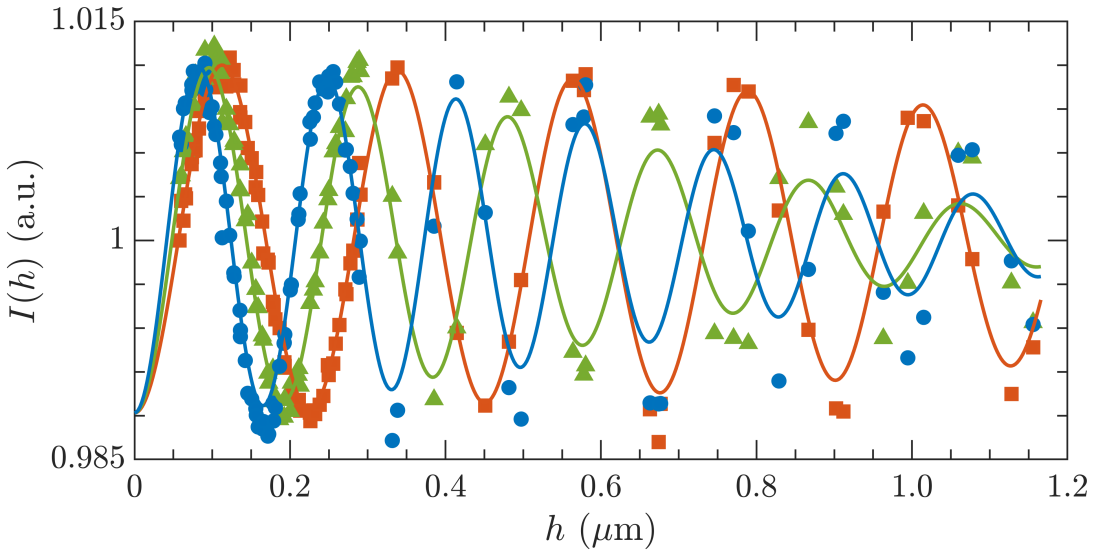

Figure 2.26: Curves: theoretical model of intensities as a function of thickness, given by Eq. (2.14). Data points: value of the intensity (for each colour) of a point in the image as a function of the recovered thickness at this point. The agreement between the two serves as a consistency check for the measurement procedure explained in the main text. Symbols as in Fig. 2.21.

Finally, in Fig. 2.26 we compare the experimental interference intensities as a function of the obtained thicknesses with the interference model of each colour, Eq. (2.14). The agreement between data points and theoretical curves, particularly for $h < 0.3\,\mu$m, serves as a checking procedure of the consistency of the measurements. The faster loss of visibility in the theory indicates that we are perhaps overestimating the effect of the quasi-monochromatic emission. This does not represent an issue on these peaks because the thickness is obtained from the interference extrema and not by a fit of the intensities as is the case for small h.

2.3.3.3 Summary

In this section, we have detailed the 3-colour interferometric technique allowing us to measure the thickness profiles below the micrometre scale, until a minimum thickness of about 10 nm. We have moreover checked the coherence of the recovered data with the optical model that we have used.

Although we are using a very basic optical setup, we obtain a good accuracy of the profiles, with a precision of around 10 nm and a sensitivity threshold of 20 nm, for thicknesses up to a couple of microns. Other experimental limitations that may be improved for future experiments are discussed in the next section.

2.3.4 Experimental limitations

We have introduced in the previous section two techniques used for measuring the thickness profile of the liquid film during the dynamics, one for thicknesses above the mi-

crometre scale, the free-surface synthetic Schlieren method (FS-SS); and the other one for determining the thickness of the ultra-thin film, 3-colour interferometry.

Both these techniques are based on the optical setup showed in Fig. 2.8 consisting on a LED panel and a monochrome camera. This is admittedly a simple setup that could be improved for an increased accuracy. For example, we have noticed that the objective we use has a small chromatic aberration. This means that once the focus with a particular colour (say, blue) is done, the images taken in the same conditions with the other two colours are slightly blurred. Some other problems associated with the intensity variations of the LED and the thermalization of the camera had to be taken into account too.

In the sections below, we comment other limitations specific to each measurement technique.

2.3.4.1 Free-surface synthetic Schlieren method

As mentioned earlier, the major drawback of the FS-SS method is that it cannot provide a measurement of the absolute thickness, since it is based on the measurement of surface gradients. From the experimental point of view, this characteristic is undesirable also because the displacements of the speckle pattern are very sensitive to setup vibrations or changes in light intensity even at the pixel level [33, 44]. These can generate offsets on the gradients that, once integrated, provoke spurious slopes on the recovered profiles. In our setup, assuming symmetry of the profiles with respect to the origin, this problem can sometimes be corrected for the first profiles. If these spurious slopes appear at long times, when the ultra-thin film extends in a region with a typical length of several millimetres it is possible to remove, from the whole surface, the mean plane of the ultra-thin film to obtain an approximately correct surface.

There are two situations in which an offset can be added to the recovered profile Δh to obtain a fair approximation of the absolute thickness profile h. The first one is for sufficiently short times in which the surface deformation has not reached the boundaries of the field view, so that the relative thickness can be offset to the initial thickness h_0. The second one is for the long-time regime, when the thickness of the ultra-thin film at the centre is below 0.1 µm, which is the typical precision of our implementation of FS-SS. Thus, the central value of the recovered surface can be offset as a first approximation to zero. In Fig. 2.27 we illustrate these two possibilities with profiles of the same experiment. This approximation gives a good picture of the overall dynamics. Although the transition regime cannot be offset, in principle one could get information about, for example, the curvature of the profile at the ultra-thin film to verify the assumption that the Laplace pressure can be neglected.

At the current resolution, the implemented FS-SS method has a typical height error of 0.1 µm (see Fig. 2.14). Although this represents a very good resolution when compared with the initial thickness (~ 30 µm), it would not be enough to resolve the ultra-thin film dynamics at very long times.

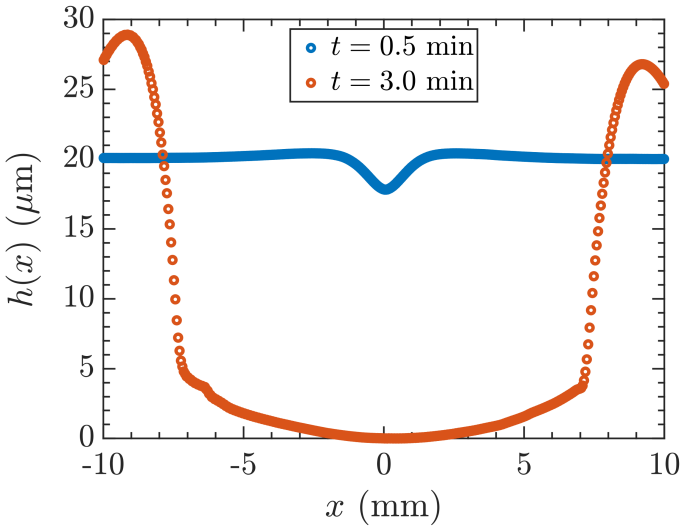

Figure 2.27: Thickness profile Δh at two different times obtained with FS-SS in an experiment performed with n-hexadecane (initial thickness $h_0 = 20\,\mu$m, dissipated power $P = 62.3\,$mW). The blue data, which is on the short-time regime, has been offset so that the value at the boundaries is equal to h_0. The orange data, which is on the long-term regime, has been offset so that its minimum lies at zero.

2.3.4.2 Interferometry

In experiments with silicone oils, we shall see in chapter 3 that the ultra-thin film evolves very slowly. The slow dynamics (recall the discussion on the velocities in Sec. 1.3 of chapter 1) makes the difference between successive images of an experiment, typically taken at an interval of 10 min, to be small. In the final hours of an experiment, the variation of the recovered thickness close to the heating line at $x = 0$ can become smaller than the noise threshold, which is roughly around 20 nm as discussed above. If fringes are still seen towards the borders of the image, their displacement is of a subpixel scale and, although the stationary state has not yet been reached, they may appear to be stationary. This makes any specific profile appears almost identical with the previous one within experimental errors, hence the need to work with the complete dynamic surface $h(t, x)$ to obtain long term trends as will be shown in chapter 3.

2.3.4.3 Effect of adsorbed particles at the surface

Another crucial experimental limitation comes from particles adsorbed at the surface of the slide.

Surface impurities have two different origins. The first comes from the deposition of the electrical circuits on the bottom side of the glass substrate, as has been noted ealier. Even if it is done in a white room, small imperfections remain due to posing the top side of the slide at different surfaces. This effect has been minimized by using an auxiliary glass slide as a supporting surface whenever possible. However, due to technical limitations it is not always feasible to use the auxiliary slide. On the bottom side, tiny spots of the deposited materials (chrome and gold) can also be seen, probably because of imperfections in the photoresist that constitutes the mask of the circuit.

During the deposition of the liquid film on the slide, we limit the presence of dust on the slide by working under a laminar flow hood, and the slide is cleaned with acetone and isopropanol before spin-coating the liquid film. As noted before, we cannot use stronger techniques for cleaning the surface, since it may damage or destroy the circuit providing the thermal field. The liquid is always filtered (syringe filter with pores of size 0.2 µm) before spin coating, thus reducing the possible presence of particles on the initial film.

The second major source of impurities is constituted by dust particles present in the air adsorbed at the surface during the experiments, since the latter are not performed in a controlled atmosphere. From the experimental images (see Fig. 2.18), dust particles are seen to perturb the flow in an area with typical radius of roughly half a millimetre.

In experiments performed with the FS-SS technique, these particles are not very important due to their small size. However, they are very inconvenient for the interferometric technique. The dust particles generate black dips in the image intensity, that must be especially avoided at the central region lying below the first order interference fringe to be able to recover the thickness of the ultra-thin film ($h \lesssim 81\,\text{nm}$). Since these depositions cannot be controlled, it is only after the experiment that for the image analysis a suitable region of interest has to be selected so that it has no visible dust particle in the ultra-thin film region at late experimental times (and, if possible, neither in the region of fringes). Since we work with a heating line of length 10 mm transversal to the flow direction (i.e. in the y axis of the experiment), it is generally possible to find close to the centre a region spanning around 1 mm along this line that is not affected by dust particles for several millimetres in the transversal direction (x-axis), along which the intensities can be averaged to reduce pixel noise as explained in Sec. 2.3.3.

2.3.4.4 Asymmetry of profiles due to border effects

Technical limitations on the size of the glass slide that supports the liquid makes its lateral dimension comparable to the length of the overall thermocapillary effect. Although care has been put to design a suitable experimental cell where the glass slide is attached, we have seen some leaks of liquid occurring over the course of some experiments, sometimes generating slow liquid currents that can be seen in the displacements obtained by DIC in the borders of the experimental images.

In previous examples of thickness profiles obtained with FS-SS, figures 2.14 and 2.27, we can see for the profiles at long times an asymmetry with respect ot the centre where the thermal line is. Since the height at the borders sets the strength of the gravitational pressure opposing the flow of liquid coming from the heating line, a lower thickness on one side allows the thermocapillary effect to be effective over a longer distance. This explains why the flat region in the centre of the last profile in Fig. 2.14 has developed slightly more to the right (positive x), since the border thickness on this side is lower. This effect may also be accompanied with small global displacements of the speckle pattern due to mechanical vibrations or the incorrect thermalization of the camera that generate spurious slopes on the integrated profiles, as explained before.

As with the profiles obtained with FS-SS, it is possible to check the symmetry of the recovered height profile with 3-colour interferometry, to evaluate the relevance of border effects in the central ultra-thin film region. In Fig. 2.28 we show height profiles at different times obtained with the method described above in Sec. 2.3.3 (see Sec. 3.2 of chapter 3

for details about the liquid and experimental conditions). We superpose profiles obtained at both sides of the heating line (one series with circles, the other one with triangles; same colour indicates same experimental time).

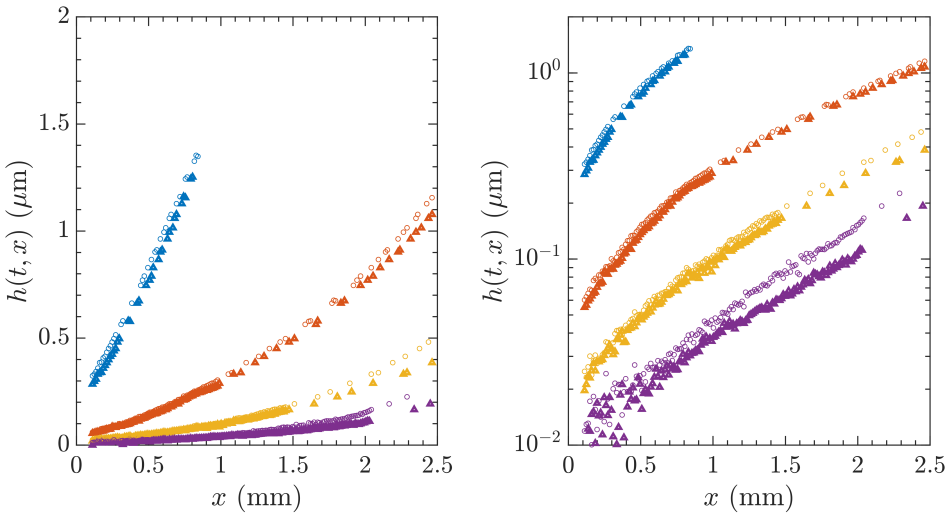

Figure 2.28: Experimental height profiles $h(t, x)$ at different times, taken at both sides of the heating line. The profiles on the right panel are the same as in the left panel but in logarithmic scale in the y-axis. Circles are for one side of the heating line, triangles for the other one. Same colour indicates profiles obtained at the same time. Experimental details of this experiment are given in Sec. 3.2.2.2 of chapter 3.

We can see that there is a small vertical offset that is specially noticeable for thicknesses over 200 nm, however the profile shape remains the same. These differences are to be expected at the micrometer scale, for the reasons discussed before in the context of the FS-SS measurements about edge effects, but are not a limit of the interferometry measurements. At the longest time (purple data), the difference in the thickness of the ultra-thin film is of the order of the precision of the measurement, around 10 nm as explained above. We therefore conclude that in the thickness region that we are interested in, ranging roughly from 10 to 100 nm, the existing small asymmetries are not a concern, since the evolution of the height profile shows the same shape and temporal dependence. In the following, we will only report the curves for one of the sides.

2.4 Performing an experiment

In this section, we summarize the main steps to perform an experiment in our setup, based on the techniques we have explained in previous sections.

2.4.1 Preliminary conditions

Before performing an experiment, a choice must be made about the technique to be used. That is, if large scale phenomena are to be studied, then FS-SS is used. If, on the other hand, the focus will be on the dynamics of the ultra-thin film, then interferometry will be

chosen. Both techniques cannot be used simultaneously for two reasons. The first one is that they need the camera to be focused at different planes: the spot pattern for FS-SS and the top of the slide for interferometry. These planes are about 5 mm apart, so that both techniques cannot be simultaneously applied because of the loss of resolution (in either sense). The second reason is that the speckle pattern needs a larger light intensity, which would saturate the image on the region devoted to the interferometry. Once the technique is decided, the camera is focused at the corresponding plane.

The image acquisition during an experiment is automated with a LabView program that synchronizes camera and LED. In this program, the time interval at which images will be taken and the small delay between the image at each colour are set. We typically use a time interval of 10 min with a delay of 2 s. Additionally, it is possible to obtain a number of quick frames with each colour and average them to diminish the effect of high-frequency intensity variations. The resulting average will serve as the image of the particular colour used. We usually average 5 images taken at a frequency of 10 Hz.

The camera is thermalized during a couple of hours before an experiment is launched. Since the variations of intensity we need to measure are very small, we have seen that the intensity drift during the thermalization can bias the measurements with both techniques.

2.4.2 Film deposition

To deposit the initial thin film, the surface of the glass is cleaned first with acetone and isopropanol, using the spin coater at high revolution speed to remove them. Afterwards, we let a couple of minutes for them to evaporate completely.

The deposition of the thin film is also done with the spin coater, having first filtered the liquid. A calibration previously done allows to set the time, revolutions per minute and acceleration needed to obtain an initial thickness h_0 on a certain interval. These parameters can vary from liquid to liquid and have to be adjusted for each one, in particular depending on their viscosity.

After the spin coating has ended, the cell is carefully transported to the profilometer to measure the thickness of the resulting film. This measurement was explained in Sec. 2.3.1.

2.4.3 Launching the experiment

Once the initial thickness is known, the cell is again carefully moved from the profilometer to the experimental setup used to monitor the dynamics. The cell is clamped to an external support, and the electrical contacts connected to the main circuit providing the necessary current for generating the thermal field.

The order of magnitude of the thermal field θ_{max} imposed given a dissipation power P is roughly known, see Sec. 2.2.2.2 above. The resistance of the circuit is easily measured with a multimeter, and a DC power supply provides the necessary potential. A multimeter measuring the current through the circuit allows to check that the system is stable.

Once in place, the experiment is launched. Images are saved in the computer connected to the camera as soon as they are taken. The dynamics can be thus checked at any point during an experiment. This is important since the experiment may take a couple of days to finish, and it is necessary to know that the surface stays sufficiently clean during this time (i.e. there are not many dust particles impeding the measurement).

2.4.4 Image analysis

Once the experiment is finished, the images are analysed according to the technique used. In the case of FS-SS, images on a single wavelength are enough, see Sec. 2.3.2. For the 3-colour interferometry, the three wavelengths are needed, see Sec. 2.3.3.

In either case, we do not analyse the full images. Rather, from the last image, a suitable clean region of interest is defined, which is used for all the preceding images too as discussed in 2.3.3. Afterwards, the appropriate method is applied to the intensity images to recover the height profile as explained in previous sections.

The precise number of height profiles analysed in each experiment varies depending on its duration and the period at each images are taken. Typically, the large scale dynamics of FS-SS can be fully characterized analysing around 10 profiles. The evolution of the ultra-thin film, which is used for obtaining the derivative of disjoining pressure with respect to the thickness, as explained in Sec. 1.7 of chapter 1, requires a more detailed analysis, typically of about 100 thickness profiles.

2.5 Numerical integration

We add here a commentary about the numerical integration scheme used to integrate the thin film equation (1.12) discussed in chapter 1, and the origin of the difficulties we have encountered when trying to solve it.

2.5.1 Complexity

The thin film equation, Eq. (1.12) of chapter 1, is a highly non-linear partial differential equation (PDE). The highest derivative is fourth-order, $\partial_x^4 h$, which greatly constraints the spatial and temporal steps that are needed to perform a correct integration. We tried to implement a custom finite-differences integration scheme, but it suffered from numerical instabilities.

A second difficulty lies in the nature of the problem we are trying to solve, which contains two very different height scales. As we have seen, starting with a thickness around $h_0 \sim 30\,\mu\text{m}$, the thermocapillary effect provokes the thinning of the film down to nanometres around the position of maximum thermal field. This local difference in 3 to 4 orders of magnitude makes it difficult to fix relative and absolute error tolerances. Moreover, as noted in the discussion of chapter 1, the longer the time the slower the dynamics becomes: the characteristic time scale of the pure-thermocapillary regime when the pressure contributions can be neglected against the action of thermocapillarity is $t_0 \sim 1\,\text{min}$, but once the intermolecular interactions, through the disjoining pressure, are effective, the time scale gets increased dramatically to $t_{\text{utf}} \sim 4.5$ days. These factors result in a very slow integration.

Finally, a characteristic of the thermal field that is generated by the heating line presented above in Sec. 2.2.2 is its exponential decay with a small parabolic correction at its maximum. Again, the width of this correction is very small ($\sim 100\,\mu\text{m}$) compared to the typical extent of the thermocapillary effect (several millimetres). To correctly resolve the dynamics, a very small space step is needed to correctly describe the thermal

maximum, and at the same time a sufficiently large integration region to avoid border effects.

In the literature, studies giving numerical results of the thin liquid film generally focus on relaxation dynamics, for example on the spreading of a droplet on a substrate. The main equation is generally written, with our notation, in the form

$$\partial_t h = \partial_x \left\{ M(h) \partial_x^3 h \right\} \tag{2.15}$$

where the shape of the mobility $M(h)$ depends on the slip condition at the surface (see for instance [45–47]). In the problem of the spreading of a droplet, the difficulty posed by this family of equations is how to describe the moving boundary condition at the contact line, and the conditions under which the solution is unique [46]. The conditions imposed typically include volume conservation and positive thickness, plus a point at which the thickness is zero and some condition on the contact angle, which sometimes is set at a fixed value.

In the case of films, numerical solutions have been provided, for example, for the relaxation of polymers over a pre-existing film of the same material [48], or the instabilities of liquids under evaporation until breakup, for instance [49]. A detailed numerical method for the solution of thermocapillary driven films (in the absence of intermolecular forces) is given for example in [50].

In our case, volume conservation is imposed in the derivation of the thin film equation, and this constraint is replaced by the boundary condition at infinity, $h(t, \infty) = h_0$. Furthermore, the repulsive intermolecular interactions prevent the complete dewetting of the film, suppressing all the problems with moving boundary conditions and satisfying the positivity condition for the thickness. However, when the interactions are attractive the liquid is unstable and breaks down once the thickness goes below the micrometre scale. In the numerical integrations, the thickness drops rapidly to zero and our integration scheme cannot converge for long-times.

2.5.2 Implementation

To solve the numerical integration, we use the `pdepe` function available in MATLAB to solve PDE's. This function implements an iterative algorithm with an adaptative time step, which is an advantage in a multi-time scale problem like ours. It also admits non-constant spacing between spatial points. This versatility allows us to separate the points on the spatial dimension logarithmically, instead of linearly. Thus, the point density is higher at the centre where the gradient of the thermal field driving the dynamics varies the most, and diminishes as the spatial coordinate grows where the dynamics should be much more smooth and the gradients small. This logarithmic grid is reflected to negative values of x, the integration being always done in a region symmetric with respect to the origin.

The numerical integration is performed in dimensionless variables $X \equiv x/w_0$, $T \equiv t/t_0$ ($t_0 = 2\eta w_0^2/\Delta\gamma h_0$ is the pure thermocapillary time scale as defined in chapter 1), $H(X,T) \equiv h(x,t)/h_0$, and $\Theta(X) = \theta(x)/\theta_{max}$. For a typical numerical integration, we provide a spatial grid of $\sim 5 \times 10^3$ points from $X = -50$ to $X = 50$, to ensure that the boundaries do not have an effect on the dynamics. We also provide times (typically with a period of $\Delta T = 1$ to 10) at which we want the solution to be computed. Internally, the

function `pdepe` works with both variable space and time discretizations, that do not need to coincide with the provided grids. The numerical integration discussed in chapter 1 took about 10 h to finish. In the numerical integrations, we have checked that the change in volume of liquid remained very small for all profiles obtained, since the evolution must conserve the volume by construction.

The numerical integration does not always reach the longest time scales we are interested in, say $T \gg 100$ when using physically reasonable parameters. The main issue appears to be the resolution of the ultra-thin film region, which has a very slow dynamics at a very small scale.

Notwithstanding these problems, the obtained profiles have been useful to get a picture of the regimes and scales of the thermocapillary dynamics. In particular, it has served as a starting point in the analysis of the pure-thermocapillary regime and the time scale associated to it.

2.6 Conclusion

In this chapter, we have presented the experimental techniques implemented to measure the thickness of a thin liquid film under the effect of thermocapillarity.

We first described the experimental cell, consisting on a glass substrate to which an electric circuit has been printed. The liquid is deposited on the side of the slide opposite the circuit. We have characterised the thermal field produced by the circuit on the surface on which the liquid is deposited using an infrared camera. We have determined the orders of magnitude of the main parameters controlling the found exponential shape of the thermal field, its maximum value θ_{max}, which depends on the dissipated power P roughly as $\theta_{max} \approx (0.4\,\mathrm{K\,mW^{-1}})P$, and a decay length $w_0 \sim 5\,\mathrm{mm}$.

We have introduced two techniques for measuring the thickness profile of the film as it is driven by thermocapillarity. The first one is an implementation of the free-surface synthetic Schlieren method, which measures the thickness by recovering first its gradient due to the refraction of light. This technique provides accurate thicknesses above the micrometre scale witha precision of 0.1 µm, but these are relative to an undefined mean plane, and we will use it in following chapters mainly for comparison purposes. The second one is a 3-colour interferometric technique capable of resolving the dynamics below 1 µm down to 20 nm, with a precision of around 10 nm.

We have also detailed the procedure for performing an experiment. We have explained how the technique to be used is chosen depending on the region of the dynamics to be explored, the cleaning and deposition process of the initial film with a spin coater, the monitoring during an experiment with a custom LabView program, and the typical number of frames we analyse with each technique.

Finally, we briefly discussed the numerical implementation and problems with solving the thin film equation described in chapter 1, which is mainly due to the large differences in orders of magnitudes both for thickness regimes and time scales.

In the following chapters, we apply the techniques measuring the thickness of the film to uncover the effect of intermolecular forces in the dynamics of thin liquid films driven by thermocapillarity.

Chapter 3

Thin wetting films

3.1 Introduction

In chapter 1 we introduced the dynamics of a thin liquid film on a solid substrate driven by thermocapillarity. At regions where the thermal gradient is large, a local ultra-thin film of nanometric thickness can appear. The lateral dimension of this ultra-thin film is controlled by the decay length of the thermal field, and therefore it can have a very large lateral dimension compared to its thickness. We are interested in the dynamics of this ultra-thin film as it is affected by the intermolecular forces of the system which we aim to measure.

We introduced an experimental setup in chapter 2 that, as we will show below, allows us to monitor the dynamics of the height profile, $h(t, x)$ in a range roughly from 20 nm to a couple of micrometres. The profile traverses a local regime in which all pressure contributions are negligible against thermocapillarity. This regime can be used to experimentally obtain the gradient of the thermal field. The measurement of the dynamics of the film until a quasi-static flow, together with the extracted thermal field, will be shown to provide the information needed to obtain the dependence of the derivative of the disjoining pressure (representing the intermolecular forces of the system) as a function of the thickness of the film.

In Sec. 3.2 we give an overview of the experimental profiles obtained with the system presented in chapter 2 using silicone oils. We recall the measurement techniques introduced in chapter 2 and discuss the different dynamical regimes that were anticipated in chapter 1. We focus in Sec. 3.3 in the pure-thermocapillary regime introduced in Sec. 1.4 of chapter 1, and we show its appearance for different values of initial thicknesses h_0 and dissipated powers P. We introduce a procedure to recover the gradient of the thermal field using only the thickness profiles measured of this local regime. This information is used later on in Sec. 3.4, where the deviation from the master dynamics of the pure-thermocapillary regime, linked to the intermolecular forces of the system, is analysed. In particular, we are able to measure the dependency with the film thickness of the derivative of the disjoining pressure modelling the intermolecular forces.

3.2 General evolution

In this section, we discuss the physical properties of the silicone oils used for the experiments shown throughout the chapter, and show measurements of their dynamics with the two techniques introduced in chapter 2. These two techniques are an implementation of free-surface synthetic Schlieren (FS-SS) method [33], used mainly for characterising the dynamics over the micrometre scale, and a 3-colour interferometric technique (similar to the ones of Refs. [51, 52]) used for measuring the height profile in the ultra-thin film region. We also discuss some additional experimental considerations regarding the limitations of each technique, and the solutions adopted if necessary.

3.2.1 System

In this chapter, we focus our attention on thin silicone oil films, commonly used for studying the dynamics of thin liquid films, on glass substrates as explained in chapter 2. Silicone oils are non-polar liquids that wet glass, and therefore their dynamics under the thermocapillary effect is described by the thin film equation formulated in chapter 1. They have been recently used in our group as a model liquid in the analysis of the influence of intermolecular interactions on the surface thermal fluctuations of nanometre-thin films [28].

3.2.1.1 Silicone oils

In our experiments, silicone oils of two manufacturers have been used. Their properties are listed in table 3.1. Two were ABCR oils (polydimethylsiloxane, trimethylsiloxy terminated) of viscosities 10 cSt [53] and 20 cSt [54]. The third oil used is Rhodorsil 47V20 [25], made from a mixture of polydimethylsiloxane with molecular masses between 2800 to 3200 g/mol and a nominal viscosity of 20 cSt. This broad distribution of molecular weight, resulting in a large polydispersity index, may introduce undesired effects on the flow due to a distribution of viscosities that is not well defined (see Fig. 3.1, which reproduces Graph 1 on Ref. [25]). These effects may be particularly relevant when considering nanometric films. Although no information about the polydispersity of ABCR oils is available, the fact that it is not a mixture indicates that it should be very close to 1 (no dispersity). Indeed, the nominal values are given to the second decimal place. Using silicone oils with the same nominal viscosity but different polydispersity can serve to compare its impact on the dynamics of ultra-thin films with nanometric thicknesses.

Oil	η (mPa s)	ρ (kg m^{-3})	Molecular weight (g mol^{-1})
ABCR AB111838	9.35	935	1250.00
ABCR AB112154	19	950	1900.00
Rhodorsil 47V20	19	950	2800-3200

Table 3.1: Summary of nominal values of viscosity η, density ρ and molecular weight of the silicone oils used in this chapter. Data for the ABCR oils as given in Refs. [53, 54], respectively. Data for Rhodorsil 47V20 at 25 °C from Ref. [25].

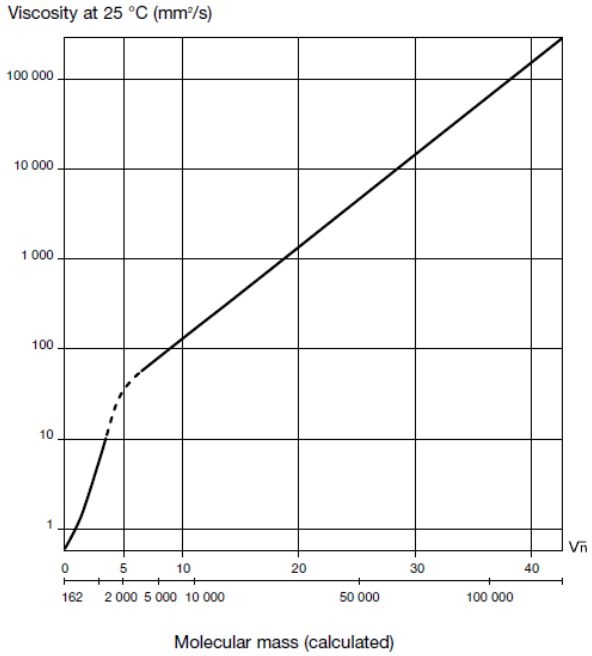

Figure 3.1: Viscosity of Rhodorsil 47V oils as a function of molecular mass, from Ref. [25].

3.2.1.2 Glass substrate

The substrate used, as explained in chapter 2, is a thin microscope cover slide (Menzel-Gläser, Thermo Scientific). On the bottom of these glass slides a microprinted electric circuit is deposited, which will serve as the source of the heating thermal field by power dissipation. The thickness of the slides is 100 µm, which is thin enough to allow the thermal field to be efficiently established throughout and in the top surface where the film will be deposited. The intrinsic roughness of the surface at the nanometre scale, to which ultra-thin films of nanometric thicknesses may conform, will not be a major concern since the resolution of the experimental images is about 12 µm/px, so that local thickness variations within this area will be averaged out. Moreover, as discussed in chapter 2, we cannot measure thicknesses below 20 nm. Thus, for the effect of our discussion, we assume that the slide is perfectly flat. The major source of film inhomogeneities are dust particles deposited on the slide during the length of a experiment (from half to several days).

3.2.2 Measurement of the height profile evolution

3.2.2.1 Thin film

One purpose of this thesis is to obtain a characterization of the effect of intermolecular forces on the dynamics of thin liquid films driven by thermocapillarity. Before analysing the dynamics at the ultra-thin film level, which we set loosely speaking under 0.5 µm, a characterization of the large scale phenomena is in order.

To check that the dynamics behaves as expected from the thin film equation derived in chapter 1, we have performed measurements of the dynamics of films with initial

thicknesses around $h_0 \sim 30\,\mu\text{m}$ using a free-surface synthetic Schlieren (FS-SS) method [33].

This technique, as explained in Sec. 2.3.2 of Ch. 2, is a two-step procedure based on the measurement of the gradient $\boldsymbol{\nabla} h$ of the free surface, which produces the refraction of the image of a speckle pattern situated between the illumination and the experimental cell. The integration of this gradient leads to the measurement of a relative local height $\Delta h(t, \mathbf{x})$ (up to an integration constant). This height $\Delta h(t, \mathbf{x})$ is then averaged over the y axis, parallel to the heating line, to obtain $\Delta h(t, x)$, which are the profiles that we will discuss in the following.

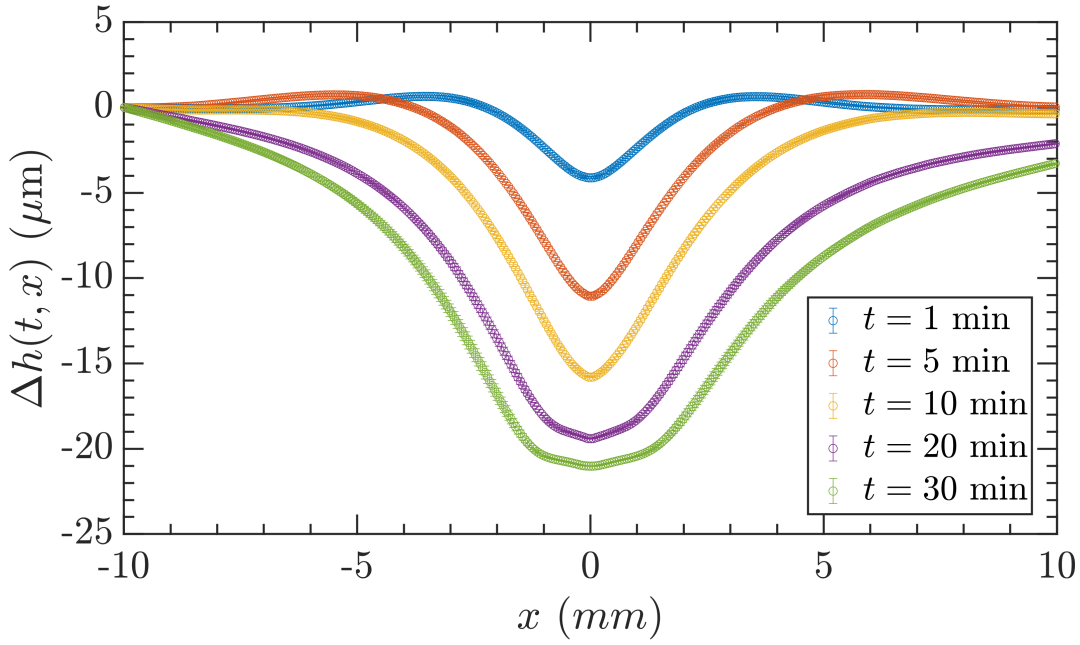

Figure 3.2: Relative height variation $\Delta h(t, x)$ obtained with FS-SS for an experiment with ABCR silicone oil of viscosity $\eta = 19\,\text{mPa s}$, mean thickness $h_0 = 40(4)\,\mu\text{m}$ and dissipated power $P = 0.67(9)\,\text{mW}$. Error bars represent the standard deviation of the average along the direction of the heating line, as explained in chapter 2. The leftmost value of all the curves is arbitrarily set to zero.

In Fig. 3.2 we show the relative height $\Delta h(t, x)$ obtained from an experiment of the ABCR oil of viscosity 19 mPa s, starting with a film of mean thickness $h_0 = 40(4)\,\mu\text{m}$, with dissipated power at the heating line $P = 0.67\,\text{mW}$ (estimated maximum thermal difference of $\theta_{max} \sim 0.47\,\text{K}$, see the discussion about the relationship of these two quantities below on Sec. 3.3). For illustration purposes, we have arbitrarily fixed the leftmost value of the relative thickness to zero.

As time passes, the initially flat profile is disturbed by the thermocapillary effect that drags the liquid away from the centre, generating large overshoots. This region grows to have a lateral extent of several millimetres, while it flattens under the influence of the thermocapillary effect. These profiles are qualitatively similar to the evolution obtained from the numerical integration of the dynamical equation Eq. (1.12) shown in Fig. 1.2 of chapter 1.

The two last profiles shown, at times 20 and 30 min, are not completely symmetric with respect to $x = 0$ representing the position of the heating line. In this case, we attribute the asymmetry to an edge effect, see the discussion in Sec. 2.3.4 of chapter 2.

Using FS-SS, we are thus able to characterise the evolution of the thin films above the micrometre level, with a good resolution of about 0.1 µm. However, it fails to give an absolute thickness measurement and the long-ranged effects of thermocapillary provoke an unknown offset between profiles, so that a quantitative comparison between experiments is not possible except in the short-time and long-time regimes, see Sec. 2.3.4 of chapter 2. Therefore, we reserve the use of FS-SS to the qualitative comparison of the dynamics of the thin films at the initial times, when the deformation of the surface has not yet reached the boundaries of the field of view and the thicknesses are above the micrometre. This will be useful in the chapter 4, when we will compare the results of silicone oils with the dynamics of two alkanes on the same substrate.

To analyse the ultra-thin film appearing at the central region, which is established when the thickness has been thinned down below the micrometre scale, we will use another technique based on interferometry, as explained in the next section.

3.2.2.2 Ultra-thin film

To obtain absolute measurements of the thickness profile, in particular in the ultra-thin film region near the heating point, we use a 3-colour interferometric technique. As explained in Sec. 2.3.3 of chapter 2, we use the transmission interference of the light produced by a LED panel located under the experimental cell. The LED provides light on 3 quasi-monochromatic wavelengths (emission peaks at red, $\lambda_R = 635\,\text{nm}$; green, $\lambda_G = 518\,\text{nm}$; and blue, $\lambda_B = 463\,\text{nm}$) that can be independently controlled. Each wavelength generates a set of equal-thickness interference fringes when shined through the experimental cell, when the thickness is below a couple of micrometres. From the interference extrema recorded in an image it is possible to recover the thicknesses that are proportional to the phase of the transmission interference, $h \propto \lambda_\alpha / 4 n_\ell$ where n_ℓ is the refractive index of the liquid. The use of three wavelengths allows to determine the orders of the fringes unequivocally. For thicknesses below the first (blue) interference maxima at $h \approx 81\,\text{nm}$, the height profile can be obtained from finding the thickness h that minimizes the distance from experimental intensity values to the theoretical intensity curves, as detailed in chapter 2. This technique provides thicknesses from around 20 nm to a couple of micrometers. The wide area covered by the ultra-thin film, that can be of several millimetres as shown below, allows the resolution of several interference fringes over a long period of time.

A typical measurement is shown in Fig. 3.3 for an experiment performed with the same silicone oil from ABCR as in last section with similar experimental parameters (both techniques cannot be simultaneously used in our current setup for reasons discussed in Sec. 2.4 of chapter 2). The initial thickness is $h_0 = 36(2)\,\mu\text{m}$, and the dissipated power is $P = 0.81(1)\,\text{mW}$. As expected from the discussion of the time scales and velocity field of chapter 1, the dynamics becomes very slow (typical velocity $\sim 0.4\,\mu\text{m/s}$ at $t = 200\,\text{min}$ for a maximum temperature difference of $\theta_{max} = 1\,\text{K}$). However, this evolution is still noticeable over a scale of several hours, reaching a quasi-steady dynamics. The evolution is slowest near the centre, as shown in the right panel of Fig. 3.3 where the changes of

thickness at a given x position diminishes with time.

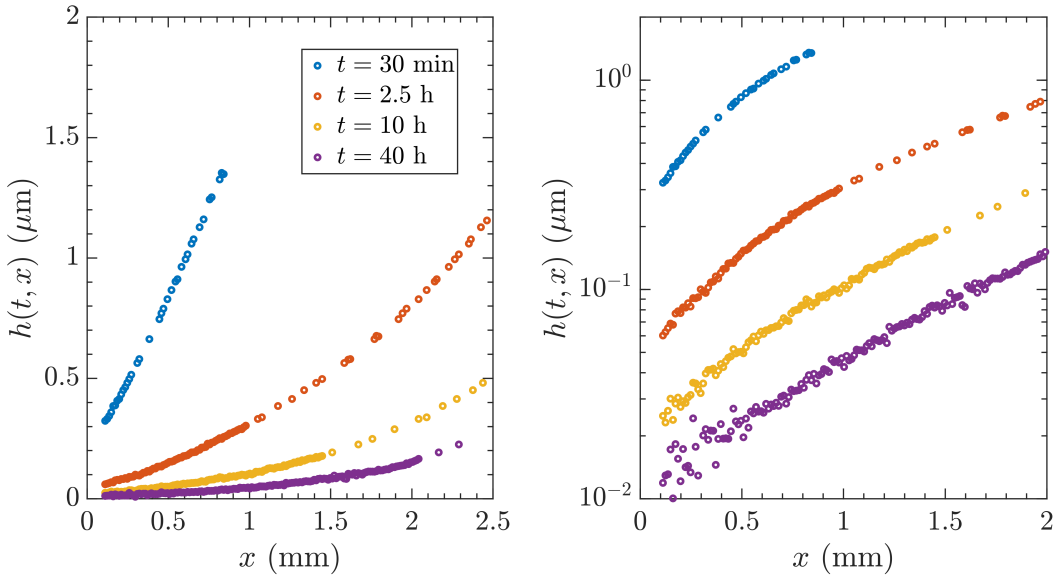

Figure 3.3: Left panel: Evolution of the height profile $h(t, x)$ obtained by 3-colour interferometry in an experiment with $h_0 = 36\,\mu$m. Note that the profiles are not plotted for times increasing linearly. Right panel: same profiles, plotted with a logarithmic y-axis to show thicknesses at the tens of nanometres scale.

These figures show that the 3-colour interferometric technique allows us to measure the evolution of the absolute thickness of the film below the micrometre scale, in a lateral region of several millimetres, with a good precision of about 10 nm as explained in Sec. 2.3.3.2 of chapter 2. The dynamics of the ultra-thin film can be followed for several hours, even days, to obtain thickness profiles ranging from 20 nm to 1 µm.

3.2.3 Conclusion

In this section we have presented an overview of the experimental techniques used for measuring the dynamics of the height profile at different scales.

FS-SS captures the phenomena at the tens of micrometers scale, including the development of overshoots and the establishment of an almost-flat ultra-thin film near the heating source. These characteristics are correctly described by the thin film equation, and this technique gives a good resolution compared with the initial thicknesses considered with a typical standard deviation of 0.1 µm along the averaging direction. However, the lack of an absolute thickness reference makes the quantitative comparison between experiments difficult, except at very short times as we will see in chapter 4. To study the effects of intermolecular forces below the micrometre scale we need a better resolution, and the interferometric technique is preferred when analysing the dynamics of the height profile.

We use a 3-colour interferometric technique that allows us to recover absolute thicknesses over the range roughly from 20 nm to 1 µm, with a precision of about 10 nm. The establishment and dynamics of the central ultra-thin film can be followed during several

hours or even days. Although a quasi-steady regime is achieved at long times, there is still a residual dynamics that can only be appreciated after several hours. The slow dynamics at long times points to the need of studying the full dynamics of the system, rather than focusing on the particular profile at any given time, as outlined in chapter 1. This will have the advantage of providing information about the thermal field felt by the liquid, that will in turn be used to extract information about the intermolecular interactions of the system opposing the thermocapillary effect.

In the next section, se show that a pure-thermocapillary regime, where all pressure contributions can be neglected, is attained in a wide variety of experimental conditions over an experimentally-reasonable time scale. We use the analytical predictions derived in Sec. 1.4.1 of chapter 1 to recover the thermal parameters characterising this evolution. Later on, we will show that the effect of disjoining pressure for ultra-thin films can be measured from the evolution of the height profiles together with the knowledge about the thermal field gained in the pure-thermocapillary regime.

3.3 Pure-thermocapillary regime

In chapter 1, we discussed the existence of an intermediate-time regime in which the profile's shape at the central region, where the thermal gradient is strongest, was solely determined by the imposed thermal field. In short, during this regime, all pressure contributions are negligible with respect to the surface stress generating the thermocapillary effect. We saw that, with the typical parameters of our system, it is expected to appear when the thickness is around $\sim 0.5\,\mu m$, so that gravity and disjoining pressures are small, and when the thickness profile is sufficiently flat so that the Laplace pressure is small. This regime occurs locally after an initial transient time in the central region.

In this section, we show the existence of this regime under different experimental conditions. This is an important step before the study of the effect of intermolecular forces, since from the moment it is established we can safely neglect Laplace and gravitational pressures at this region, as discussed in chapter 1. Furthermore, we show that it is possible to recover the gradient of the thermal field directly from experimental profiles. This measurement allows us to characterize the thermal field directly from the experiment. This characterization is sufficiently robust so that experimental profiles done under the same heating geometry but with different parameters can be collapsed onto a same master curve by a suitable rescaling. It will also be useful in the following section, when we address the problem of recovering the disjoining pressure characterising the intermolecular forces from the height profile dynamics.

3.3.1 Master curve

3.3.1.1 Consideration of pressure contributions

We recall in this section the considerations leading to the approximation that the pressure contributions can be, under certain circumstances, locally neglected against the action of the thermocapillary effect. This was illustrated in Sec. 1.4.1 of chapter 1.

In the system considered, a central peaked temperature field is imposed on the film. At this region the film is thinned down and an ultra-thin film starts to develop, connected

with the bulk film via a receding wedge. The receding of the wedge makes the height profile around the centre essentially flat (slopes below 1×10^{-3} rad in a region of several millimetres), giving a vanishing Laplace pressure contribution. Moreover, the micrometer thickness makes gravity small and, at the same time, the film is still too thick to render the intermolecular forces relevant. It is under these conditions that the pure-thermocapillary regime may be established.

The reduced thin film equation when only thermocapillary is present can be analytically solved. The details of this computation are given in appendix B. The evolution of the height profile $h(t, x)$ under the pure-thermocapillary condition satisfies

$$h(t,x) \simeq \frac{2\eta}{\gamma_\theta t} \frac{1}{2\sqrt{|\partial_x \theta|}} \int_0^x \frac{ds}{\sqrt{|\partial_s \theta|}} \tag{3.1}$$

where η is the dynamical viscosity of the liquid, γ_θ is the coefficient of variation of surface tension with respect to temperature, that for the case of silicone oils is $\gamma_\theta = 6.5 \times 10^{-5}\,\mathrm{N\,m^{-1}\,K^{-1}}$ [26]. In this expression, $\theta(x)$ is the thermal field acting on the liquid, measured with respect to the ambient temperature. The approximation symbol of Eq. (3.1) indicates that this expression is valid for times much larger than the characteristic time $t_0 \equiv 2\eta w_0^2/(\gamma_\theta \theta_{max} h_0)$ where w_0 and θ_{max} are, respectively, the decay length and the maximum value of the thermal field.

Since the pure-thermocapillary regime is solely controlled by the gradient of the thermal field $\partial_x \theta(x)$, finding this dynamics experimentally can be useful to characterize the thermal properties of the temperature profile. In our system, we have seen in Sec. 2.2.2 of chapter 2 that the thermal field behaves approximately as an exponential decay, $\theta(x) \approx \theta_{max} \exp(-|x|/w_0)$ (except below the typical width of the heating line, $|x| < 0.1\,\mathrm{mm}$). Therefore, we will focus on obtaining a measurement of the maximum thermal difference θ_{max} and the thermal decaying length w_0. Assuming that a series of experiments is done on the same geometry and a similar thermal field, using these two parameters it should be possible to recover a common master evolution by rescaling the variables with suitable scales. We will show how this master evolution is indeed found in different experiments and that, moreover, it is possible to obtain the gradient of the thermal field from experimental profiles.

3.3.1.2 Experimental example

Let us consider again the experiment shown above in Fig. 3.3, performed with the ABCR oil of viscosity $\eta = 19\,\mathrm{mPa\,s}$ and experimental parameters $h_0 = 36(2)\,\mu\mathrm{m}$ and $P = 0.81(1)\,\mathrm{mW}$. We consider on Fig. 3.4 several experimental profiles (left panel), obtained at different times with 3-colour interferometry, and the corresponding product $h(t, x) \times t$ (right panel). The three profiles marked with circles, at $t = 1.5$, 2.5 and 3.5 h, show a good collapse on a region of about 2 mm when multiplied by their corresponding times. The yellow data at $x > 2\,\mathrm{mm}$ is between 1 and 2 µm, so that we expect here the contribution of Laplace and gravity pressures to be still present.

The time interval in which this collapse occurs is defined to be the intermediate time section of the experiment, in which we find what we have called the pure-thermocapillary regime. For earlier times (profiles marked with inverted triangles) the profiles are close to the collapse and their shape is very similar (on the region to which we have access),

but they are still slightly above it. This short-time profiles are on the micrometre scale where the contributions of gravity and Laplace pressures is still relevant to the dynamics and the pure-thermocapillary regime has not yet been reached. For this experiment, $t_0 \simeq 4\,\text{min}$ (the values for w_0 and θ_{max} are obtained experimentally as detailed below). This coincides well with what we see in the right panel of Fig. 3.4, where the profiles for $t = 20$ and 30 min do not collapse completely with the following ones.

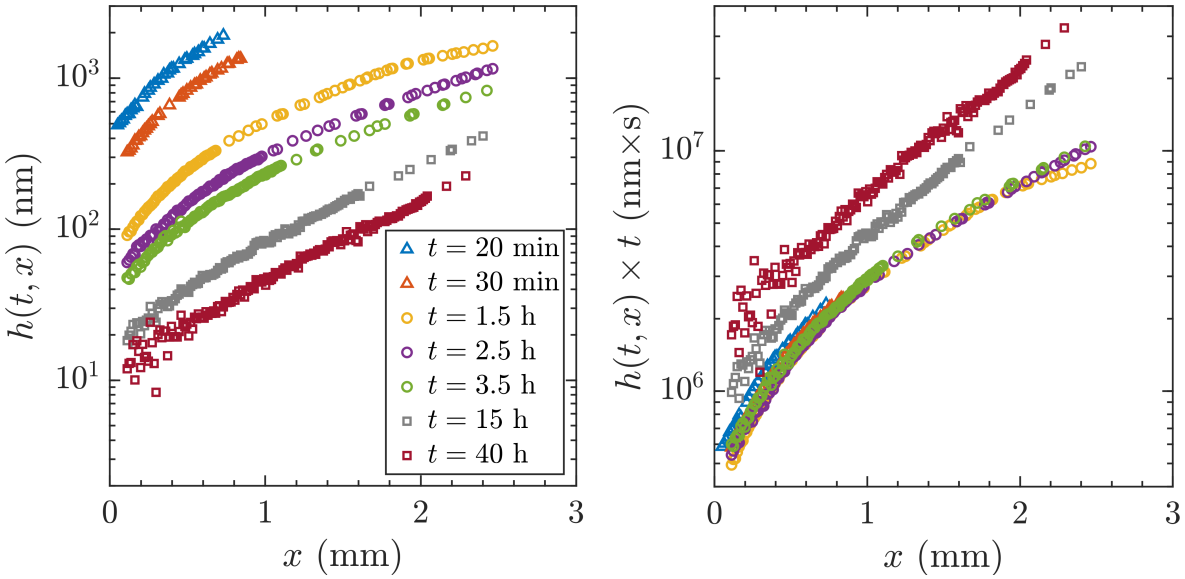

Figure 3.4: Left panel: experimental height profiles of the experiment shown before in Fig. 3.3 (but at different times). Right panel: product $h(t,x) \times t$ for the profiles on the left panel, coloured as before. Symbols represent the regime to which the profile corresponds: triangles, short time; circles, intermediate time; squares, long time. See main text for details.

Looking at the collapsing profiles on the right panel (marked with circles), it is interesting to note that there exists a small deviation from the collapse near the centre ($x < 0.5\,\text{mm}$). The left panel shows that in this small region the profiles have thicknesses below 100 nm. This signals the onset of the thickness range in which disjoining pressure is relevant.

For longer times (squares) the profiles are well below 100 nm (in this central region $x < 2\,\text{mm}$), where the presence of intermolecular forces is already expected. In this case, the intermolecular forces oppose the thinning effect of thermocapillary, effectively slowing down this dynamics. It is for this reason that these profiles, when multiplied by the time, appear above those following the pure-thermocapillary regime.

We refine the search of collapsing profiles and, for the experiment shown above in Fig. 3.4, we take the 12 profiles measured with 3-colour interferometry each 10 min between 40 min and 2.5 h. The profiles chosen lay between roughly 0.1 and 1 µm in the central region. As noted above, it is in this thickness range that the system follows the pure-thermocapillary dynamics satisfying Eq. (3.1). These profiles are shown in the left panel of Fig. 3.5, and their corresponding products $h(x,t) \times t$ together with the temporal average $\langle h(x,t) \times t \rangle$ in the right panel.

The collapse of the curves is remarkably good over the range to which 3-colour inter-

ferometry gives access to, and over an extent of a couple of millimetres. Small deviations occur for the highest and lowest thicknesses where, respectively, the action of gravity and Laplace pressures or of disjoining pressure may have a small role. These deviations are of minor importance and out of the range in which we compute $\langle h(x,t) \times t \rangle$. To perform the temporal average $\langle h(x,t) \times t \rangle$, since we do not have continuous data, we interpolate for the profiles at each time using a spline interpolation. At the same time, since the data of all profiles does not reach the same distance x, we consider the average of the data only until $x = 1.8\,\text{mm}$. We have checked that adding some extra profiles to the average for either shorter or longer times does not affect the overall curve.

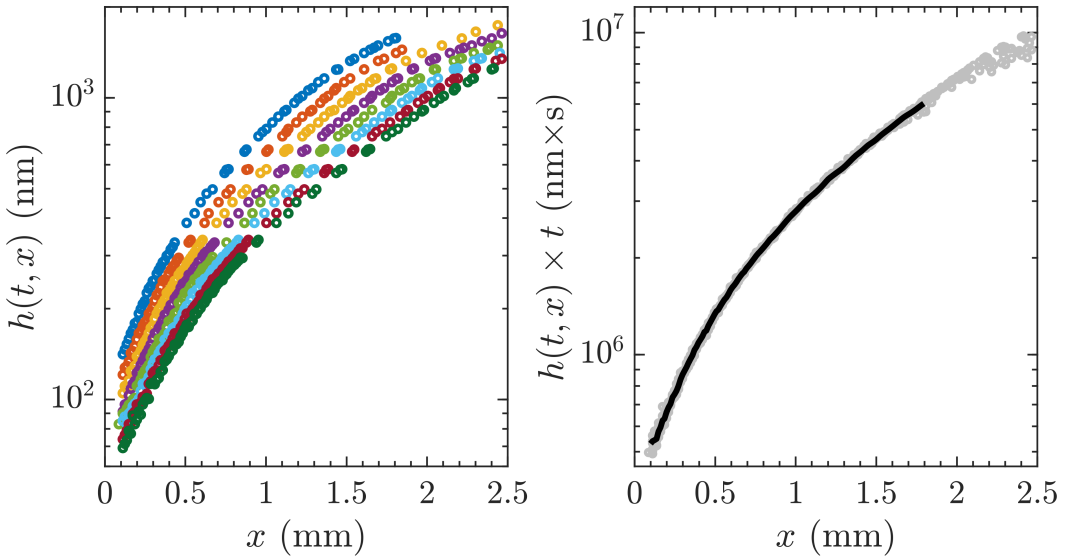

Figure 3.5: Left panel: thickness measurements each 10 min between 80 min and 150 min (8 profiles), for the same experiment as in Fig. 3.4. Right panel: product $h(x,t) \times t$ computed with the profiles of the left panel (grey circles), and their temporal average $\langle h(x,t) \times t \rangle$ (black line). See main text for details.

3.3.1.3 Extraction of the gradient of the thermal field

According to Eq. 3.1, the product $h(t,x) \times t$ under the pure-thermocapillary condition should therefore be a function of the position x but otherwise independent of time. We have seen in Fig. 3.5 that for some time it is possible to find this collapse experimentally, and that we can chose profiles $h(t,x)$ on a certain time interval to define a well defined temporal average $\langle h(x,t) \times t \rangle$.

Coming back to the equation describing the pure-thermocapillary regime (3.1), we can now write

$$\langle h(x,t) \times t \rangle \simeq \frac{2\eta}{\gamma_\theta} \frac{1}{2\sqrt{|\partial_x \theta|}} \int_0^x \frac{ds}{\sqrt{|\partial_s \theta|}} \tag{3.2}$$

where we have measured the left hand side of the equation. If we invert Eq. (3.2), we can obtain a measurement of the gradient of the thermal field $\partial_x \theta$ imposed on the liquid, directly from the experiment.

Isolating the thermal factors, and assuming that every function is well-behaved, equation 3.2 can be rewritten as

$$\frac{d}{dx}\left[\int_0^x \frac{ds}{\sqrt{|\partial_s\theta|}}\right]^2 = \frac{\gamma_\theta}{2\eta}\langle h(x,t)\times t\rangle. \tag{3.3}$$

from where

$$\int_0^x \frac{ds}{\sqrt{|\partial_s\theta|}} = \left[\frac{\gamma_\theta}{2\eta}\int_0^x \langle h\times t\rangle ds\right]^{\frac{1}{2}}. \tag{3.4}$$

Taking the derivative on both sides and rearranging,

$$\partial_x\theta = -\frac{2\eta}{\gamma_\theta}\frac{1}{\langle h(x,t)\times t\rangle^2}\int_0^x \langle h(x,t)\times t\rangle ds, \tag{3.5}$$

where the sign was chosen so that the thermal field decays towards the borders. The right hand side can be computed numerically from the experimental $\langle h(x,t)\times t\rangle$.

Let us illustrate this result with the average $\langle h(x,t)\times t\rangle$ shown in the right panel of Fig. 3.5 above. In our case, computing the full integral from $x = 0$ requires the extrapolation of values for $x \lesssim 0.1\,\text{mm}$. We use the simplest extrapolation assigning the minimum measured value of $\langle h(x,t)\times t\rangle$ to points in this small region, getting a constant curve at $x \approx 0$. This choice is motivated by the fact that, as commented before, we expect that the temperature is roughly constant in the width of the heating line, and thus the film will have a roughly constant value near $x = 0$. A consequence of this choice is that, by the integral of Eq. 3.6, the effective thermal field $\theta(x)$ will have a parabolic maximum, which is a good behaviour as a first approximation. The derivative $\partial_x\theta(x)$, numerically computed from Eq. (3.5), is shown in Fig. 3.6.

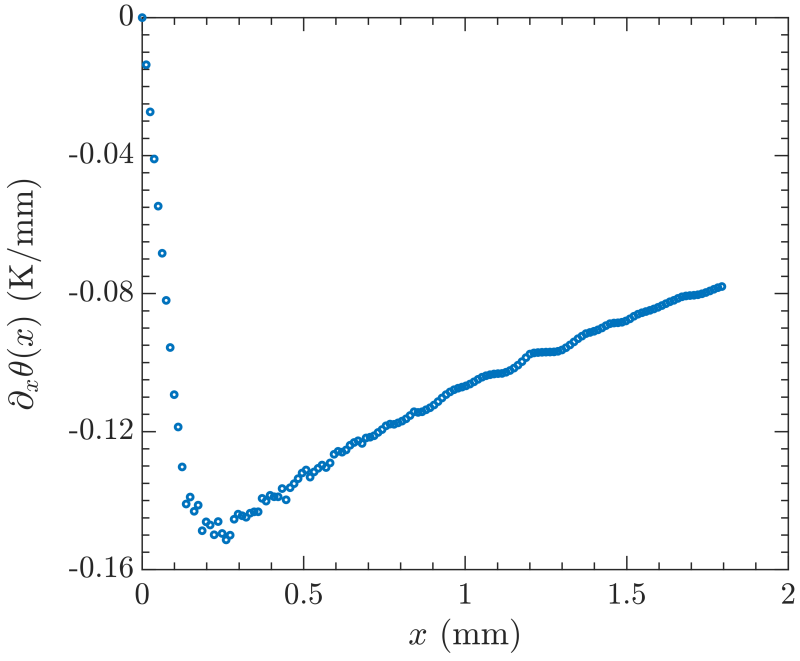

Figure 3.6: Gradient of the thermal field $\partial_x\theta(x)$ obtained experimentally, by using Eq. (3.5) with $\langle h(x,t)\times t\rangle$ as shown in Fig. 3.5 with a constant extrapolation at $x \lesssim 0.1\,\text{mm}$.

Since the collapse of profiles is good, the obtained gradient has a clean shape. Again, we have checked that adding or subtracting some profiles from the average $\langle h(x,t) \times t \rangle$ does not affect this result. The gradient of the thermal field $\partial_x \theta$ can thus be determined directly from experimental profiles, which is the only function needed to characterise the thermocapillary effect. This characterisation is important not only because it does not rely on any previous knowledge of the thermal field imposed, but also because $\partial_x \theta$ is a quantity needed for the characterization of the intermolecular forces of the system, as was explained in Sec. 1.7 of chapter 1. This problem will be revisited later on in Sec. 3.4.

3.3.1.4 Heuristic thermal field

Integrating Eq. (3.5), it is possible to obtain an experimental measurement of the thermal field $\theta(x)$. This allows to establish a heuristic model for $\theta(x)$ in the absence of any prior knowledge. For example, in our case, the heuristic model discussed below serves as the thermal field used in the numerical integration of the thin film equation, that we used in chapter 1 to illustrate the theoretical framework.

The integration of Eq. (3.5) leads to

$$\theta(x) - \theta(0) = -\frac{2\eta}{\gamma_\theta} \int_0^x \left\{ \frac{1}{\langle h(x,t) \times t \rangle^2} \int_0^u \langle h(x,t) \times t \rangle ds \right\} du, \tag{3.6}$$

which represents the thermal field with respect to its maximum at the centre. The right hand side can be numerically evaluated from experimental data as in the previous section.

In our case we expect, from the infrared measurements presented in chapter 2 and the discussion of appendix C, an exponential decay for long x, $x \gg 0.1\,\text{mm}$, with a parabolic maximum at the position of the heating line. To describe these features, we choose the following heuristic model

$$\theta(x) = \theta_{max} \left[\text{sech}\left(\frac{x}{\delta}\right) \right]^{\frac{\delta}{w_0}} \tag{3.7}$$

where the parameters θ_{max}, w_0 and δ represent the maximum temperature variation imposed, the thermal decaying length and the typical size of the heating line, respectively. These parameters can be fitted to the data by using Eq. (3.6).

In Fig. 3.7 we show the resulting thermal field $\theta(x)$ obtained by first, evaluating the right hand side of Eq. (3.6) from the experimental average $\langle h(x,t) \times t \rangle$ obtained earlier in Fig. 3.5; second, fitting the heuristic model (3.7) to obtain θ_{max}, w_0 and δ; and third, offsetting the data, obtained in the first step, by the value of θ_{max} obtained in the second step.

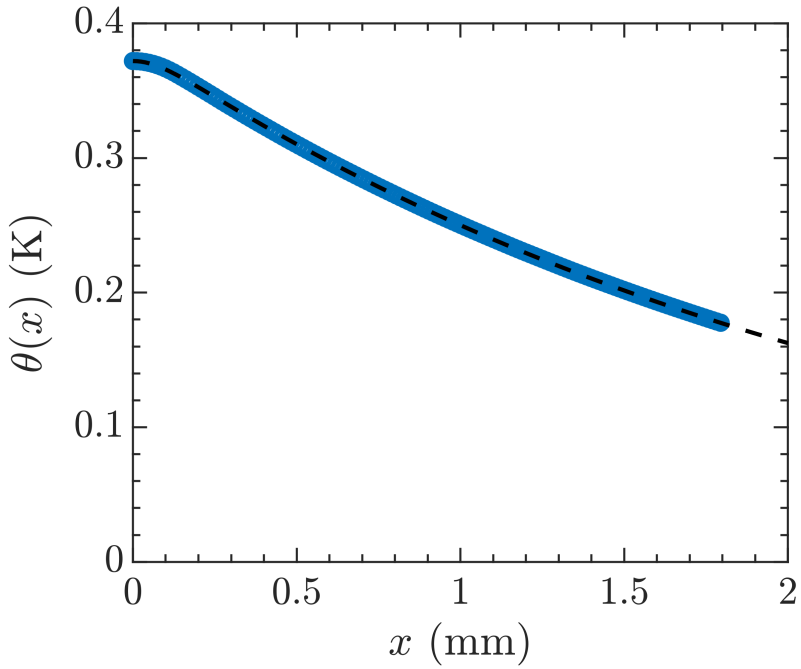

Figure 3.7: Blue data: Resulting thermal field obtained from the inversion of the pure-thermocapillary regime using the experimentally obtained average $\langle h(x,t) \times t \rangle$ from collapsing profiles, as explained in the main text. Black dashed curve: thermal field $\theta(x)$ using the heuristic model Eq. (3.7) fitted with Eq. (3.6). The parameters used are $\theta_{max} = 0.372\,\mathrm{K}$, $w_0 = 2.32\,\mathrm{mm}$ and $\delta = 0.114\,\mathrm{mm}$.

The perfect agreement between data and curve validates the heuristic model. The parameters obtained by the fit (with 95% confidence intervals) are $\theta_{max} = 0.372(2)\,\mathrm{K}$, $w_0 = 2.32(2)\,\mathrm{mm}$ and $\delta = 0.114(1)\,\mathrm{mm}$. Note that errors simply indicate the confidence level of the non-linear fit without taking into account the error of $\langle h(x,t) \times t \rangle$, which is nonetheless small. Taking a couple of profiles for shorter or longer times produced a variation of parameters of at most 10%, proving that this method is robust against the choice of the interval in which the average is performed. Note that the decay length w_0 is comparable to the x-range covered by the data. One should be therefore cautious before trying to make extrapolations of the behaviour for larger x, which may deviate from this model. A comparison of the values of the thermal field parameters with those obtained by the infrared measurement explained in Sec. 2.2.2 of chapter 2 is done below on Sec. 3.3.2.2. However, up to $x \sim 2\,\mathrm{mm}$, which is already quite a large range considering that the thickness of the film is below $1\,\mu\mathrm{m}$, this model correctly describes the dynamics.

The heuristic model also allows to compute the master curve as given in Eq. (3.2) and compare it with the experimental average $\langle h(x,t) \times t \rangle$. This comparison is done in Fig. 3.8. Indeed, the heuristic thermal field is able to recover the shape of the pure-thermocapillary dynamics.

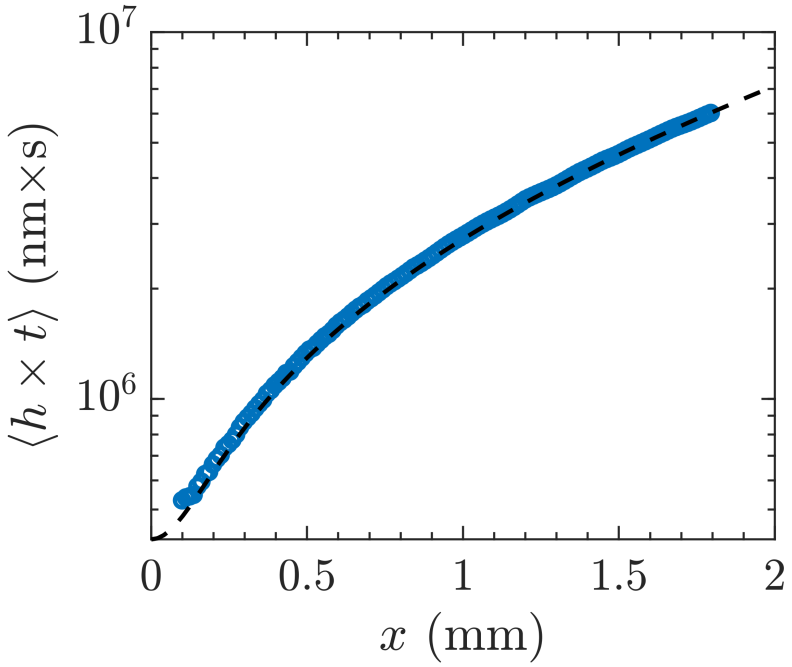

Figure 3.8: Comparison of the experimental average $\langle h(x,t) \times t \rangle$ (points, same as the right panel of Fig. 3.5) with the master curve (3.2) (red solid curve) computed using the heuristic thermal field (3.7) with parameters $\theta_{max} = 0.372\,\mathrm{K}$, $w_0 = 2.32\,\mathrm{mm}$ and $\delta = 0.114\,\mathrm{mm}$.

3.3.2 Collapse of experiments

3.3.2.1 Summary of results

We consider a series of experiments performed with different silicone oils under the same geometry, using different initial thicknesses and dissipated powers to analyse the existence of the pure-thermocapillary regime under a range of parameters. For each of them, we first identify the candidate profiles satisfying this regime by considering the plot of $h(t,x) \times t$, and then fitting the collapsing profiles to the master curve (3.6) as described above, obtaining experimental values of w_0, θ_{max} and δ for each of them. The resulting measurements are summarised in table 3.2, were the initial thickness h_0 and dissipated power P are also listed for reference. The lengths w_0 and δ, linked to the geometry of the heating pattern, are quite consistent for all 6 experiments. The thermal field decays exponentially with a characteristic length $w_0 \sim 2\,\mathrm{mm}$ when $x \gg \delta \sim 0.1\,\mathrm{mm}$. The dependence of the maximum thermal field θ_{max} with respect to the dissipated power P is discussed below in Sec. 3.3.2.2.

Note that there are two experiments (rows 2 and 6) which show a larger central width, $\delta \sim 0.3\,\mathrm{mm}$. In these experiments, we did not measure profiles early enough so that the thicknesses close to the centre ($x < \delta$) were above $\sim 50\,\mathrm{nm}$. Therefore, although there was a collapse for larger x, the central region could not be well described due to the effect of intermolecular interactions on small thicknesses. As we have noted, this contribution opposes the thinning effect of thermocapillary slowing down the dynamics, which smooths out the shape at the centre. This explains the larger value of δ for these experiments.

Nevertheless, this is a local effect that does not affect the overall decaying behaviour for longer x, as will be shown in the collapse of experiments of Fig. 3.9.

Oil	P (mW)	h_0 (µm)	w_0 (mm)	θ_{max} (K)	δ (mm)	Colour
ABCR 20 cSt	0.81(1)	36(2)	2.32(2)	0.372(3)	0.114(1)	Blue
ABCR 20 cSt	3.02(2)	23(2)	2.09(8)	1.57(3)	0.39(2)	Orange
ABCR 10 cSt	0.81(1)	26(5)	2.37(3)	0.405(3)	0.122(3)	Yellow
ABCR 10 cSt	7.6(2)	26(3)	2.30(3)	6.04(4)	0.111(3)	Purple
Rhodorsil 20 cSt	1.75(1)	42(4)	1.79(3)	1.06(1)	0.119(5)	Green
Rhodorsil 20 cSt	2.70(2)	56(8)	1.89(2)	1.770(8)	0.280(6)	Grey

Table 3.2: Summary of relevant parameters of the experiments considered for Fig. 3.9. The dissipated power P is computed from the imposed current and the resistance of the heating line, errors come from the precision of the measurement instruments. The initial thickness h_0 is the mean of 2 to 4 measurements of the thickness of the film at different positions with a profilometer, errors are standard deviations. The thermal parameters w_0, θ_{max} and δ are the result of the fit to the thermal master curve given by Eq. (3.6) as explained in the main text, errors give confidence intervals from the nonlinear fit. The colour column refers to the colour for each particular experiment in Fig. 3.9.

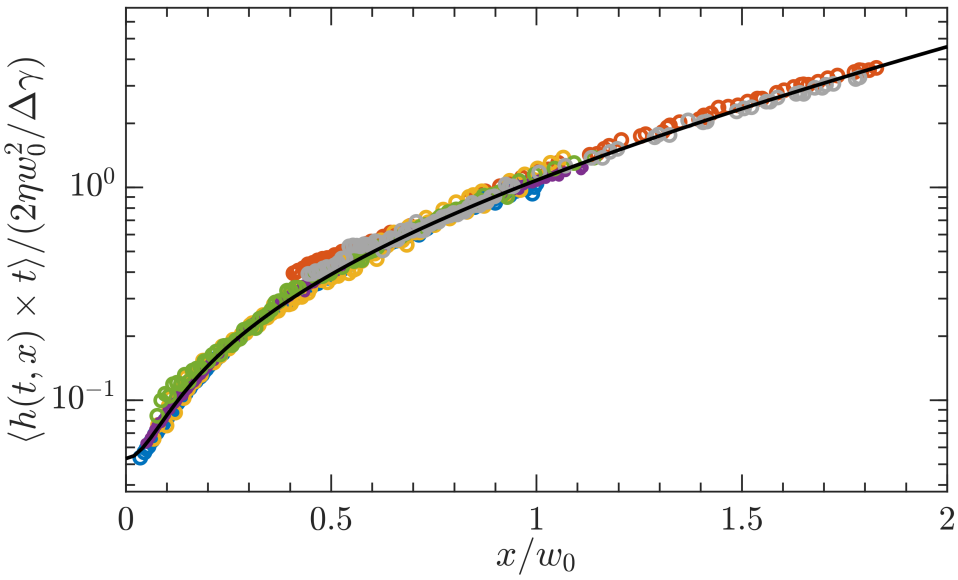

Figure 3.9: Collapse of scaled experimental profiles $\langle h(t,x)\times t\rangle/(2\eta w_0^2/\Delta\gamma)$ under the pure-thermocapillary regime, with parameters tabulated on table 3.2. The black solid line is the scaled analytical expression given by Eq. (3.2), computed with the heuristic thermal field 3.7 with parameters $w_0 = 1\,\text{mm}$, $\theta_{max} = 1\,\text{K}$ and $\delta = 0.1166\,\text{mm}$. The value of δ chosen is the mean of the experimental value of δ for rows 1, 3, 4 and 5 of table 3.2.

The thermal decaying length w_0 also varies slightly from experiment to experiment. In appendix C we discuss a minimal thermal model to understand the exponential decay of the thermal field. This model depends on an unknown characteristic length of heat

dissipation, that can be linked to the geometry of the cell and the effectiveness of dissipation to the surroundings. Therefore, small variations due to the actual thickness of the slides used or the conduction of heat to the borders of the slide are to be expected. Moreover, we are fitting the exponential behaviour of the thermal field in an spatial range typically smaller or of the same order as w_0, which may also affect its value. However, this variation is not critical since it is small and w_0 is determined and used independently on each experiment.

Since all the experiments are performed under the same geometry, after obtaining the thermal parameters of each of them it is possible to rescale the variables to collapse all experimental data under the same master curve. In particular, we rescale $\langle h(t,x) \times t \rangle$ with $h_0 t_0 = 2\eta w_0^2/\Delta\gamma$ and the spatial direction with w_0. This is done in Fig. 3.9, where we see good agreement between all 6 experiments. The collapse shows that the pure-thermocapillary regime can be generally found and, as a consequence, that for these locally promoted ultra-thin films the effect of Laplace and gravity contributions are negligible after a transient initial time of some minutes.

The difference in viscosity or polidispersity does not seem to have a noticeable effect on the master curve. Note that there is an experiment performed with a much higher dissipated power that the rest, for which a higher θ_{max} is found. Although $\theta_{max} \sim 6\,\mathrm{K}$, it collapses nicely with the rest of experiments. We can therefore also conclude that the variation of physical properties of the liquid with temperature other than surface tension is a next order effect on the dynamics, having no contribution in this range of experimental parameters.

3.3.2.2 Comparison with infrared measurements

In Sec. 3.3.1.4, the fitted parameters w_0, θ_{max} and δ are obtained with an heuristic thermal field $\theta(x)$ behaving as an exponential decay for $x \gg \delta$. These measurements can be compared with an independent characterization of the imposed thermal field that was performed with an infrared camera. We measured the surface temperature profile of some bare experimental cells, that is, without liquid, that resulted for different dissipated powers. These measurements are detailed in chapter 2.

The thermal field on the surface of the glass slide obtained with the infrared camera is exponentially decaying for $x >> 0.1\,\mathrm{mm}$, in a way similar to the heuristic thermal field given by Eq. (3.7) defined in the previous section. However, we find consistent discrepancies for the quantitative values of w_0 and θ_{max} between the infrared measurements and the corresponding ones obtained from experimental thickness profiles in the pure-thermocapillary regime. The characteristic length measured with the infrared camera was around $w_0 \sim 5\,\mathrm{mm}$, that is around two to three times the value obtained by the experimental procedure explained in Sec. 3.3.1.3, $w_0 \sim 2\,\mathrm{mm}$. Also, we obtained in the infrared measurements a correspondence between the dissipated power P imposed and the maximum thermal field measured θ_{max}, that is given by $\theta_{max} \approx (0.4\,\mathrm{K/mW})P$ (dashed line of Fig. 3.10). If we compare the recovered experimental θ_{max} with the correspondence obtained for a bare glass slide, we see that the fitted values are always above this trend, behaving as $\theta_{max} \approx (0.7\,\mathrm{K/mW})P$ (solid line of Fig. 3.10).

As explained in chapter 2, the thermal measurements had several limitations, so that $\theta_{max} \approx (0.4\,\mathrm{K/mW})P$ is to be understood as an order of magnitude estimation. More

importantly, the infrared measurements have been done with the bare substrate, while here we study the ultra-thin liquid film. Since the thermal model (see appendix C) has a parameter that characterises the loss of heat from the slide to the surrounding medium, it is possible that this loss is different whether this medium is the liquid or the air.

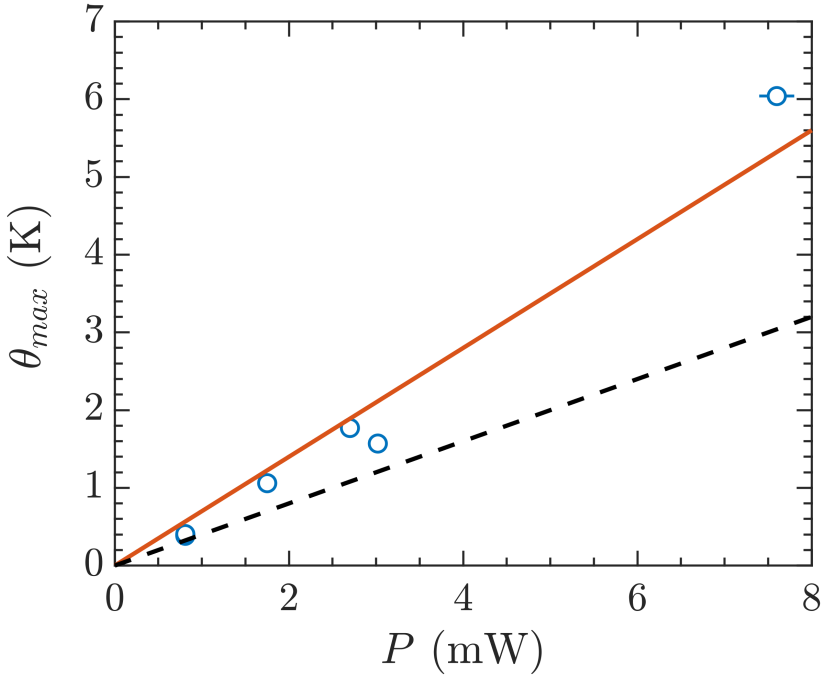

Figure 3.10: Points: Fitted values of θ_{max} as a function of the dissipated power P. Error bars for P come from the instruments precision, error bars of θ_{max} represent confidence intervals of the nonlinear fit explained in Sec. 3.3.1.3. Dashed line: Relationship $\theta_{max} \approx (0.4\,\mathrm{K/mW})P$ obtained with the infrared camera. Solid line: Relationship $\theta_{max} \approx (0.7\,\mathrm{K/mW})P$ fitted to the data.

Although the infrared measurements do not quantitatively agree with the thermal field extracted from the data, the important result is that we find the same shape with both methods and that, furthermore, the values of w_0, θ_{max} and δ are on the right order of magnitude.

3.3.3 Conclusion

In this section, we have investigated the existence of a pure-thermocapillary regime in which the pressure contributions to the liquid film (Laplace, gravity and disjoining pressure) are all negligible when compared to the thermocapillary effect. Following the analytical expectation, we have found that some experimental profiles $h(t, x)$, roughly in the thickness range 0.1 to 1 µm, collapse onto a same curve when multiplied by the corresponding times, $h(t, x) \times t$. Using the average of $\langle h(t, x) \times t \rangle$ over these profiles allows to directly compute the gradient of the thermal field $\partial_x \theta$ from experiments. This gradient will be useful in the next section as it is needed for the extraction of disjoining pressure.

Integrating numerically the obtained gradient gives a measurement of the thermal field $\theta(x)$. This can be useful to obtain a heuristic model of $\theta(x)$ in the absence of other

prior knowledge. In our case, we are able to recover the characteristics of the thermal field that we have measured independently with an infrared camera, as explained in chapter 2. In particular, the thermal field in our system decays exponentially, except near the heating line ($x < 0.1\,\mathrm{mm}$) where it is nearly constant. Our heuristic model is parametrized by the maximum temperature difference θ_{max}, the thermal decaying length w_0 and the central width δ. The exponential decay is consistent with the shape of the infrared camera on bare substrates, however neither θ_{max} nor w_0 agrees quantitatively with these measurements, with a factor 2-3 between the results from experiments and from the infrared measurements. This discrepancy may be related to the fact that the infrared measurements are done on the bare substrate, therefore changing the dissipation properties of the model (see appendix C). However, this fit provides an effective thermal field that satisfies the conditions of the pure-thermocapillary regime.

We have found the pure-thermocapillary regime in various experiments performed with liquids of different viscosities on independent experimental cells under the same dissipation geometry. All experiments could be collapsed into a single master curve by rescaling the variables with suitable parameters. This behaviour seems not to be affected in the range of parameters explored by polydispersity or changes in physical properties of the liquid dependent upon temperature. It is important to note that fitting this curve is made independently of the initial thickness h_0, which is the second control parameter of the experiments. In the present context, the initial thickness has an influence only in the initial transient dynamics, which lasts some minutes at most.

Following Eq. (3.1), as this dynamics evolves, the thickness becomes smaller with time since $h \propto 1/t$. This implies that the height of the film can attain values of tens of nanometres for which disjoining pressure effects may be important. Indeed, as viewed earlier in Fig. 3.4, a deviation from the pure-thermocapillary regime is expected at long times as the intermolecular forces become more relevant. In the following section we focus our attention on how this deviation can be used to provide a measurement of the dependence of the derivative of the disjoining pressure on the thickness of the film.

3.4 Measurement of the disjoining pressure

Our aim in this section is to obtain a characterization of the intermolecular forces opposing the thermocapillary effect from the measurement of the dynamic evolution of the height profile $h(t, x)$. In Sec. 3.3 we have shown that the system traverses a pure-thermocapillary regime near the centre, characterised by the fact that all pressure contributions (Laplace, gravity and disjoining pressure) are negligible against the thinning effect of thermocapillarity. Although this regime is limited both in time and extent, it can be used to extract the gradient of the thermal field $\partial_x\theta(x)$ directly from the experimental profiles. Obtaining this gradient is important since, as we will shortly explain, it is needed to recover the disjoining pressure acting on the liquid, which describes the intermolecular interactions of our solid/liquid/air system. Once the system enters this regime, we can safely ignore both gravity and Laplace contributions at this central area, since we are left with an ultra-thin film of thicknesses below 100 nm with very small gradients. Therefore, we will be able to link the deviation from the pure-thermocapillary evolution to the effect of intermolecular interactions.

To put our measurements in context, before presenting experimental results in our system we review in the next section some of the techniques that have been developed to measure the disjoining pressure of ultra-thin liquid films.

3.4.1 Common experimental approaches

Before explaining several techniques developed to measure disjoining pressures, let us recall the basic concepts behind the disjoining pressure between two interacting media through a third medium. A detailed explanation can be found in the classical book by Israelachvili, Ref. [4], which we follow.

The effect of intermolecular interactions is characterised by an interface potential $\Phi(h)$ originating mainly from van der Waals molecular forces characterised by a pairwise-interaction potential $V(r)$, r being the distance between molecules. In vacuum, intermolecular interactions typically behave as $V(r) \sim -C/r^6$, where C depends on the nature of the molecules. Considering two bodies at a minimum distance h, the interface potential $\Phi(h)$ between the two can be obtained by integrating all intermolecular contributions through the potential $V(r)$. Depending on the geometry of the bodies, the interface potential $\Phi(h)$ can depend differently on the distance h between them.

This procedure can be extended to interactions of two media through a third medium. In our case, these interacting media are the glass and air through the liquid film. The solid/liquid and liquid/air interfaces can be seen as approximately flat interfaces at a distance h (the thickness of the film).

Consider a thin liquid film covering a solid surface, thin enough so that gravity can be neglected, as represented in Fig. 3.11. If one were to try to diminish its thickness, the existence of the interface potential $\Phi(h)$ implies that a work needs to be exerted. The force (per unit surface) needed is the disjoining pressure of the system (in this case, solid/liquid/air), and it is defined as $\Pi(h) \equiv -\partial_h \Phi(h)$. If $\Pi(h) > 0$, the interaction between the interfaces is repulsive; in the opposite case of $\Pi(h) < 0$ there is an attraction between interfaces. The relevance of these quantities to describe different wetting scenarios will be further discussed later on in Sec. 4.2.2.1 of chapter 4.

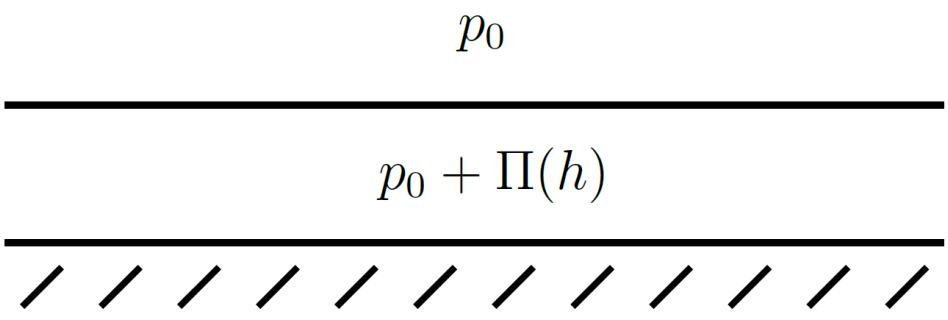

Figure 3.11: A thin, homogeneous liquid film covers a solid, subject to atmospheric pressure p_0. The effect of intermolecular interactions of the system gives rise to an extra pressure contribution, the disjoining pressure $\Pi(h)$ describing the interaction between the interfaces.

From a microscopic perspective, assuming additivity of interatomic interactions, the interface potential between flat surfaces $\Phi(h)$ can be shown to be $\Phi(h) = -A_H/(12\pi h^2)$, from where the resulting disjoining pressure is $\Pi(h) = -A_H/(6\pi h^3)$. This expression is referred to as the London-Hamaker theory of van der Waals interactions in what follows [55, 56]. Typical values of the Hamaker constant A_H are between 10^{-21} to 1×10^{-19} J. The sign convention followed is that a negative Hamaker constant $A_H < 0$ signifies repulsive intermolecular interactions, positive intermolecular interactions are characterised by a positive Hamaker constant $A_H > 0$. This form of of $\Phi(h)$ assumes non-retarded (instantaneous) interactions. As we shall see in some results from the literature commented below, sometimes the finite propagation of electromagnetic interactions is invoked to explain the experimental results. The resulting retarded London-Hamaker disjoining pressure in this case depends on thickness as $\Pi(h) = -B_H/h^4$, which decays more rapidly than in the non-retarded model. The constants A_H and B_H of the system can be approximated from the corresponding constants of the interactions in vacuum. A more general theory is obtained from the macroscopic continuum approach due to Lifshitz [57], which shows that the Hamaker constant A_H of the system can be computed from the dielectric permittivities of the media and, loosely speaking, is proportional to the difference between the dielectric permittivities of the solid and the liquid. However, measurements of dielectric permittivities are not always available on a sufficiently large frequency range to compute A_H precisely. Some approximations for computing A_H can be made, but they have been shown to not always be reliable as they may give values that differ several orders of magnitude (or even in sign) with the full computation [58].

The measurement of the disjoining pressure is an experimentally challenging task due to the small scales involved and the need of controlling the surface and ambient cleanness. To put our results of next sections in context, we review here experimental techniques proposed in the last decades for measuring the disjoining pressure of liquids on solid surfaces. In general, these measurements are done in equilibrium systems where a pressure is imposed and the equilibrium thickness measured via interferometry or ellipsometry. When possible, we comment on particular studies for non-polar liquids, on which we have focused in this thesis, which compare their experimental results with the van der Waals interactions commented above. The case of polar liquids is generally different due to the need of considering the effect of the charges of the molecules composing the liquid and/or the (maybe charged) surface [4]; these charges are responsible for relatively large values of $\Pi(h)$ and are typically easier to measure up to thicknesses of about 100 nm.

3.4.1.1 Vapour adsorption

One of the first proposed experimental setups to measure the disjoining pressure was by monitoring the adsorption of a nanometric liquid layer on a solid surface. A bare dry solid substrate is put in an atmosphere of controllable pressure of the liquid under study. In this condition, an ultra-thin film of liquid forms on the solid substrate and its thickness can be measured via ellipsometry. Relating the imposed vapour pressure with the disjoining pressure, its dependence with the equilibrium thickness can be established.

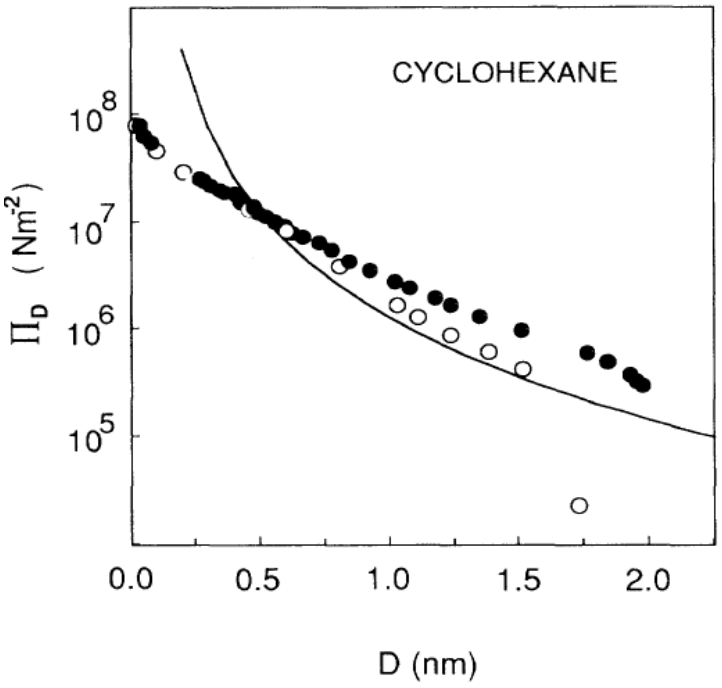

Figure 3.12: Measurement of disjoining pressure Π_D as a function of the thickness D of an adsorbed layer of cyclohexane on mica, taken from Ref. [59]. The open and closed symbols indicate measurements carried out on different mica sheets, size represents the error. The solid line is the prediction for van der Waals forces with retardation, which in the notation of the figure would be written as $\Pi_D \propto 1/D^4$.

The thickness of the obtained film is at most of a couple of nanometres, with subnanometric errors. This can be used for testing the validity of theories at molecular scales. For example, in the study of Beaglehole [59], it was shown that the obtained disjoining pressure from the adsorption of cyclohexane on a smooth mica surface deviates from the Lifshitz theory of van der Waals forces with retardation. Their measurement is reproduced in Fig. 3.12. Although the Lifshitz prediction (solid line) gives the right order of magnitude for the interaction, it does not describe the disjoining pressure as a function of the thickness. It is also interesting to note the difficulty of obtaining reproducible conditions when different mica sheets are used.

3.4.1.2 Submerged gas bubble

A second technique uses the thin liquid film formed between a gas bubble and a solid substrate. The bubble is submerged in bulk liquid and gently pushed towards the solid. Controlling the size of the bubble allows to equate the capillary pressure across the surface of the bubble with the disjoining pressure of the remaining film. After equilibrium has been reached, the thickness of this film is measured using an interferometric technique. This technique allows precise temperature control, but it has the drawback of having to change the bubble size for each desired pressure [6].

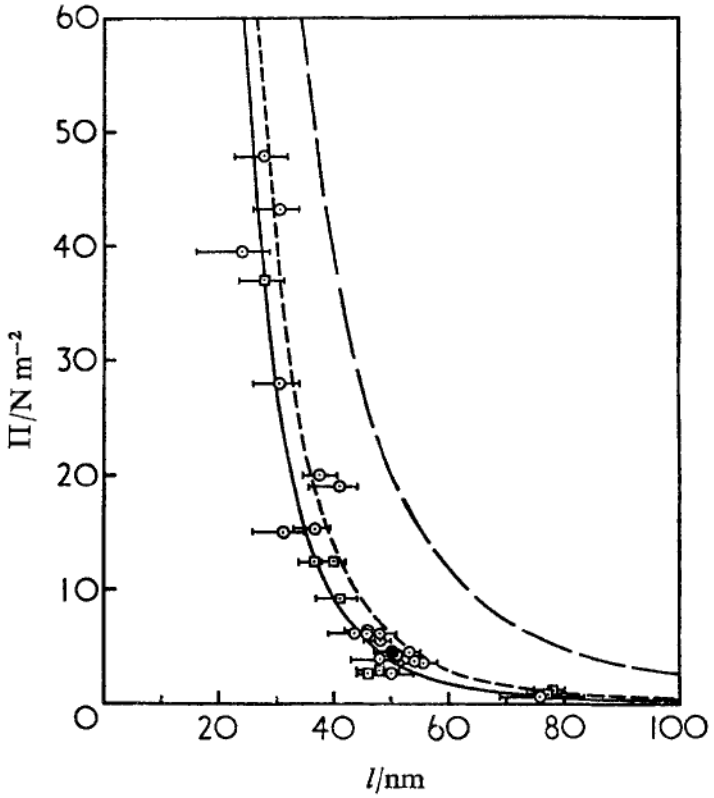

Figure 3.13: Measurement of disjoining pressure Π as a function of the thickness l for alkane films on α-alumina (circles: n-decane, squares: n-octane), from Ref. [60]. Solid curve: computed from the polarizabilities of the materials with the Lifshitz theory. Long-dashed curve: non-retarded London-Hamaker theory, $\Pi \sim 1/l^3$. Short-dashed curve: retarded London-Hamaker theory, $\Pi \sim 1/l^4$. These theoretical curves are computed for n-decane. More details can be found in Ref. [60].

With this method, it is possible to obtain $\Pi(h)$ one thickness at a time, in a thickness range of tens of nanometres. For example, T. D. Blake [60] measured the disjoining pressure of n-octane an n-decane on α-alumina in the 20 to 80 nm range. The reported results are reproduced in Fig. 3.13, from where it is concluded that the effect of retardation in van der Waals forces $\Pi(h) \propto 1/h^4$ needs to be considered to represent the intermolecular interactions. It was estimated that the Hamaker constant of this system was about 1×10^{-19} J for both liquids, but a precise value cannot be obtained. The main source of error in this experiment was in the recovery of the absolute thickness of the liquid film by interferometry, affected by residual roughness of the substrate. Reported estimated errors are on the order of 5 nm.

3.4.1.3 Thin film pressure balance

The thin film pressure balance technique consists on establishing a thin film in the hole of an annulus of porous material. This annulus is connected with a capillary tube that may control the hydrostatic pressure. Alternatively, the gas pressure may be set with a piston pump. The central area of the annulus is covered by a thin film of the liquid, that may or may not be supported by a solid. Its thicknesses is again obtained via interferometry

or ellipsometry [6].

This technique is commonly used for determining the disjoining pressure of polar liquids. For example, it was used by Ciunel *et al.* [61] to study the stability of aqueous solutions in charged wafers. Points along disjoining pressure isotherms are presented for a range of thicknesses between 20 and 70 nm, which contrary to our case are dominated by electrostatic effects and behave as an exponential decay $\Pi(h) \sim \exp(-h/\ell_D)$ characterised by the Debye length ℓ_D. The find a Debye length between 25 and 30 nm for different types of salts, which compares well with the theoretical expectation of $\ell_D \simeq 30\,\text{nm}$.

3.4.1.4 Surface force apparatus

A surface force apparatus consists in confining the liquid between two extremely homogeneous surfaces, usually made out of mica [62]. Note that this is a solid/liquid/solid system, whereas ours is a solid/liquid/air system. In this case, what is monitored is not a pressure but the surface forces based on the deflection of a cantilever. The equilibrium thickness is measured by interferometry.

This allows to measure confined liquids and investigate the disjoining pressure of a wide range of thicknesses, from 0.5 to 100 nm [7]. Below 10 nm, polar liquids or aqueous solutions typically show a rapidly varying disjoining pressure due to the presence of different contributions on top of van der Waals forces, coming from electrostatic charges and the liquid structure at the scale of the interface [4]. For thicker films, the contribution of retarded van der Waals interactions may become dominant and is needed to describe the experimental results [7].

3.4.1.5 Indirect measurement via surface thermal fluctuations

The previous techniques can give direct measurements of the disjoining pressure by equilibrating it with other pressure sources. Another possibility is extracting its strength from its effects in other thermodynamic phenomena, such as the power spectrum of surface fluctuations at a given temperature. In a recent experimental work in our group [28], the value of the Hamaker constant of silicone oils from Rhodorsil on glass substrates is obtained by fitting from the low-frequency spectrum of the thermal surface fluctuations of oil films. The dependence $\Pi(h) = -A_H/(6\pi h^3)$ was assumed. The setup for measuring the surface fluctuations is presented in Fig. 3.14, in which a laser beam has three roles. First, it promotes the thermocapillary effect by absorption at the substrate. Second, it provides dynamical measurements by interferometry of the thickness under its beam (in our notation this would correspond to measure $h(t, 0)$, note however that the resulting flow due to the laser beam is axisymmetric). Third, it is used to measure the fluctuations of the free surface of the liquid.

The fluctuation spectra are obtained for films of constant thicknesses between 8 and 30 nm. An example for two oils with different viscosities (10 and 20 cSt as in our study, of the Rhodorsil 47V series) is shown in Fig. 3.15. The spectra are fitted with the Hamaker constant A_H as the only adjustable parameter assuming $\Pi(h) = -A_H/(6\pi h^3)$. It is found that its value is around $A_H = -2 \times 10^{-19}\,\text{J}$ for both oils.

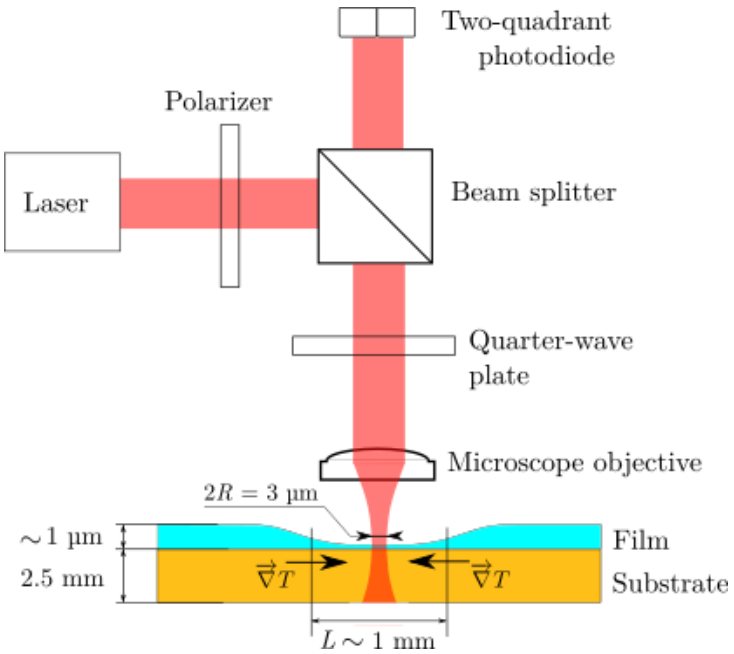

Figure 3.14: Setup for measuring the surface fluctuations of liquid films under a laser beam (not to scale), from Ref. [28]. The thinning of the film is generated by the light absorption at the substrate via the thermocapillary effect.

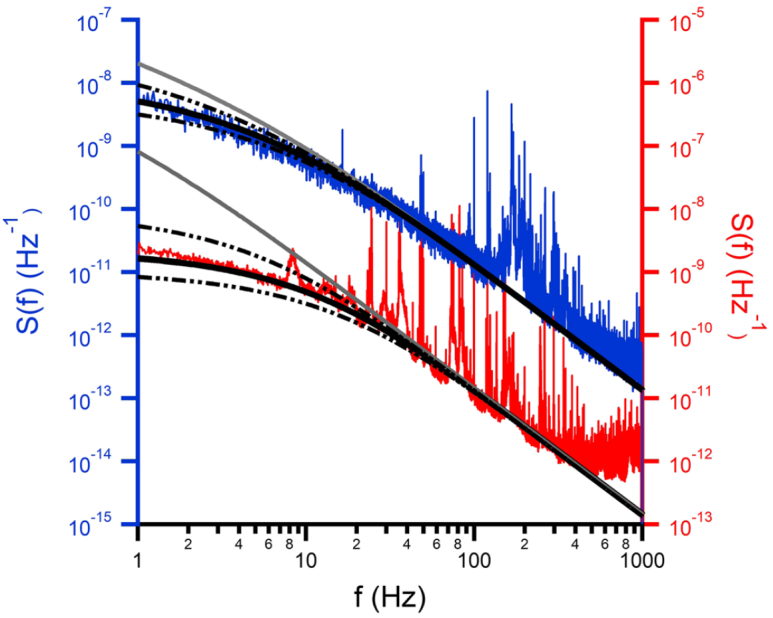

Figure 3.15: Fluctuation spectra $S(f)$ of two oil films, from Ref. [28]. Blue data (left axis): oil of viscosity 19 mPa s with a thickness of 30.3 nm. Red data (right axis): oil of viscosity 9.3 mPa s with a thickness of 12.9 nm. The solid lines represent the theoretical spectra without (grey lines) and with (black lines) intermolecular forces effects assuming the van der Waals disjoining pressure $\Pi(h) = -A_H/6\pi h^3$. Dash-dotted lines correspond to spectra computed with Hamaker constants differing by $\pm 50\%$.

Although the system is similar to the setup presented in this thesis in that it uses

thermocapillarity to obtain a film of nanometric thickness, the measurement of the height is local and the value of the temperature difference θ_{max} is not known and has to be estimated a posteriori ($\theta_{max} < 1\,\mathrm{K}$) [28]. Furthermore, a specific expression of the disjoining pressure must be assumed before fitting the data.

3.4.1.6 Conclusion

We have reviewed several common techniques for measuring the disjoining pressure of different systems of liquids on solid surfaces. We have mainly focused on reviewing studies on non-polar liquids, because in polar liquids the contribution of electrical layers dominates the disjoining pressure giving an exponentially decay with thickness for nanometric films, with the characteristic decay controlled by a Debye length.

The experimental data available is scarce, and usually in a small thickness range around the nanometre range. From the experiments shown above, we see that in general the resulting disjoining pressure in the 10 to 100 nm thickness range have been related to retarded van der Waals interactions, with a dependence with thickness as

$$\Pi(h) = -\frac{B_H}{h^4}, \tag{3.8}$$

but only an order of magnitude can be measured for the value of B_H. The adequacy found is not always good for nanometric thicknesses.

In contrast to the techniques commented in the previous section for studying non-polar liquids, which measure the disjoining pressure at equilibrium thickness, our measurements rely on the dynamics of the height profile over an extended area of several millimetres. The data of figures 3.12 and 3.13 are from techniques where usually the regions explores are, respectively, around 1 µm and 100 µm. In addition, the disjoining pressure is not controlled with an auxiliary pressure reservoir, and although we attain a quasi-steady regime on the experiments it is not an equilibrium system.

3.4.2 Inversion procedure

In Sec. 1.7 of chapter 1, we explained how to obtain the dependence of the derivative of the disjoining pressure with respect to the film thickness, $\partial_h\Pi(h)$, from the measurement of the dynamic surface $h(t,x)$. Once the pure-thermocapillary regime previously discussed has been established, both Laplace and gravity pressures can be locally neglected near the centre where only an ultra-thin film remains. The thin film equation (Eq. (1.12) of chapter 1) can then be reduced to only contain the disjoining pressure opposing the effect of thermocapillarity. The former term can be isolated, and we reach the following relationship between the derivative of the disjoining pressure $\Pi(h)$ with respect to the film thickness and the remaining terms

$$-\partial_h\Pi(h) = \frac{1}{h^3\partial_x h}\left\{\frac{3}{2}\gamma_\theta h^2\partial_x\theta(x) - 3\eta\int_0^x \partial_t h(t,u)\,du\right\}. \tag{3.9}$$

Inside the curly brackets on the right hand of this equation, we find the thermocapillary effect plus a term that is related to the exiting flux of liquid from the centre.

We evaluate this expression using the experimental thickness profiles $h(t,x)$ and the analytical derivative of the heuristic thermal field $\theta(x) = \theta_{max}\left[\mathrm{sech}\,(x/w_0)\right]^{\delta/w_0}$ obtained

via the pure-thermocapillary regime discussed earlier in Sec. 3.3.1.4. Note that the profiles $h(t, x)$ are time dependent, but if the reduced evolution equation leading to Eq. (3.9) holds, the resulting $-\partial_h \Pi(h)$ should be time-independent.

Some considerations about the numerical evaluation of Eq. (3.9) are in order. On the one hand, the numerical evaluation of this expression is cumbersome due to the need to perform numerical derivatives both in space and time domains. These are greatly affected by high-frequency noise in the data for the films at long-times with thicknesses around 10 nm and requires applying a smoothing filter to h. On the other hand, we do not have information below $x \approx 0.1$ mm, because the electrical circuit is opaque. Hence, in order to evaluate the integral of Eq. (3.9) we need to extrapolate the profiles in this small region.

For performing both operations, smoothing and extrapolation, we first mirror the surface h to negative values of x defining $h(t, -x) \equiv h(t, x)$. This allows us to apply a Gaussian moving average that smooths out the data, and to then perform an interpolation of the region near $x = 0$.

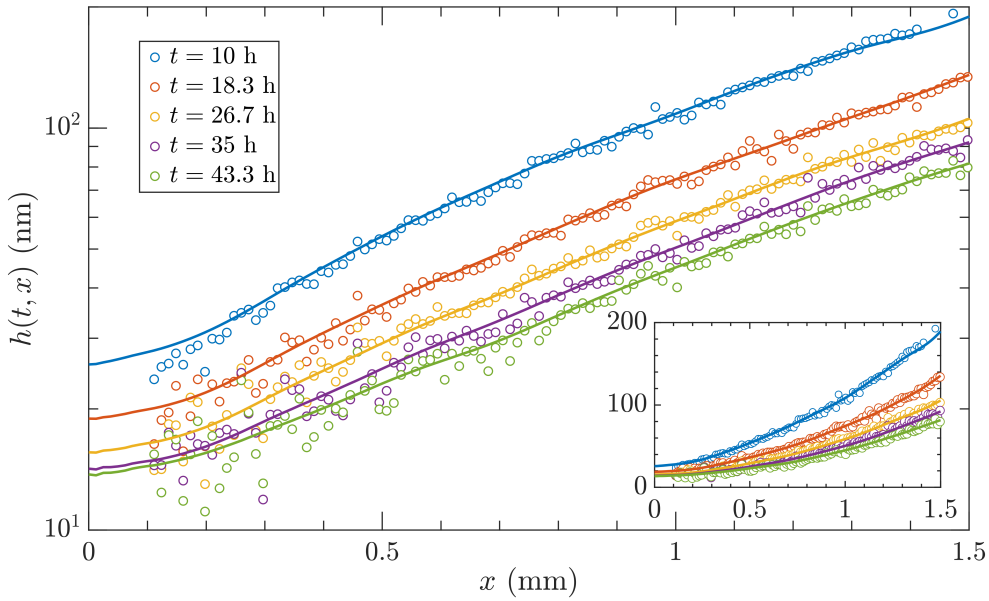

Figure 3.16: Example of profiles after smoothing and interpolation at the centre (solid lines) compared with raw data (circles), in semilogarithmic scale. The inset show the same curves in a linear scale. This height profiles correspond to the same experiment as those shown before in figures 3.3 and 3.5.

Some profiles are shown in Fig. 3.16 before (data points) and after (curves) this procedure. Plotting the smooth profiles versus the raw data points, Fig. 3.17, show that the smoothing procedure does not deviate more than 10 nm from the original data in the desired range, a deviation that is within the experimental precision. The worst agreement is for the smallest thicknesses close to the sensitivity level of our measurements, about 20 nm. An important improvement that should be made in future experiments is trying to reduce this sensitivity down to the nanometre level. Once the profiles have been smoothed out, the derivatives $\partial_x h$ and $\partial_t h$ appearing in Eq. (3.9) are numerically approximated using a 5-point stencil in each dimension. Note that the spatial derivative $\partial_x h$, which is a very small quantity in the ultra-thin film, appears in the overall denominator of

Eq. (3.9). Hence, errors in evaluating this derivative can have an important impact on the determination of $-\partial_h \Pi(h)$. For all the experimental curves shown in the following sections, we have checked that varying the interpolating parameters and methods does not change the overall results and conclusions.

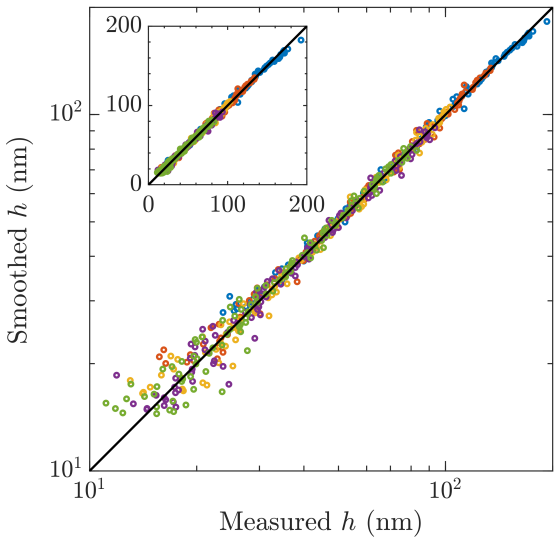

Figure 3.17: Plot of the smoothed profiles as a function of the original thicknesses (main panel in log-log, inset in linear scale) for the profiles of Fig. 3.16 above. The black line has slope one, and would represent complete agreement. The deviations of the smoothed profiles from experimental data are always below 10 nm.

As commented above, the extrapolation at the centre is needed to evaluate the integral of Eq. (3.9). Note that the ultra-thin film extends laterally over several millimetres, so that the weight of this region on the evaluation of the integral should be small when considering large x ($\gg 0.1$ mm). It is also noteworthy that the integral represents the exiting flow of liquid from the central region. Since in the system considered the intermolecular forces oppose the thermocapillary effect establishing a stable ultra-thin film, the system approaches a steady state in which no further liquid gets removed from the centre. Therefore, for very long times the integral should eventually vanish. We have seen in the evaluation of Eq. (3.9) from experimental profiles that the first term coming from thermocapillary was indeed the most relevant one for the profiles at the latest times. It is because of this reason that a good determination of the gradient of the thermal field explained in Sec. 3.3 was needed. Another advantage of using dynamics profiles $h(t, x)$ is that we obtain a large redundancy of data for each thickness, as will be shown in the following section.

With these ingredients, we present now the result of computing Eq. (3.9) from experimental data, using the experiment commented in Sec. 3.3 as an example.

3.4.3 Experimental result

After following the procedure outlined in the previous paragraph, we obtain a measurement of the derivative of the disjoining pressure with respect to the thickness of the film by evaluating Eq. (3.9) with experimental data.

The result is shown in Fig. 3.18 for the experiment discussed previously in Sec. 3.3, for which profiles were shown in Fig. 3.3. We compute Eq. (3.9) using nearly 200 experimental profiles measured each $\Delta t = 10\,\text{min}$ for times between $t = 12\,\text{h}$ and $t = 44\,\text{h}$, and all of the resulting profiles are included in Fig. 3.18. Although in this computation we use the extrapolation of thickness profiles at the centre to evaluate the integral of the temporal derivative $\partial_t h$ as explained in the previous section, we do not plot points corresponding to extrapolated thicknesses $h(t, x)$ in the $x < 0.1\,\text{mm}$ region. We obtain continuous measurements over one decade of thicknesses between 10 and 200 nm. This represents a typical range in which disjoining pressure can be obtained with experimental techniques designed to measure intermolecular forces, as discussed in Sec. 3.4.1 above.

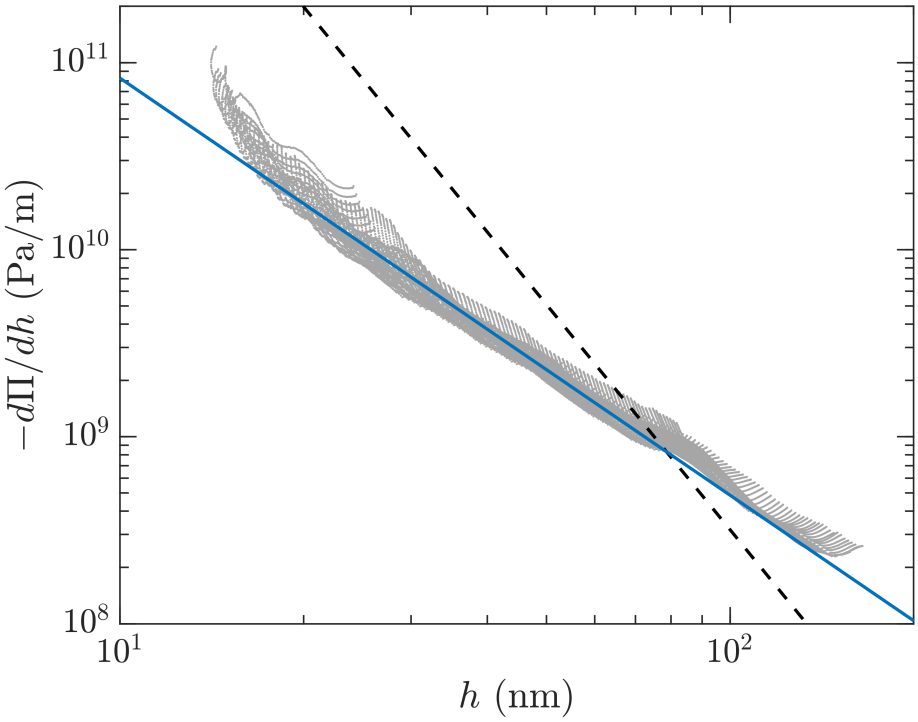

Figure 3.18: Derivative of the disjoining pressure as a function of the film's thickness obtained from experimental data (189 profiles, $\Delta t = 10\,\text{min}$). The dashed line indicates the theoretical expectation $-\partial_h \Pi(h) = -A_H/2\pi h^4$ with the value $A_H = -2 \times 10^{-19}\,\text{J}$ reported in [28]. Blue line: $-\partial_h \Pi(h) \propto 1/h^{2.2}$.

All the profiles follow a similar same power-law behaviour, which can be fitted to $-\partial_h \Pi \propto B/h^\alpha$. The exponent α is obtained from the slope of a linear fit of the logarithms of the data, $\log(\partial_h \Pi(h)) \propto -\alpha \log(h)$. We obtain an exponent $\alpha = 2.2$ (blue line). The collapse of points obtained at different times is acceptable, but their dispersion impedes of obtaining an specific value for the magnitude B of the interaction.

The power-law behaviour of disjoining pressure is typical of non-polar liquids [4], but considering typical van der Waals molecular interactions the obtained derivative of the disjoining pressure behaves as $-\partial_h \Pi \propto 1/h^4$ (or $-\partial_h \Pi \propto 1/h^5$ in the retarded case in which the finite velocity of transmission of the electromagnetic interactions is considered). This was the dependency we used to illustrate the theoretical discussion of chapter 1. In

a recent experimental study performed in our group [28] in a similar system of silicone oil on a glass substrate (explained in more detail in Sec. 3.4.1 below) it was shown with an indirect measurement that, assuming $\Pi(h) = -A_H/(6\pi h^3)$, the Hamaker constant A_H representing the strength of the intermolecular interactions is $A_H = -2 \times 10^{-19}$ J (the precise shape of $\Pi(h)$ was not directly determined). We include in Fig. 3.18 the prediction $-\partial_h\Pi(h) = -A_H/2\pi h^4$ using the reported value $A_H = -2 \times 10^{-19}$ J [28] (dashed line). Although our result does not have the same exponent since it behaves as $-\partial_h\Pi(h) \propto h^{-2.2}$, it is interesting to note that both are roughly on the same orders of magnitude in the thickness range that we can measure.

3.4.4 Comparison of results for different silicone oils

In Sec. 3.4.1, we have reviewed typical experimental approaches for measuring the disjoining pressure in systems of liquids supported by solid substrates. Focusing on the results of non-polar liquids, the results reported appear to indicate that, in the range of thickness from 10 to 100 nm, retarded van der Waals interactions are at the origin of the observed disjoining pressure. Thus, we may expect that in our measurements of the derivative of disjoining pressure with respect to the thickness of the film the relationship $-\partial_h\Pi(h) \propto 1/h^5$ should be found.

However, in the example showed above in Fig. 3.18, we have found that the measured $-\partial_h\Pi(h)$ behaves as $-\partial_h\Pi(h) \propto 1/h^{2.2}$, far from both the retarded and non-retarded behaviour. We compare in the following figures the result of this first experiment and 5 other performed with different silicone oils. The experiments are done with different parameters, as listed in table 3.3. Note that we compare oils with different viscosities. However, according to experiments performed recently in our group as explained in Sec. 3.4.1 above, we should not expect a significant difference between oils of viscosities 10 cSt and 20 cSt [28].

Oil	P (mW)	h_0 (µm)	α	Figure, panel
ABCR 20 cSt	0.81(1)	36(2)	2.2	3.19, left
ABCR 10 cSt	0.81(1)	26(5)	2.2	3.19, right
ABCR 10 cSt	7.6(2)	26(3)	2.8	3.20, left
ABCR 10 cSt	7.8(7)	50(1)	2.9	3.20, right
Rhodorsil 20 cSt	1.75(1)	42(4)	2.9	3.21, left
Rhodorsil 20 cSt	2.70(2)	56(8)	2.9	3.21, right

Table 3.3: Summary of the experimental parameters for the experiments shown in Figs. 3.19 to 3.21. The parameter α corresponds to the exponent of the thickness h in a power-law fit to the data, $-\partial_h\Pi(h) \propto 1/h^\alpha$ (see main text for details). In the last column, we indicate the figure and panel where the result of each experiment can be found.

The extraction of the derivative of the disjoining pressure as a function of the thickness is done from the evaluation of Eq. (3.9) as explained in Sec. 3.4.2. Each experiment is done in a different experimental cell. All the obtained results cover a thickness range between roughly 10 and 100 nm. The main origin of the dispersion of points comes from

the numerical evaluation of the derivatives appearing in Eq. (3.9). In the figures, we also include the best fit to a power-law $-\partial_h \Pi(h) \propto 1/h^\alpha$. The obtained values of the power α for each experiment is indicated in table 3.3.

In Fig. 3.19 we show the obtained $-\partial_h \Pi(h)$ as a function of the thickness for two experiments performed with oils with different viscosities. The oil used for obtaining the data on the left panel was ABCR 20 cSt oil, $\eta = 19\,\mathrm{mPa\,s}$, and on the right it was ABCR 10 cSt oil, $\eta = 9.3\,\mathrm{mPa\,s}$. Both experiments where done with the same dissipated power $P = 0.81\,\mathrm{mW}$ and similar initial thickness. In each panel, several curves are plotted (the number is given in the caption). Each data set corresponds to Eq. (3.9) computed with the height thickness at different times. Although they are computed at different times, the resulting $\partial_h \Pi(h)$ should be time-independent and thus all experimental curves should collapse. Although not perfect, the collapse of the curves is quite good for these experiments. As expected from the results of Ref. [28], no significant variation with viscosity is obtained.

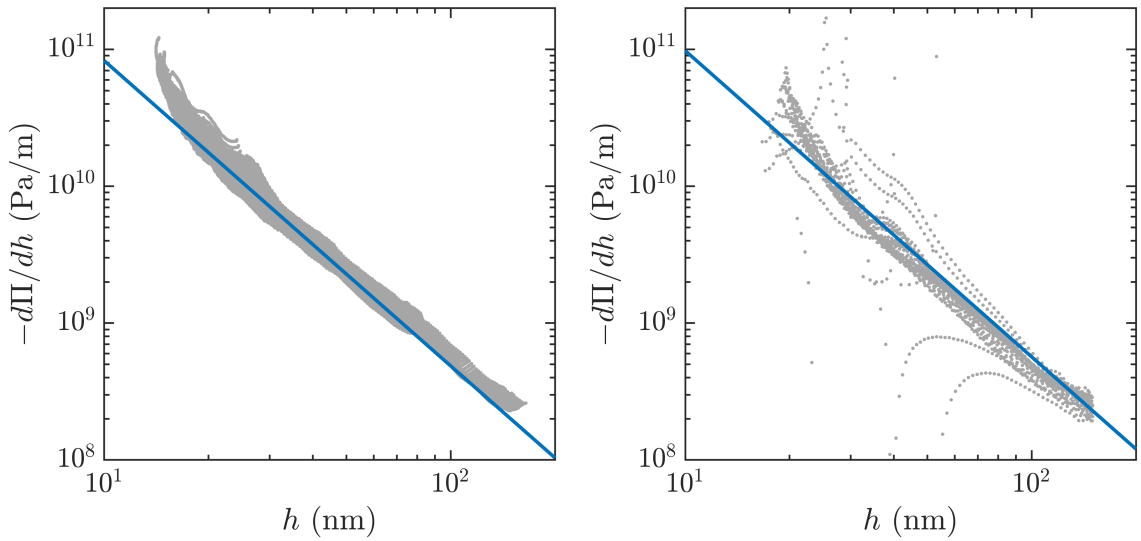

Figure 3.19: Comparison of the derivative of the disjoining pressure $\partial_h \Pi(h)$ as a function of the film's thickness obtained from experiments done with ABCR 20 cSt oil (left panel; same as Fig. 3.18) and ABCR 10 cSt oil (right panel, 32 profiles, $\Delta t = 25\,\mathrm{min}$). Blue lines are best fits to $-\partial_h \Pi(h) \propto 1/h^\alpha$. On both panels $\alpha = 2.2$.

The derivative of disjoining pressure behaves as a power-law with the thickness of the film over roughly a thickness decade from around 15 nm to 150 nm. We perform a linear fit of the logarithm of the data, to obtain the decay exponent from the resulting slope. In both graphs we find a fitted decaying power $\alpha = 2.2$, which is an exponent much smaller than the exponent of either retarded ($\alpha = 5$) or non retarded ($\alpha = 4$) London-Hamaker interactions. Both blue lines are on a similar order of magnitude.

We next consider two experiments with higher dissipated powers. In Fig. 3.20 we compare the obtained $-\partial_h \Pi(h)$ for two experiments performed with ABCR 10 cSt oil with similar dissipated power, $P = 7.6(2)\,\mathrm{mW}$ for the experiment on the left panel and $P = 7.8(7)\,\mathrm{mW}$ for the experiment on the right panel. These experiments are thus done with a relatively high maximum thermal difference $\theta_{max} \simeq 6\,\mathrm{K}$ (recall Fig. 3.10). The

initial thickness h_0 of the second one is about two times higher than h_0 for the first one. This difference should have no effect in the results, since once the pure-thermocapillary regime is (locally) established the dynamics lose memory of the initial configuration (see Sec. 1.4 of chapter 1).

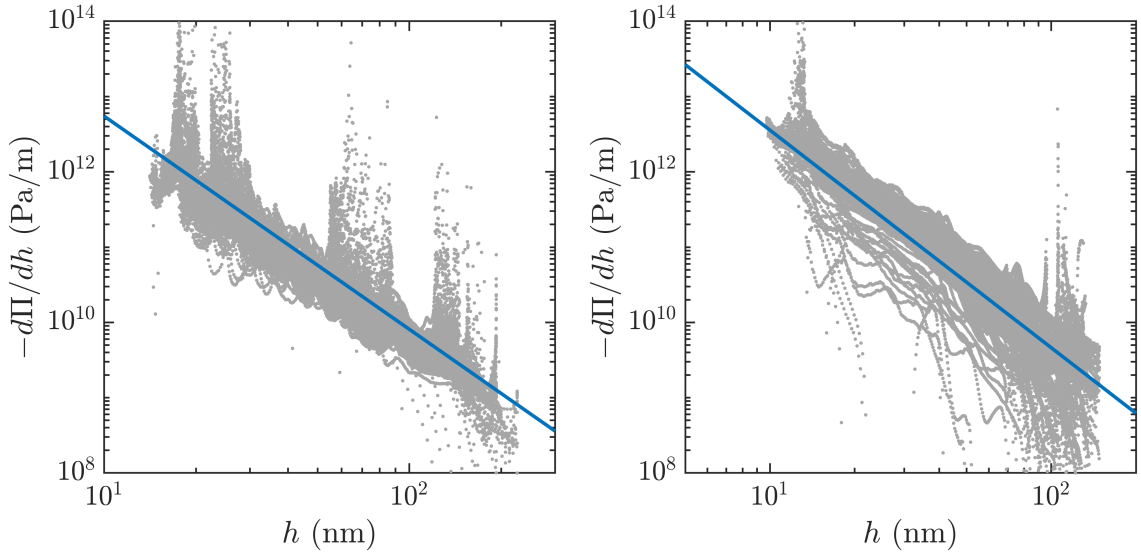

Figure 3.20: Comparison of the derivative of the disjoining pressure $\partial_h\Pi(h)$ as a function of the film's thickness obtained from two experiments done with ABCR 10 cSt oil (left: 101 profiles, $\Delta t = 1\,\text{min}$; right: 140 profiles, $\Delta t = 1\,\text{min}$). Blue lines are best fits to $-\partial_h\Pi(h) \propto 1/h^{\alpha}$. On the left panel the exponent is $\alpha = 2.8$, on the right one $\alpha = 2.9$.

Comparing the two panels of Fig. 3.20, we can see that neither this difference in initial thickness nor the greater value of dissipated power with respect to the experiments of Fig. 3.19 had any noticeable difference in the dynamics nor on the result of the extraction of $\partial_h\Pi(h)$. Indeed, we still obtain a power-law decay and, moreover, both experiments give comparable results. The peaks appearing specially on the left panel are a consequence of the numerical derivatives that are needed to compute Eq. (3.9). The obtained fitted decaying power is $\alpha = 2.8$ on the left and $\alpha = 2.9$ on the right. The similarity between the curves, which are of the same oils, points to the reproducibility of the measurements even when a high power is imposed or there exists a substantial difference between the initial height thickness h_0.

Finally, we show results for two experiments done with Rhodorsil 20 cSt oil in Fig. 3.21. These experiments have similar features to the experiments with ABCR oils. We found a power law decay with an exponent $\alpha = 2.9$ for both. This value agrees with the ones obtained above for ABCR oils but not with the theoretical prediction of the disjoining pressure from van der Waals contributions. Note that for the experiment on the right the number of curves that could be obtained is rather small and with a large time step between them, which increases the dispersion of results. However, they agree with the trend seen for the ABCR oils and thus we do not see any significant effect of polydispersity on the recovery of disjoining pressure.

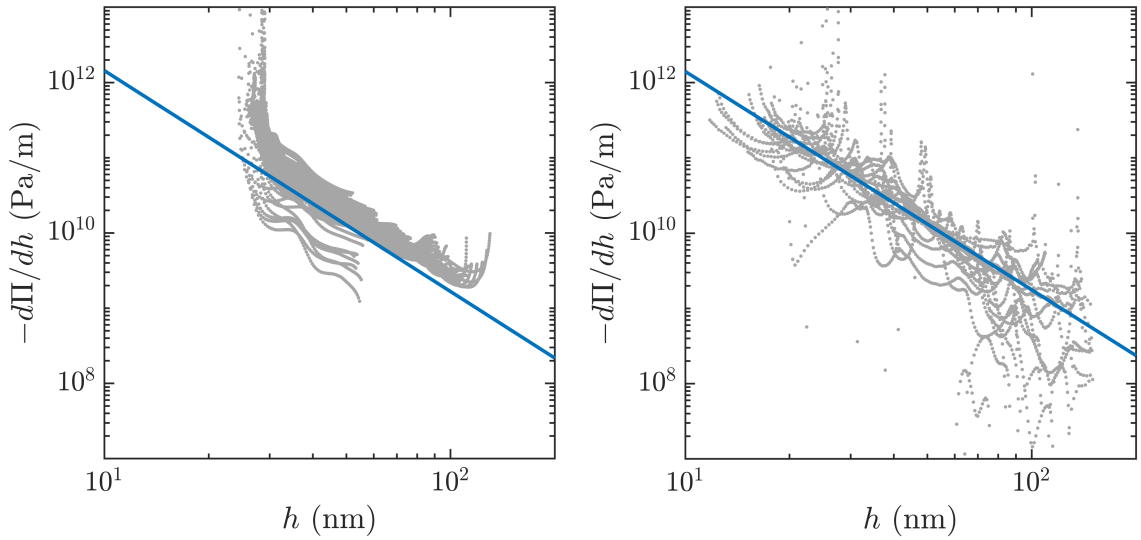

Figure 3.21: Comparison of the derivative of the disjoining pressure $\partial_h \Pi(h)$ as a function of the film's thickness obtained from two experiments done with Rhodorsil 20 cSt oil (left: 116 profiles, $\Delta t = 10\,\text{min}$; right: 20 profiles, $\Delta t = 1\,\text{h}$). Blue lines are best fits to $-\partial_h \Pi(h) \propto 1/h^\alpha$. For both experiments we find a value $\alpha = 2.9$ for the exponent.

These figures show that it is possible to measure the derivative of the disjoining pressure with respect to the thickness from the dynamical measurement of the evolution of a thin liquid film. For a variety of silicone oils with different viscosities and polydispersities, we find always a power-law decay $\partial_h \Pi(h) \propto 1/h^\alpha$ with $2 < \alpha < 3$, which does not correspond to the London-Hamaker theory. At present, we do not have an explanation of the origin of this exponent.

Future improvements of the setup may lead to better accuracy in the determination of α and an extended thickness range below the nanometre. Moreover, this method could be extended to the study of other non-polar liquids.

3.4.5 Conclusion

In summary, we have been able to compute the derivative of the disjoining pressure $\partial_h \Pi(h)$ with respect to thickness from experimental data, applying the inversion procedure explained in Sec. 3.4.2. This derivative behaves as a power law $\partial_h \Pi(h) \propto h^{-\alpha}$, with an exponent in the range $2 < \alpha < 3$. Although some large deviations sometime appears in our curves coming from the numerical derivatives that have to be computed we find this order consistently in all experiments analysed, which are furthermore performed with silicone oils for two different viscosities and polydispersities.

In the literature, is has been generally found that the intermolecular interactions of nonpolar liquids on solid substrates can be approximately described by the retarded van der Waals disjoining pressure, $\Pi(h) \propto -B_H/h^4$, although the value of the constant B_H is usually given as an order of magnitude. This dependency with thickness would give a derivative $\partial_h \Pi(h) \propto 1/h^5$, so that it is a steeper decay ($\alpha = 5$) that for non-retarded interactions ($\alpha = 4$). It is clear that, in our case, the obtained α represents a smoother

decay than any of these values, and in particular it cannot be associated with the retarded van der Waals interactions as has been the case in other systems.

We do not have at the present moment an explanation for the value of α. However, it is interesting to note that, as in Fig. 3.18, the order of magnitude of $\partial_h \Pi$ found is close to that of the derivative computed with the non-retarded London-Hamaker expression, taking the Hamaker constant recently found for silicone oils on glass in our group [28]. Hence, even if the exponent law does not agree, the gradient for the disjoining pressure measured is always around the same order of magnitude as the one expected with van der Waals interactions. It would be interesting for further work to reduce the sensitivity of the system down to the nanometre scale, in order to enlarge the thickness range and be able to compare the results with other systems at smaller scales.

3.5 Conclusion

In this chapter, we have shown the possibility of obtaining the derivative of the disjoining pressure $\partial_h \Pi(h)$ of a glass/oil/air system in a large thickness range from a dynamical measurement of the thickness profile driven by thermocapillarity.

For doing this, we have first validated the existence of a pure-thermocapillary regime defined in chapter 1 as a dynamical regime in which the pressure contributions within the liquid (Laplace, gravity and disjoining pressures) are all negligible when compared to the thinning effect of thermocapillarity. This regime appears locally at the region near the maximum thermal field imposed, usually when the thickness of the film is in a range roughly from 0.1 to 1 µm and the slopes very small (in our case $\sim 1\times10^{-3}$ rad). During this regime, the product $h(t,x)\times t$ collapse onto a master curve defined solely by the gradient of the imposed thermal field $\partial_x \theta$, and can be computed from liquid parameters without reference to the initial thickness of the film. From the experimental temporal average of $h(t,x)\times t$, we have shown that it is possible to obtain an experimental measurement of $\partial_x \theta$ with a good accuracy. This is an essential step since the gradient of the thermal field is needed to obtain the measurement of $\partial_h \Pi(h)$. It can also be used to obtain a heuristic model of the thermal field $\theta(x)$ acting on the liquid, which in our case serves to define the analytical thermal field used in the numerical integration of the thin film equation that accompanied the discussion of chapter 1.

The appearance of the pure-thermocapillary regime marks the point after which both Laplace and gravity pressure contributions are locally negligible. Under the action of thermocapillarity, the local thickness thins down to tens of nanometres where disjoining pressure effects are expected. Indeed, the collapse of $h(t,x)\times t$ is lost for long times when the dynamics slows down because of the opposing effect of the repulsive intermolecular interactions acting on the system. We have shown that this dynamic effect measured on experimental profiles, together with the previous determination of the gradient of the thermal field, can be used to determine the derivative of the disjoining pressure with respect to the thickness of the film. We find a power-law dependence, $\partial_h \Pi(h) \propto h^{-\alpha}$, with an exponent α between 2 and 3, over a decade of thickness ranging roughly from 10 to 100 nm. The difference in viscosity or polydispersity of the silicone oils used does not affect this result, nor the choice of experimental parameters within the range of values explored.

The exponent α found does not agree with the theoretical expectation of van der Waals interactions, whether non-retarded ($\alpha = 4$) or retarded ($\alpha = 5$). In the literature, experiments with other systems of a non-polar liquids on solid substrates are scarce, and to the best of our knowledge there have not been a study of disjoining pressure on the same system as ours. Typically, the techniques used, as reviewed in Sec. 3.4.1, allow only to obtain measurements of the disjoining pressure at selected values, comprising data points in a thickness range on the scale of nanometres or at most of a few tens of nanometres. The analysis of these experiments typically requires to consider retarded van der Waals interactions. In contrast, we are able to obtain continuous measurements over a decade of thicknesses ranging from roughly 10 to 100 nm and our results indicate a much smoother decay of the intermolecular interactions, which clearly cannot be due to retarded van der Waals interactions. Interestingly, the theoretically evaluated non-retarded interaction gives however the correct order of magnitude of the experiments using the Hamaker constant that has been indirectly determined for a similar glass/oil/air system [28].

Further experiments with increased accuracy will be needed to explore the thicknesses below 10 nm in order to probe the disjoining pressure of this system at the nanometric scale, thus obtaining results also at the thickness scale of other experimental techniques.

In this chapter, we have focus only on understanding the thermocapillary-driven dynamics of silicone oils, which completely wet the glass surface. We now turn our attention, in chapter 4, to preliminary results on other dynamics showing the variety of phenomena that can be studied with this simple setup. In particular, we turn our attention first to films of alkanes, which show a dynamics different to the one of silicone oils in that they appear to break up under the action of thermocapillarity, and in a second section to the study of the relaxation towards equilibrium from the nonequilibrium, (quasi-)steady regime appearing in thermocapillary experiments.

Chapter 4

Other dynamics

4.1 Introduction

In previous chapters, we have presented an experimental setup that allows to observe the dynamics of thin liquid films driven by the thermocapillary effect down to the tens of nanometres scale. In chapter 3, we have focused on the study of the evolution of silicone oils, which are liquids usually employed on industrial applications because of their good wetting properties.

In this chapter, we present an overview of the extension of this setup to two different dynamic scenarios. In Sec. 4.2 we discuss the thermocapillary-driven evolution of thin films of alkanes. As we shall see, these behave differently than silicone oil once the thickness of the film reaches the range in which intermolecular forces are significant. In particular, the alkane films break up and a contact line appears at the macroscale. This breakup leads to the formation of an ultra-thin "foot" that recedes until it becomes absorbed at the macroscopic contact line. In contrast with the experiments of silicone oils studied in chapter 3, the alkane films reach a stationary state within an experimentally attainable time scale of some hours. In Sec. 4.3 we make a preliminary account on "rewetting" processes, both with silicone oils and alkanes, in which we follow the relaxation dynamics of the films starting from the (quasi-)steady state, by removing the thermal field that drives the dynamics. As in the case of the thermocapillary evolution, there is a clear difference between the dynamics of silicone oils and the alkane films. This relaxation process is slow and smooth for silicone oils, whereas for the alkanes the wedge does not move once the "foot" has been absorbed.

4.2 Thermocapillary-driven dynamics of alkane films

As discussed earlier in the introduction of chapter 3, glass is a high energy surface which should be completely wet by liquids. In short, this means that when liquids are deposited on this surface they tend to spread to maximize the surface that is covered, as we have seen is the case with the silicone oils. Typical wetting scenarios will be discussed below in Sec. 4.2.2.1.

In this section, we focus on the dynamics of thin films of two alkanes, n-hexadecane and 2,2,4,4,6,8,8-heptamethylnonane, on the same glass substrates as before. These liquids,

in contrast to silicone oils, form unstable films that appear to break under the action of the thermocapillary effect, once a thickness below the micrometre scale is attained. The ultra-thin film left behind by the receding wedge is not stable: it forms a foot with a clear boundary that recedes away from the central heating line too.

4.2.1 Physical properties of alkanes

We investigate the dynamics of hexadecane and 2,2,4,4,6,8,8-heptamethylnonane (HMN), which show a weaker tendency to wet the surface as compared to silicone oil. Linear alkanes such as hexadecane have been shown to show interesting wetting properties, of which we give a brief review in Sec. 4.2.2.2. The properties of ultra-thin films of hexadecane on glass has already been studied in our group [63], where a nanometric solid-like layer of hexadecane giving rise to a finite negative slip length [64, 65] could be investigated through its effect on the surface thermal fluctuations. On the other hand, HMN is a highly branched isomer of hexadecane which does not show any particular confinement effect [66], making it useful to better interpret the results of the experiments on the tens of nanometres scale.

Their relevant physical properties are listed on table 4.1, where we also list for comparison the values of the Rhodorsil 47V20 oil used on experiments of chapter 3.

Liquid	η (mPa s)	ρ (kg m^{-3})	γ_0 (mN m^{-1})
Hexadecane	2.2	733	27.5
HMN	2.8	784	24
Rhodorsil 47V20	19	950	20.6

Table 4.1: Summary of nominal values at 20 °C of viscosity η, density ρ and surface tension γ_0 of the two alkanes used in this chapter, together with values (at 25 °C) of one of the silicone oils used in the experiments discussed in Ch. 3. "HMN" stands for 2,2,4,4,6,8,8-heptamethylnonane. Data for hexadecane from Ref. [67]. Data for HMN from Ref. [68]. Data for Rhodorsil 47V20 from Ref. [25].

The values for alkanes are given at 20 °C. The experiments are typically performed at 24 °C, higher than the melting temperatures of hexadecane ($\simeq$ 18 °C) [69] and HMN ($\simeq -4$ °C) [70]. To be several degrees above the melting temperature is important for experiments with hexadecane, which linear structure can result in complex surface behaviour as will be explained later on in Sec. 4.2.2.2.

The alkanes have a smaller density ρ and a higher surface tension γ_0 than the silicone oil. Thus, they have a somewhat higher capillary length $\ell_0 \equiv \sqrt{\gamma_0/\rho g}$. For the silicone oils, $\ell_0 \simeq 1.49$ mm, whereas for hexadecane $\ell_0 \simeq 1.96$ mm and for HMN $\ell_0 \simeq 1.77$ mm. These values are somewhat closer to the decay length of the thermal field obtained in chapter 3, $w_0 \sim 2.2$ mm, but they are still smaller. Thus, the effect of the Laplace pressure at the initial times will be slightly larger than in the case of silicone oil. The viscosity of hexadecane and HMN is smaller than the viscosity of the silicone oils discussed in chapter 3. Since the viscosity of the liquid sets the time scale, we expect the dynamics to be quicker.

The variation of surface tension with temperature, γ_θ, is similar for the alkanes and silicone oil. In Fig. 4.1 we show a measurement of the surface tension of hexadecane as

a function of temperature in the range from 20 to 50 °C.[1] A linear fit to the data gives $\gamma_\theta = 8.7 \times 10^{-5}\,\mathrm{N\,m^{-1}\,K^{-1}}$, which compares well with literature values [71] and is indeed close to the value for silicone oil $6.5 \times 10^{-5}\,\mathrm{N\,m^{-1}\,K^{-1}}$ [26].

Apart from these differences in the specific values of the physical properties involved, we do not expect any significant difference in the thermocapillary dynamics wherever the height profile of the film is thick enough so that intermolecular forces are negligible.

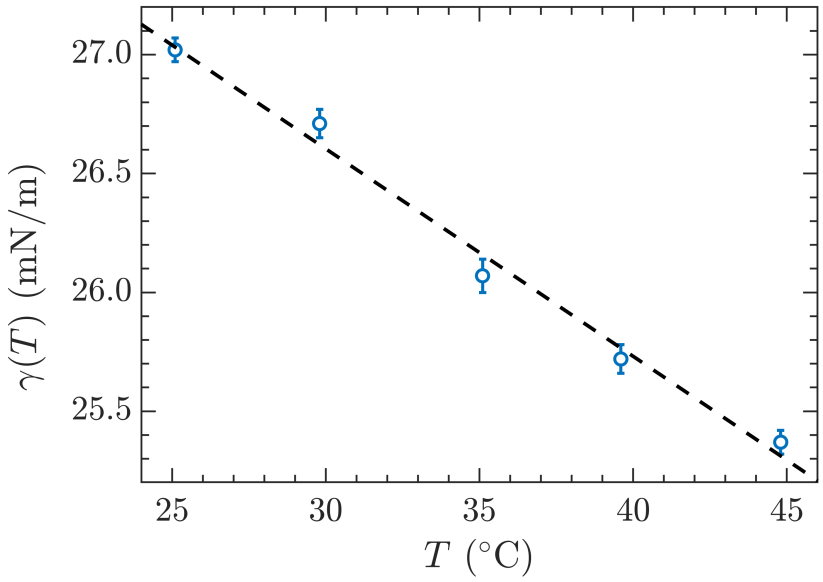

Figure 4.1: Surface tension of hexadecane as a function of temperature, measured with a pendant drop rheometre. Temperature errors are smaller than the symbol size. The black dashed line is the best linear fit to the data. From the slope of the fit we get $\gamma_\theta = 8.7 \times 10^{-5}\,\mathrm{N\,m^{-1}\,K^{-1}}$.

4.2.2 Stability of the alkane films

During the deposition of the film by spin coating prior to the experiments, we sometimes saw that the films broke generating large, macroscopically "dry" regions. In the following, when we refer to these break up regions as "empty", we always mean that they appear to not contain liquid to the naked eye (differentiated from the film by the formation of a macroscopic wedge) but we do not claim that there is not an ultra-thin (nanometric) film remaining.

We link this break up at the initial deposition step to surface inhomogeneities, which was common if the initial thickness was below $h_0 \sim 10\,\mu\mathrm{m}$. Sometimes tiny dust particles deposited on the film generated perfectly symmetrical patches around them. Other times this effect appeared to be related to some surface defect, since after redoing the spin coating the patches appeared at the same regions. We recall here that we cannot use common cleaning techniques (e.g. using a piranha solution) which would destroy the circuit. Before deposition, the surface is simply cleaned with acetone and isopropanol. A preliminary step using a UV/ozone system has also been tried but no change in the results were seen.

[1] We thank H.-P. Tran for performing these measurements.

As already mentioned in chapter 3, impurities deposited on the surface throughout the experiment are unavoidable. Although in the experiments with the silicone oils their effect was constrained to a local deformation of the flow and the image analysis could be generally performed, the unstable behaviour of the alkanes make the effect of impurities much more pronounced, since the break-up of the film can be generated anywhere. The spontaneous dynamics that ensues gets mixed with the expected thermocapillary dynamics. An example of this is shown in Fig. 4.2. The interference pattern of the ultra-thin film gets destroyed because the film recedes after becoming unstable on top of a surface impurity.

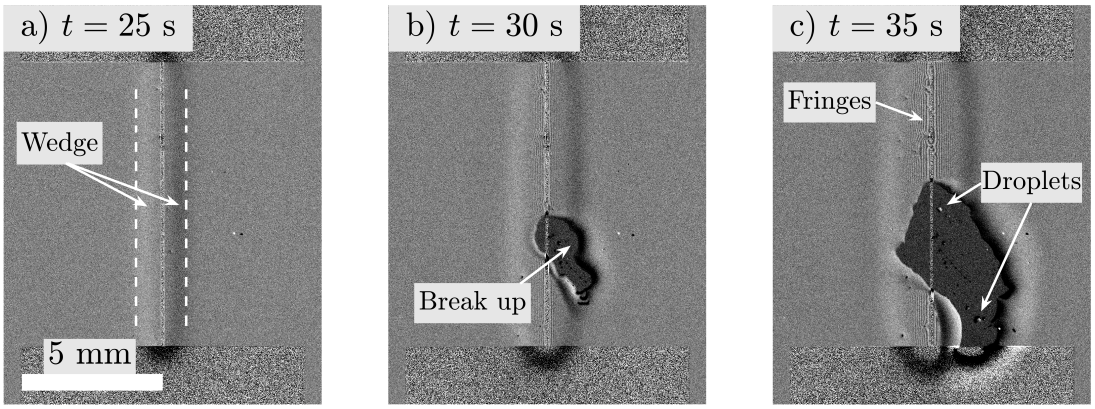

Figure 4.2: Film break up in a thermocapillary experiment with a hexadecane film of initial thickness $h_0 = 10.5(7)\,\mu\text{m}$ and dissipated power $P = 5(1)\,\text{mW}$. The images shown here are the result of dividing each experimental image by a reference one, the latter corresponding to an image of the initial flat film as explained in Sec. 2.3.3.2 of chapter 2. The break up is due to surface impurities. a) Initially, the dynamics proceeds as expected, and the formation of the wedge starts. b) Once the higher interference fringes ($h \sim 2\,\mu\text{m}$) appear close to the centre, the film becomes unstable due to surface impurities and breaks up. c) The film recedes from this region and tiny droplets may form on top of some surface defects. During this process the film on the top half of the image continues the thinning dynamics of thermocapillary, but the quick enlargement of the break up area destroys the interference.

This major difficulty has impeded the obtention of reproducible conditions, which is an issue that must be solved in future experiments. Nevertheless, we have obtained a clear picture of the dynamics of the alkane films driven by thermocapillarity. As we shall see in section 4.2.3, there exists a difference in the dynamics at large and small scales, with two different time scales. We can see how the system reaches a steady-state where there exists a macroscopically "empty" region at the centre and the bulk liquid on the outside. As we shall see in following sections from interferometric data, the thickness at the "empty" region lies below the sensitivity threshold of our measurements which is about 20 nm (see chapter 2). Therefore, we cannot say with certainty that these macroscopically emptied

regions are indeed dewetted or if a nanometric layer of liquid remains.

4.2.2.1 Summary of wetting-related concepts

As we will briefly review below, alkanes show specific wetting properties. To clarify this discussion and the interpretations of the results of the following sections, we recall here the three typical situations that may occur depending on the spreading parameter of the liquid, S and the repulsive or attractive character of the interaction potential of the system $\Phi(h)$. We report here the discussion given in Ref. [30]. The total surface energy of a film of thickness h is the sum of interfacial tensions (the macroscopic contributions) and of the interaction potential (the microscopic contribution),

$$\mathcal{E}(h) = \gamma_{SL} + \gamma_0 + \Phi(h), \tag{4.1}$$

where γ_{SL} is the surface energy at the solid/liquid interface. In the macroscopic limit (thick film, $h \to \infty$) $\mathcal{E}(\infty) = \gamma_{SL} + \gamma_0$ and $\Phi(\infty) = 0$. In the limit of vanishing thickness (bare substrate, $h \to 0$) $\mathcal{E}(0) = \gamma_{SV}$, where γ_{SV} is the surface energy of the solid/vapour system. Hence, $\Phi(0) = \gamma_{SV} - (\gamma_{SL} + \gamma_0) = S$. That is, the value of the energy associated with intermolecular forces at vanishing thickness must be given by the spreading parameter. Let us note that the precise shape of $\Phi(h)$ is not known for thicknesses less than a typical molecular cut-off scale a, typically of some Å. Within this limits, $\Phi(h)$ may have different dependencies leading to different wetting regimes, the more relevant to our discussion are sketched in Fig. 4.3. For a film to be stable, its thickness h must satisfy $\partial_h^2 \Phi(h) > 0$.

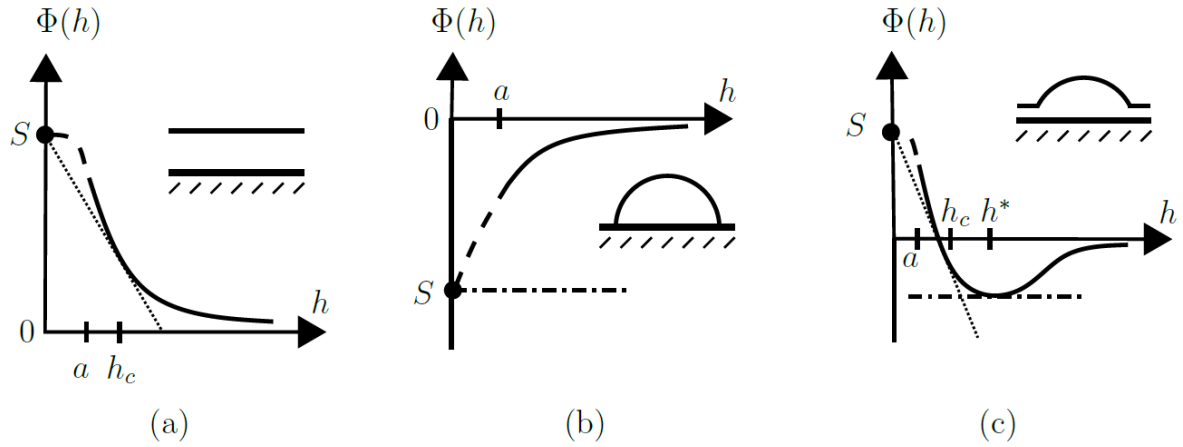

Figure 4.3: Interfacial potential $\Phi(h)$ corresponding to different wetting scenarios. (a) Complete wetting. (b) Partial wetting. (c) Pseudo-partial wetting. In all cases, S is the spreading parameters and a is a molecular length scale below which the shape of $\Phi(h)$ is unknown. Other details are explained in the main text.

From a hydrodynamical point of view, it is useful to introduce an associated pressure contribution to the interaction energy $\Phi(h)$. This is the disjoining pressure $\Pi(h)$, associated to the intermolecular interactions as the negative of the derivative of the interface

potential $\Pi(h) \equiv -\partial_h \Phi(h)$. The main theories about the disjoining pressure $\Pi(h)$ have been reviewed above in Sec. 3.4.1 of chapter 3. Defined in this way, $\Pi(h)$ has a fundamental role on the equilibrium of interfacial tensions: if there are values of the thicknesses for which the disjoining pressure is the same, then the film can have simultaneously sections with different thicknesses in equilibrium.

We consider three typical scenarios. Complete wetting, Fig. 4.3(a), is characterised by $S > 0$ and a monotonously decreasing $\Phi(h)$ ($\Pi(h) > 0$), where the liquid tends to spread to form a homogeneous film. This is the case illustrated in the hydrodynamic model of chapter 1 and of the experiments with silicone oils showed in chapter 3. In a complete wetting situation, the liquid may spread until its thickness reaches a critical value h_c, typically of a few Å, below which it would become metastable or unstable.

Partial wetting, Fig. 4.3(b), occurs in the opposite case, when $S < 0$ and $\Phi(h)$ is monotonously increasing ($\Pi(h) < 0$), leading to the formation of a contact line and the apparition of drops. The contact angle β is related to the value of the spreading parameter S via $-S = \gamma_0(1 - \cos\beta)$.

Finally, a third case involves $S > 0$ and a non-monotonic interaction potential as in Fig. 4.3(c). In the case of a potential having a minimum at some thickness h^*, the tangent of Φ at this point ($= -\Pi(h^*) = 0$) is the same as a point at infinity representing a thick film ($= -\Pi(\infty) = 0$). Since both thicknesses have the same disjoining pressure, they can coexist in equilibrium, and a drop with a macroscopic contact angle sits on top of a nanometric homogeneous film of liquid that covers the surface. This case is called pseudo-partial wetting, and consists of a drop with a finite angle that coexists with a nanometric film covering the surface.

This schematic summary will be useful to compare the behaviour of the alkane films at nanometric thicknesses with the ultra-thin films of silicone oils, and to infer the probable characteristics of the interface potential $\Phi(h)$ of the alkanes on our glass substrates.

4.2.2.2 Brief review of wetting behaviour of alkanes

The dynamics of films of linear alkanes has been studied because they are commonly used organic liquids that have the particularity that their structure favours the formation of a frozen molecular layer at solid surfaces under some circumstances, see Ref. [72] for a recent review. This leads to curious wetting behaviours, e.g. it has been shown that some alkanes on silica, including hexadecane, can form partially wetting liquid droplets that stand on top of "terraces" of solid-like layers of alkane, for temperatures around the melting point [73].

When deposited on clean glass, drops of hexadecane has been recently shown to spread continuously whereas shorter alkanes form drops with contact angles below 10° [74]. This effect is attributed to a Maragoni-type effect resulting from drop evaporation.

Hexadecane has also been shown to have a negative slip length on glass substrates [63]. This means that in a hydrodynamics setting the velocity field does not become zero precisely at the solid/liquid interface, but rather at a finite length above it. This length is nanometric, -4 nm as measured in Refs. [63–65]. The linear nature of the hexadecane molecule favours the formation of an ordered solid-like layer. HMN, a highly branched isomer of hexadecane, does not present a finite slip length [66]. Interestingly enough, in the studies done in our group mentioned earlier (Ref. [63]), thermocapillarity was used as

the means to obtain hexadecane films of nanometric thicknesses on glass which, contrary to our case, were stable.

As noted above, in our experiments the alkane films show break up due to impurities on the surface, a process usually known as heterogeneous nucleation [75], which is a first indication that the intermolecular interactions are different than in the case of the oil on our glass substrate. This difference will be also clear when we analyse thermocapillary experiments, as discussed in Sec. 4.2.3. We note that the break up promoted by thermocapillarity for a partially wetting film [tri(ethyleneglycol) supported by a polycarbonate substrate] has been analysed in the context of surface patterning, where the main interest was in determining the breakup times [76]. In that case, the break up is linked to the film reaching a threshold thickness (spinodal instability). In our experiments, we focus on analysing the dynamics below the micrometre scale after the break-up has happened, which results in a characteristic receding ultra-thin film.

This brief review serves to illustrate the richness of behaviours that may be encountered when considering the wetting properties of alkanes on solid substrates, either spontaneous or driven. Before discussing our experimental results, we discard a strong non-wetting behaviour of the alkanes on our substrates by performing measurements of the contact angle of small droplets. These measurements are considered in the next section.

4.2.2.3 Contact angle

Before presenting the result of the thermocapillary dynamics on hexadecane and HMN, we show in this section preliminary measurements of the (macroscopic) contact angle of these liquids on our substrates. The equilibrium contact angle of a drop is determined by the equilibrium of surface tensions at the contact line. The equilibrium contact angle of a system is difficult to measure accurately, since it may take very long times to reach and any impurity on the surface may pin the contact line. Since our study is focused in films, our aim with these measurements is to discard a strong non-wetting behaviour.

An example of image of 0.5 µL drops of hexadecane and HMN is shown in figures 4.4 and 4.5, respectively. These drops are deposited on a bare glass slide, cleaned in the same way as in an experiment with acetone and isopropanol as explained above. For both hexadecane and HMN, we obtained an averaged angle over several measurements of around 4°. The drops did not evaporate for several days.

This finite contact angle appears to indicate that the liquids do not wet completely the substrate, contrary to expectation. However, it is quite a small angle and the equilibrium state may have not been reached, since the spreading of a drop may last for several days, even a week [77], until it reaches the equilibrium state. Later on in Sec. 4.2.4, we will discuss the possibility of pseudo-partial wetting, that is, that the liquids do have a positive spreading parameter but that the equilibrium state is characterised by the coexistence of a drop sitting on top of a nanometric-thick film, as explained before in Sec. 4.2.2.1. This possibility will be discussed under the light of the experimental results of the driven dynamics of the alkane films, which is analysed in the next section.

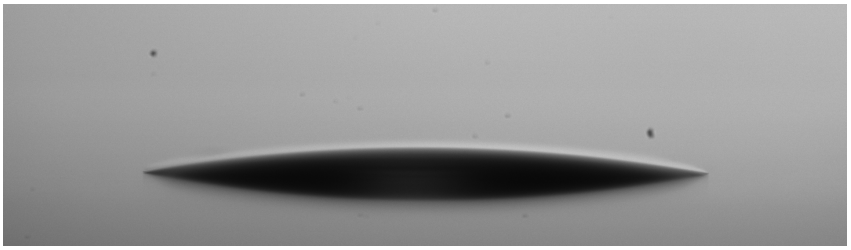

Figure 4.4: Example of drop of hexadecane of 0.5 µL deposited on a bare glass slide, of the type used in the experiments, to measure the contact angle on this surface.

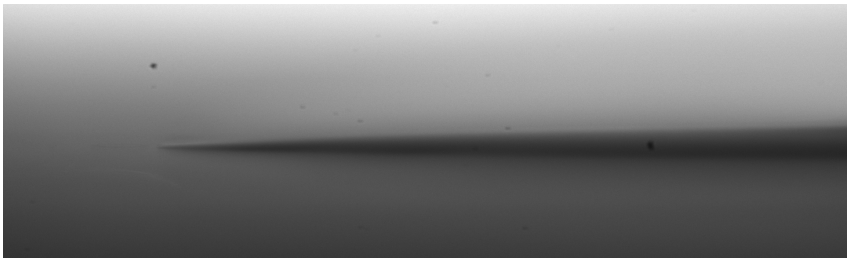

Figure 4.5: Example of drop of HMN of 0.5 µL deposited on a bare glass slide, of the type used in the experiments, to measure the contact angle on this surface.

4.2.3 Experimental observations

We investigate in this section the dynamics driven by thermocapillary when applied to hexadecane or HMN. The evolution of both of them is very similar. Because of the common apparition of spontaneous breakup of the film, we use examples of successful experiments with either of them to illustrate the different dynamical aspects.

We divide this section into the three time regimes that we discussed in chapter 1. We first briefly comment the dynamics at the initial times, in which thermocapillary is opposed by Laplace and gravitational pressures. Since disjoining pressure has no role for thicknesses above the micrometre scale, the evolution is shown to be as for the silicone oils in this short-time regime. Once the film enters the region of thicknesses $h \sim 0.1-1$ µm, the film crosses the pure-thermocapillary effect quicker than silicone oil and soon breaks. The resulting ultra-thin film forms a receding foot with a clear boundary that recedes faster than the wedge. Contrary to the case of silicone oil, the alkane films reach a stationary state within the experiment duration. We study how it is established by following the receding dynamics of the wedge and the ultra-thin film. We show how the foot gets eventually absorbed by the bulk.

4.2.3.1 Short times

In our experiments, the initial thickness is of order $h_0 \sim 30$ µm. Therefore, during the initial times the contribution of disjoining pressure is negligible, as we discussed in chapter 1. The short-times regime is controlled by the generic contributions of Laplace and gravity pressures, and not by the system-specific intermolecular forces. Therefore, the experiments with alkanes should show a similar evolution to the dynamics of silicone oils films in comparable experimental situations.

We would want to compare the results with alkanes to those with silicone oil at times which are equivalent from the point of view of the dynamics. Thus, some scaling of the time scale will be necessary. The time scale we have focused on in chapter 3 has been that of the thermocapillary regime. This was defined in Sec. 1.4 of chapter 1 as $t_0 = 2\eta w_0^2/\Delta\gamma h_0$, where we recall that h_0 is the initial film thickness, w_0 is the decay length of the thermal field driving the dynamics and $\Delta\gamma = \gamma_\theta \theta_{max}$ is the maximum surface tension variation given a maximum temperature difference θ_{max}. From the interferometric measurements of chapter 3, we know that the experimental value of θ_{max} can be approximated from the dissipated power P as $\theta_{max} \approx (0.7\,\mathrm{K/mW})\,P$. Thus, we will use $\tilde{\theta}_{max} = (0.7\,\mathrm{K/mW})\,P$ as an approximation of the maximum thermal field. Similarly, we take $\tilde{w}_0 = 2.2\,\mathrm{mm}$, see table 3.2 on chapter 3. With these estimations, we can scale the time by $\tilde{t} = 2\eta\tilde{w}_0^2/(\gamma_\theta\tilde{\theta}_{max}h_0)$, which should give a reasonable approximation to t_0 computed from the real experimental parameters.

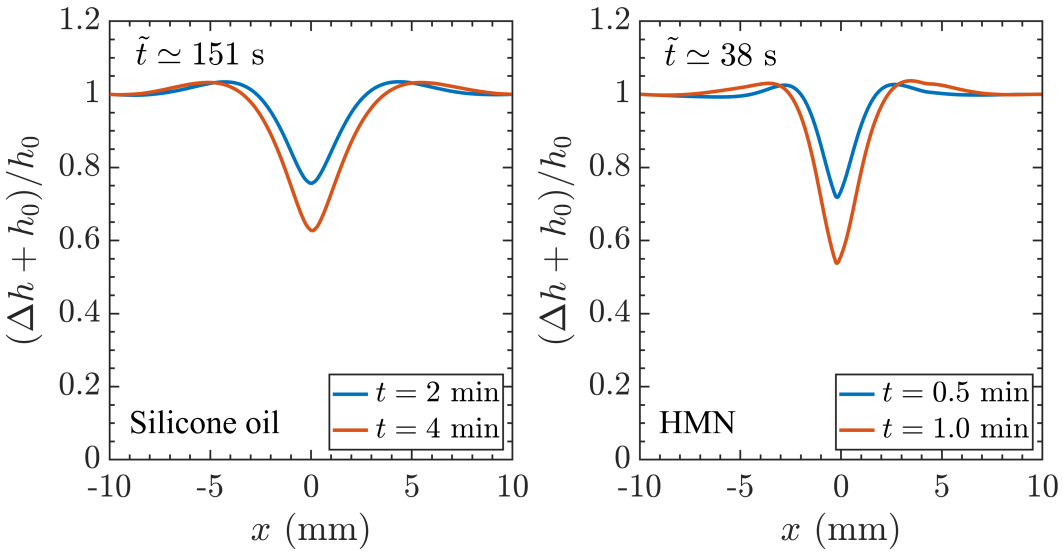

Figure 4.6: Experimental profiles Δh obtained with FS-SS, with an offset to the initial thickness h_0 and normalized for better comparison. Left panel: experiment performed with ABCR 20 cSt oil, with initial thickness $h_0 = 40(4)\,\mu\mathrm{m}$ and dissipated power $P = 0.67(1)\,\mathrm{mW}$ (estimated thermal difference $\tilde{\theta}_{max} = 0.47\,\mathrm{K}$). Right panel: Experiment performed with HMN with $h_0 = 26(2)\,\mu\mathrm{m}$ and $P = 1.01(1)\,\mathrm{mW}$ ($\tilde{\theta}_{max} = 0.7\,\mathrm{K}$).

In figure 4.6 (right panel) we show the short time profiles of an experiment performed with HMN, done with initial thickness $h_0 = 26(2)\,\mu\mathrm{m}$ and $P = 1.01(1)\,\mathrm{mW}$. We compare it with the short-time dynamics of the experiment with ABCR 20 cSt (left panel) that we previously showed in Fig. 3.2 of chapter 3, with $h_0 = 40(4)\,\mu\mathrm{m}$ and $P = 0.67(1)\,\mathrm{mW}$. These profiles were obtained using FS-SS, a technique explained earlier in chapter 2 which is based on the relationship between the refracted images of a speckle pattern situated below the cell due to the deformed liquid/air interface and the gradient of the film. This technique only recovers the thickness variation Δh with respect to the horizontal plane, so that an offset must be added to compare both experiments. To better compare both dynamics, we arbitrarily offset the profiles so that they have their corresponding initial thicknesses at the border of the measured region, and normalize them by h_0. The

approximated thermocapillary time scale is $\tilde{t} = 38\,\mathrm{s}$ for the HMN experiment and $\tilde{t} = 151\,\mathrm{s}$ for the ABCR oil, so that the dynamics for HMN should be around 4 times faster than for silicone oil. Thus, we plot profiles that are approximately at the same normalized times $t/\tilde{t}$.

The overall behaviour is very similar in both experiments. The small differences in the profiles can be attributed to the specific values of the liquids' physical properties and the experimental parameters h_0 and P. Indeed, as noted earlier, the specific values of the density and the surface tension determine the precise contributions of gravity and Laplace pressures, which are the main opposing mechanism to the thermocapillary effect at the beginning, as discussed in Sec. 1.3.1 of chapter 1. Note also that, although we have chosen to normalize the time by the scale corresponding to the pure-thermocapillary regime, it has not been yet reached since the minimum thickness of the profiles is well above $\sim 1\,\mu\mathrm{m}$, which may also contribute to the small differences in the profiles.

Thus, we can say that the initial thermocapillary dynamics is comparable to the one of silicone oil. The only major difference is in the time scale, which is several times faster due to the lower value of the viscosity for the alkanes. From the experimental point of view, this is important since it allows to reach the stationary state within some hours, as will be explained in Sec. 4.2.3.3 below.

4.2.3.2 Intermediate times

At later times, the thermocapillary effect continues thinning the film near the centre. Let us briefly recall some general observations of chapter 3 when considering the evolution of silicone oil films. When the local thickness of silicone oils at the region near the maximum of the thermal field is in the range roughly from 0.1 to 1 µm, the system traverses a regime where all pressure contributions are negligible against the effect of thermocapillarity. This pure-thermocapillary regime is identified by a collapse of profiles when the product $h(t,x) \times t$ is computed, and can be described by a master curve depending solely on the gradient of the thermal field $\partial_x\theta(x)$. When the profiles go under about 0.1 µm, the intermolecular forces become a relevant contribution for the dynamics and the evolution changes. In the case of silicone oil on our glass substrate, the disjoining pressure opposes the thinning of the film. This translates in a dramatic slowing down of the dynamics, and we can observe the apparition of quasi-steady, stable ultra-thin films.

As commented above, the situation is different with the alkane films. These appear to be easily affected by surface inhomogeneities, leading to macroscopic break up of the films. Moreover, following the thinning effect of thermocapillarity, when the effect of intermolecular forces becomes relevant, we shall see a different behaviour than in the case of silicone oil films. In Fig. 4.7 we show the evolution of the thickness profile $h(t,x)$ obtained via 3-colour interferometry (explained in Sec. 2.3.3 of chapter 2) of an experiment with a HMN film of initial thickness $h_0 = 19(1)\,\mu\mathrm{m}$, submitted to a dissipated power $P = 1.18(1)\,\mathrm{mW}$. To better differentiate the dynamics at the micrometre and nanometre scales, we plot the profiles both in linear (left panel) and semilogarithmic plots (right panel).

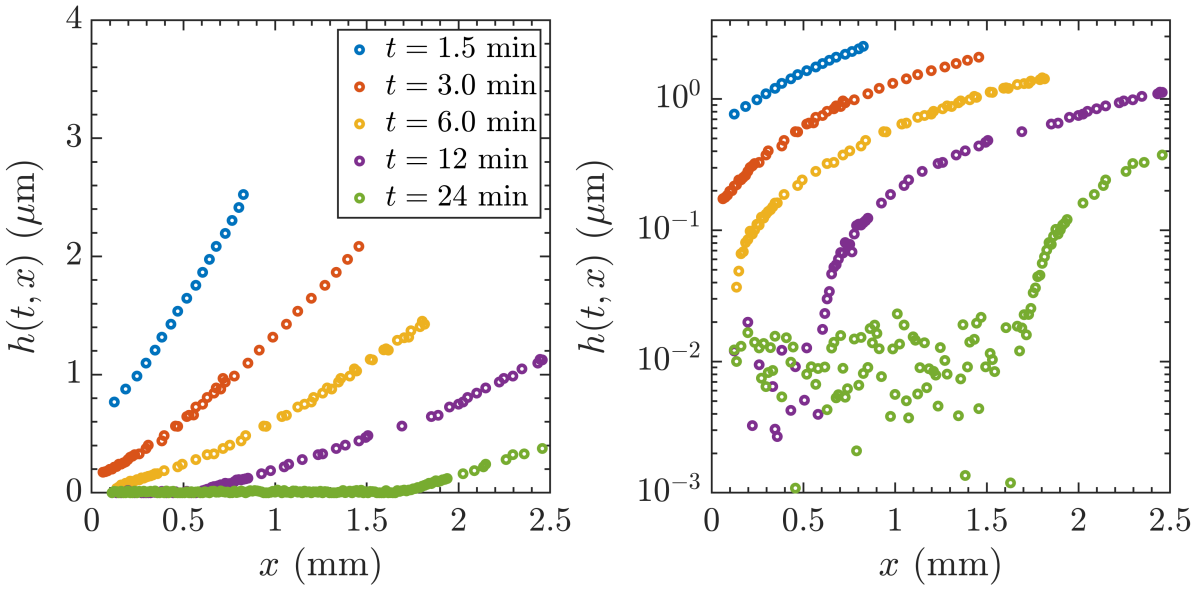

Figure 4.7: Left panel: experimental thickness profiles of HMN in an experiment of initial thickness $h_0 = 19(1)\,\mu$m and dissipated power $P = 1.18(1)\,$mW. Right panel: same profiles in a semilogarithmic plot.

At the micrometre scale (left panel), the evolution follows the thinning dynamics driven by the thermocapillary effect as discussed in chapter 1. The thickness decreases steadily, which diminishes the strength of the gravitational pressure. The slope of the profiles is small and continues decreasing, so that the Laplace pressure is also small at this region. At the same time, at this scale the effect of disjoining pressure is negligible. Therefore, at this thickness range $h(t,x)$ should follow the pure-thermocapillary regime that we introduced in Sec. 1.4 of chapter 1.

Before commenting on this regime, first we turn our attention to the dynamics at the tens of nanometres scale (Fig. 4.7 right panel). Driven by thermocapillarity, the thickness close to the centre reaches the range below 100 nm where intermolecular forces become relevant. At this moment, the minimum thickness at the centre drops down (yellow line at $x \approx 0$), leading to the apparition of a film of constant nanometric thickness. This central region is followed by a "foot" that recedes, as the thermocapillary effect leads the thickness at larger x below 100 nm.

Let us recall that our current noise level is precisely at 20 nm. Hence, we cannot differentiate if a liquid layer with a thickness of some nanometres remains or if, on the contrary, the liquid has completely evacuated the central region. In the case of HMN, which does not present any specific ordering at the solid interface [66], we do not expect any freezing phenomena of liquid at the solid/liquid interface. We will later show in the section dedicated to the stationary state, Sec. 4.2.3.3 an example of an experiment of hexadecane showing the same dynamics. The noisy character of the data at the central region impedes the recovery of the dependence of the derivative of the disjoining pressure $\partial_h \Pi(h)$ as a function of the thickness of the film as we did for silicone oils in chapter 3.

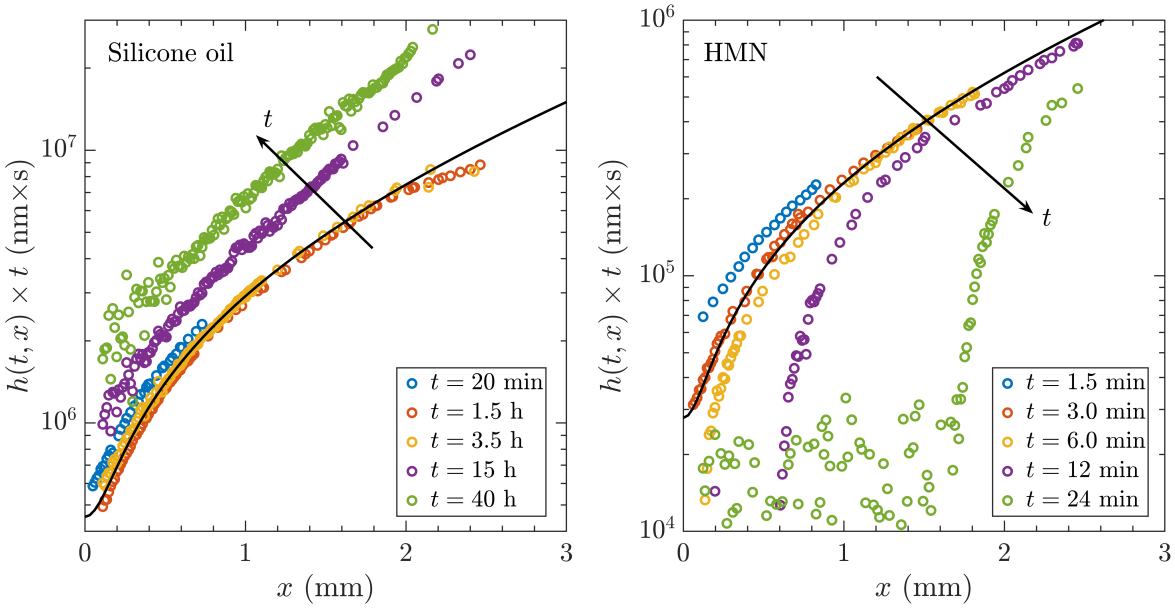

Figure 4.8: Comparison of dynamic behaviour of silicone oil (left panel) and of HMN (left panel) at the onset of disjoining pressure effects. We plot the product $h(t,x) \times t$ obtained from 3-colour interferometry measurements of the thickness profiles of both liquids. Data for the silicone oil is the same as in Fig. 3.4 of chapter 3 ($h_0 = 36(2)\,\mu$m, $P = 0.81(1)$ mm), data for HMN from Fig. 4.7 ($h_0 = 19(1)\,\mu$m, $P = 1.18(1)$ mm). In both cases, the black curve indicates the master curve obtained with the pure-thermocapillary evolution, Eq. (1.22) of chapter 1. The master curve has been computed with the heuristic thermal field $\theta(x) = \theta_{max}[\mathrm{sech}(x/w_0)]^{\delta/w_0}$ (see Sec. 3.3.1.3 of chapter 3). Left panel: $w_0 = 2.46$ mm, $\theta_{max} = 0.38$ K, $\delta = 0.11$ mm. Right panel: $w_0 = 2.2$ mm, $\theta_{max} = 0.5$ K, $\delta = 0.09$ mm.

To illustrate the difference of behaviour between HMN and silicone oil, we compare in Fig. 4.8 an experiment of silicone oil (left panel) (already discussed previously, see Fig. 3.4 of Ch. 3) with the HMN experiment (right panel) of Fig. 4.8. We plot the product $h(t,x) \times t$ since, as we explained in chapter 1, a collapse of the profiles marks the establishment of the pure-thermocapillary regime in which all pressure contributions are negligible against the driving force. For both films, the evolution of the thicknesses at the beginning, when $h > 0.1\,\mu$m (blue and orange curves on both plots), can be described as the film transitioning locally from the initial regime (in which Laplace and gravity pressures are relevant), to the regime in which the thermocapillary effect dominates all other contributions. The black curve on each plot represents the master curve

$$h \times t \simeq \frac{2\eta}{\gamma_\theta} \frac{1}{2\sqrt{|\partial_x \theta|}} \int_0^x \frac{ds}{\sqrt{|\partial_s \theta|}}, \tag{4.2}$$

discussed in Sec. 1.4 of chapter 1, computed with respective physical parameters. As discussed in Sec. 3.3.1.3 of chapter 3, the gradient of the thermal field $\partial_x \theta(x)$ can be obtained experimentally using Eq. (4.2) from experimental profiles, and the thermal field can be fitted with the heuristic expression $\theta(x) = \theta_{max}[\mathrm{sech}(x/w_0)]^{\delta/w_0}$ (the fitting parameters are given in the caption of Fig. 4.8).

Once the thickness reaches 100 nm, the different intermolecular forces have opposite effects. In the case of silicone oil, the disjoining pressure slows down the thinning effect of thermocapillary and the evolution becomes very slow, as discussed previously in chapter 3. Therefore, in a plot of $h(t,x) \times t$ the profiles are above the master curve (4.2), since the thinning stops. This is the effect seen in the right panel of Fig. 4.8 for the silicone oil experiment. On the other hand, we have shown in the previous Fig. 4.7 the height of HMN quickly dropping below 10 nm (our current sensitivity). Therefore, here disjoining pressure acts as a destabilising force that enhances the thinning dynamics of thermocapillarity, and the profiles $h(t,x) \times t$ appear below the master curve.

The deceleration of the dynamics of silicone oil and the acceleration of the HMN dynamics have quite different magnitudes. Let us consider the last curves of each panel of Fig. 4.8. In the case for silicone oil (left panel), the data at $t = 40\,\mathrm{h}$ remains within roughly one decade above of the master curve (say, in the $x < 2\,\mathrm{mm}$), after a time factor of around $\sim 40\,\mathrm{h}/1.5\,\mathrm{h} \simeq 27$ since the pure-thermocapillary regime is attained. On the other hand, the instability of HMN provokes that the same deviation from the master curve (this time from below) is observed within a time factor of $\sim 24\,\mathrm{min}/3\,\mathrm{min} = 8$, around three times smaller than in the case of silicone oil. This simple argument also points in the direction that intermolecular interactions in the system are generating an instability of the film.

In the following section, we follow the foot as it recedes towards the wedge. The liquid is driven towards the wedge and gets absorbed into the bulk liquid, and a stationary state can be found where all the central region has been macroscopically emptied.

4.2.3.3 Stationary state

In chapter 3 we commented the fact that the stationary state was not reached in experiments with silicone oils, due to the slowing down of the dynamics induced by the opposition of disjoining pressure to the thinning effect of thermocapillary. In experiments with alkane films, however, we have seen in the previous section that the disjoining pressure provokes the breaking up of the film and a ultra-thin foot appears, which quickly recedes from the centre. The height profile in the central region is sketched in Fig. 4.9, where we show the main variables used to describe the dynamics of the foot and the wedge, representing their boundaries x_f, x_w and their angles β_f, β_w, respectively. In this section, we will see that this foot disappears at the wedge, and that the latter attains a stationary position after several hours.

We show the spatio-temporal evolution of the interference pattern of a silicone oil experiment and one of hexadecane in Fig. 4.10, both performed with similar dissipated power P. Note that the time range shown for the oil lasts for three times longer than that of hexadecane. The approximate thermocapillary time scale of the oil experiment is $\tilde{t} \simeq 104\,\mathrm{s}$, for hexadecane $\tilde{t} \simeq 39\,\mathrm{s}$. That is, we expect that the experiment with hexadecane should have a typical dynamics two to three times faster than the evolution of the silicone oil film, hence the choice of the different ranges. The size of the central area where fringes can be seen grows roughly satisfying this relative time scale. The steady state is reached in the hexadecane after around 3 h, while the evolution of the silicone oil continues during roughly two days of experiment (not shown).

Finding a proper region for averaging the intensities is complicated by the fact that

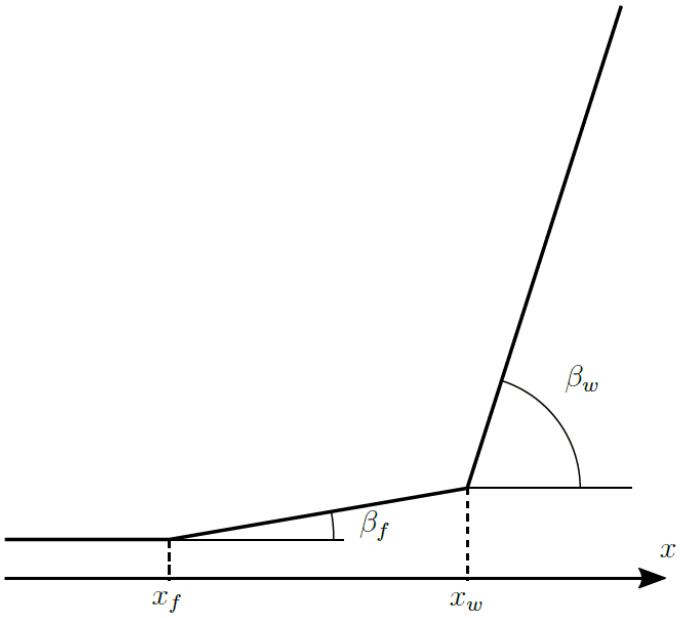

Figure 4.9: Sketch of variables used for describing the position and angle of the foot (x_f, β_f) and the wedge (x_w, β_w) arising from the break up of the alkane films.

inhomogeneities in the surface lead to a non-flat boundary of the receding ultra-thin film. This results in inhomogeneities of the interference profile as in Fig. 4.10, where the fringes are distorted at some regions, e.g. between $x = 2.2$ and $x = 3.2\,\text{mm}$. In this experiment, some small droplets (marked with arrows in Fig. 4.10) of alkanes remained for some time covering surface impurities before disappearing. We have seen in other experiments, however, droplets of comparable sizes lasting much longer. We stress the fact that these droplets appear at surface inhomogeneities, they are few and randomly distributed and do not arise from spinodal decomposition. We have found that in some slides the breaking up of the film followed a circular path on the surface that we link to a step of the photolitography process for the deposition of the circuit. During this step, the side of the slide that will support the liquid is pressed against a surface with circular grooves which may have marked the surface. These surface defects are difficult to mitigate due to technical constraints, however they should be corrected in future experiments. Nevertheless, the interference patterns can still be analysed and insights can be gained about the dynamics of the alkane films, in particular the receding of its foot.

Another common occurrence in the experiments with the alkanes is the appearance of fringes which in the spatio-temporal plot have a "V" shape near the wedge, as in the region marked with a dotted rectangle in Fig. 4.10. This pattern represents a non-monotonous thickness, that is, the apparition of a small "ripple" at the transition region between the central ultra-thin film and the wedge. This effect has been encountered in similar thin film systems where thermocapillary drives the fluid against gravity on an inclined plane [17, 18].

In figure 4.10 the formation of the receding macroscopic wedge, identified with the boundary for the central region where fringes can be seen, is similar for both liquids. The homogeneous-intensity region for large x corresponds to the "bulk" thin film. This is

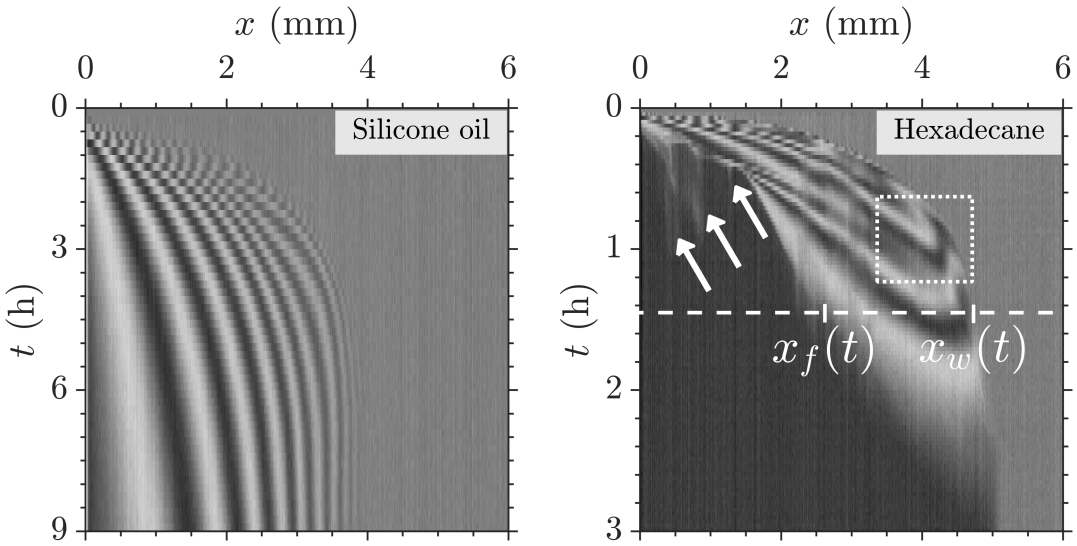

Figure 4.10: Comparison of spatio-temporal evolution of the interference pattern for an experiment of ABCR 20 cSt oil (left panel) and an experiment with hexadecane (right panel). Experimental parameters: silicone oil $h_0 = 36(2)\,\mu\text{m}$, $P = 0.81(1)\,\text{mW}$, $\tilde{t} \simeq 104\,\text{s}$; hexadecane $h_0 = 13.0(2)\,\mu\text{m}$, $P = 0.95(9)\,\text{mW}$, $\tilde{t} \simeq 39\,\text{s}$. Note that the thermocapillary time scale of hexadecane is roughly 3 times higher than that of the oil, hence the choice of different temporal range in the plots. Arrows point to the formation of tiny droplets (radius $\sim 0.1\,\text{mm}$) due to the presence of particles on the surface, which disappear from the images after some time. $x_f(t)$ and $x_w(t)$ denote in the main text the position of the foot and the wedge, respectively, see Fig. 4.9. The square shows a region in which the thickness profile is non-monotonous, see main text for details.

expected since it depends on the generic interplay of the thermocapillary effect with the Laplace and gravity pressures, and both experiments are done under the same heating geometry. The short time dynamics was shown above in Sec. 4.2.3.1.

However, the difference in behaviour within the ultra-thin film can be clearly seen from the interference fringes. For silicone oils, multiple interference fringes can be continuously observed where the ultra-thin film is establishing, and the thickness grows steadily right up to the macroscopic wedge, where the larger slope makes the space between fringes too small to distinguish them. This does not necessarily mean that the angle is very large, since assuming that interference extrema 1 pixel apart could be differentiated, the maximum slope resolved would only be about 0.4°. On the other hand, the instability of the alkane film generates a collapse of the ultra-thin film once the contribution of disjoining pressure is not negligible. In experiments with alkanes we never see as many fringes as with silicone oil, and the transition between the ultra thin film and the wedge is more abrupt.

In the interference profiles, the fringes move away from the centre faster that the wedge, and after some time they disappear into the wedge. This is shown in Fig. 4.11, where we plot the evolution of the position of the foot $x_f(t)$ and the wedge $x_w(t)$, as defined in Fig. 4.10. Once the foot forms, the intermolecular interactions force it to quickly recede, leaving behind a region of constant intensity in the spatio-temporal plot.

The central region in this case consists either in a constant-thickness ultra-thin film on the scale of nanometres, or else on the surface being completely dewetted. Our current experimental resolution does not allow us to differentiate these two possible scenarios, as we have seen above in Fig. 4.7 in an experiment with HMN. This absorption of fringes at the wedge is explored next, since their disappearance marks the establishment of the steady-state regime.

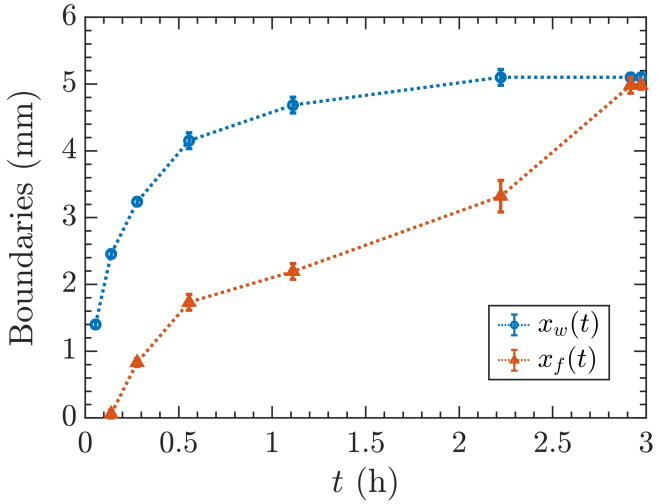

Figure 4.11: Position of the wedge, $x_w(t)$, and of the ultra-thin film boundary, $x_f(t)$, obtained from the spatio-temporal evolution of the interference panel shown in the right panel of Fig. 4.10.

In Fig. 4.12 we show the long term evolution of experimental profiles of an experiment with hexadecane with initial thickness $h_0 = 13.0(2)\,\mu\text{m}$ and dissipated power $P = 0.95(9)\,\text{mW}$. As in the case of HMN commented earlier in Fig. 4.7, the alkane film is unstable: when the thickness near the centre is thinned down to below 100 nm, it quickly collapses to a constant thickness (around our current experimental precision). A foot forms that recedes from the centre, with a different time scale than the macroscopic wedge as shown before in Fig. 4.11. Note that although the foot shown in Fig. 4.12 is further from the central line than the foot of Fig. 4.7 for the HMN experiment, its shape is similar, which means that then interplay between thermocapillarity and disjoining pressure has not changed greatly despite the fact that the thermal field is becoming weaker with the distance.

The foot approaches the macroscopic wedge, the latter's position marked by the lines seen on the right of the plots. The position of the macroscopic wedge can be approximated from the interferometric evolution, see Fig. 4.10. We assume for illustration purposes that the wedge has a slope of 4°, which is the typical contact angle we have measured for the alkanes in our substrates, see Sec. 4.2.2.3. The section of the foot under $\sim$ 100 nm collapses under the action of disjoining pressure, generating the receding displacement. For sufficiently long times, in this case around 3 h, the foot gets absorbed into the wedge.

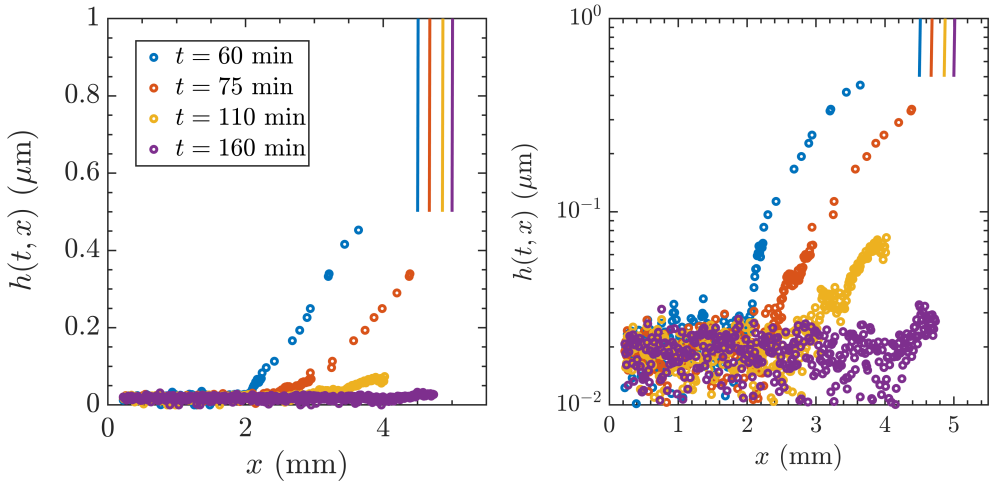

Figure 4.12: Left panel: long-time experimental thickness profiles of hexadecane in an experiment of $h_0 = 13.0(2)\,\mu\text{m}$ and $P = 0.95(9)\,\text{mW}$. Right panel: same profiles in a semilogarithmic plot. The almost-vertical lines at the right of both plots indicate an estimation of the position of the macroscopic wedge, obtained by the change in image intensity from where the fringes are seen to the mean homogeneous intensity outside the central region, as can be seen in Fig. 4.10. These lines have a slope of 4° (note the difference in scales between the horizontal and vertical axes), which is the typical angle that we have found in preliminary measurements of the contact angle, see Sec. 4.2.2.3 above (but also Fig. 4.21 below).

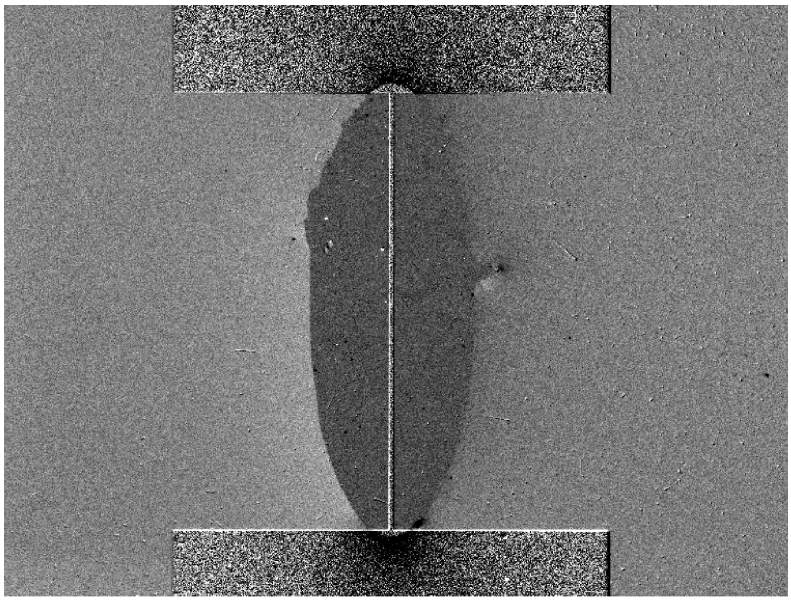

Figure 4.13: Stationary state of a film of HMN with initial thickness $h_0 = 24(1)\,\mu\text{m}$ and dissipated power $P = 46(9)\,\text{mW}$. The dark oval-shaped region in the centre is macroscopically "empty". In Sec. 4.3.2 it will be shown that it is stable even if the thermal field is removed. The width of the square paddles is 10 mm.

The wedge reaches its stationary state position after some hours. This state is not due to the particular distribution of surface inhomogeneities or dust particles of the surface. Instead, as can be seen from the shape of the central "empty" region (darker central area) of Fig. 4.13, its shape is related to the thermal field. This shape compares well with the characteristics of the thermal field, see Fig. 2.3 on chapter 2, that can be described with a minimal model of thermal loss as shown in appendix C. We have seen that increasing the dissipated power once the stationary state has been reached makes the wedge recede to the a new steady-state position leaving again the foot behind, before the latter recedes again. The shape of the wedge boundary after this reconfiguration is still a slightly bigger version of the dark region at the centre of Fig. 4.13.

4.2.4 Interpretation

We have seen in the previous examples of the dynamics of the thin alkane films that on this system they are unstable, meaning that large patches can become macroscopically "empty" of liquid. This process can occur due to the presence of surface defects or impurities, or it can be provoked as a consequence of the thinning dynamics of the thermocapillary effect. In the present section, we discuss some plausible explanations for these results.

4.2.4.1 Numerical results on attractive intermolecular forces

To gain some qualitative understanding of the resulting dynamics if the intermolecular forces were attractive, we make use of the numerical integration of the thin film equation that we explained in chapter 1.

To do this, we set the disjoining pressure to be of the usually assumed form $\Pi(h) = -A_H/6\pi h^3$, previously used in the numerical integration of chapter 1. We perform a series of integrations using nominal values of hexadecane as physical parameters, but changing the sign of the Hamaker constant A_H. We fix the typical order of magnitude $|A_H| = 1 \times 10^{-19}\,\mathrm{J}$ and consider the change in dynamics with both signs, plus a case without disjoining pressure ($A_H = 0$). The case $A_H > 0$ ($A_H < 0$) represents attractive (repulsive) intermolecular interactions. The specific value of A_H is not a concern here, since we would like only to observe the qualitative differences that may be encountered.

In Fig. 4.14 we show profiles obtained from the numerical integration of the thin film equation, computed with physical parameters of hexadecane (Sec. 4.2.1) with initial thickness $h_0 = 10\,\mu\mathrm{m}$, a maximum thermal field of $\theta_{max} = 1\,\mathrm{K}$ and a thermal decay length $w_0 = 2\,\mathrm{mm}$. As explained above, the Hamaker constant is set to be $A_H = 1 \times 10^{-19}\,\mathrm{J}$ (attractive intermolecular interactions). The dynamics for the first minutes proceeds similarly as the case of silicone oil. However, one the height profile at the centre reaches a thickness below 100 nm (see inset), we find that an instability develops. Unfortunately, the thickness tombs towards zero at $x = 0$ and our numerical scheme cannot integrate further.

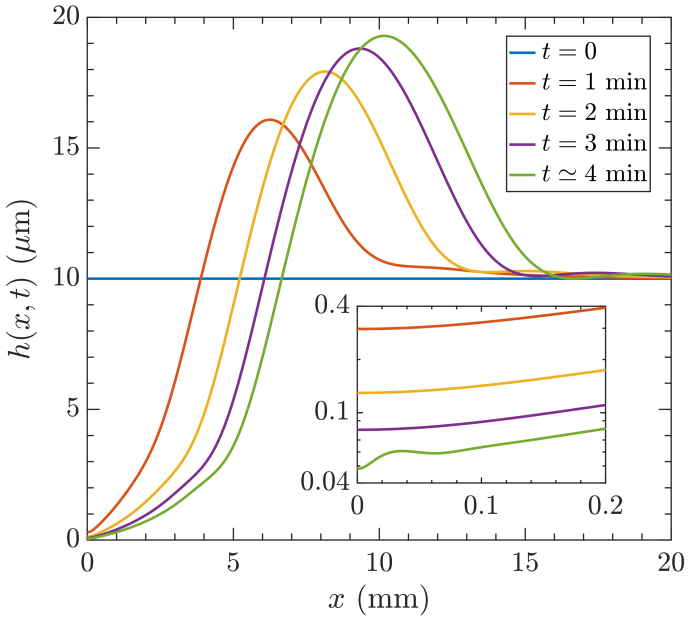

Figure 4.14: Thickness profiles of the numerical integration of the thin film equation as discussed in chapter 1. The inset shows a zoom at the central region, the profile at $t \simeq 4\,\text{min}$ when the thickness is below $\sim 70\,\text{nm}$ shows an instability. The numerical method that we use, explained in Sec. 2.5 of chapter 2, cannot integrate further. Physical parameters for hexadecane, $h_0 = 10\,\mu\text{m}$, $\theta_{max} = 1\,\text{K}$, $A_H = +1 \times 10^{-19}\,\text{J}$.

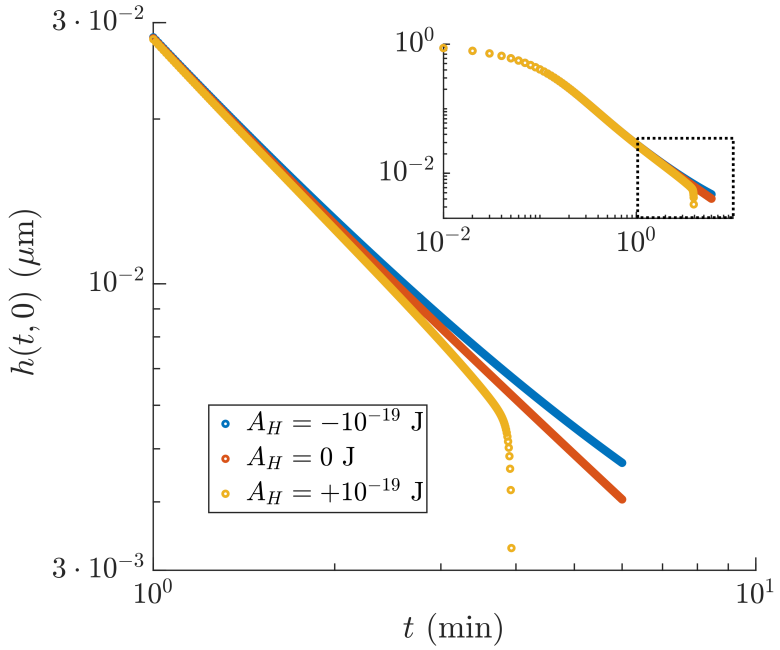

Figure 4.15: Comparison of the temporal evolution of the thickness at the centre, $h(t,0)$, where the thermal difference is maximum, obtained from the numerical integration of the thin film equation with same parameters except for the Hamaker constant. The inset shows the full integration time, the rectangle marks the region plotted in the main panel.

In Fig. 4.15 we show the resulting numerical evolution at the centre, $h(t, 0)$, for the integrations performed with $A_H = -1 \times 10^{-19}$ J, $A_H = 0$, and $A_H = +1 \times 10^{-19}$ J. The rest of quantities are maintained constant. At the beginning the thinning dynamics is the same regardless of the disjoining pressure, since the only relevant contribution comes from the Laplace pressure (recall Sec. 1.3.1 of chapter 1). The difference is seen when the thickness reaches a value of about 100 nm. When the Hamaker constant A_H is negative (repulsive intermolecular interactions), the thinning becomes slower with time and will eventually reach some finite steady-state value. This is analogous to the process we have seen with the silicone oils. However, when A_H is positive (attractive intermolecular interactions) it provokes the quick drop of thickness at the centre, which will break up the film into two separated regions (this last state is never reached in our numerical integration).

We recognize this qualitative difference as the one occurring when comparing experiments with silicone oil and the alkane films on the same glass substrates, as discussed in Fig. 4.8. The time scale until the break up, of the order of minutes, compares well with the experimental break up times, see Fig. 4.7 in Sec. 4.2.3.2 above. Furthermore, we note that the thickness at which both behaviours diverge is on the order found in experiments, around 100 nm. Therefore, these numerical results points to the presence of attractive intermolecular interactions in our system.

4.2.4.2 Possible explanation of the dynamics

We have seen in the previous section that an attractive intermolecular interaction shows qualitatively similar dynamics to the one measured in experiments. However, glass is a high energy surface that should in general be wetted by all liquids, and instead we see the formation of a clearly defined contact angle characteristic of partial-wetting. According to some studies, an hexadecane drop should present total wetting on glass at room temperature [74] (however, the dynamics shown lasts less than a minute and the long-term state is not discussed, which may be important for determining the equilibrium state [77]). Moreover, an argument for some type of surface crystalization cannot be sustained since HMN behaves exactly as hexadecane and the working temperature is far from the melting temperature of HMN, $T_m \approx -4\,^{\circ}\mathrm{C}$ [70].

Therefore, there remains two possible explanations of the behaviour of these alkanes on our glass substrates. The first one is that indeed both hexadecane and HMN would in fact undergo complete wetting, but surface inhomogeneities are the cause of the behaviour we observe. As noted earlier, the surface cannot be cleaned with effective common procedures, e.g. using a pirahna solution because they would destroy the electric contacts. However, the effect of surface inhomogeneities cannot explain the marked difference between the alkanes films and the films of silicone oils which do wet completely the surface. Moreover, the stationary state is clearly linked to the thermal field imposed.

The second possibility is that our glass/alkane/air system presents pseudo-partial wetting. As explained earlier in Sec. 4.2.2.1, this would mean that the spreading parameter of the alkanes is positive but the interaction potential is not monotonic. If this were the case, it would be possible for a macroscopic contact line to be in equilibrium with a nanometric liquid layer. This would correspond to the situation we observe, not only for the thermocapillary-driven dynamics, but also for the stationary state not evolving if the

thermal field is suddenly removed, as will be explained in Sec. 4.3.2.

4.2.5 Conclusion

The break up of thin films of hexadecane and HMN on glass substrates under the influence of the thermocapillary effect has been studied. We have shown how the effect of intermolecular forces for these liquids is seen when the thickness is below approximately 100 nm. Contrary to the establishment of a stable ultra-thin film as in the case of the silicone oils discussed in chapter 3, the intermolecular forces of both alkanes promote a similar destabilization of the film, and the thickness drops down to the resolution limit of our interferometric setup at 20 nm. This mechanism produces the appearance of a nanometric receding foot that moves faster than the wedge at the micrometre scale, so that after some time it gets absorbed by the bulk liquid.

A qualitative comparison with numerical results shows that a negative disjoining pressure would describe well the threshold thickness and the rupture time scale. However, the glass is a high energy surface that should be wetted by the alkanes. Therefore, it is possibly the case that these alkanes have a pseudo-partial wetting behaviour on our substrates. This would explain the characteristics of the stationary state, which shows a macroscopic wedge and a central area which is void of liquid except perhaps for a film of constant thickness below 20 nm. The boundary between the two is determined by the characteristics of the thermal field.

More details about the stationary state will be given in the following section, in which we briefly discuss some relaxation experiments in which we remove the thermal field after the (quasi-)steady state of the thermocapillary evolution has been reached, both for silicone oils and the alkane films.

4.3 Relaxation dynamics

Until now, we have focused on the driven dynamics of the thin film by imposing a gradient in surface tension on the liquid/air interface. The dynamics promotes the apparition of a ultra-thin film in the central region, the dynamics at long times controlled by the interplay between the thermocapillary effect and the intermolecular interactions of the system. In the long run, a non-equilibrium (quasi-)steady state appears which, given a liquid, could be possible to design by changing the gradient of the thermal field. This represents an opportunity to study the relaxation flows of more complex configurations than the prototypical wetting of a spreading droplet.

In this section, we discuss preliminary experiments in the the dynamics of the films when, after a certain time, the thermal field is removed and the film evolves towards some equilibrium configuration. The film can either fill again the central region or adopt an equilibrium configuration with a wedge and a definite (macroscopic) contact line, depending on the equilibrium of surface energies as explained in Sec. 4.2.2.1. As we will shortly see, the first behaviour is seen in silicone oils and the second one on alkane films.

In our experiments of this relaxation dynamics, we have seen that if a displacement of the wedge occurs it is very asymmetric, regardless of the type of liquid. This can be explained by the presence of dust deposited on the surface, which disturbs the incoming front. Since this can happen anywhere, it is generally the case that the flow is not in the

direction normal to the heating line (the direction we use as x-axis in our discussion). Therefore, finding an appropriate region where we can analyse the interference fringes following the method explained in chapter 2 is not always possible, and reproducibility remains as a problem to be solved by finding a better way to protect the surface of major defects. Nevertheless, the relaxation dynamics always shows similar features, and we can obtain the typical dynamical scales involved. As we shall see, we can call this evolution "relaxation" since its typical time scale is much larger than the couple of minutes (at most) that the thermal field takes to cool down (see Fig. 2.4 of chapter 2).

We discuss first experiments with silicone oil, differentiating the dynamics of the incoming wedge from the ultra-thin film, which appears to be stationary. We explain this absence of evolution by making use of the reduced thin film equation when only disjoining pressure is considered, and noticing the effect of the particular shape of the height profiles at the quasi-stationary state, which grow exponentially due to the shape of the thermal field.

In films of alkanes, in which the stationary state of the thermocapillary evolution is reached, the situation when the thermal field is removed is different. The wedge remains stationary, and the central region is not refilled. We show measurements of the evolution of the wedge's angle before and after the thermal field is removed, showing that it remains roughly constant. Its value will be shown to be similar to the contact angle of the spreading drops we measured above in Sec. 4.2.2.3.

4.3.1 Silicone oils

4.3.1.1 Experimental observation

A relaxation experiment performed with silicone oil consists on removing the thermal field once a quasi-steady state has been reached, since we have not achieved to observe the establishment of the stationary state in the range of experimental parameters investigated.

When the imposed thermal field is removed, the bulk liquid at the borders advances towards the ultra-thin film region. The wedge gets steeper, which compresses the interference fringes until they cannot be resolved (as commented above in Sec. 4.2.3.3, the maximum slope resolved with interferometry is only about 0.4° at most). In independent measurements with FS-SS, we have observed angles up to 4°, depending on the experimental parameters. From the experiment images, we saw that after 5 h the central region was completely refilled. We have seen in different experiments that the wedge advances generally with a speed on the order of 2 to 4 mm/h. To obtain a precise value is difficult as a consequence of the dust deposited on the surface as commented above, which can make the incoming dynamics very irregular.

We focus here in the dynamics of the ultra-thin film. In Fig. 4.16 we show an example of the evolution of a thin oil film (ABCR 10 cSt oil) from the moment when the thermal field is removed, after having been driven for 4 h by the thermocapillary effect. Note that the time t is given relative to the moment at which the thermal field is removed.

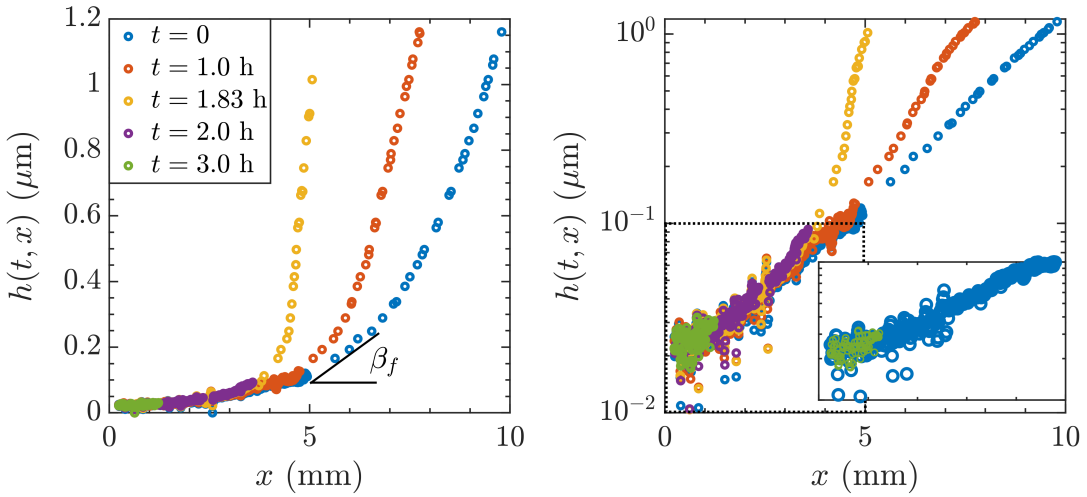

Figure 4.16: Rewetting experiment with ABCR 10 cSt oil, after the thermocapillary dynamics during 4 h. Initial thickness $h_0 = 35(1)$ µm. Dissipated power (before removing the thermal field) $P = 7.6(2)$ mW. The time t is given relative to the removal of the thermal field. The right panel shows the same data as the left one, with logarithmic y-axis. The meaning of the angle β_{utf} is discussed in the main text. The inset on the right panel shows a zoom of the marked dotted rectangle for the first ($t = 0$, blue) and last ($t = 3.0$ h, green) profiles. Blue data points have been enlarged and green data points have been reduced (with respect to the main plot) for better comparison.

It is interesting to note that the thickness of the ultra-thin film at the central region remains constant (within the experimental precision) until the wedge advances to fill the central region. That is, during this rewetting dynamics the ultra-thin film is not filled with the bulk liquid even after several hours, which would create a steady increase in its thickness. For the last two curves (purple, $t = 2$ h and green, $t = 3$ h) the wedge is too steep to recover the thickness from the interference profiles.

4.3.1.2 Interpretation

To explain why we do not observe any dynamics of the ultra-thin film, we analyse the structure of the reduced thin film equation when only disjoining pressure acts on the film, taking as initial condition the first profile of Fig. 4.16.

Let us consider the reduced thin film equation when only the disjoining pressure term is present,

$$\partial_t h + \frac{1}{3\eta}\partial_x \left\{ h^3 \partial_x \Pi(h) \right\} = 0. \tag{4.3}$$

Writing the disjoining pressure as

$$\Pi(h) = \frac{A}{h^\nu}, \tag{4.4}$$

where $\nu = \alpha - 1$ in the notation of chapter 3 for the derivative of $\Pi(h)$ with respect to the thickness, we obtain

$$\partial_t h - \frac{\nu A}{3\eta}\partial_x \left\{ h^{2-\nu} \partial_x h \right\} = 0. \tag{4.5}$$

The answer to why the ultra-thin film remains static lies on the shape of the profiles when the thermal field is removed. Looking at the first curve of the right panel of Fig. 4.16, it is clear that the thickness grows roughly exponentially, as shown in Fig. 4.17. It can be modelled with $h(0,x) \simeq h_i \exp(x/w_0)$ where $h_i \simeq 11.5\,\text{nm}$ and w_0 is the thermal decay length $w_0 \simeq 2.1\,\text{mm}$.

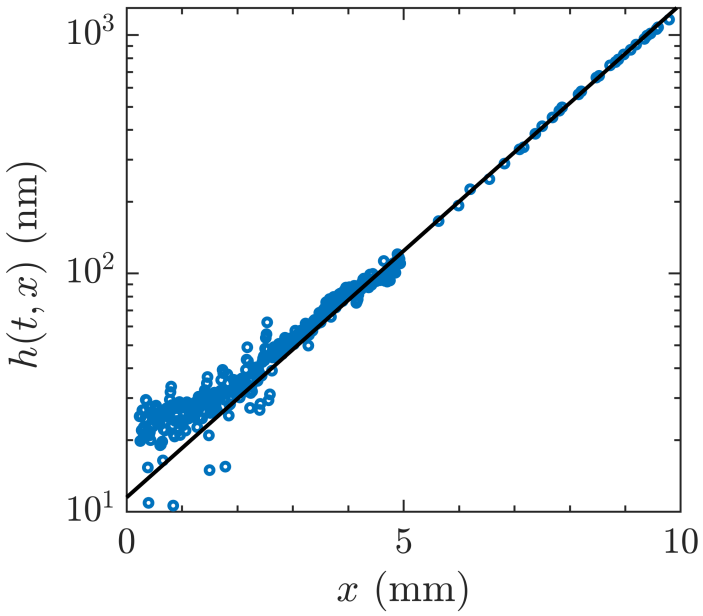

Figure 4.17: Approximately exponential shape $h = h_i \exp(x/w0)$ of the first profile ($t = 0$) of Fig. 4.16, with $h_i = 11.5\,\text{nm}$ and $w_0 = 2.1\,\text{mm}$ (black curve).

Substituting in Eq. (4.5), we find that the profile's growth behaves as

$$\partial_t h\big|_{t=0} = \frac{\nu A}{3\eta w_0} \partial_x \left\{ [h(0,x)]^{3-\nu} \right\}. \tag{4.6}$$

As a consequence, because of the exponential shape of the thermal field imposing the a corresponding exponential growth on the thickness, a film with $\Pi(h) \propto h^{-3}$ would be stationary even if the thermal field is removed.

From the results of chapter 3, we have seen that in our system we have $1 < \nu < 2$. Therefore

$$\partial_t h\big|_{t=0} = \frac{A}{3\eta w_0^2} \nu(3-\nu)[h(0,x)]^{3-\nu}, \tag{4.7}$$

where we have used again the exponential dependence of the thickness profile when the thermal field is removed. Taking $\nu \sim 1.5$ and the value $A \sim 1 \times 10^{-8}\,\text{Pa}\,\text{m}^{1.5}$ from the results of chapter 3, we obtain

$$\partial_t h\big|_{t=0} \sim (1\,\text{nm/h}) \exp\left(1.5 x/w_0\right). \tag{4.8}$$

Therefore, the evolution of the exponential profile will be very slow, even for x comparable to the original thermal length w_0. This explains why the ultra-thin film, which evolves only under the influence of disjoining pressure, appears to be static with the current experimental resolution.

For the thicker part of the film, the contribution of Laplace and gravity pressures pushes the liquid to recover a homogeneous profile as the initial condition of the experiment. Because of the presence of the ultra-thin film the liquid can flow towards the centre, which in the profiles translates in a displacement of the wedge, the only obstacle being the surface inhomogeneities. However, as we shall see in the following section, the presence of the ultra-thin film is essential for the wedge to advance towards the centre.

This dynamics has ingredients similar to those of a spreading, non-volatile drop over a solid substrate in the total wetting regime. In a complete wetting scenario a small drop deposited on a surface does not spread directly on the bare substrate, but its macroscopic contact line is preceded by a nanometric precursor film generated by the intermolecular forces [1]. In our case, the ultra-thin film could be seen as an analog of the precursor film that precedes the apparent contact line (the wedge).

The relaxation of the droplet due to capillary forces makes the apparent contact angle diminish with time as a consequence of its finite volume, which is described by Tanner's law $\beta(t) \propto t^{-3/10}$ [78]. To compare the evolution of the angle of relaxation, let us summarize here the derivation of Tanner's law, following Ref. [30]. A sketch of the system considered is shown in Fig. 4.18, where V represents the velocity of the apparent contact line. The driving mechanism of the drop on top of a existing film is the capillarity force (per unit length)

$$F = \gamma_0 \left(1 - \cos\beta\right) \tag{4.9}$$

which for small angles behaves as $F \simeq \gamma_0 \beta^2/2$.

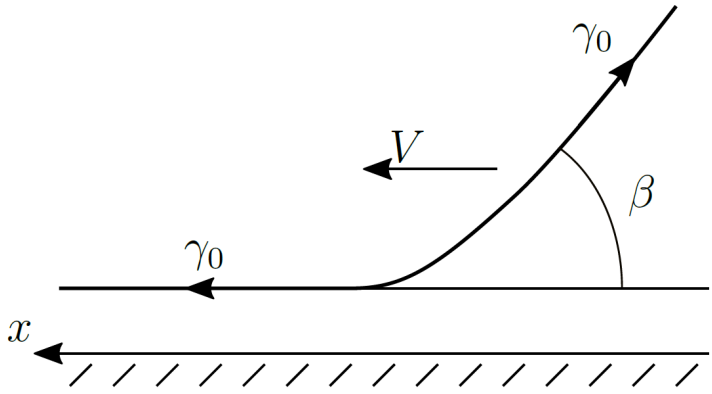

Figure 4.18: Sketch of a drop spreading in the presence of a wetting film.

The advancing of the apparent contact line is countered by the viscous dissipation. The dissipated viscous power at velocity V scales as

$$FV \propto \frac{\eta \ell}{\beta} V^2 \tag{4.10}$$

where the dimensionless, slow varying factor ℓ is defined as $\ell = \log\left(L/a\right)$, computed from a characteristic macroscopic length L (typically the size of the drop) and a cut-off molecular length a. Taking the expression (4.9) for the capillary force, using the small angle approximation $F \simeq \gamma_0 \beta^2/2$, the velocity of the contact angle V is related to the contact angle β when capillary forces are at the origin of the displacement as

$$V \propto \frac{\gamma_0}{\eta \ell} \beta^3. \tag{4.11}$$

From this equation, if conservation of the volume of the drop is assumed, the evolution of the angle $\beta(t)$ can be shown to behave with time as $\beta(t) \propto t^{-3/10}$. Thus, the slope of the apparent contact line diminishes with time. Since we work with films, the same condition cannot be applied to obtain an expression for $\beta(t)$. However, if capillarity is the driving force of the relaxation, we should still observe $V \propto \beta^3$.

During our discussion of previous chapters, we have argued that gravity plays a more important role than the Laplace pressure in the overall dynamics of the films. Following a similar argument as the above one, let us find which should be the scaling of the velocity with the angle of the wedge when driven by gravity instead of capillary forces. Relevant parameters are sketched in Fig. 4.19. We consider a small displacement Δx of the wedge, and compute the variation of potential energy produced by the displacement of the volume (per unit length) $\Delta h L$ from the top of the film to the wedge, a region that we approximate as a parallelepiped of volume AB×BC. Here $\Delta h \ll h_0$ and L is a macroscopic length. We assume that the curvature between the wedge and the film is small, which in principle should be the case as we saw in Sec. 1.3 of chapter 1.

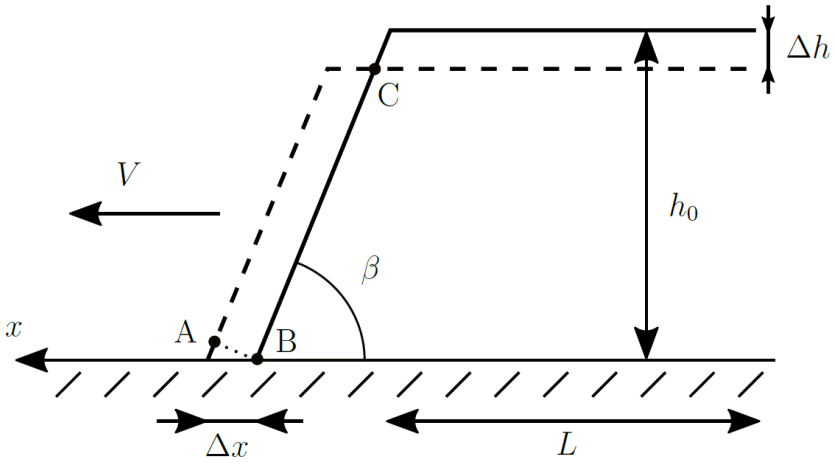

Figure 4.19: Sketch of the moving wedge under the action of gravity. The boundary of the initial profile (solid line) moves a distance Δx to the left (dashed line) in a small time difference Δt.

Initially, the potential energy of this volume upper (per unit length) is $E_p^0 = \rho g h_0 \Delta h L$. When it has moved to the wedge,

$$E_p = \int_0^h \rho g z dz \Delta x \simeq \frac{1}{2}\rho g h_0^2 \Delta x. \tag{4.12}$$

Now, we assume that the volume transferred is conserved, taking the identity $\Delta h L =$ AB×BC. But it can be seen that AB $= \Delta x \sin\beta$ and BC $\simeq h_0/\sin\beta$, hence $\Delta h L = \Delta x h_0$, which is independent of the angle. Therefore the variation of potential energy (per unit length) is

$$\Delta E = \frac{1}{2}\rho g h_0^2 \Delta x - \rho g h_0^2 \Delta x = -\frac{1}{2}\rho g h_0^2 \Delta x. \tag{4.13}$$

Now, the dissipated viscous power can be approximated as $\Delta E/\Delta t$. Since $\Delta x = V \Delta t$,

$$\frac{\Delta E}{\Delta t} = -\frac{1}{2}\rho g h_0^2 V. \tag{4.14}$$

Equating with the definition 4.10, we find the scaling

$$V \propto \frac{\rho g h_0^2}{\eta \ell} \beta. \tag{4.15}$$

Therefore, when gravity is the driving force the velocity should depend linearly with the angle.

From the experimental profiles obtained with 3-colour interferometry, as shown in Fig. 4.16, we can obtain a measurement of the angle β_{utf} at the region between the central ultra-thin film and the wedge, as defined in Fig. 4.19. We measure the slope β_{utf} of the ultra-thin film at $h \simeq 0.1\,\mu\text{m}$. This thickness is chosen because, as can be seen in the right panel of Fig. 4.16, the wedge slowly advances at this scale but the central ultra-thin film remains static below this thickness. Hence β_{utf} can be seen as a advancing analogous of the receding foot angle β_f discussed in the experiments with alkanes, Sec. 4.2.3.

This small displacement of the wedge at this thickness can be used to obtain the velocity V of the incoming wedge. We can thus measure the scaling of V with the angle β_{utf}, and compare it with the predictions of the previous models to check whether this relaxation dynamics is controlled by capillary forces ($V \propto \beta^3$) or by gravity ($V \propto \beta$).

To measure the velocity V for the experiment showed above in Fig. 4.16, we measure the evolution of the position of the ultra-thin film $x_{utf}(t)$ at $h = 0.1\,\mu\text{m}$ where the angle $\beta_{utf}(t)$ is measured as explained above. The evolution of these quantities is shown, respectively, in the left and right panels of Fig. 4.20. We find that $x_{utf}(t)$ (with respect to its position at $t = 0$) appears to grow linearly with time, giving a constant velocity $V \approx 1.7 \times 10^{-7}\,\text{m}\,\text{s}^{-1}$. However, the data range that we could cover is very small, and the angle β_{utf} barely changes a factor 2, so that these experiment should be checked against future experiments. Nevertheless, although this experiment is not conclusive, a linear scaling $V \propto \beta_{utf}$ appears to be more plausible than $V \propto \beta_{utf}^3$, meaning that gravity should be the main driving force of this relaxation.

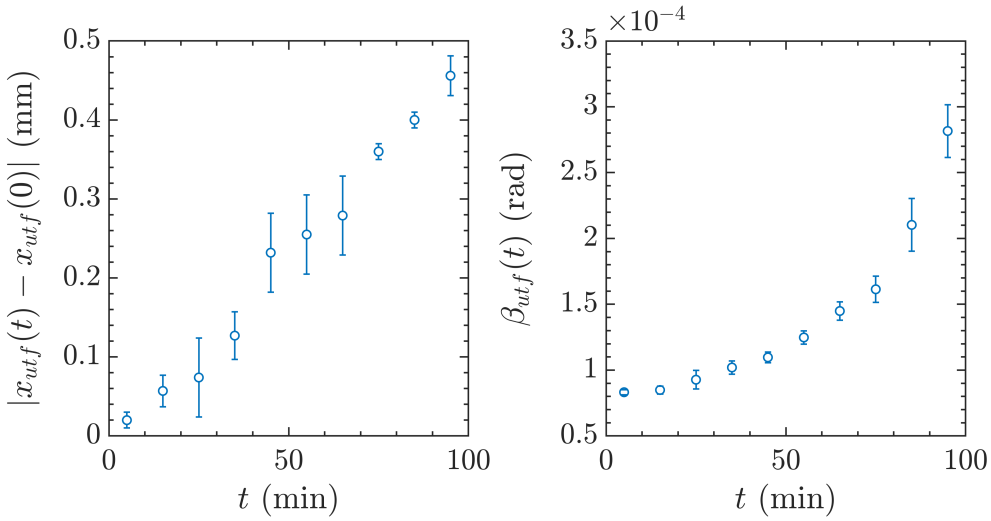

Figure 4.20: Left panel: evolution of the position of the ultra-thin film $x_{utf}(t)$ at $h = 0.1\,\mu\text{m}$, with respect to its initial position when the relaxation experiment begins, $x_{utf}(0) \simeq 4.8\,\text{mm}$, for the experiment shown in Fig. 4.16. Right panel: corresponding evolution of the angle $\beta_{utf}(t)$ of the ultra-thin film at $h \simeq 0.1\,\mu\text{m}$.

A pure capillary forcing can be moreover discarded by considering the Cox-Voinov law [79, 80] giving the exact dependence between V and β in this scenario,

$$V = \frac{\gamma_0}{9\eta\ell}\beta^3 \tag{4.16}$$

and taking the experimental parameters to estimate the velocity we should expect in the capillary case. Taking the physical values of the oil $\gamma_0 \simeq 2\times10^{-2}\,\mathrm{N\,m^{-1}}$, $\eta \simeq 1\times10^{-2}\,\mathrm{Pa\,s}$, together with the approximation $\ell \approx 16$ ($L \approx 1\times10^{-3}\,\mathrm{m}$, $a \approx 1\times10^{-10}\,\mathrm{m}$) and the experimental order of magnitude $\beta_{utf} \sim 1.5\times10^{-4}\,\mathrm{rad}$, we get $V \sim 5\times10^{-14}\,\mathrm{m\,s^{-1}}$, which is several orders of magnitude smaller than the experimental value $1.7\times10^{-7}\,\mathrm{m\,s^{-1}}$. Therefore, from this preliminary experiment we can conclude that in this system it is very likely that gravity is the driving force of the advancing wedge. Further experiments with increased resolution can be envisioned to better investigate this evolution.

4.3.2 Alkanes

In Sec. 4.2.3.3 we saw that experiments with hexadecane showed the apparition of a macroscopically "empty" region (within the experimental resolution). In this section we investigate a follow-up of this experiments in which we remove the thermal field driving the dynamics.

The results of Sec. 4.2.3 points to the existence of two dynamics: one for the bulk thin film and a quicker one for a ultra-thin foot that is absorbed towards the wedge. The stationary state arises when the foot has completely being absorbed into the bulk and the wedge reaches a stationary state at some distance from heating source (typically several millimetres away, depending on the maximum thermal field imposed). When we remove the thermal field driving the dynamics, we find in general that the contact line remains pinned and there is no further dynamics. As we showed in Fig. 4.13 above, the shape of the boundary between the central and outer areas resembles the characteristic shape of the thermal field that we measured with the infrared camera (see Fig. 2.3 of chapter 2).

Let us mention here that we have performed some preliminary experiments in which we remove the thermal field before the ultra-thin film has disappeared completely. The wedge generally tends to move covering the remaining part of the foot, in a way that appears qualitatively similar to that of silicone oil, by visual inspection of the experimental images. The difference with respect to silicone oil is that the foot can still have some residual dynamics. When the boundary of the wedge reaches the boundary of the foot, the former stops and we recover the case of the stationary wedge.

In the final part of this section, we focus on the measurement of the wedge's angle, and compare it to the contact angle that we measured previously (Sec. 4.2.2.3). In Fig. 4.21 we show the evolution of the position of the wedge $x_w(t)$ (top panel, blue) and its angle, denoted $\beta_w(t)$ (bottom panel), measured by FS-SS during a full "thermocapillary–then–relaxation" experiment. Initially the dynamics are driven by thermocapillarity ($t < t_{off}$), and we can see how the wedge forms early on and recedes from the centre while its angle relaxes slowly. In the images of this experiment, the receding boundary of the foot $x_f(t)$ could be seen (defined analogously as in the experiment showed in Fig. 4.10, right panel). The red data on the top panel indicates for comparison the position of this boundary as it is formed and finally absorbed at the wedge.

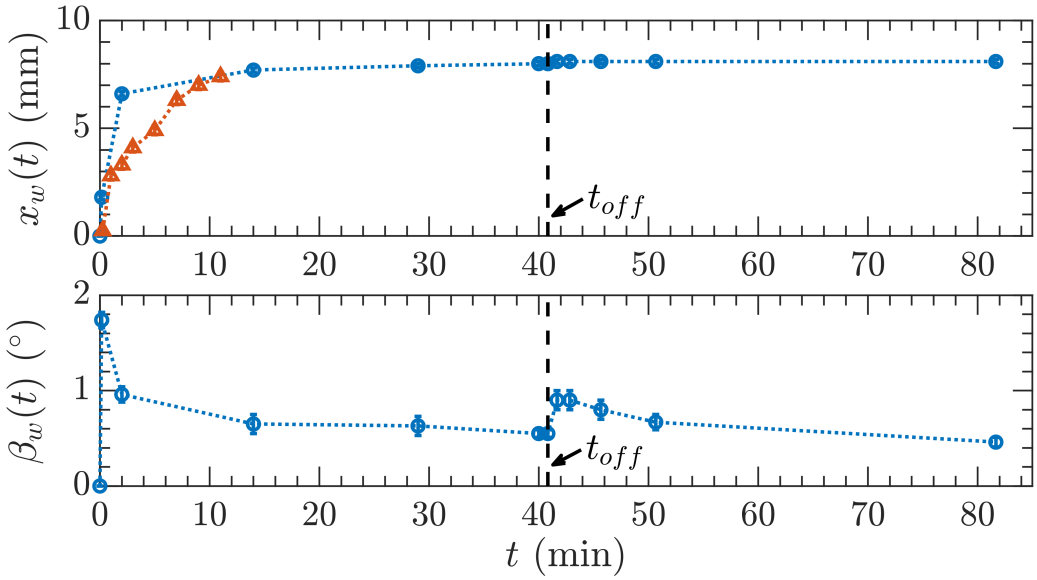

Figure 4.21: Evolution of the wedge's position $x_w(t)$ (top panel) and angle $\beta_w(t)$ (bottom panel) in an experiment performed with hexadecane, initial thickness $h_0 = 20(2)\,\mu$m and dissipated power $P = 62(6)\,$mW. The red triangles on the top panel, similarly to Fig. 4.11, indicate the receding boundary $x_f(t)$ of the ultra-thin film, which is absorbed at the boundary at $t \sim 11\,$min. The time labelled as t_{off} (dashed line) marks the time at which the thermal field was removed.

At the time t_{off} the current is turned off and the system is free to relax to an equilibrium position. We observe that the position of the wedge x_w remains fixed (top panel of Fig. 4.21). As shown in the bottom panel, the wedge first becomes slightly more steeper and then its angle β_w continues relaxing slowly due to some remaining large scale dynamics. This instantaneous change may be understood as originating from the small change in surface tension when the thermal field is removed, which in this case is $\Delta\gamma/\gamma_0 \sim 0.1$.

These stationary states for both liquids are always stable and they do not relax further even after several days. This can be explained assuming that these alkanes on our glass substrate promote a pseudo-partial wetting regime, as explained before in Sec. 4.2.4, meaning that in equilibrium the thin film can coexist with a nanometric one at the central region.

4.4 Conclusion

In this chapter, we have used the experimental setup introduced in chapter 2 and applied in chapter 3 to the study of thin films of silicone oils (which completely wet the surface) to do preliminary observations of: first, the dynamics of two alkanes, hexadecane and HMN, when driven by the thermocapillary effect; and second, of the relaxation dynamics of both silicone oils and the alkanes when the thermal field is removed after some time.

In the first part, we have seen that in our system the alkane films tend to break up when thinned down to the tens of nanometres scale. After the pure-thermocapillary regime, discussed in detail in chapter 3, the thickness at the centre quickly drops down to the noise level of our interferometric setup (around 10 nm). This generates a receding

ultra-thin foot that advances by the collapse of the film under the action of intermolecular forces. We are able to recover and follow the height profile of this foot, which moves away from the centre faster than the macroscopic wedge. The foot disappears, being absorbed in the bulk. Due to our resolution limit, we cannot currently say whether the central area is completely dewetted or if a nanometric layer remains. In contrast to the case of the silicone oils, the system reaches the stationary state within a experimentally manageable timescale. The angle of the wedge is about 1°, which is of the order of magnitude of the contact angle we measured for droplets deposited on our support surfaces. The boundary between the central, macroscopically "empty" region, and the outer thin-film is controlled by a line of constant temperature of the thermal field. No difference has been observed between hexadecane and HMN in the thermocapillary evolution, even at the smallest scales resolved. This implies that the observed dynamics does not depend on the particular wetting behaviour that hexadecane may have near the melting point (recall Sec. 4.2.2.2). We suggest that the observed behaviour results from pseudo-partial wetting, meaning that in our glass/alkane/air system the interface potential describing the intermolecular interactions is not monotonous, resulting in the coexistence in equilibrium of the outer thin film and a nanometric film in the central region.

In the second part, we have shown some preliminary results about the relaxation dynamics of the system starting from the (quasi-)steady state. These experiments consist on removing the thermal field driving the dynamics after the system has reached this state. We see that the dynamics depends crucially on the presence of the ultra-thin film.

In the case of silicone oils, the wedge moves towards the centre covering the stable ultra-thin film, with a typical velocity on the order of some millimetres per hour. Due to the exponential shape of the thickness profile (a result we link to the thermal field being also exponential) at the moment at which the thermal field is removed, together with the power-law behaviour of the disjoining pressure, $\Pi(h) \propto 1/h^{\nu}$, we show that the dynamics depending solely on $\Pi(h)$ would produce a dynamics lying below our resolution level, and thus the ultra-thin film appears static. In the case of the alkane films, since the ultra-thin film is unstable and the central region appears homogeneous, the removal of the thermal field has no effect on the structure of the stationary state. The wedge remains at the same position, and there is a small instantaneous change of the angle of the wedge probably due to the small increase in surface tension when the thermal field is removed.

Once the issue of the surface inhomogeneities can be solved (or at least diminished), a more detailed analysis could be obtained. Nevertheless, these preliminary results exemplify the variety of interface phenomena that can be characterised in our setup as a result of the driving of the thermocapillary effect.

Conclusion and perspectives

In this thesis, we have studied the evolution of thin liquid films supported by a glass substrate driven by the thermocapillary effect. A microprinted electrical circuit located on the bottom side of the substrate provides, via the Joule effect, the thermal gradient promoting the dynamics. We are able to control the local thinning dynamics of the thin film from an initial thickness of tens of micrometres to an ultra-thin film – tens of nanometres thick – with a temperature difference of only a few Kelvins. Two optical techniques, implementing a free-surface synthetic Schlieren method and 3-colour interferometry, allow us to measure the evolution of the height profile of the liquid. We identify three different dynamical regimes. In the first one, the gradient of surface tension promotes an interfacial flow, dragging the liquid away from the heating source where the gradient of the thermal field is maximum. A depression appears in the liquid film over the maximum of the thermal field, and the liquid removed from this central region generates symmetric overshoots towards the outer region. Once the central depression reaches the micrometre scale, two symmetric, receding wedges form, leaving behind an ultra-thin film in the central region. The height profile at the central region is measured using a 3-colour interferometric technique with a precision of about 10 nm over a lateral size of several millimetres, in a thickness range from 20 nm to 1 µm, during a time scale ranging from hours to days. Within the framework of the thin film equation, we describe and experimentally verify the existence of a local intermediate-time regime in which all pressure contributions are negligible against the action of the thermocapillary effect. From this description, we show that it is possible to determine the gradient of the thermal field driving the dynamics from experimental height profiles. Therefore, we are able to provide self-consistent results and to fully validate the model.

For longer times, as the film continues thinning down below the scale of 100 nm, the measurement of the evolution of the height profile allows us to investigate the effects of intermolecular interactions in the thermocapillary-driven dynamics. We have studied first the dynamics of a glass/silicone oil/air system. When driven by thermocapillarity, the silicone oil attains a quasi-steady state with a stable ultra-thin film over a scale of one day. The measurements of the evolution of the height profile, together with the obtained temperature gradient, allows us to measure the derivative of the disjoining pressure with respect to the thickness of the film. We obtain reproducible measurements over a continuous thickness range between 10 and 100 nm. This range is larger than the one typically explored by experimental techniques for measuring disjoining pressures. No experiment could be found in the literature determining the disjoining pressure of this non polar system. As expected, the resulting derivative of the disjoining pressure behaves as a power-law with thickness. However, the exponent of this power-law does not correspond to the London-Hamaker theory computed from dipolar interactions. Instead,

a slower decrease of the interaction with thickness is found, which remains unexplained. These results open the way to test other systems which interactions have been measured with other techniques for comparison.

In a second part, we have studied the dynamics of two alkanes, hexadecane and 2,2,4,4,6,8,8-heptamethylnonane, on the same system. Before reaching the region where intermolecular forces are important, the dynamics has the same characteristics as in the case of silicone oil. However, and conversely to silicone oils, the measured evolution shows that these liquids do not form any stable ultra-thin film. Instead, the film becomes unstable and we observe the formation of a receding foot of liquid that gets absorbed at the wedge. The thickness at the central region drops to some value below the sensitivity threshold of our interferometric setup, which is around 20 nm. Glass is a high energy surface that should get wetted by these alkanes. In the literature, it is generally admitted that, at temperatures larger enough than its melting point, hexadecane wets glass (see, for example, [74]). However, it is well known that even wetting droplets may take a long time to attain an equilibrium configuration, which may reach the scale of a week [77]. Hence, not many experiments reach this time frame to verify the equilibrium configuration. We provide arguments showing that a plausible interpretation of our results is that, in fact, both alkanes exhibit pseudo-partial wetting behaviour on our glass substrate. Actually, with usual wetting experiments it is difficult to discriminate between total and pseudo-partial wetting behaviours when the equilibrium angles are small. In contrast, thermally-induced dewetting is qualitatively very different for silicone oils and alkanes, and thus offers a new method to clearly define the wetting behaviour of liquids.

Our results open the way for many other experimental investigations of wetting at very small scales. Experiments with alternative liquid/substrates can easily be thought of, either for measuring intermolecular forces or probe wetting behaviours. For instance, non-wetting liquids could be used since only formation of an initial thick film is required. We have limited our study to poorly volatile liquids but evaporation should not interfere with thermally induced dewetting since the outer part of the liquid film constitutes a reservoir that could feed the central part and compensate evaporation. Besides, the silicone oil of smaller viscosity we have used is expected to evaporate significantly over the long times involved in the experiment, and did not present qualitatively different behaviours than the more viscous silicone oil. In the specific case of water, the unavoidable presence of surface active contaminants would result in a complex coupling of solutal and thermal Marangoni effect [81], which would prevent measurements of disjoining pressure from the dewetting dynamics. However, the latter could provide further information on the coupling between Marangoni flows. Other solid substrates could also be considered, in particular to improve the cleanness of the substrate. For instance a mica substrate could be cleaved just before depositing the liquid film and thus offer a perfectly clean surface. The main limitation on the substrate resides in its thermal properties: a conductive substrate is prohibited since it would not sustain the thermal gradient.

In order to measure the intermolecular forces in a larger thickness range, the more obvious improvement is to decrease the sensitivity threshold of the interferometric thickness measurement. In the present version, the use of achromatic optics, or compensation of the optical paths between the different wavelengths should constitute a major step forward. Other measurement techniques could also be considered such as ellipsometric microscopy which is particularly well suited for ultra-thin films. A larger contrast between optical

indexes than the one of the investigated systems would however be needed.

Finally, other geometries of thermal gradients can be thought of. Preliminary experiments have shown that, using a circular geometry, it is possible to form drops of wetting liquids as shown in Fig. 4.22. The induced contact angle could be tuned by adjusting the thermal gradient. The control that the thermal field provides for designing non-equilibrium steady states, as discussed preliminarily in the last chapter, can also be envisioned as a tool for studying the relaxation or spreading dynamics from specific configurations.

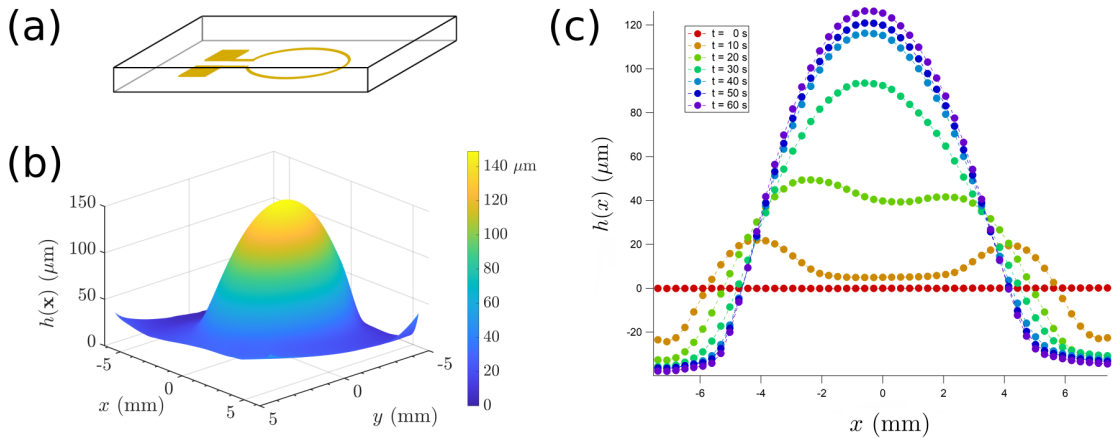

Figure 4.22: (a) Annular circuit for forming non-equilibrium drops of wetting liquids. (b) Measurement with FS-SS of a non-equilibrium drop of silicone oil in the stationary state. (c) Evolution of the thickness profiles (relative to the initial thickness) before reaching the stationary state shown in (b) along $y = 0$, showing initially the advancing of an overshoot towards the centre from the position of the heating annulus and the formation of a drop with an apparent contact angle. This contact angle may be controlled by varying the thermal gradient via θ_{max}.

Appendix A

Dynamical effect of temperature dependent properties

In chapter 1, we have introduced the thin film equation describing the dynamics of the height profile $h(x,t)$ of a thin liquid film supported by a solid substrate in the presence of a thermal field $\theta(x)$. The resulting evolution is determined by Eq. (1.12), which we rewrite here as

$$\partial_t h + \partial_x \left\{ \frac{1}{\eta} \left(\frac{h^3}{3} \partial_x \left[\gamma(x) \partial_x^2 h - \rho g h - \frac{A_H}{6\pi h^3} \right] + \frac{h^2}{2} \partial_x \gamma(x) \right) \right\} = 0. \tag{A.1}$$

The terms inside the squared brackets are the different pressure contributions to the dynamics: Laplace, gravitational and disjoining pressures. The term proportional to the gradient of the surface tension $\partial_x \gamma$ represents the driving stress of the thermocapillary effect, and appears due to the dependence of the surface tension γ on the temperature, $\gamma[\theta(x)] \equiv \gamma(x)$. The variation of $\gamma(x)$ is small, so that the Laplace pressure can be approximated by $\gamma_0 \partial_x^2 h$ where γ_0 is the surface tension at the reference temperature. As explained in the main text, the surface tension gradient generates a drag on the surface that locally thins the liquid around the maximum thermal field gradient.

Among the assumptions made to reach this equation, we have assumed that the viscosity η and the density ρ are independent of temperature. In this appendix, we discuss the effect of including the dependence on temperature for each property.

A.1 Thin film equation with temperature dependent properties

As discussed in the main text, the thermal Péclet number of this system is small, Pe$\sim 10^{-3}$, and the temperature can be assumed to be homogeneous throughout the thickness of the film. Hence, we will only discuss the variations along the spatial dimension and write $\eta[\theta(x)] \equiv \eta(x)$ and $\rho[\theta(x)] \equiv \rho(x)$. The value of these properties at the reference temperature (say, 25 °C), are noted η_0 and ρ_0, respectively.

The derivation of the thin film equation starts again from the Navier-Stokes equations

in the limit of slow dynamics and small gradients,

$$-\partial_x p + \eta(x)\partial_z^2 v_x = 0, \tag{A.2}$$

$$\partial_z p = 0 \tag{A.3}$$

with the velocity $v_x = v_x(t, x, z)$ and similarly for the pressure p, subject to the boundary conditions

$$v_x|_{z=0} = 0, \tag{A.4}$$

$$\partial_z v_x|_{z=h} = \frac{1}{\eta(x)}\partial_x \gamma \tag{A.5}$$

expressing, respectively, the non-slip condition at the solid/liquid interface and stress balance at the free interface.

The velocity field is thus

$$v_x = \frac{1}{\eta(x)}\left\{\frac{1}{2}\left(z^2 - 2zh\right)\partial_x p + z\partial_x \gamma\right\}. \tag{A.6}$$

We consider once again the conservation of volume for finding the evolution of $h(t, x)$, with the same pressure contributions to p as before. The resulting equation is

$$\partial_t h + \partial_x\left\{\frac{1}{\eta(x)}\left(\frac{h^3}{3}\partial_x\left[\gamma_0\partial_x^2 h - \rho(x)gh - \frac{A_H}{6\pi h^3}\right] + \frac{h^2}{2}\partial_x\gamma(x)\right)\right\} = 0. \tag{A.7}$$

Comparing this expression with Eq. (A.1), it is clear that small variations of the density or the viscosity won't change essentially the thermocapillary dynamics, since the dependence of the evolution on these properties has not changed. In particular, there is no new term added to the equation, and the dynamics still comes from the interplay between the pressures and the gradient of the thermal field, without the intervention of the viscosity.

A.2 Effect of $\eta(x)$ and $\rho(x)$ on the stationary state

Before commenting the possible dynamic effects of $\eta(x)$ and $\rho(x)$, let us focus on the stationary state that would follow from Eq. (A.7). The stationary state $\overline{h} = \overline{h}(x)$ is the solution of

$$\partial_x\left\{\frac{1}{\eta(x)}\left(\frac{\overline{h}^3}{3}\partial_x\left[\gamma_0\partial_x^2\overline{h} - \rho(x)g\overline{h} - \frac{A_H}{6\pi\overline{h}^3}\right] + \frac{\overline{h}^2}{2}\partial_x\gamma(x)\right)\right\} = 0. \tag{A.8}$$

Integrating from x to infinity, since all derivatives vanish at infinity, we are left with

$$\frac{\overline{h}^3}{3}\partial_x\left[\gamma_0\partial_x^2\overline{h} - \rho(x)g\overline{h} - \frac{A_H}{6\pi\overline{h}^3}\right] + \frac{\overline{h}^2}{2}\partial_x\gamma(x) = 0. \tag{A.9}$$

Since the viscosity is only linked to the time scale of the dynamics dissipation, it does not contribute to the stationary state as in the constant $\eta(x) = \eta_0$ case.

The stationary state, as discussed in Sec. 1.5 of chapter 1, is divided into two regions, one central region close to the maximum thermal field gradient, and an outer one far from it. The extent of the central region is controlled by the typical decay length of the thermal field. To make the discussion more concrete, we recall that in our case the thermal field behaves approximately as an exponential decay, $\theta(x) \simeq \theta_{max} \exp(-|x|/w_0)$ (see the discussion in Sec. 2.2.2 of chapter 2) with w_0 on the order of several millimetres. We will be concerned only in the case in which the thermal field is strong enough to promote the establishment of an ultra-thin film of typical thicknesses of tens of nanometres, as explained in chapter 1.

The region close to the centre ($x \ll w_0$), where the thermocapillary effect is stronger, is characterised by the establishment of a ultra-thin film region when the intermolecular forces are repulsive ($A_H < 0$). With typical thickness of tens of nanometres, the gravitational pressure will be small compared to the disjoining pressure and can be neglected. This is more so if the density depends with temperature, since it diminishes as the temperature is higher. This change is furthermore very small in our system, see below. Thus, the dependence of the density on temperature does not have a noticeable effect at this region.

Further from the centre ($x \gg w_0$), the thickness is roughly flat and of the order of the initial thickness, $h_0 \sim 30\,\mu\text{m}$. Here gravity is the dominant pressure contribution. However, since this region is far from the maximum of the central field the temperature rise is weak here. Therefore, the density will be close to its reference value ρ_0, and again its dependence with temperature is not relevant when determining the shape of the stationary state.

As a consequence, the dependence of density with temperature may only be relevant at the transition from the ultra-thin to the thin-film, where it will modulate the precise shape of a wedge in its interplay with the Laplace pressure but not produce any significant change.

The stationary state is thus essentially unchanged if temperature-dependent viscosity and density are considered.

A.3 Effect of $\eta(x)$ and $\rho(x)$ on the dynamics

The effect of the temperature dependence of the viscosity and the density on the dynamics will depend on how strong their dependence is for the liquid considered. In this thesis, we use in our experiments two main types of liquids, silicone oils (chapter 3) and alkanes (chapter 4). We obtain in this section orders of magnitudes of the variations of η and ρ under experimental conditions. In the experiments, we have usually worked with a maximum temperature difference (with respect to room temperature) around $\theta_{max} \sim 1\,\text{K}$, although for some experiments we reached $\theta_{max} \sim 7\,\text{K}$ (see table 3.2 on chapter 3). For the present discussion, we consider a limiting case such that the room temperature is $T_0 = 298\,\text{K}$ and that the temperature difference reaches a high value of $\theta_{max} = 10\,\text{K}$. The maximum absolute temperature attained would thus be $T_{max} = 308\,\text{K}$.

A.3.1 Silicone oils

Let us consider first the silicone oils. We focus here on Rhodorsil 47V20 oil which, as noted in the main text (see Sec. 3.2 of chapter 3), is produced from a mixture of polydimethylsiloxanes with different molecular weights. The distribution of viscosities and densities could result in some unexpected dynamic effect. This oil has reference viscosity $\eta_0 = 19\,\mathrm{mPa\,s}$ and density $\rho_0 = 950\,\mathrm{kg\,m^{-3}}$ at 25 °C.

According to the technical specification [25] the viscosity diminishes with temperature T (given in kelvin) as

$$\eta(T) = \eta_0 \exp\left([1683\,\mathrm{K}] \left\{ \frac{1}{T} - \frac{1}{T_0} \right\} \right). \tag{A.10}$$

Inserting $T = T_{max}$, we have $\eta(T_{max}) \simeq 0.83\,\eta_0$, that is, around a 20% change between the central value and the reference value. This change may affect the time scale of the local dynamics very near the centre, where the thermal field is maximum. Therefore, experiments at larger temperatures differences will need to take into account this effect. However, as explained in chapter 1, the dynamics of silicone oil becomes very slow, so that even with this variation of viscosity there will not be significant changes in the behaviour of the film. This is seen in chapter 3 when comparing experiments done with $\theta_{max} \sim 1\,\mathrm{K}$ with others done at $\theta_{max} \sim 7\,\mathrm{K}$, since no significance difference is found neither in the dynamics nor in the measurements obtained. Moreover, because of the exponential dependence on the temperature variation, for a typical experiment with $\theta_{max} = 1\,\mathrm{K}$ the deviation is only about a 2%.

The variation of density is much smaller. The dependence of $\rho(T)$ on temperature can be fitted to a cubic relationship [25], which gives $\rho(T_{max}) = 944\,\mathrm{kg\,m^{-3}}$. Compared with $\rho_0 = 950\,\mathrm{kg\,m^{-3}}$, this only represents a variation of about 0.6% and can be neglected.

A.3.2 Alkanes

The situation is similar with the alkanes used, *n*-hexadecane and its isomer 2,2,4,4,6,8,8-heptamethylnonane (HMN). Comparing available experimental data of each liquid shows a very similar dependency of density and viscosity on temperature [67, 68]. Therefore, it is enough to consider one of them.

The viscosity and density of HMN at $T_0 = 298\,\mathrm{K}$ are $\eta_0 = 3.2\,\mathrm{mPa\,s}$ and $\rho_0 = 781\,\mathrm{kg\,m^{-3}}$ [68]. From the experimental data in the range from 273.15 to 373.15K, a 3-order polynomial can be fitted to describe the reduction of $\eta(T)$ and a linear relationship describes the dependence of the density $\rho(T)$ with temperature.

As a result, comparing the variation of $\eta(T)$ and $\rho(T)$ from T_0 to $T_{max} = 308\,\mathrm{K}$, we obtain that viscosity varies by 20% and density by 0.9%. (The same orders of magnitude are obtained for hexadecane.) These values are very similar to the ones obtained for the silicone oil in the preceding section and thus the same conclusions apply: first, that the variation of density with temperature in the experimental range considered is negligible; and second, that the thermal field imposed should not be too strong to avoid local differences in the dynamic timescale. The effect of viscosity would affect the specific value of the velocity field, but it would not imply any new dynamic phenomena as was seen by the comparison of Eq. (A.1) and Eq. (A.7).

A.4 Conclusion

The preceding discussion on the effect of the temperature dependence of viscosity and density on the dynamics can be summed up in the conclusion that, within the current experimental range of parameters, neither of them would imply any major change in the dynamics of the system nor in the structure of the stationary state reached.

This is particularly true of the density, which has a variation of less than 1% for the liquids we use in the small range of temperatures studied. The local variation of viscosity can be larger, up to 20% if a thermal field with $\theta_{max} = 10\,\mathrm{K}$ is considered. However, the viscosity does not participate in the relationship between the pressures and the thermocapillary effect which drives the dynamics, as seen in Eq. (A.7). It would only become a local prefactor which may slightly accelerate the dynamics at the position of maximum thermal field where thermocapillarity is strongest, but otherwise the dynamics will have the same features as it has with the constant reference values. For typical experiments with $\theta_{max} \sim 1\,\mathrm{K}$ the variation would be correspondingly smaller.

Appendix B

Pure-thermocapillary dynamics

In this appendix we solve the dynamic equation

$$\partial_t h_{\mathrm{M}} - \frac{\Delta\gamma}{2\eta}\partial_x \left\{h_{\mathrm{M}}^2 \partial_x \Theta\right\} = 0. \tag{B.1}$$

corresponding to Eq. (1.19) of the main text, which represents the case in which all pressure terms are negligible against the action of thermocapillarity.

B.1 Nondimensionalization

For simplicity, we will work with the dimensionless variables

$$X \equiv \frac{x}{w_0}, \qquad H \equiv \frac{h_{\mathrm{M}}}{h_0}, \qquad T \equiv \frac{t}{t_0}, \tag{B.2}$$

where w_0, h_0, and $t_0 = 2\eta w_0^2/\Delta\gamma h_0$ are defined as in the main text, with which we obtain the dimensionless equation

$$\partial_T H - \partial_X \left\{H^2 \partial_X \Theta\right\} = 0. \tag{B.3}$$

B.2 Solution by separation of variables

We look for a solution of the form

$$H(T, X) = g(T) f(X). \tag{B.4}$$

obtaining the condition

$$\frac{\partial_T g(T)}{g(T)} = \frac{\partial_X \left\{f^2(X)\partial_X \Theta\right\}}{f(X)} = -c, \tag{B.5}$$

where c is a constant to be defined.

The temporal part of the equation is solved immediately, giving

$$g(T) = \frac{1}{1 + cT}. \tag{B.6}$$

The spatial part of the equation can be reduced to the linear equation in f

$$2\partial_X f\,\partial_X\Theta + f\partial_X^2\Theta = -c. \tag{B.7}$$

The solution of the homogeneous equation ($c = 0$) is

$$f_H(X) = \frac{K}{\sqrt{|\partial_X\Theta|}}, \tag{B.8}$$

where K is an integration constant.

Using variation of parameters by making K a function of X, $K \to K(X)$, one can find the following solution of the complete equation:

$$f(X) = \frac{K'}{\sqrt{|\partial_X\Theta|}} + \frac{c}{2\sqrt{|\partial_X\Theta|}}\int_0^X \frac{ds}{\sqrt{|\partial_s\Theta(s)|}}, \tag{B.9}$$

where K' is another constant.

Since the thermal field has a maximum at the centre, the derivative of the thermal field vanishes at $X = 0$. To avoid the divergence of the first term, we impose $K' = 0$. The second term does not diverge: as $X \to 0$, we have $\partial_X\Theta(X) \simeq X\partial_X^2\Theta(0)$ and

$$f(X \to 0) \to \frac{c}{2\sqrt{X|\partial_X^2\Theta(0)|}}\int_0^X \frac{ds}{\sqrt{s|\partial_X^2\Theta(0)|}} = \frac{c}{|\partial_X^2\Theta(0)|}. \tag{B.10}$$

Putting everything together, we get the solution in terms of the thermal field $\Theta(x)$,

$$H(T, X) = \frac{1}{1 + cT}\frac{c}{2\sqrt{|\partial_X\Theta|}}\int_0^X \frac{ds}{\sqrt{|\partial_s\Theta(s)|}}. \tag{B.11}$$

We have not yet identified the parameter c on Eq. (B.11). Let us come back to the original equation (B.3). Due to the parity of the thermal field, and thus of the height profile, the evolution at the centre ($X = 0$) satisfies

$$\partial_T H(T, 0) - H^2(T, 0)\,\partial_X^2\Theta(0) = 0, \tag{B.12}$$

giving the reference evolution

$$H(T, 0) = \frac{1}{1 + \left|\partial_X^2\Theta(0)\right| T}. \tag{B.13}$$

Comparing this expression with the previous result (B.11), it is easy to see that one should identify c with the curvature of the thermal field at the centre, $c = \left|\partial_X^2\Theta(0)\right|$ so that $f(X \to 0) \to 1$ and

$$g(T) = \frac{1}{1 + \left|\partial_X^2\Theta(0)\right|T} = H(0, T). \tag{B.14}$$

Putting everything together, in dimensional variables the complete solution reads

$$h_{\mathrm{M}}(t, x) = \frac{h_0}{1 + c(t/t_0)}\frac{c}{2\sqrt{|\partial_X\Theta|}}\int_0^X \frac{ds}{\sqrt{|\partial_s\Theta(s)|}}, \tag{B.15}$$

which is discussed in the main text.

B.3 Heating-up time scale

Let us point out here that we have assumed that the thermal field $\Theta(x)$ is constant over time; in particular, that it acts from $t = 0$ without a transient heating period. If the thermal field has a time modulation independent of the position, such that we can substitute $\Theta(x) \to g_\theta(t)\Theta(x)$ in Eq. (B.1), the preceding discussion still holds and Eq. (B.15) would slightly change to

$$h_{\mathrm{M}}(t,x) = \frac{h_0}{1+\frac{c}{t_0}\int_0^t g_\theta(u)du}\,\frac{c}{2\sqrt{|\partial_X\Theta|}}\int_0^X \frac{ds}{\sqrt{|\partial_s\Theta(s)|}}, \tag{B.16}$$

where $c = \left|\partial_X^2\Theta(0)\right|$ as before. If $g_\theta(t) = 1$ the previous result is recovered.

We have measured how the maximum temperature difference imposed grows over time from the initially homogeneous thermal field.[1] It is well described by

$$g_\theta(t) = 1 - e^{-t/t_\theta}, \tag{B.17}$$

with $t_\theta \sim 15\,\mathrm{s}$. This means that the temporal part of the height profile $g(t)$ should now read

$$g(t) = \left[1 + \frac{c}{t_0}\left(t - t_\theta\left[1 - e^{-t/t_\theta}\right]\right)\right]^{-1}, \tag{B.18}$$

which essentially delays the dynamics by a time t_θ. Since this time scale is much smaller than the typical experimental duration discussed in the context of wetting liquids (about 1 day, see Sec. 3.2 of chapter 3), this is a correction that can be neglected in the long time regime.

[1] See Sec. 2.2.2 in chapter 2 for more details about the thermal measurements.

Appendix C

Thermal field model

In this appendix, we present a minimal model to obtain the thermal field generated by the heating line used in experiments, as explained in chapter 2.

C.1 Model

We consider a glass slide of thickness e and of thermal conductivity κ. A heating line of length L, of zero width, represents the heat source. The heating line defines the y axis, extending between $-L/2$ and $L/2$ on the $z = 0$ plane. The heat source function $\Phi(\mathbf{x}) = \Phi(x, y)$ is represented as

$$\Phi(\mathbf{x}) = \Phi_0 \delta(x) W\left(\frac{L}{2} - y\right) \tag{C.1}$$

with Φ_0 the input power density, $W(u)$ the rectangular window function and $\delta(x)$ the delta function. The system is sketched in Fig. C.1.

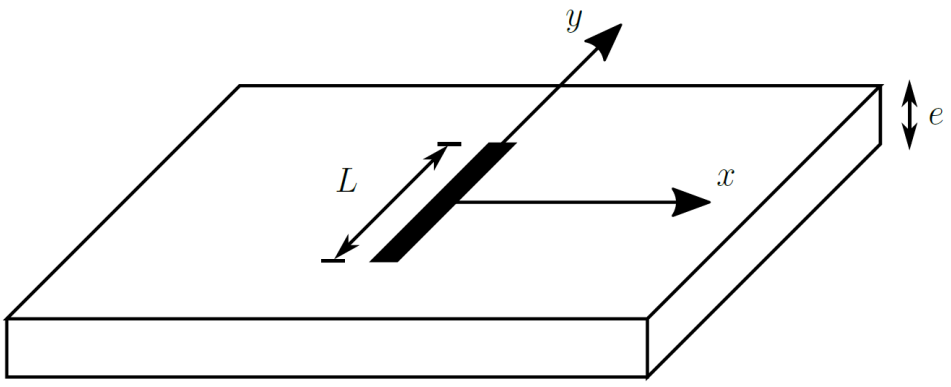

Figure C.1: Sketch of the heating configuration (not to scale). A heating line of length L lies in the centre of a slide of thickness e much smaller than L.

The thickness e is assumed to be much smaller than its other dimensions, so that the slide is modelled as having infinite extension along the x and y directions. It is also assumed that e is small enough so that the thermal field is constant in the vertical direction

throughout the slide. We focus on finding the excess temperature field $\theta(\mathbf{x}) = \theta(x, y)$ generated by the heat source $\Phi(\mathbf{x})$ at the plane of the slide, $z = 0$.

In the experiments, part of the heat will be transmitted to the media around the slide, in particular to a thin liquid film deposited on top of the slide. To model this thermal loss, we add to the heat equation a term proportional to the temperature. This term requires the inclusion of a characteristic length scale of the loss, denoted by μ^{-1}. This scale may depend both on the thermal conductivity of the material that is in contact with the slide, as well as in geometrical factors such as the finite size of the slide in the real setup. These considerations will be important when comparing the thermal field of the bare experimental glass slide, measured with an infrared camera, to the thermal field obtained directly in thermocapillary experiments (see Sec. 3.3.1.3 on chapter 3).

The stationary heat loss equation under these conditions is written as

$$\Delta\theta = \mu^2\theta - \frac{1}{e\kappa}\Phi(\mathbf{x}). \tag{C.2}$$

Performing the Fourier transform of Eq. (C.2) on both spatial variables we obtain

$$\left[\mu^2 + k_x^2 + k_y^2\right]\tilde{\theta}(\mathbf{k}) = \frac{1}{e\kappa}\tilde{\Phi}(\mathbf{k}), \tag{C.3}$$

where the tilde represents the Fourier transform of the corresponding function. The Fourier transform of the source $\Phi(\mathbf{x})$ given by Eq. C.1 is

$$\tilde{\Phi}(\mathbf{k}) = 2\Phi_0\frac{\sin\left(k_y L/2\right)}{k_y}. \tag{C.4}$$

To obtain $\theta(\mathbf{x})$ from Eq. C.3, the inverse Fourier transform has to be computed. Taking into account the symmetry of the system along x,

$$\theta(\mathbf{x}) = \frac{1}{(2\pi)^2}\frac{2\Phi_0}{e\kappa}\iint_{\mathbb{R}^2}\frac{\sin\left(k_y L/2\right)}{k_y}\frac{\cos(k_x x)\cos(k_y y)}{\mu^2 + k_x^2 + k_y^2}\,dk_x dk_y. \tag{C.5}$$

The inverse transform on k_x is a Lorentzian, that can be performed to give

$$\theta(\mathbf{x}) = \frac{1}{2\pi}\frac{2\Phi_0}{e\kappa}\int_{-\infty}^{\infty}\frac{\sin\left(k_y L/2\right)}{k_y}\frac{e^{-|x|\sqrt{k_y^2+\mu^2}}}{\sqrt{k_y^2+\mu^2}}\cos(k_y y)\,dk_y. \tag{C.6}$$

Combining the trigonometric functions containing k_y, this expression can be rewritten as

$$\theta(\mathbf{x}) = \frac{1}{2\pi}\frac{\Phi_0}{e\kappa}\left[F\left(y + \frac{L}{2}\right) - F\left(y - \frac{L}{2}\right)\right] \tag{C.7}$$

where we have defined

$$F(s) = \int_{-\infty}^{\infty}\frac{\sin(k_y s)}{k_y}\frac{e^{-|x|\sqrt{k_y^2+\mu^2}}}{\sqrt{k_y^2+\mu^2}}\,dk_y. \tag{C.8}$$

This auxiliary function can be better understood by noting that its derivative is[1]

$$F'(s) = 2\int_0^\infty \cos(k_y s)\frac{e^{-|x|\sqrt{k_y^2+\mu^2}}}{\sqrt{k_y^2+\mu^2}}\,dk_y \tag{C.9}$$

$$= 2K_0\left(\mu\sqrt{s^2+x^2}\right), \tag{C.10}$$

where $K_0(u)$ is the modified Bessel function of the second kind. Therefore, the thermal loss field is finally expressed as

$$\theta(\mathbf{x}) = \frac{\Phi_0}{\pi e\kappa}\int_{y-L/2}^{y+L/2} K_0\left(\mu\sqrt{s^2+x^2}\right)\,ds. \tag{C.11}$$

The thermal field has its maximum at the centre,

$$\theta(0,0) = \frac{\Phi_0}{\pi e\kappa}\int_{-L/2}^{L/2} K_0\left(\mu|s|\right)\,ds \equiv \theta_{max}, \tag{C.12}$$

so that we can express the thermal field as

$$\theta(\mathbf{x}) = \theta_{max}\frac{\int_{y-L/2}^{y+L/2} K_0\left(\mu\sqrt{s^2+x^2}\right)\,ds}{\int_{-L/2}^{L/2} K_0\left(\mu\,|s|\right)\,ds}. \tag{C.13}$$

In this expression, we note the relevance of the dissipation length μ^{-1} in establishing the extent in which the heat source is effective.

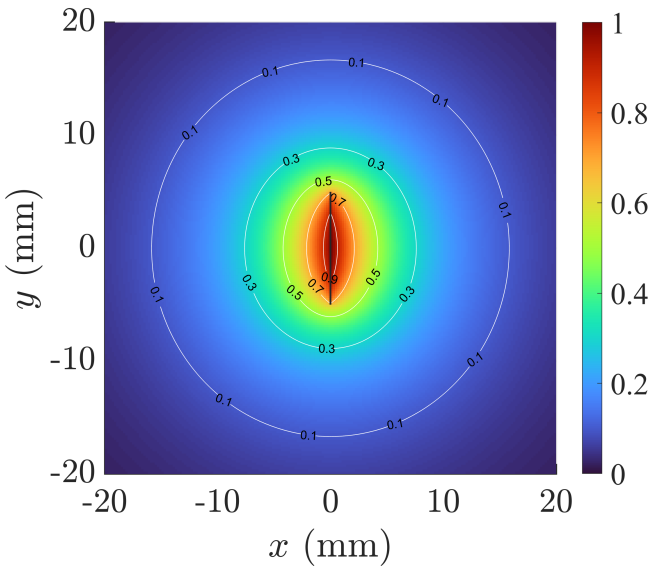

Figure C.2: Thermal field $\theta(\mathbf{x})$ computed from Eq. (C.13) with $L = \mu^{-1} = 10\,\text{mm}$ and $\theta_{max} = 1\,\text{K}$. The black line indicates the position of the heating source.

In Fig. C.2 we show the resulting thermal field $\theta(\mathbf{x})$ computed from Eq. (C.13) with parameters $L = \mu^{-1} = 10\,\text{mm}$, and $\theta_{max} = 1\,\text{K}$. The length of the line, $L = 10\,\text{mm}$ is

[1] Cf. equation 3.961.2 of Ref. [82].

fixed by the printed circuit of the experiment, see Sec. 2.2.1.2 of chapter 2. The value of the dissipation length μ^{-1} has been chosen from the typical order of magnitude found in infrared measurements, see Sec. 2.2.2 of chapter 2. The thermal field is almost circular at large distances from the line, while nearby the source the thermal field has an oval-like shape. By varying the dissipation length μ^{-1}, it can be seen that the distance at which the thermal field is approximately circular scales roughly as $\sim \mu L^2$.

C.2 Exponential behaviour in 1D

In the experiments, as explained in Sec. 2.2.2 of chapter 2, we will consider the thermal field only around the $y = 0$ line, and usually at distances $|x| < L$. At this small region the lines of constant temperature are approximately parallel to the heating line, as can be seen in Fig. C.2. In Fig. C.3 we show the thermal field of Fig. C.2 along the $y = 0$ line, $\theta(x, 0)$ (blue curve). It can be roughly fitted to an exponential decay, $\theta(x, 0) \simeq \theta_{max} \exp(-|x|/w_0)$ (black dashed line). The fit gives $w_0 = 6.4\,\text{mm}$, which means that it does not represent the dissipation length $\mu^{-1} = 10\,\text{mm}$ which sets the long-range behaviour of the thermal field. In experiments, we have also found this disagreement (see Sec. 2.2.2 of 2).

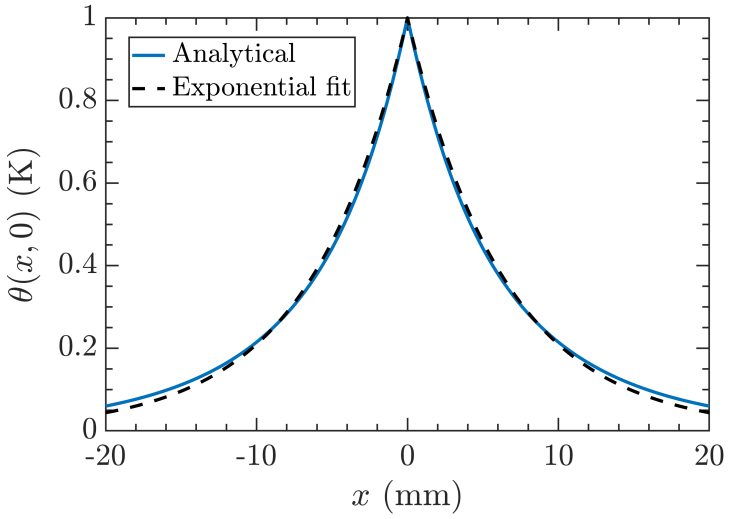

Figure C.3: Thermal field of Fig. C.2 along the $y = 0$ line, $\theta(x, 0)$ (blue curve). The dashed black line is a fit to an exponential decay, $\theta(x) \simeq \theta_{max} \exp(-|x|/w_0)$, giving the decay length $w_0 = 6.4\,\text{mm} < \mu^{-1}$.

It is possible to show that the fitted length w_0 would be equal to μ only in the case of an infinitely long heating line, $L \to \infty$. In this limit the thermal field is only a function of x,

$$\theta(x) = \frac{2\Phi_0}{\pi e \kappa} \int_0^\infty K_0\left(\mu\sqrt{s^2 + x^2}\right) ds, \tag{C.14}$$

which represents the invariance of the system along the y direction. By a change of

variables $\theta(x)$ can be expressed as

$$\theta(x) = \frac{2\Phi_0}{\pi e\kappa} |x| \int_0^\infty K_0 (\mu x \cosh u) \cosh u \, du. \tag{C.15}$$

The integral can be found in tables[2] and the thermal field reduces to

$$\theta(x) = \frac{\Phi_0}{\pi e\kappa} |x| \left[K_{1/2} \left(\frac{\mu x}{2} \right) \right]^2 = \frac{\Phi_0}{\pi e\kappa} |x| \frac{\pi e^{-\mu|x|}}{2\mu |x|} \tag{C.16}$$

$$= \frac{\Phi_0}{2\mu e\kappa} e^{-\mu|x|}, \tag{C.17}$$

which is a pure exponential decay with characteristic length $w_0 = \mu$.

In the infrared measurements the full thermal field $\theta(\mathbf{x})$ is obtained, as shown in Sec. 2.2.2 of chapter 2, so the situation will be closer to the one of Fig. C.3 where an effective decay length $w_0 < \mu^{-1}$ along the x-axis is measured.

[2] Cf. equation 6.664.6 of Ref. [82].

Bibliography

[1] P. G. de Gennes. "Wetting: statics and dynamics". In: *Reviews of Modern Physics* 57.3 (July 1, 1985), pp. 827–863. ISSN: 0034-6861. DOI: 10.1103/RevModPhys.57.827. URL: https://link.aps.org/doi/10.1103/RevModPhys.57.827.

[2] Daniel Bonn et al. "Wetting and spreading". In: *Reviews of Modern Physics* 81.2 (May 27, 2009). Publisher: American Physical Society, pp. 739–805. DOI: 10.1103/RevModPhys.81.739. URL: https://link.aps.org/doi/10.1103/RevModPhys.81.739.

[3] Alexander Oron, Stephen H. Davis, and S. George Bankoff. "Long-scale evolution of thin liquid films". In: *Reviews of Modern Physics* 69.3 (July 1, 1997), pp. 931–980. ISSN: 0034-6861, 1539-0756. DOI: 10.1103/RevModPhys.69.931. URL: https://link.aps.org/doi/10.1103/RevModPhys.69.931.

[4] Jacob N Israelachvili. *Intermolecular and surface forces. With Applications to Colloidal and Biological Systems*. Academic press, 2011.

[5] N. V. Churaev. "Surface Forces in Wetting Films". In: *Colloid Journal* 65.3 (May 1, 2003), pp. 263–274. ISSN: 1608-3067. DOI: 10.1023/A:1024292618059. URL: https://doi.org/10.1023/A:1024292618059 (visited on 08/27/2021).

[6] Benilde Saramago. "Thin liquid wetting films". In: *Current Opinion in Colloid & Interface Science* 15.5 (Oct. 1, 2010), pp. 330–340. ISSN: 1359-0294. DOI: 10.1016/j.cocis.2010.05.005. URL: https://www.sciencedirect.com/science/article/pii/S1359029410000476 (visited on 07/07/2021).

[7] Jacob N. Israelachvili and Gayle E. Adams. "Measurement of forces between two mica surfaces in aqueous electrolyte solutions in the range 0–100 nm". In: *Journal of the Chemical Society, Faraday Transactions 1: Physical Chemistry in Condensed Phases* 74.0 (1978). Publisher: Royal Society of Chemistry, pp. 975–1001. DOI: 10.1039/F19787400975. URL: https://pubs.rsc.org/en/content/articlelanding/1978/f1/f19787400975 (visited on 07/08/2021).

[8] Matthieu Roché et al. "Marangoni Flow of Soluble Amphiphiles". In: *Physical Review Letters* 112.20 (May 20, 2014). Publisher: American Physical Society, p. 208302. DOI: 10.1103/PhysRevLett.112.208302. URL: https://link.aps.org/doi/10.1103/PhysRevLett.112.208302 (visited on 09/04/2021).

[9] M. Arangalage et al. "Dual Marangoni effects and detection of traces of surfactants". In: *Soft Matter* 14.17 (2018). Publisher: Royal Society of Chemistry, pp. 3378–3386. DOI: 10.1039/C8SM00266E. URL: https://pubs.rsc.org/en/content/articlelanding/2018/sm/c8sm00266e (visited on 09/04/2021).

[10] Dolachai Boniface et al. "Self-propulsion of symmetric chemically active particles: Point-source model and experiments on camphor disks". In: *Physical Review E* 99.6 (June 17, 2019). Publisher: American Physical Society, p. 062605. DOI: 10.1103/PhysRevE.99.062605. URL: https://link.aps.org/doi/10.1103/PhysRevE.99.062605 (visited on 09/04/2021).

[11] H Bouasse. *Capillarité, Delagrave*. Paris, 1924.

[12] E. S. Benilov. "Dependence of the surface tension and contact angle on the temperature, as described by the diffuse-interface model". In: *Physical Review E* 101.4 (Apr. 27, 2020). Publisher: American Physical Society, p. 042803. DOI: 10.1103/PhysRevE.101.042803. URL: https://link.aps.org/doi/10.1103/PhysRevE.101.042803 (visited on 09/03/2021).

[13] Allen V. Hershey. "Ridges in a Liquid Surface Due to the Temperature Dependence of Surface Tension". In: *Physical Review* 56.2 (July 15, 1939), pp. 204–204. ISSN: 0031-899X. DOI: 10.1103/PhysRev.56.204. URL: https://link.aps.org/doi/10.1103/PhysRev.56.204.

[14] T. R. Anthony and H. E. Cline. "Surface rippling induced by surface-tension gradients during laser surface melting and alloying". In: *Journal of Applied Physics* 48.9 (Sept. 1, 1977). Publisher: American Institute of Physics, pp. 3888–3894. ISSN: 0021-8979. DOI: 10.1063/1.324260. URL: https://aip.scitation.org/doi/citedby/10.1063/1.324260 (visited on 09/01/2021).

[15] D. A. Willis and X. Xu. "Transport Phenomena and Droplet Formation During Pulsed Laser Interaction With Thin Films". In: *Journal of Heat Transfer* 122.4 (Apr. 19, 2000), pp. 763–770. ISSN: 0022-1481. DOI: 10.1115/1.1288931. URL: https://doi.org/10.1115/1.1288931 (visited on 09/01/2021).

[16] Jonathan Phillip Singer. "Thermocapillary approaches to the deliberate patterning of polymers". In: *Journal of Polymer Science Part B: Polymer Physics* 55.22 (Nov. 15, 2017), pp. 1649–1668. ISSN: 08876266. DOI: 10.1002/polb.24298. URL: http://doi.wiley.com/10.1002/polb.24298.

[17] A.L. Bertozzi, A. Münch, and M. Shearer. "Undercompressive shocks in thin film flows". In: *Physica D: Nonlinear Phenomena* 134.4 (Dec. 1999), pp. 431–464. ISSN: 01672789. DOI: 10.1016/S0167-2789(99)00134-7. URL: https://linkinghub.elsevier.com/retrieve/pii/S0167278999001347.

[18] Jeanman Sur, Andrea L. Bertozzi, and Robert P. Behringer. "Reverse Undercompressive Shock Structures in Driven Thin Film Flow". In: *Physical Review Letters* 90.12 (Mar. 26, 2003), p. 126105. ISSN: 0031-9007, 1079-7114. DOI: 10.1103/PhysRevLett.90.126105. URL: https://link.aps.org/doi/10.1103/PhysRevLett.90.126105.

[19] Chen-Yi Yan, Kai-Xin Hu, and Qi-Sheng Chen. "Thermocapillary instabilities of liquid layers on an inclined plane". In: *Physics of Fluids* 30.8 (Aug. 1, 2018). Publisher: American Institute of Physics, p. 082101. ISSN: 1070-6631. DOI: 10.1063/1.5039149. URL: https://aip.scitation.org/doi/full/10.1063/1.5039149 (visited on 09/01/2021).

[20] Ramkarn Patne, Yehuda Agnon, and Alexander Oron. "Thermocapillary instabilities in a liquid layer subjected to an oblique temperature gradient". In: *Journal of Fluid Mechanics* 906 (Jan. 10, 2021), A12. ISSN: 0022-1120, 1469-7645. DOI: 10.1017/jfm.2020.747. URL: https://www.cambridge.org/core/product/identifier/S0022112020007478/type/journal_article (visited on 03/03/2021).

[21] JB Brzoska, F Brochard-Wyart, and F Rondelez. "Motions of droplets on hydrophobic model surfaces induced by thermal gradients". In: *Langmuir* 9.8 (1993), pp. 2220–2224.

[22] Anton A Darhuber and Sandra M Troian. "Principles of microfluidic actuation by modulation of surface stresses". In: *Annu. Rev. Fluid Mech.* 37 (2005), pp. 425–455.

[23] Amar S. Basu and Yogesh B. Gianchandani. "Virtual microfluidic traps, filters, channels and pumps using Marangoni flows". In: *Journal of Micromechanics and Microengineering* 18.11 (Oct. 2008). Publisher: IOP Publishing, p. 115031. ISSN: 0960-1317. DOI: 10.1088/0960-1317/18/11/115031. URL: https://doi.org/10.1088/0960-1317/18/11/115031 (visited on 09/01/2021).

[24] Alireza Karbalaei, Ranganathan Kumar, and Hyoung Cho. "Thermocapillarity in Microfluidics—A Review". In: *Micromachines* 7.1 (Jan. 21, 2016), p. 13. ISSN: 2072-666X. DOI: 10.3390/mi7010013. URL: http://www.mdpi.com/2072-666X/7/1/13.

[25] *Rhodorsil Oils 47 Technical information*. URL: https://www.silitech.ch/wp-content/uploads/2021/03/32.pdf.

[26] E. Ricci, R. Sangiorgi, and A. Passerone. "Density and surface tension of dioctylphthalate, silicone oil and their solutions". In: *Surface and Coatings Technology* 28.2 (June 1, 1986), pp. 215–223. ISSN: 0257-8972. DOI: 10.1016/0257-8972(86)90060-5. URL: https://www.sciencedirect.com/science/article/pii/0257897286900605.

[27] M. J. Tan, S. G. Bankoff, and S. H. Davis. "Steady thermocapillary flows of thin liquid layers. I. Theory". In: *Physics of Fluids A: Fluid Dynamics* 2.3 (Mar. 1990), pp. 313–321. ISSN: 0899-8213. DOI: 10.1063/1.857781. URL: http://aip.scitation.org/doi/10.1063/1.857781.

[28] C. Clavaud et al. "Modification of the Fluctuation Dynamics of Ultrathin Wetting Films". In: *Physical Review Letters* 126.22 (June 4, 2021). Publisher: American Physical Society, p. 228004. DOI: 10.1103/PhysRevLett.126.228004. URL: https://link.aps.org/doi/10.1103/PhysRevLett.126.228004.

[29] J. P. Burelbach, S. G. Bankoff, and S. H. Davis. "Steady thermocapillary flows of thin liquid layers. II. Experiment". In: *Physics of Fluids A: Fluid Dynamics* 2.3 (Mar. 1990), pp. 322–333. ISSN: 0899-8213. DOI: 10.1063/1.857782. URL: http://aip.scitation.org/doi/10.1063/1.857782.

[30] Pierre-Gilles De Gennes and Françoise Brochard-Wyart. *Gouttes, bulles, perles et ondes*. Belin Éducation, 2015.

[31] *DG001U-E Photometry Form*. FLIR Advanced Thermal Solutions.

[32] *DCO19U-L SC7000 User Manual*. FLIR.

[33] Frédéric Moisy, Marc Rabaud, and Kévin Salsac. "A synthetic Schlieren method for the measurement of the topography of a liquid interface". In: *Experiments in Fluids* 46.6 (June 2009), pp. 1021–1036. ISSN: 0723-4864, 1432-1114. DOI: 10.1007/s00348-008-0608-z. URL: http://link.springer.com/10.1007/s00348-008-0608-z.

[34] Jörg Schilling et al. "Absolute interfacial distance measurements by dual-wavelength reflection interference contrast microscopy". In: *Physical Review E* 69.2 (Feb. 12, 2004), p. 021901. ISSN: 1539-3755, 1550-2376. DOI: 10.1103/PhysRevE.69.021901. URL: https://link.aps.org/doi/10.1103/PhysRevE.69.021901.

[35] Jolet de Ruiter, Frieder Mugele, and Dirk van den Ende. "Air cushioning in droplet impact. I. Dynamics of thin films studied by dual wavelength reflection interference microscopy". In: *Physics of Fluids* 27.1 (Jan. 1, 2015). Publisher: American Institute of Physics, p. 012104. ISSN: 1070-6631. DOI: 10.1063/1.4906114. URL: https://aip.scitation.org/doi/full/10.1063/1.4906114 (visited on 06/28/2021).

[36] J. Blaber, B. Adair, and A. Antoniou. "Ncorr: Open-Source 2D Digital Image Correlation Matlab Software". In: *Experimental Mechanics* 55.6 (July 2015), pp. 1105–1122. ISSN: 0014-4851, 1741-2765. DOI: 10.1007/s11340-015-0009-1. URL: http://link.springer.com/10.1007/s11340-015-0009-1.

[37] Justin Blaber. *Ncorr*. URL: https://github.com/justinblaber/ncorr_2D_matlab (visited on 08/24/2021).

[38] Matthew Harker and Paul O'Leary. "Direct regularized surface reconstruction from gradients for Industrial Photometric Stereo". In: *Computers in Industry*. Special Issue: 3D Imaging in Industry 64.9 (Dec. 1, 2013), pp. 1221–1228. ISSN: 0166-3615. DOI: 10.1016/j.compind.2013.03.013. URL: https://www.sciencedirect.com/science/article/pii/S0166361513000663 (visited on 08/24/2021).

[39] Matthew Harker and Paul O'Leary. *Surface Reconstruction from Gradient Fields: grad2Surf Version 1.0*. URL: https://www.mathworks.com/matlabcentral/fileexchange/43149-surface-reconstruction-from-gradient-fields-grad2surf-version-1-0 (visited on 08/24/2021).

[40] Eugene Hecht. *Optics, 5e, Global Edition*. Pearson Education, 2017.

[41] Joachim Rädler and Erich Sackmann. "Imaging optical thicknesses and separation distances of phospholipid vesicles at solid surfaces". In: *Journal de Physique II* 3.5 (May 1, 1993). Publisher: EDP Sciences, pp. 727–748. ISSN: 1155-4312, 1286-4870. DOI: 10.1051/jp2:1993163. URL: http://dx.doi.org/10.1051/jp2:1993163 (visited on 08/18/2021).

[42] David L. Camin, Alphonse F. Forziati, and Frederick D. Rossini. "Physical Properties of n-Hexadecane, n-Decylcyclopentane, n-Decylcyclohexane, 1-Hexadecene and n-Decylbenzene". In: *The Journal of Physical Chemistry* 58.5 (May 1954), pp. 440–442. ISSN: 0022-3654, 1541-5740. DOI: 10.1021/j150515a015. URL: https://pubs.acs.org/doi/abs/10.1021/j150515a015 (visited on 07/13/2021).

[43] T. L. Van Raalte. "Measurement of the Refractive Index of Silicone Oils for the UKAEA". In: *Journal of the Optical Society of America* 50.1 (Jan. 1, 1960), 85_2. ISSN: 0030-3941. DOI: 10.1364/JOSA.50.0085_2. URL: https://www.osapublishing.org/abstract.cfm?URI=josa-50-1-85_2.

[44] M Legrand et al. "CCD image sensor induced error in PIV applications". In: *Measurement Science and Technology* 25.6 (June 1, 2014), p. 065207. ISSN: 0957-0233, 1361-6501. DOI: 10.1088/0957-0233/25/6/065207. URL: https://iopscience.iop.org/article/10.1088/0957-0233/25/6/065207.

[45] Josephus Hulshof. "Some Aspects of the Thin Film Equation". In: *European Congress of Mathematics*. Ed. by Carles Casacuberta et al. Progress in Mathematics. Basel: Birkhäuser, 2001, pp. 291–301. ISBN: 978-3-0348-8266-8. DOI: 10.1007/978-3-0348-8266-8_25.

[46] Jürgen Becker and Günther Grün. "The thin-film equation: recent advances and some new perspectives". In: *Journal of Physics: Condensed Matter* 17.9 (Mar. 9, 2005), S291–S307. ISSN: 0953-8984, 1361-648X. DOI: 10.1088/0953-8984/17/9/002. URL: https://iopscience.iop.org/article/10.1088/0953-8984/17/9/002.

[47] Amir Alizadeh Pahlavan et al. "Thin Films in Partial Wetting: Internal Selection of Contact-Line Dynamics". In: *Physical Review Letters* 115.3 (July 17, 2015). Publisher: American Physical Society, p. 034502. DOI: 10.1103/PhysRevLett.115.034502. URL: https://link.aps.org/doi/10.1103/PhysRevLett.115.034502 (visited on 08/28/2021).

[48] Thomas Salez et al. "Numerical solutions of thin-film equations for polymer flows". In: *The European Physical Journal E* 35.11 (Nov. 2012), p. 114. ISSN: 1292-8941, 1292-895X. DOI: 10.1140/epje/i2012-12114-x. URL: http://link.springer.com/10.1140/epje/i2012-12114-x (visited on 08/28/2021).

[49] J. P. Burelbach, S. G. Bankoff, and S. H. Davis. "Nonlinear stability of evaporating/condensing liquid films". In: *Journal of Fluid Mechanics* 195 (Oct. 1988). Publisher: Cambridge University Press, pp. 463–494. ISSN: 1469-7645, 0022-1120. DOI: 10.1017/S0022112088002484. URL: https://www.cambridge.org/core/journals/journal-of-fluid-mechanics/article/nonlinear-stability-of-evaporatingcondensing-liquid-films/2FC7FE3FF8AC853536CBCBF985929558 (visited on 08/28/2021).

[50] E. V. Barakhovskaia, I. V. Marchuk, and A. A. Fedorets. "Thermocapillary deformation in a locally heated layer of silicone oil". In: *Journal of Physics: Conference Series* 754 (Oct. 2016). Publisher: IOP Publishing, p. 032002. ISSN: 1742-6596. DOI: 10.1088/1742-6596/754/3/032002. URL: https://doi.org/10.1088/1742-6596/754/3/032002 (visited on 08/28/2021).

[51] Katsuichi Kitagawa. "Thin-film thickness profile measurement by three-wavelength interference color analysis". In: *Applied Optics* 52.10 (Apr. 1, 2013), p. 1998. ISSN: 1559-128X, 2155-3165. DOI: 10.1364/AO.52.001998. URL: https://www.osapublishing.org/abstract.cfm?URI=ao-52-10-1998.

[52] Calum S. Butler et al. "Local determination of thin liquid film profiles using colour interferometry". In: *The European Physical Journal E* 39.2 (Feb. 2016), p. 14. ISSN: 1292-8941, 1292-895X. DOI: 10.1140/epje/i2016-16014-9. URL: http://link.springer.com/10.1140/epje/i2016-16014-9.

[53] *AB111838 | CAS 9016-00-6*. URL: https://abcr.com/de_en/ab111838 (visited on 07/07/2021).

[54] *AB112154 | CAS 63148-62-9*. URL: https://abcr.com/de_en/ab112154 (visited on 07/07/2021).

[55] H. C. Hamaker. "The London—van der Waals attraction between spherical particles". In: *Physica* 4.10 (Oct. 1, 1937), pp. 1058–1072. ISSN: 0031-8914. DOI: 10.1016/S0031-8914(37)80203-7. URL: https://www.sciencedirect.com/science/article/pii/S0031891437802037 (visited on 08/29/2021).

[56] F. London. "The general theory of molecular forces". In: *Transactions of the Faraday Society* 33 (1937), 8b. ISSN: 0014-7672. DOI: 10.1039/tf937330008b. URL: http://xlink.rsc.org/?DOI=tf937330008b (visited on 08/29/2021).

[57] B. V. Derjaguin, I. I. Abrikosova, and E. M. Lifshitz. "Molecular attraction of condensed bodies". In: *Physics-Uspekhi* 58.9 (Sept. 1, 2015). Publisher: IOP Publishing, p. 906. ISSN: 1063-7869. DOI: 10.3367/UFNe.0185.201509i.0981. URL: https://iopscience.iop.org/article/10.3367/UFNe.0185.201509i.0981/meta (visited on 07/08/2021).

[58] Norman F. Owens and Peter Richmond. "Hamaker constants and combining rules". In: *Journal of the Chemical Society, Faraday Transactions 2: Molecular and Chemical Physics* 74.0 (1978). Publisher: Royal Society of Chemistry, pp. 691–695. DOI: 10.1039/F29787400691. URL: https://pubs.rsc.org/en/content/articlelanding/1978/f2/f29787400691 (visited on 07/07/2021).

[59] D. Beaglehole et al. "Inadequacy of Lifshitz theory for thin liquid films". In: *Physical Review Letters* 66.16 (Apr. 22, 1991). Publisher: American Physical Society, pp. 2084–2087. DOI: 10.1103/PhysRevLett.66.2084. URL: https://link.aps.org/doi/10.1103/PhysRevLett.66.2084 (visited on 07/08/2021).

[60] Terence D. Blake. "Investigation of equilibrium wetting films of n-alkanes on α-alumina". In: *Journal of the Chemical Society, Faraday Transactions 1: Physical Chemistry in Condensed Phases* 71.0 (1975). Publisher: Royal Society of Chemistry, pp. 192–208. DOI: 10.1039/F19757100192. URL: https://pubs.rsc.org/en/content/articlelanding/1975/f1/f19757100192 (visited on 07/07/2021).

[61] Katarzyna Hänni-Ciunel, Natascha Schelero, and Regine von Klitzing. "Negative charges at the air/water interface and their consequences for aqueous wetting films containing surfactants". In: *Faraday Discussions* 141.0 (Nov. 25, 2008). Publisher: The Royal Society of Chemistry, pp. 41–53. ISSN: 1364-5498. DOI: 10.1039/B809149H. URL: https://pubs.rsc.org/en/content/articlelanding/2009/fd/b809149h (visited on 07/28/2021).

[62] J. N. Israelachvili and G. E. Adams. "Direct measurement of long range forces between two mica surfaces in aqueous KNO 3 solutions". In: *Nature* 262.5571 (Aug. 1976), pp. 774–776. ISSN: 1476-4687. DOI: 10.1038/262774a0. URL: https://www.nature.com/articles/262774a0 (visited on 07/08/2021).

[63] B. Pottier, C. Frétigny, and L. Talini. "Boundary Condition in Liquid Thin Films Revealed through the Thermal Fluctuations of Their Free Surfaces". In: *Physical Review Letters* 114.22 (June 1, 2015). Publisher: American Physical Society, p. 227801. DOI: 10.1103/PhysRevLett.114.227801. URL: https://link.aps.org/doi/10.1103/PhysRevLett.114.227801.

[64] D. Y. C. Chan and R. G. Horn. "The drainage of thin liquid films between solid surfaces". In: *The Journal of Chemical Physics* 83.10 (Nov. 15, 1985). Publisher: American Institute of Physics, pp. 5311–5324. ISSN: 0021-9606. DOI: 10.1063/1.449693. URL: https://aip.scitation.org/doi/10.1063/1.449693 (visited on 08/21/2021).

[65] J. M. Georges et al. "Drainage of thin liquid films between relatively smooth surfaces". In: *The Journal of Chemical Physics* 98.9 (May 1, 1993). Publisher: American Institute of Physics, pp. 7345–7360. ISSN: 0021-9606. DOI: 10.1063/1.465059. URL: https://aip.scitation.org/doi/10.1063/1.465059 (visited on 08/21/2021).

[66] N. N. Gosvami, S. K. Sinha, and S. J. O'Shea. "Squeeze-Out of Branched Alkanes on Graphite". In: *Physical Review Letters* 100.7 (Feb. 20, 2008). Publisher: American Physical Society, p. 076101. DOI: 10.1103/PhysRevLett.100.076101. URL: https://link.aps.org/doi/10.1103/PhysRevLett.100.076101 (visited on 08/21/2021).

[67] Gyan P. Dubey and Monika Sharma. "Temperature and Composition Dependence of the Densities, Viscosities, and Speeds of Sound of Binary Liquid Mixtures of 1-Butanol with Hexadecane and Squalane". In: *Journal of Chemical & Engineering Data* 53.4 (Apr. 1, 2008). Publisher: American Chemical Society, pp. 1032–1038. ISSN: 0021-9568. DOI: 10.1021/je7007654. URL: https://doi.org/10.1021/je7007654 (visited on 08/15/2021).

[68] Dianne J. Luning Prak et al. "Density, Viscosity, Speed of Sound, Bulk Modulus, Surface Tension, and Flash Point of Binary Mixtures of n -Dodecane with 2,2,4,6,6-Pentamethylheptane or 2,2,4,4,6,8,8-Heptamethylnonane". In: *Journal of Chemical & Engineering Data* 59.4 (Apr. 10, 2014), pp. 1334–1346. ISSN: 0021-9568, 1520-5134. DOI: 10.1021/je5000132. URL: https://pubs.acs.org/doi/10.1021/je5000132.

[69] B. M. Ocko et al. "Surface freezing in chain molecules: Normal alkanes". In: *Physical Review E* 55.3 (Mar. 1, 1997), pp. 3164–3182. ISSN: 1063-651X, 1095-3787. DOI: 10.1103/PhysRevE.55.3164. URL: https://link.aps.org/doi/10.1103/PhysRevE.55.3164.

[70] *2,2,4,4,6,8,8-HEPTAMETHYLNONANE | 4390-04-9*. URL: https://www.chemicalbook.com/chemicalProductProperty_EN_CB3251935.htm (visited on 08/21/2021).

[71] Gabor Korosi and E Sz Kovats. "Density and surface tension of 83 organic liquids". In: *Journal of Chemical and Engineering Data* 26.3 (1981), pp. 323–332.

[72] Diana Cholakova and Nikolai Denkov. "Rotator phases in alkane systems: In bulk, surface layers and micro/nano-confinements". In: *Advances in Colloid and Interface Science* 269 (July 1, 2019), pp. 7–42. ISSN: 0001-8686. DOI: 10.1016/j.cis.2019.04.001. URL: https://www.sciencedirect.com/science/article/pii/S0001868619300557 (visited on 08/15/2021).

[73] Paul Lazar, H. Schollmeyer, and H. Riegler. "Spreading and Two-Dimensional Mobility of Long-Chain Alkanes at Solid/Gas Interfaces". In: *Physical Review Letters* 94.11 (Mar. 22, 2005), p. 116101. ISSN: 0031-9007, 1079-7114. DOI: 10.1103/PhysRevLett.94.116101. URL: https://link.aps.org/doi/10.1103/PhysRevLett.94.116101.

[74] Samira Shiri et al. "Thermal Marangoni Flow Impacts the Shape of Single Component Volatile Droplets on Thin, Completely Wetting Substrates". In: *Physical Review Letters* 127.2 (July 8, 2021). Publisher: American Physical Society, p. 024502. DOI: 10.1103/PhysRevLett.127.024502. URL: https://link.aps.org/doi/10.1103/PhysRevLett.127.024502 (visited on 08/21/2021).

[75] R. Seemann, S. Herminghaus, and K. Jacobs. "Dewetting Patterns and Molecular Forces: A Reconciliation". In: *Physical Review Letters* 86.24 (June 11, 2001), pp. 5534–5537. ISSN: 0031-9007, 1079-7114. DOI: 10.1103/PhysRevLett.86.5534. URL: https://link.aps.org/doi/10.1103/PhysRevLett.86.5534.

[76] H. M. J. M. Wedershoven et al. "Infrared laser induced rupture of thin liquid films on stationary substrates". In: *Applied Physics Letters* 104.5 (Feb. 3, 2014). Publisher: American Institute of Physics, p. 054101. ISSN: 0003-6951. DOI: 10.1063/1.4863318. URL: https://aip.scitation.org/doi/full/10.1063/1.4863318 (visited on 04/19/2021).

[77] Elías Pérez, Erik Schäffer, and Ullrich Steiner. "Spreading Dynamics of Polydimethylsiloxane Drops: Crossover from Laplace to Van der Waals Spreading". In: *Journal of Colloid and Interface Science* 234.1 (Feb. 1, 2001), pp. 178–193. ISSN: 0021-9797. DOI: 10.1006/jcis.2000.7292. URL: https://www.sciencedirect.com/science/article/pii/S0021979700972928.

[78] L H Tanner. "The spreading of silicone oil drops on horizontal surfaces". In: *Journal of Physics D: Applied Physics* 12.9 (Sept. 14, 1979), pp. 1473–1484. ISSN: 0022-3727, 1361-6463. DOI: 10.1088/0022-3727/12/9/009. URL: https://iopscience.iop.org/article/10.1088/0022-3727/12/9/009.

[79] O. V. Voinov. "Hydrodynamics of wetting". In: *Fluid Dynamics* 11.5 (Sept. 1, 1976), pp. 714–721. ISSN: 1573-8507. DOI: 10.1007/BF01012963. URL: https://doi.org/10.1007/BF01012963 (visited on 09/02/2021).

[80] R. G. Cox. "The dynamics of the spreading of liquids on a solid surface. Part 1. Viscous flow". In: *Journal of Fluid Mechanics* 168 (July 1986). Publisher: Cambridge University Press, pp. 169–194. ISSN: 1469-7645, 0022-1120. DOI: 10.1017/S0022112086000332. URL: https://www.cambridge.org/core/journals/journal-of-fluid-mechanics/article/dynamics-of-the-spreading-of-liquids-on-a-solid-surface-part-1-viscous-flow/97CAB1BF3439F4B1AA429FFA37C80C42 (visited on 09/02/2021).

[81] T. Bickel. "Effect of surface-active contaminants on radial thermocapillary flows". In: *The European Physical Journal E* 42.10 (Oct. 7, 2019), p. 131. ISSN: 1292-895X. DOI: 10.1140/epje/i2019-11896-5. URL: https://doi.org/10.1140/epje/i2019-11896-5 (visited on 09/05/2021).

[82] Izrail Solomonovich Gradshteyn and Iosif Moiseevich Ryzhik. *Table of integrals, series, and products*. Academic press, 2014.

RÉSUMÉ

La description hydrodynamique des liquides à très petites échelles nécessite de considérer des effets spécifiques à ces échelles, tels que les forces intermoléculaires. Nous nous sommes intéressés à ces effets en étudiant le comportement de films liquides sur des substrats solides, d'épaisseurs de quelques dizaines de microns, qui sont manipulés par des gradients thermiques. Les écoulements Marangoni résultant des gradients thermiques permettent un démouillage contrôlé des films liquides. En utilisant deux techniques optiques différentes, nous avons mesuré les profils de hauteur de ces films en fonction du temps, pour des épaisseurs couvrant 3 décades et avec une résolution de quelques nanomètres. La dynamique expérimentale d'amincissement des films est discutée à l'aide d'une résolution numérique de l'équation de films minces. On montre que l'effet thermocapillaire produit un régime local qui est caractérisé uniquement par l'interaction du gradient de la tension de surface et de la pression de disjonction. L'évolution maîtresse qui en résulte permet de caractériser complètement le gradient du champ thermique. La déviation par rapport à cette courbe maîtresse résulte de l'effet des forces intermoléculaires, et la dérivée d'une pression de disjonction a pu être obtenue à partir de données expérimentales pour des épaisseurs allant de 10 à 100 nm. Dans le cas de liquides mouillants (huiles silicone sur un substrat en verre), la pression de disjonction suit une loi de puissance avec l'épaisseur qui ne peut pas être décrite par le modèle de van der Waals communément supposé. Par ailleurs, nous fournissons des résultats sur des films instables de deux alcanes sur le même substrat, qui se rompent par l'effet combiné de la thermocapillarité et des forces intermoléculaires attractives. Dans ce cas, il se forme un pied ultra-mince qui recule vers une ligne de contact macroscopique. Enfin, l'effet du film ultra-mince sur la dynamique de relaxation des films lors de la suppression du champ thermique moteur est également étudié. Dans le cas de l'huile de silicone, on montre comment la forme du film ultra-mince affecte la récupération de la configuration homogène initiale. Dans le cas des films d'alcane, la ligne de contact reste fixe une fois que le champ thermique est supprimé.

MOTS CLÉS

Propriétés physico-chimiques, mouillage, films utra minces

ABSTRACT

A hydrodynamic description of liquids at very small scales requires to consider effects specific to these scales, such as intermolecular forces. We have investigated these effects by studying the behaviour of supported liquid films of thicknesses of a few tens of microns, that are driven by thermal gradients. The Marangoni flows resulting from the thermal gradients allow a controlled dewetting of the liquid films. Using two different optical techniques, we have measured the height profiles of these films as a function of time, for thicknesses spanning 3 decades and with a resolution of a few nanometers. The experimental thinning dynamics is discussed with the help of a numerical resolution of the thin-film equation. We show that the thermocapillary effect produces a local regime which is solely characterised by the interplay of the surface tension gradient and the disjoining pressure. The resulting master evolution allows to fully characterise the gradient of the thermal field. Deviations from this master curve result from the effect of intermolecular forces, and the derivative of a disjoining pressure could be obtained from experimental data for thicknesses ranging from 10 to 100 nm. In the case of wetting liquids (silicone oils on a glass substrate), the disjoining pressure follows a power-law with thickness that cannot be described by the commonly assumed van der Waals model. In addition, we provide results on unstable films of two alkanes on the same substrate, which break up by the combined effect of thermocapillarity and attractive intermolecular forces. In this case, an ultra-thin foot that recedes towards a macroscopic contact line is formed. Finally, the effect of the ultra-thin film in the relaxation dynamics of the films upon removing the driving thermal field is also studied. In the case of silicone oil, we show how the shape of the ultra-thin film affects the recovery of the initial homogeneous configuration. In the case of alkane films, the contact line remains fixed once the thermal field is removed.

KEYWORDS

Physico-chemical properties, wetting, ultra thin films

RÉSUMÉ

La description hydrodynamique des liquides à très petites échelles nécessite de considérer des effets spécifiques à ces échelles, tels que les forces intermoléculaires. Nous nous sommes intéressés à ces effets en étudiant le comportement de films liquides sur des substrats solides, d'épaisseurs de quelques dizaines de microns, qui sont manipulés par des gradients thermiques. Les écoulements Marangoni résultant des gradients thermiques permettent un démouillage contrôlé des films liquides. En utilisant deux techniques optiques différentes, nous avons mesuré les profils de hauteur de ces films en fonction du temps, pour des épaisseurs couvrant 3 décades et avec une résolution de quelques nanomètres. La dynamique expérimentale d'amincissement des films est discutée à l'aide d'une résolution numérique de l'équation de films minces. On montre que l'effet thermocapillaire produit un régime local qui est caractérisé uniquement par l'interaction du gradient de la tension de surface et de la pression de disjonction. L'évolution maîtresse qui en résulte permet de caractériser complètement le gradient du champ thermique. La déviation par rapport à cette courbe maîtresse résulte de l'effet des forces intermoléculaires, et la dérivée d'une pression de disjonction a pu être obtenue à partir de données expérimentales pour des épaisseurs allant de 10 à 100 nm. Dans le cas de liquides mouillants (huiles silicone sur un substrat en verre), la pression de disjonction suit une loi de puissance avec l'épaisseur qui ne peut pas être décrite par le modèle de van der Waals communément supposé. Par ailleurs, nous fournissons des résultats sur des films instables de deux alcanes sur le même substrat, qui se rompent par l'effet combiné de la thermocapillarité et des forces intermoléculaires attractives. Dans ce cas, il se forme un pied ultra-mince qui recule vers une ligne de contact macroscopique. Enfin, l'effet du film ultra-mince sur la dynamique de relaxation des films lors de la suppression du champ thermique moteur est également étudié. Dans le cas de l'huile de silicone, on montre comment la forme du film ultra-mince affecte la récupération de la configuration homogène initiale. Dans le cas des films d'alcane, la ligne de contact reste fixe une fois que le champ thermique est supprimé.

MOTS CLÉS

Propriétés physico-chimiques, mouillage, films utra minces

ABSTRACT

A hydrodynamic description of liquids at very small scales requires to consider effects specific to these scales, such as intermolecular forces. We have investigated these effects by studying the behaviour of supported liquid films of thicknesses of a few tens of microns, that are driven by thermal gradients. The Marangoni flows resulting from the thermal gradients allow a controlled dewetting of the liquid films. Using two different optical techniques, we have measured the height profiles of these films as a function of time, for thicknesses spanning 3 decades and with a resolution of a few nanometers. The experimental thinning dynamics is discussed with the help of a numerical resolution of the thin-film equation. We show that the thermocapillary effect produces a local regime which is solely characterised by the interplay of the surface tension gradient and the disjoining pressure. The resulting master evolution allows to fully characterise the gradient of the thermal field. Deviations from this master curve result from the effect of intermolecular forces, and the derivative of a disjoining pressure could be obtained from experimental data for thicknesses ranging from 10 to 100 nm. In the case of wetting liquids (silicone oils on a glass substrate), the disjoining pressure follows a power-law with thickness that cannot be described by the commonly assumed van der Waals model. In addition, we provide results on unstable films of two alkanes on the same substrate, which break up by the combined effect of thermocapillarity and attractive intermolecular forces. In this case, an ultra-thin foot that recedes towards a macroscopic contact line is formed. Finally, the effect of the ultra-thin film in the relaxation dynamics of the films upon removing the driving thermal field is also studied. In the case of silicone oil, we show how the shape of the ultra-thin film affects the recovery of the initial homogeneous configuration. In the case of alkane films, the contact line remains fixed once the thermal field is removed.

KEYWORDS

Physico-chemical properties, wetting, ultra thin films